Iron oxychloride/biochar nanocomposite for heterogeneous advanced oxidation of sulphamethoxazole in water

by

NOMPUMELELO ANGEL SIMAMANE

submitted in accordance with the requirements

for the degree of

MSc in CHEMISTRY

in the subject

School of Science

at the

UNIVERSITY OF SOUTH AFRICA

Supervisor: **Dr. GCINA MAMBA**

Co-supervisors: **PROF. THABO TI NKAMBULE**

DR. TSHEPO J MALEFETSE

July 2026

DECLARATION

Name: Nompumelelo Angel Simamane

Student number: 18070906

Degree: MSc in Chemistry

The precise title of the dissertation or thesis as it appears on the copies submitted for examination:

IRON OXYCHLORIDE/BIOCHAR NANOCOMPOSITE FOR HETEROGENEOUS ADVANCED OXIDATION OF SULPHAMETHOXAZOLE IN WATER

I hereby declare that this dissertation is my own work and that all sources used or quoted have been properly indicated and acknowledged through complete references.

I also confirm that this thesis has been evaluated using plagiarism detection software and complies with the institutional standards for academic originality.

I also affirm that neither this work nor any portion of it has been submitted before for examination at the University of South Africa or any other higher education institution for a different qualification.

Signature:  **Date**: 01/07/2026

SUMMARY

Biochar/iron oxychloride (BC/FeOCl) nanocomposites were synthesised using ultrasonic-assisted wet impregnation and calcination for the degradation of sulphamethoxazole (SMX) in the presence of visible light. Structural, morphological, surface, and chemical properties were characterised using UV-vis-DRS, XRD, FESEM-EDS, HRTEM, XPS, BET, and FT-IR to relate material features to photocatalytic performance. The BC/FeOCl composite achieved 90.1% SMX removal within 120 min under visible light, attributed to improved adsorption, charge separation, and reactive species generation. The influence of catalyst composition, dosage, pH, pollutant concentration, and environmental water matrices was investigated to establish practical relevance. In addition, the effect of the synthesis route on oxidant activation was further evaluated by comparing wet impregnation-pyrolysis and ultrasonic-assisted mechanical mixing methods for PMS and H_2O_2 activation. The impregnated composite showed superior efficiency due to enhanced Fe^{2+}/Fe^{3+} redox cycle and improved interfacial contact. Scavenging studies identified dominant reactive species, and reusability tests confirmed catalyst stability after repeated cycles.

Key Terms: Photocatalysis; Sulphamethoxazole; BC/FeOCl; Sulphate radical-based AOPs; Peroxymonosulphate; Water treatment.

DEDICATION

This work is lovingly dedicated to **God**, my ever-present source of strength, wisdom, and guidance throughout this journey. Without His grace and faithfulness, none of this would have been possible.

I also dedicate it to my **late grandmother (B.I Simamane)**, whose love, prayers, and unwavering belief in me continue to inspire and motivate me every day. Her strength and nurturing spirit laid the foundation for the person I have become and reminded me, even in her absence, that I could do this. I further dedicate this work to my **late mother (M. Mnyandu)**, though she left when I was really young, I remember how much she praised education and I am 100% sure she is proud where she is. Lastly, to my **late big brother (T. Simamane)**, who recently left us while I was nearing completion of this work. His unconditional love, belief in my potential, and constant encouragement through every stage of my life meant the world to me. Losing him was one of the greatest challenges I have faced, but his memory continues to give me strength. I know he is watching over me with pride.

ACKNOWLEDGEMENTS

- I wish to extend my heartfelt gratitude to my supervision team, **Dr. Gcina Mamba**, **Prof. Thabo T.I. Nkambule**, and **Dr. Tshepo J. Malefetse**, for their unwavering support, insightful guidance, and encouragement throughout my MSc studies. Their mentorship, constructive feedback, and patience played a pivotal role in helping me complete this thesis successfully.
- My appreciation also goes to the **Institute for Nanotechnology and Water Sustainability (iNanoWS)** and the **Urban Water Cycle & Water Treatment Technologies (UWC & WTT)** thematic area at the **University of South Africa**. The constructive comments, suggestions, and discussions I received from the team members greatly enriched my research and enhanced the overall quality of my work.
- I gratefully acknowledge the financial support received from **iNanoWS**, University of South Africa, which made this research work possible
- I am equally appreciative of the **Departments of Chemistry and Chemical Engineering** for their technical assistance in the laboratory, particularly with the use of UV–Vis spectroscopy. My sincere thanks go to **Dr. Potlako Mafa** for his guidance with electrochemical characterisation techniques and for taking the time to proofread my published paper, which significantly improved the final outcome.
- I would also like to extend my heartfelt thanks to some of the PhD students, namely **Mr. Anele Tshaka** and **Mr. Mope Edwin Malefana**, for their kind assistance with SEM and XPS data analysis. Their willingness to share their expertise was greatly appreciated. Special thanks are due to my fellow MSc colleague, **Ms. Nonhle Siphelele Neliswa Mabaso**, for the many discussions we shared while exchanging ideas on degradation analyses, and for her generosity in offering me a place to stay close to campus whenever my experiments ran late into the night.
- Lastly, I wish to express my deepest gratitude to my very special **family members and friends** for their emotional, mental, and financial support throughout this journey. A heartfelt thank you to my aunt, **M.L.M. Simamane**, who lovingly took over my care from my grandmother and supported me in

every possible way, and to my father (**Mr D.A. Simamane**) for his constant love and presence. Your unwavering belief in me has been a source of comfort and strength, and for that, I am forever grateful.

PUBLICATIONS AND PRESENTATIONS

Conference Presentations

- **Nompumelelo Angel Simamane**, P.J Mafa, N. Chaukura, T.T.I Nkambule, T.J Malefetse, and G. Mamba. Poster presentation. Heterogeneous peroxymonosulphate activation over FeOCl/Biochar nanocomposite for advanced oxidation of antibiotics in water. 8th International Water Association Specialist Conference on Natural Organic Matter (NOM8) and the IWA Particle Separation Conference. 3 – 8 December 2023.
- **Nompumelelo Angel Simamane**, P.J Mafa, N. Chaukura, T.T.I Nkambule, T.J Malefetse, and G. Mamba. Flash presentation and poster. Biochar/iron oxychloride binary nanocomposite for the oxidation of the sulphamethoxazole in water. Pan Africa Chemistry Network Congress 2024-Nairobi, Kenya. 29-31 October 2024.

Publications

- N. A Simamane, P.J. Mafa, N. Chaukura, T.T.I Nkambule, T.J. Malefetse, and G. Mamba, Leveraging biochar/iron oxychloride heterostructures for sulphamethoxazole pollution mitigation in water: Influential factors, environmental relevance, and mechanistic insights, **Published in** *Surfaces and Interfaces* 72 (2025) 107351, https://doi.org/10.1016/j.surfin.2025.107351. (Impact factor:6.3, Q1, Citation score: 8.5)
- N.A. Simamane, T.T.I Nkambule, T.J. Malefetse, G Mamba, Harnessing PMS/visible light photocatalysis over Biochar/FeOCl for efficient sulphamethoxazole degradation: Influence of materials synthesis protocol and environmental validation, **Published** in *Next Materials* 12 (2026)102387, https://doi.org/10.1016/j.nxmate.2026.102387 (Impact factor: 3.35, Q2, Citation score: 1.9)

ABSTRACT

The increasing occurrence of antibiotic contaminants in aquatic environments presents a growing challenge for water purification and public health, particularly due to their environmental persistence and their capacity to promote antimicrobial resistance. Among these contaminants, SMX, a widely used sulphonamide antibiotic, has been frequently detected in surface and wastewater systems. This study focuses on the synthesis, characterisation, and catalytic performance of biochar-supported iron oxychloride (BC/FeOCl) nanocomposites for the degradation of SMX through visible light-driven advanced oxidation processes. In the first part of this work, FeOCl was selected as a catalytic component because of its suitable bandgap, visible-light response, and strong oxidative potential. Biochar was then integrated as a support material to enhance surface area, pollutant adsorption, and charge transfer efficiency. The BC/FeOCl composite was synthesised via ultrasonic-assisted wet impregnation and calcination method and exhibited superior photocatalytic performance, achieving 90.1% SMX degradation in 120 min under visible light, outperforming pristine FeOCl (70.0%) and BC (43.2%). The enhanced activity was attributed to the synergistic interaction between FeOCl and biochar, which was later elucidated through comprehensive structural, morphological, and surface characterisation. Detailed characterisation using XRD, FESEM-EDS, HRTEM, XPS, FT-IR, UV-vis-DRS, and BET confirmed improved charge separation and suppressed recombination in the BC/FeOCl composite. Radical scavenging experiments indicated that hydroxyl radicals ($HO^{\bullet}$) and photogenerated holes (h^{+}) were the dominant reactive species. The catalyst also maintained high activity in various environmental water matrices, confirming its applicability in real-world water systems.

The second phase of this work examined two different synthesis methods, namely the wet impregnation and pyrolysis method for WP-BC/FeOCl, and the ultrasonic-assisted mechanical mixing method for MM-BC/FeOCl for the activation of peroxymonosulphate (PMS) and hydrogen peroxide (H_2O_2) for the removal of SMX in water. The wet impregnation and pyrolysis method confirmed better photodegradation activities using UV-vis, FEEM, and UV_{254}. The WP-BC/FeOCl demonstrated higher SMX removal (94.9%) than the MM-BC/FeOCl counterpart (82.3%) within 120 min, attributed to a higher Fe^{2+} content and improved morphology enhancing redox cycling.

Reactive species identification revealed singlet oxygen ($^1O_2$) as the predominant oxidant during PMS activation, followed by sulphate ($SO_4^{\bullet -}$) and hydroxyl radicals ($HO^\bullet$). However, H_2O_2 activation over 6-BC/FeOCl showed even stronger initial performance, achieving up to 89.0% degradation efficiency in the first 20 min due to synergistic effects between the catalyst and H_2O_2. Optimal H_2O_2 concentration (3 mM) and mildly acidic conditions (pH 5) enhanced hydroxyl radical generation through Fe(II)/Fe(III) redox cycling within FeOCl, as represented by the Fenton-like reactions ($Fe^{3+} + H_2O_2 \rightarrow Fe^{2+} + HO_2^\bullet + H^+$; $Fe^{2+} + H_2O_2 \rightarrow Fe^{3+} + HO^\bullet + HO^-$). At higher oxidant dosages, radical self-scavenging reduced efficiency, aligning with established Fenton system behaviour. These results highlight the superior activation of H_2O_2 compared to PMS, particularly in the initial degradation phase, due to enhanced electron mobility and efficient $HO^\bullet$ generation facilitated by Fe–O and Fe–Cl linkages in the biochar-supported structure.

Overall, this work demonstrated that the integration of FeOCl with biochar significantly enhances both photocatalytic and oxidant-activated degradation of SMX. The findings emphasise how synthesis route, surface chemistry, and redox behaviour collectively influence catalytic efficiency and reactive species generation. The BC/FeOCl nanocomposite was subjected to reuse tests, after which XRD and FT-IR analysis were conducted to determine its structural integrity. The results presented a promising, sustainable approach for removing persistent pharmaceutical contaminants from water and advancing environmentally relevant oxidation technologies.

TABLE OF CONTENTS

Description	page no.
DECLARATION	i
SUMMARY	ii
DEDICATION	iii
ACKNOWLEDGEMENTS	iv
PUBLICATIONS AND PRESENTATIONS	vi
ABSTRACT	vii
TABLE OF CONTENTS	ix
LIST OF FIGURES	xiii
LIST OF TABLES	xvi
LIST OF ACRONYMS	xvii
Chapter 1 INTRODUCTION	1
1.1 Background	1
1.2 Problem statement	2
1.3 Justification of the study	3
1.4 Aim and objectives of the study	5
1.5 Research questions	5
1.6 Chapter summary and dissertation overview	6
References	10
Chapter 2 LITERATURE REVIEW	14
2.1 Emerging compounds	14
2.2 Pharmaceuticals in the aquatic environment	16
2.2.1 Sulphonamides in freshwater systems	20
2.3 Environmental pollution	22
2.4 Removal of antibiotics from water	23

2.5 Advanced oxidation processes for removal of antibiotics 25
2.5.1 Ozonation 27
2.5.2 Sonolysis 28
2.5.3 Fenton-based processes 28
2.5.4 Photocatalytic processes 31
2.5.5 Iron-oxychloride-based photocatalysts 33
2.5.6 Carbon-based materials in photocatalysis 36
2.5.7 Biochar-based nanocomposites photocatalysts 37
2.5.8 Sulphate radical-based advanced oxidation processes 40
2.5.9 Peroxymonosulphate/persulphate catalytic/photo-catalytic activation 42
2.6 Chapter Summary 45
References 47
Chapter 3 EXPERIMENTAL METHODOLOGY 69
3.1 Introduction 69
3.2 Materials and reagents 70
3.3 Overview of synthesis methods for supported metal-based photocatalysts 70
3.3.1 Ultrasound-assisted wet impregnation 70
3.3.2 Calcination 71
3.3.3 Synthesis of biochar/iron oxychloride heterojunctions 72
3.4 Characterisation of the prepared materials 75
3.4.1 Zeiss Field Emission Scanning Electron Microscope 76
3.4.2 High-resolution transmission electron microscopy 78
3.4.3 Energy dispersive spectroscopy 79
3.4.4 Fourier-transform infrared spectroscopy 80
3.4.5 X-ray diffraction analysis 81
3.4.6 Brunauer-Emmet-Teller analysis 82
3.4.7 X-ray photoelectron spectroscopy 83

3.4.8 Ultraviolet-visible spectroscopy 84
3.5 Advanced oxidation experiments 85
3.5.1 Photocatalytic oxidation of sulphamethoxazole 86
3.5.2 PMS-assisted photocatalytic degradation of SMX 86
3.5.3 Degradation kinetics 87
3.6 Chapter Summary 89
References 90
Chapter 4 BIOCHAR/IRON OXYCHLORIDE PHOTOCATALYTIC DEGRADATION OF SULPHAMETHOXAZOLE IN WATER 96
4.1 Introduction 96
4.2 Results and Discussion 97
4.2.1 Surface morphology and microstructural analysis 97
4.2.2 X-ray diffraction and textural properties 100
4.2.3 Functional groups and chemical analysis 101
4.2.4 Optical properties and electrochemical measurements 103
4.2.5 Photocatalytic degradation of sulphamethoxazole 106
4.2.6 Effect of the initial sulphamethoxazole concentration and the photocatalyst dosage 108
4.2.7 Influence of the initial pH of the pollutant solution 110
4.2.8 Effects of organic matter and inorganic anions 112
4.2.9 Probing the Influential Reactive Species 113
4.2.10 Degradation of sulphamethoxazole in different water matrices 114
4.2.11 SMX degradation analysis using fluorescence excitation-emission matrix 116
4.2.12 Investigation of the stability of the photocatalyst 121
4.2.13 Possible charge generation and transfer pathways 122
4.3 Chapter summary 123
References 125

Chapter 5: Degradation of sulphamethoxazole using pms-assisted Biochar/FeOCl nanocomposite 131
5.1 Introduction 131
5.2 Results and discussion 131
5.2.1 Morphological and microstructural characterisation 131
5.2.2 XRD and functional group analysis 134
5.2.3 Sulphamethoxazole photocatalytic degradation 141
5.3 Key reaction parameters 144
5.3.1 Sulphamethoxazole, PMS, and photocatalyst dosage 144
5.3.2 Effect of solution pH 145
5.3.3 Effect of coexisting inorganic ions and natural organic matter 147
5.3.4 Identification of reactive species 148
5.3.5 Sulphamethoxazole degradation in different water matrices 149
5.3.6 Photo-Fenton-like sulphamethoxazole degradation 154
5.3.7 Mechanism of SMX degradation by the WP-BC/FeOCl/PMS system 156
5.3.8 Recyclability studies 159
5.4 Chapter summary 160
References 162
Chapter 6 Conclusion and recommendations 170
6.1 Conclusion 170
6.2 Recommendations 172
APPENDICES 174

LIST OF FIGURES

Figure ..... **page no.**
Figure 1.1: Dissertation structure 7
Figure 2.1: Types of EPs from various sources that can be monitored using targeted and screening approaches [9]. 15
Figure 2.2: Several pharmaceutical compounds commonly found in the environment [25] 17
Figure 2.3: Different pathways of the introduction of antibiotics into the environment [32]. 19
Figure 2.4 General structure of sulphonamide antibiotics [51]. 20
Figure 2.5 Structure of sulphamethoxazole [57]. 21
Figure 2.6 Working mechanism of the advanced oxidation process [78]..... 26
Figure 2.7 Schematic representation of the photocatalysis mechanism 32
Figure 2.8 An illustration of the partial pyrolysis method for the synthesis of FeOCl 33
Figure 2.9 Molecular structure of FeOCl [117]..... 34
Figure 2.10 A basic illustration of biochar synthesis from biomass via pyrolysis 38
Figure 2.11 Typical degradation mechanism of the BC-supported photocatalyst for organic pollutants in water/wastewater [151]..... 39
Figure 2.12 Structures of the PS and PMS. The yellow colour is the sulfur atom, and the red colour is the oxygen atom. The dashed line represents the fission position of O-O bond for the formation of sulphate radicals [155]. 42
Figure 2.13 Typical example of a mechanism of PMS activation over FeOCl [174]. 43
Figure 3.1 The synthesis of CO_3O_4/MCM-41-U using an ultrasonic-assisted wet-impregnation [5]. 71
Figure 3.2 The calcination method for the synthesis of ultrathin g-C_3N_4/FeOCl material [8]. 72
Figure 3.3 (a) Summary schematic illustration of 6-BC/FeOCl nanocomposite via ultrasonic-assisted wet impregnation and calcination method, (b) FeOCl synthesis via calcination of $FeCl_3 \cdot 6H_2O$ 74
Figure 3.4 Summary schematic illustration of MM-BC/FeOCl synthesis via the ultrasonic-assisted mechanical mixing 75
Figure 3.5 Schematic of the scanning electron microscope [14]. 77

Figure 3.6 Schematic illustration of HR-TEM [18]. 79
Figure 3.7 Basic components of the FT-IR spectrometer [23]. 80
Figure 4.1 SEM images of (a) FeOCl, (b) BC, and (c) 6-BC/FeOCl; TEM images of (d) FeOCl, (e) BC, and (f) 6-BC/FeOCl; HR-TEM image of (g) FeOCl and (h) 6-BC/FeOCl, and (i) EDS spectra of 6-BC/FeOCl 99
Figure 4.2 (a-e) EDS elemental mapping images of 6-BC/FeOCl. 100
Figure 4.3 (a) XRD patterns and (b) BET surface area, pore volume, pore diameter, and N2 adsorption-desorption isotherms of FeOCl, BC, and 6-BC/FeOCl. 101
Figure 4.4 (a) FT-IR spectra, (b) X-ray photoelectron spectroscopy (XPS) survey scan for FeOCl and 6-BC/FeOCl, high-resolution XPS of (c) Fe 2p, (d) O 1s, (e) Cl 2p of FeOCl, and 6-BC/FeOCl, respectively, and (f) C 1s of 6-BC/FeOCl..... 103
Figure 4.5 (a) UV-vis DRS spectra, (b) Tauc plots, (c) CV curve plots, (d) LSV curve plots, (e) EIS Nyquist plots, and (f) Tafel polarisation plots of FeOCl and 6-BC/FeOCl 106
Figure 4.6 (a) SMX degradation using different catalysts, (b) SMX degradation rate constants of the different catalysts, (c) UV-vis spectra for SMX degradation over 6-BC/FeOCl, (d) SMX concentration, (e) catalyst dosage, (f) initial solution pH, and (g) 6-BC/FeOCl zeta potential. Optimum conditions (SMX =10 ppm, catalyst = 0.2 g/L, pH = 5). 111
Figure 4.7 (a) Effect of different environmental inorganic ions and HA; (b) identification of predominant reactive species; (c) SMX degradation in various surface water and wastewater effluent matrices; (d) corresponding reaction rate constants for SMX removal in different surface water matrices and wastewater effluent. Optimum conditions (SMX =10 ppm, catalyst = 0.2 g/L, pH = 5). 115
Figure 4.8 FEEM spectra of sulphamethoxazole degradation in DI water (a) at 0 min, (b) after 60 min, and (c) after 120 min using 6-BC/FeOCl under visible light irradiation, and (d) specific ultraviolet (UV_{254}) absorbance removal during SMX degradation in DI, tap, wastewater effluent, and river water. 119
Figure 4.9 Sulphamethoxazole degradation fluorescence spectra for tap water (a - c), wastewater effluent (d - f), and river water (g – i) before and after photodegradation using 6-BC/FeOCl photocatalyst under visible light irradiation..... 120
Figure 4.10 (a) Reusability test and (b, and c) XRD and FT-IR spectra of 6-BC/FeOCl before and after use 122

Figure 4.11 : Proposed mechanism for SMX degradation over the 6-BC/FeOCl catalyst under visible light irradiation 123
Figure 5.1 SEM micrographs of (a) WP-BC/FeOCl and (b) MM-BC/FeOCl, along with TEM and HR-TEM images of (c, d) WP-BC/FeOCl and (e, f) MM-BC/FeOCl 133
Figure 5.2 EDS elemental mapping images of (a) WP-BC/FeOCl and (b) MM-BC/FeOCl 134
Figure 5.3 (a) XRD, (b) FT-IR, and (c) UV-vis DRS for FeOCl, WP-BC/FeOCl, and MM-BC/FeOCl. Mott-Schottky curve of (d) WP-BC/FeOCl and (e) MM-BC/FeOCl. 138
Figure 5.4 (a) XPS survey scan and high-resolution XPS of (b) C 1s, (c) O 1s, (d) Cl 2p, (e) Fe 2p, and (f) VB-XPS of WP-BC/FeOCl and MM-BC/FeOCl 141
Figure 5.5 SMX degradation under (a) different catalyst compositions and (b) corresponding rate constants. (c) Variation in SMX absorbance in the WP-BC/FeOCl/PMS/Vis system. Optimisation of (d) initial SMX concentration, (e) PMS concentration, (f) catalyst dosage, (g) pH, and (h) catalyst charge in the WP-BC/FeOCl system under PMS and visible light activation. 147
Figure 5.6 WP-BC/FeOCl + PMS analysis of (a) Effects of humic acid + coexisting anions, (b) radical trapping experiments, (c) Effect of different water matrix, (d) corresponding rate constants, and (e) UV_{254} removal of WP-BC/FeOCl during SMX degradation with and without PMS. 151
Figure 5.7 Sulphamethoxazole degradation 3D fluorescence spectra for DI water (a - c), tap water (e - f), river water (g - i), and wastewater effluent (j – l) before and after photodegradation using the WP-BC/FeOCl/PMS/Vis system 153
Figure 5.8 SMX degradation under (a) different catalyst compositions, (b) optimized H_2O_2 dosage, (c) varying pH conditions, and (d) comparison of photocatalysis, PMS activation, and Fenton-like reactions at an initial pH of 5 156
Figure 5.9 Electrochemical properties of the materials: (a) Bode phase angle, (b) EIS, and (c) CV. (d) Proposed mechanism of SMX degradation by WP-BC/FeOCl in the presence of PMS. 157
Figure 5.10 Proposed mechanism for SMX degradation over the WP-BC/FeOCl/PMS/Vis system. 159
Figure 5.11 (a) Reusability studies of WP-BC/FeOCl/PMS/vis system and (b) FT-IR spectra of fresh and used catalysts. 160

LIST OF TABLES

Table **page no**

Table 4.1: Comparison of SMX degradation in water using 6-BC/FeOCl with other photocatalysts 116
Table 4.2: Different organic compounds found in water and detected in five different regions on the fluorescence excitation-emission matrix [42]. 118
Table 4.3: Physicochemical properties of the water matrices used in the SMX degradation experiments. 120
Table 5.1: Physicochemical properties of water matrices used for the effectiveness of the WP-BC/FeOCl/PMS/Vis system over SMX degradation 151

LIST OF ACRONYMS

Acronym	Definition
AC	Activated Carbon
AOP	Advanced Oxidation Process/Processes
ARB	Antibiotic-Resistant Bacteria
ARG	Antibiotic-Resistant Genes
BET	Brunauer-Emmett-Teller
BC	Biochar
BQ	Benzoquinone
CB	Conduction Band
CCD	Charge-Coupled Device
CD	Carbon Dot
CNT	Carbon Nanotube
CV	Cyclic Voltammetry
DBP	Disinfection By-Products
DI	Deionised (Water)
DOM	Dissolved Organic Matter
DR	Diffuse Reflectance
EDS	Energy Dispersive X-ray Spectroscopy
EDC	Endocrine-Disrupting Chemical
EIS	Electrochemical Impedance Spectroscopy
EPS	Extracellular Polymeric Substances
FeOCl	Iron Oxychloride
Acronym	**Definition**

FE-SEM	Field Emission Scanning Electron Microscope
FEEM	Fluorescence Excitation-Emission Matrix
FTIR	Fourier Transform Infrared (Spectroscopy)
HA	Humic Acid
HRTEM	High-Resolution Transmission Electron Microscopy
LSV	Linear Sweep Voltammetry
MM-BC/FeOCl	Mechanical Mixing Biochar/Iron Oxychloride Composite
n.d.	No date (in referencing context)
NHE	Normal Hydrogen Electrode
NOM	Natural Organic Matter
PCP	Personal Care Products
PMS	Peroxymonosulphate
PS	Persulphate
PVDF	Poly(Vinylidene Fluoride)
PVP	Polyvinylpyrrolidone
ROS	Reactive Oxygen Species
SA	Sulphonamide Antibiotics
SEM	Scanning Electron Microscopy/Microscope
SMX	Sulphamethoxazole
SR-AOP	Sulphate Radical-based Advanced Oxidation Process
TDS	Total Dissolved Solids
TEM	Transmission Electron Microscopy/Microscope
UV-Vis	Ultraviolet-Visible (Spectroscopy)
Acronym	**Definition**
UV-Vis-DRS	UV-Visible Diffuse Reflectance Spectroscopy

VB	Valence Band
WWTP	Wastewater Treatment Plant/Process
XPS	X-ray Photoelectron Spectroscopy
XRD	X-ray Diffraction
ZnO	Zinc Oxide

CHAPTER 1

INTRODUCTION

1.1 Background

Pharmaceutical drugs, classified as emerging pollutants, are increasingly being identified in various concentrations across different water sources, including rivers [1], lakes [2], dams [3], wetlands [4], and wastewater treatment plant effluents [5]. Among these pollutants, antibiotics present a significant challenge for removal using conventional wastewater treatment methods due to their trace concentrations and high biodegradation resistance. Consequently, they persist in treated wastewater discharged into the environment [6]. Their elimination from water sources is crucial, as their persistence and tendency to bioaccumulate contribute to the rise of antimicrobial resistance, posing serious risks to human, animal, and aquatic life, as well as disrupting ecological balance [7, 8]. Numerous studies, both globally and within South Africa, have investigated the occurrence, behaviour, and fate of antibiotics in aquatic environments [9]. For instance, antibiotics such as clozapine and ibuprofen have been detected in both surface water and sediment samples from the Umgeni River in KwaZulu-Natal, with recorded concentrations ranging from 26.32–78.33 µg/L and 16.29–62.0 µg/L, respectively. Additionally, SMX levels reached 507.34 ng/g in sediment samples from the Msunduzi River [10]. Similarly, untreated sewage water in the Western Cape contained SMX at concentrations of approximately 120 ng/L [11]. However, there are currently no regulations governing the presence of antibiotics in drinking water or wastewater effluents in South Africa and internationally [12].

Moreover, wastewater treatment facilities process complex mixtures of influents originating from households, healthcare facilities, industrial discharges, and agricultural runoffs [13, 14]. Water treatment plants in developing regions, including South Africa, do not routinely monitor antibiotic contamination, allowing these substances to persist through various treatment stages [15]. The South African Blue Drop Report 2022 revealed that approximately 60% of water treatment plants failed to meet microbial compliance standards, while 77% did not meet chemical compliance benchmarks [16].

The inadequate performance of wastewater treatment systems in eliminating antibiotics, coupled with the absence of monitoring and regulatory frameworks for these contaminants in drinking water, increases the likelihood of human exposure and environmental pollution. To address this issue, advanced oxidation processes, such as ozonation, photo-Fenton reactions, photocatalysis, and sulphate radical-based oxidation, should be integrated alongside conventional treatment methods to enhance the removal of antibiotic pollutants from water sources.

1.2 Problem statement

The incomplete elimination of antibiotics by conventional water treatment methods, combined with the absence of consistent monitoring and regulatory measures in drinking water, poses a significant environmental and ecological concern. Among the various antibiotics studied, SMX was a key focus due to its persistence in aquatic environments, where it disrupts microbial communities and impacts plant growth, ultimately disturbing the balance and overall health of aquatic ecosystems [17, 18]. Additionally, SMX has been associated with adverse effects such as inhibited plant development, zebrafish embryo toxicity, malformations, oxidative stress, reduced hatch rates, and body size changes [19]. In humans, long-term exposure to this antibiotic has been linked to hematopoietic complications and urinary system dysfunction [20]. Excessive antibiotic use and the uncontrolled release of these substances into the environment have contributed to the rise of antibiotic-resistant bacteria and resistance genes. These genetic traits can spread among different microorganisms through horizontal gene transfer, worsening the AMR-associated global health crisis. This issue has already been linked to a significant number of fatalities and is projected to become even more severe [21].

Conventional wastewater treatment facilities were not originally designed to effectively eliminate antibiotics because of their complex chemical structures, stability, toxicity, and extremely low concentrations [22]. Inadequately treated wastewater effluents often carry these antibiotic contaminants into freshwater bodies, ultimately contaminating drinking water supplies. While the environmental occurrence and risks associated with SMX contamination are well documented, significant scientific uncertainties remain regarding the design of efficient Fe-based photocatalysts for its removal. Iron oxychloride (FeOCl) is a promising visible-light-responsive catalyst [1];

however, its practical application is often limited by rapid electron–hole recombination and inefficient Fe^{3+}/Fe^{2+} redox cycling [2]. Although carbonaceous materials such as biochar have been reported to enhance charge transport and catalytic activity [3], the interfacial interactions between biochar and FeOCl, and their influence on reactive oxygen species generation, remain insufficiently understood. Furthermore, limited information exists regarding how different synthesis strategies affect the structural properties, charge transfer behaviour, and degradation performance of BC/FeOCl composites. The effectiveness of these materials under different oxidation pathways, including photocatalysis, PMS activation, and H_2O_2 activation, also remains unclear.

Therefore, this study hypothesised that integrating biochar with FeOCl would enhance charge separation, improve Fe^{2+}/Fe^{3+} redox cycling, and promote the generation of reactive oxygen species, thereby improving SMX degradation. It was further hypothesised that the synthesis method would significantly influence the physicochemical characteristics and catalytic behaviour of the resulting composite.

1.3 Justification of the study

The increasing detection of antibiotic residues in aquatic environments poses a growing challenge for water quality management and environmental protection. Conventional wastewater treatment technologies are often ineffective at fully removing these persistent compounds, allowing antibiotics such as SMX to persist in treated effluents and receiving water bodies [22]. This persistence raises concerns related to ecological toxicity and the development of antibiotic resistance, highlighting the need for more effective treatment strategies capable of degrading antibiotics under environmentally relevant conditions. Advanced oxidation processes (AOPs) have emerged as promising supplementary treatment technologies due to their ability to generate highly reactive species that can transform recalcitrant organic contaminants into less harmful products [23]. Among these, photocatalysis has attracted particular attention because it can operate under mild conditions and utilise light energy to drive degradation reactions [24]. However, the practical application of conventional photocatalytic systems remains limited by issues such as inefficient charge separation, slow degradation kinetics, and incomplete mineralisation of target pollutants [25]. More recently, sulphate radical-based AOPs have been identified as an effective enhancement to traditional photocatalytic processes, offering stronger oxidation capability and improved degradation efficiency for emerging contaminants [26].

Peroxymonosulphate (PMS), in particular, has gained attention due to its stability, ease of handling, and ability to generate reactive sulphate species when appropriately activated [27]. Nevertheless, efficient PMS activation requires suitable catalysts that can promote reactive species generation while avoiding secondary pollution and excessive operational complexity [28].

Heterogeneous catalytic systems provide a practical route to addressing these challenges, as they allow catalyst recovery, reusability, and improved stability compared to homogeneous processes [29]. Iron-based materials are attractive candidates for such systems due to their low toxicity, affordability, and catalytic activity. Iron oxychloride (FeOCl), a visible-light-responsive semiconductor, has shown potential in advanced oxidation applications but suffers from limitations related to charge carrier recombination and restricted surface activity [30]. To overcome these constraints, this study proposes the development of a nanocomposite photocatalyst that integrates FeOCl with biochar. Biochar is a sustainable, low-cost carbon material derived from biomass waste and offers favourable properties such as high surface area, electrical conductivity, and pollutant adsorption capability [31]. When combined with FeOCl, biochar is expected to enhance charge transfer, suppress electron–hole recombination, and improve overall catalytic performance. The integration of these materials, therefore presents a feasible and environmentally compatible approach for improving antibiotic degradation in water. Accordingly, this research focuses on the synthesis and evaluation of a biochar-supported FeOCl nanocomposite for the degradation of SMX, with particular emphasis on visible light-driven processes and sulphate radical-based oxidation. By addressing key limitations of conventional photocatalytic systems, the proposed approach aims to contribute to the development of effective and sustainable treatment strategies for antibiotic-contaminated water. The experimental findings demonstrated that the BC/FeOCl nanocomposite exhibited high efficiency in rapidly degrading organic contaminants in water. This fundamental study provides valuable theoretical insights for the development of effective and innovative oxidation technologies.

1.4 Aim and objectives of the study

The aim of this study was to synthesise and characterise BC/FeOCl nanocomposite for SMX pollution mitigation in water via photocatalysis and photocatalytic peroxymonosulphate activation under visible light irradiation.

The specific objectives of this study were to:

- Synthesise BC/FeOCl nanocomposite using two different methods namely wet impregnation and pyrolysis method (WP-BC/FeOCl), and ultrasonic-assisted mechanical mixing method (MM-BC/FeOCl).
- Characterise the prepared BC/FeOCl nanocomposites using XRD, HRTEM, SEM-EDX, XPS, BET, EIS, UV-vis-DRS, and FT-IR.
- Evaluate the photocatalytic degradation efficiency of SMX over BC/FeOCl nanocomposites under visible light irradiation
- Compare the photocatalytic activation of PMS using WP-BC/FeOCl and MM-BC/FeOCl towards the degradation of SMX in aqueous media under visible light.
- Investigate the influence of several reaction parameters, including pH, pollutant concentration, water matrix, catalyst dosage, and PMS concentration on the degradation of SMX using UV-vis, FEEM, and UV_{254}.
- Investigate the recyclability and stability of the synthesised BC/FeOCl nanocomposite by performing repeated SMX degradation cycles under visible light and analysing the catalyst before and after use.
- Evaluate the predominant reactive species through application of scavenging tests

1.5 Research questions

To fulfil the research aim and objectives of this study, the following research questions were developed:

- Compared to individual materials, to what extent does coupling FeOCl with biochar improve the catalytic oxidation of SMX?

- How does the synthesis method (wet impregnation and pyrolysis versus ultrasonic-assisted mechanical mixing) affect the photocatalytic and PMS-assisted degradation performance of BC/FeOCl nanocomposites?
- To what extent does BC/FeOCl enhance PMS activation for SMX degradation under visible light irradiation?
- What reactive species and mechanistic pathways govern photocatalytic and PMS-assisted SMX degradation over the BC/FeOCl nanocomposite?
- How do operational parameters such as pH, catalyst dosage, PMS concentration, pollutant concentration, and water matrix influence the degradation and mineralisation of SMX?
- To what extent is SMX mineralised during photocatalytic and PMS-assisted oxidation processes?
- How stable and reusable is the BC/FeOCl nanocomposite during repeated photocatalytic degradation cycles?

1.6 Chapter summary and dissertation overview

This introductory chapter highlights the urgent need for better treatment methods to tackle antibiotic contamination in water systems. The discussion emphasised that conventional wastewater treatment cannot effectively remove pharmaceutical pollutants like SMX, which creates serious health and environmental risks by contributing to antimicrobial resistance.

The chapter further presented that sulphate radical-based advanced oxidation processes, especially photocatalytic activation of PMS, offer a promising solution for removing antibiotics from water. The BC/FeOCl nanocomposite approach combines the photocatalytic properties of iron oxychloride with biochar's supporting features, potentially solving the limitations of each material while improving overall performance under visible light.

Building on the established need for advanced treatment technologies, this dissertation is structured to investigate the synthesis, characterisation, and application of a BC/FeOCl nanocomposite in water treatment. The study is divided into 6 chapters, as outlined in **Fig. 1.1**.

Chapter 1: Introduction	Background, problem statement, aims, and dissertation structure overview.
Chapter 2: Literature Review	Literature review on pharmaceuticals, treatment methods, and photocatalysis.
Chapter 3: Experimental Methodology	Materials, synthesis methods, characterisation techniques, and experimental procedures
Chapter 4: Biochar/FeOCl photocatalytic degradation of SMX in water	6-BC/FeOCl nanocomposite synthesis, characterisation, and SMX degradation in water
Chapter 5: Degradation of SMX using PMS-assisted biochar/FeOCl nanocomposite	A comparison Study of Synthesis Methods, WP-BC/FeOCl, MM-BC/FeOCl, characterisation, PMS activation, and SMX degradation in water
Chapter 6. Conclusion and recommendations	The study is concluded, and future work is recommended.

Figure 1.1: Dissertation structure.

The structure of the dissertation, presented in **Fig. 1.1**, is explained in more detail as follows:

- **Chapter 1: Introduction -** This chapter presents the background on pharmaceutical contamination in aquatic environments, focusing on antibiotics like SMX. It outlines how conventional wastewater treatment cannot effectively remove these persistent pollutants, creating environmental and health risks.

The study aims to synthesise BC/FeOCl nanocomposites for SMX removal through photocatalysis and PMS activation. Research objectives cover synthesis, characterisation, performance evaluation, and mechanistic studies. The chapter concludes with the dissertation structure overview.

- **Chapter 2: Literature review -** This chapter reviews environmental pollution and water treatment technologies. It addresses emerging pollutants, particularly pharmaceuticals and antibiotics in aquatic environments, with a focus on SMX occurrence in South African waters. The review examines conventional treatment limitations and explores advanced oxidation processes, including photocatalysis, Fenton processes, and sulphate radical-based systems. Special attention is given to iron oxychloride (FeOCl) photocatalyst and biochar support material, reviewing their properties and potential for nanocomposite applications in pharmaceutical contaminant removal.
- **Chapter 3: Experimental methodology -** This chapter outlines the experimental approach covering materials, synthesis methods, and analytical techniques. Analytical-grade chemicals from reputable suppliers were used. Biochar was prepared by pyrolysing blue gum pine wood at 750 °C, while BC/FeOCl nanocomposites were synthesised via wet impregnation and pyrolysis method as well as ultrasonic-assisted mechanical mixing and calcination at 230 °C. Characterisation of the synthesised materials were conducted using SEM, TEM, XRD, FT-IR, XPS, BET, and UV-vis spectroscopy. The photocatalytic setup monitored SMX degradation, with kinetic analysis methods determining rate constants.
- **Chapter 4: Biochar/FeOCl photocatalytic degradation of SMX in water – Chapter 4** forms the first part of the work, which outlines the synthesis and testing of BC/FeOCl nanocomposite for SMX degradation. The composites made via ultrasonic wet-impregnation and calcination exhibited well-dispersed FeOCl, with the 6% sample showing increased surface area, lower bandgap, and enhanced charge dynamics. Under visible light, it achieved 90.1% removal in 120 min, doubled FeOCl's rate, retained activity over five cycles, and effective in various water matrices.

- **Chapter 5: Degradation of SMX using PMS-assisted BC/FeOCl nanocomposite.** This chapter forms the second part of this work, which investigates and compares BC/FeOCl nanocomposites synthesised from two different methods: wet impregnation and pyrolysis method for preparation of WP-BC/FeOCl, and the ultrasonic-assisted mechanical mixing method for MM-BC/FeOCl for PMS-assisted photocatalytic oxidation of SMX in water. The chapter also reviews how different synthesis methods affect surface characteristics, electronic structure, and the formation of reactive oxygen species which underlie pollutant degradation.
- **Chapter 6: Conclusion and Recommendations –** This chapter presents the overall conclusions drawn from the study. It synthesises the key findings from both parts of the work, highlights the main contributions of the research to photocatalytic and sulphate radical–based antibiotic degradation, and outlines recommendations for future investigations.

References

[1] S. Fekadu, E. Alemayehu, R. Dewil, B. Van Der Bruggen, Pharmaceuticals in freshwater aquatic environments: A comparison of the African and European challenge, Sci. Total Environ. 654 (2019) 324–337. https://doi.org/10.1016/j.scitotenv.2018.11.072.

[2] J. Svanfelt, J.M. Kallio, J. Eriksson, L. Kronberg, Environmental fate and hazards of the pharmaceutical diclofenac in aquatic environments, ACS Symp. Ser. 1048 (2010) 243–255. https://doi.org/10.1021/bk-2010-1048.ch011.

[3] B.P. Gumbi, B. Moodley, G. Birungi, P.G. Ndungu, Detection and quantification of acidic drug residues in South African surface water using gas chromatography-mass spectrometry, Chemosphere. 168 (2017) 1042–1050. https://doi.org/10.1016/j.chemosphere.2016.10.105.

[4] V. Matamoros, C.A. Arias, L.X. Nguyen, V. Salvadó, H. Brix, Occurrence and behavior of emerging contaminants in surface water and a restored wetland, Chemosphere. 88 (2012) 1083–1089. https://doi.org/10.1016/j.chemosphere.2012.04.048.

[5] C. Teodosiu, A.F. Gilca, G. Barjoveanu, S. Fiore, Emerging pollutants removal through advanced drinking water treatment: A review on processes and environmental performances assessment, J. Clean. Prod. 197 (2018) 1210–1221. https://doi.org/10.1016/j.jclepro.2018.06.247.

[6] J.R. Kim, E. Kan, Heterogeneous photocatalytic degradation of sulphamethoxazole in water using a biochar-supported TiO_2 photocatalyst, J. Environ. Manage. 180 (2016) 94–101. https://doi.org/10.1016/j.jenvman.2016.05.016.

[7] I.C. Vasilachi, D.M. Asiminicesei, D.I. Fertu, M. Gavrilescu, Occurrence and fate of emerging pollutants in water environment and options for their removal, Water (Switzerland). 13 (2021) 1–34. https://doi.org/10.3390/w13020181.

[8] H.K. Khan, M.Y.A. Rehman, R.N. Malik, Fate and toxicity of pharmaceuticals in the water environment: An insight on their occurrence in South Asia, J. Environ. Manage. 271 (2020) 111030. https://doi.org/10.1016/j.jenvman.2020.111030.

[9] N. Milić, M. Milanović, N.G. Letić, M.T. Sekulić, J. Radonić, I. Mihajlović, M.V. Miloradov, Occurrence of antibiotics as emerging contaminant substances in aquatic environment, Int. J. Environ. Health Res. 23 (2013) 296–310. https://doi.org/10.1080/09603123.2012.733934.

[10] M. la Farré, S. Pérez, L. Kantiani, D. Barceló, Fate and toxicity of emerging pollutants, their metabolites and transformation products in the aquatic environment, TrAC - Trends Anal. Chem. 27 (2008) 991–1007. https://doi.org/10.1016/j.trac.2008.09.010.

[11] C.A. Magwira, N. Aneck-Hahn, M.B. Taylor, Fate, occurrence and potential adverse effects of antimicrobials used for treatment of tuberculosis in the aquatic environment in South Africa, Environ. Pollut. 254 (2019) 112990. https://doi.org/10.1016/j.envpol.2019.112990.

[12] South African National Standard (SANS), SANS 241-1:2015 Drinking Water Specification, (2015) 241.

[13] I. Michael, L. Rizzo, C.S. Mcardell, C.M. Manaia, C. Merlin, T. Schwartz, C. Dagot, D. Fatta-kassinos, Urban wastewater treatment plants as hotspots for the release of antibiotics in the environment : A review, Water Res. 47 (2012) 957–995. https://doi.org/10.1016/j.watres.2012.11.027.

[14] M.C. Ncibi, B. Mahjoub, O. Mahjoub, M. Sillanpää, Remediation of emerging pollutants in contaminated wastewater and aquatic environments: Biomass-based technologies, CLEAN - Soil, Air, Water. 45 (2017) 1700101. https://doi.org/10.1002/clen.201700101.

[15] L.M. Madikizela, Y.B. Nuapia, L. Chimuka, S. Ncube, A. Etale, Target and suspect screening of pharmaceuticals and their transformation products in the Klip River, South Africa, using ultra-high–performance liquid chromatography–mass spectrometry, Environ. Toxicol. Chem. 41 (2022) 437–447. https://doi.org/10.1002/etc.5265.

[16] Sershen, N. Rodda, T.A. Stenström, S. Schmidt, M. Dent, F. Bux, N. Hanke, C.A. Buckley, C. Fennemore, Water security in South Africa: Perceptions on public expectations and municipal obligations, governance and water re-use, Water SA. 42 (2016) 456–465. https://doi.org/10.4314/wsa.v42i3.11.

[17] D. Baggio, M. R Ananda-Rajah, Fluoroquinolone antibiotics and adverse events, Aust. Prescr. 44 (2021) 161–164. https://doi.org/10.18773/austprescr.2021.035.

[18] A. Olasupo, N. Ahmed, W.M.W.A. Kamil, F.B.M. Suah, Enhanced removal of sulphamethoxazole antibiotics from aquatic samples by electromembrane extraction process, React. Funct. Polym. 173 (2022) 105211. https://doi.org/10.1016/j.reactfunctpolym.2022.105211.

[19] M.J. Benotti, R.A. Trenholm, B.J. Vanderford, J.C. Holady, B.D. Stanford, S.A. Snyder, Pharmaceuticals and endocrine disrupting compounds in U.S. drinking water, Environ. Sci. Technol. 43 (2009) 597–603. https://doi.org/10.1021/es801845a.

[20] Y. Wang, X. Zheng, D. Wang, Design concept for electrocatalysts, Nano. Research. 15 (2022) 1730–1752. https://doi.org/10.1007/s12274-021-3794-0.

[21] Y. Lv, Y. Li, X. Liu, K. Xu, Effect of soil sulphamethoxazole on strawberry (Fragaria ananassa): Growth, health risks and silicon mitigation, Environ. Pollut. 286 (2021) 117321. https://doi.org/10.1016/j.envpol.2021.117321.

[22] N.A. Sabri, S. van Holst, H. Schmitt, B.M. van der Zaan, H.W. Gerritsen, H.H.M. Rijnaarts, A.A.M. Langenhoff, Fate of antibiotics and antibiotic resistance genes during conventional and additional treatment technologies in wastewater treatment plants, Sci. Total Environ. 741 (2020) 140199. https://doi.org/10.1016/j.scitotenv.2020.140199.

[23] R. Xiao, Z. Luo, Z. Wei, S. Luo, R. Spinney, W. Yang, D.D. Dionysiou, Activation of peroxymonosulphate/persulphate by nanomaterials for sulphate radical-based advanced oxidation technologies, Curr. Opin. Chem. Eng. 19 (2018) 51–58. https://doi.org/10.1016/j.coche.2017.12.005.

[24] D.B. Miklos, C. Remy, M. Jekel, K.G. Linden, J.E. Drewes, U. Hübner, Evaluation of advanced oxidation processes for water and wastewater treatment; A critical review, Water Res. 139 (2018) 118–131. https://doi.org/10.1016/j.watres.2018.03.042.

[25] I. Epold, N. Dulova, Y. Veressinina, M. Trapido, Application of ozonation, UV photolysis, Fenton treatment and other related processes for degradation of

ibuprofen and sulphamethoxazole in different aqueous matrices, J. Adv. Oxid. Technol. 15 (2012) 354–364. https://doi.org/10.1515/jaots-2012-0215.

[26] Y. Yang, J. Jiang, X. Lu, J. Ma, Y. Liu, Production of sulphate radical and hydroxyl radical by reaction of ozone with peroxymonosulphate: a novel advanced oxidation process., Environ. Sci. Technol. 49 (2015) 7330–9. https://doi.org/10.1021/es506362e.

[27] S. Giannakis, K.-Y.A. Lin, F. Ghanbari, A review of the recent advances on the treatment of industrial wastewaters by sulphate radical-based advanced Oxidation Processes (SR-AOPs), Chem. Eng. J. 406 (2021) 127083. https://doi.org/10.1016/j.cej.2020.127083.

[28] D. Zhao, X. Liao, X. Yan, S.G. Huling, T. Chai, H. Tao, Effect and mechanism of persulphate activated by different methods for PAHs removal in soil, J. Hazard. Mater. 254–255 (2013) 228–235. https://doi.org/10.1016/j.jhazmat.2013.03.056.

[29] G. Selvabharathi, S. Adishkumar, S. Jenefa, G. Ginni, J. Rajesh Banu, I.T. Yeom, Combined homogeneous and heterogeneous advanced oxidation process for the treatment of tannery wastewaters, J. Water Reuse Desalin. 6 (2016) 59–71. https://doi.org/10.2166/wrd.2015.139.

[30] D. Xie, C. Tang, D. Li, J. Yuan, F. Xu, Enhanced photo-Fenton catalytic performance toward acid orange II by FeOCl/CdS quantum dot composites: Density functional theory calculations and mechanistic Insights, J. Phys. Chem. C 128 (2024) 3295–3306. https://doi.org/10.1021/acs.jpcc.3c08322.

[31] S. Reza, S. Afroze, M.S.A. Bakar, R. Saidur, N. Aslfattahi, J. Taweekun, A.K. Azad, Biochar characterization of invasive Pennisetum purpureum grass : effect of pyrolysis temperature, Neo. Entom. 2 (2020) 239-251. https://doi.org/10.1007/s42773-020-00048-0.

CHAPTER 2

LITERATURE REVIEW

2.1 Emerging compounds

Emerging compounds, also known as emerging pollutants, have become major causes of water contamination in recent decades [9]. The uncontrolled release of these contaminants into the environment poses severe threats to aquatic life and human health, and is typically resistant to conventional wastewater treatments [10]. These compounds include pesticides, pharmaceuticals, personal care products (PCPs), endocrine-disrupting chemicals (EDCs), disinfection byproducts (DBPs), antibiotic-resistant genes (ARG), antibiotic-resistant bacteria (ARB), and other additives and substances that are present in both surface and groundwater [11]. Many of these contaminants were unknown or unidentified a few years ago, but they have recently been identified as pollutants that may pose threats to the ecosystem [12]. The possible implications and influence they might have on ecosystems, animal life, human health, and wildlife are also attracting attention and necessitating thorough investigation.

Emerging pollutants (EPs) are manmade or naturally occurring substances that are not routinely monitored in the environment but have the potential to penetrate the environment and produce known or suspected negative ecological and/or human health consequences [9]. In some cases, EPs have been released into the environment for a long time but were overlooked until the development of improved detection technologies. Under other circumstances, the synthesis of new chemicals or changes in the usage and disposal of existing chemicals may generate new sources of emerging contaminants [7, 10]. These contaminants can persist and live for a long time because they are bio-accumulative and bioactive. According to their physical and chemical properties, EPs include inorganic, organic, and particulate pollutants, as well as their subcategories [11]. The data on EP routine monitoring programmes are currently limited, and their fate, behaviour, and ecotoxicological impacts are frequently unknown [13]. EPs can also be emitted from point pollution sources, such as wastewater treatment plants in urban or industrial areas, and diffuse sources, such as

atmospheric deposition or crop and animal production. **Fig 2.1** depicts EP types from various sources that can be monitored using targeted and screening approaches [14].

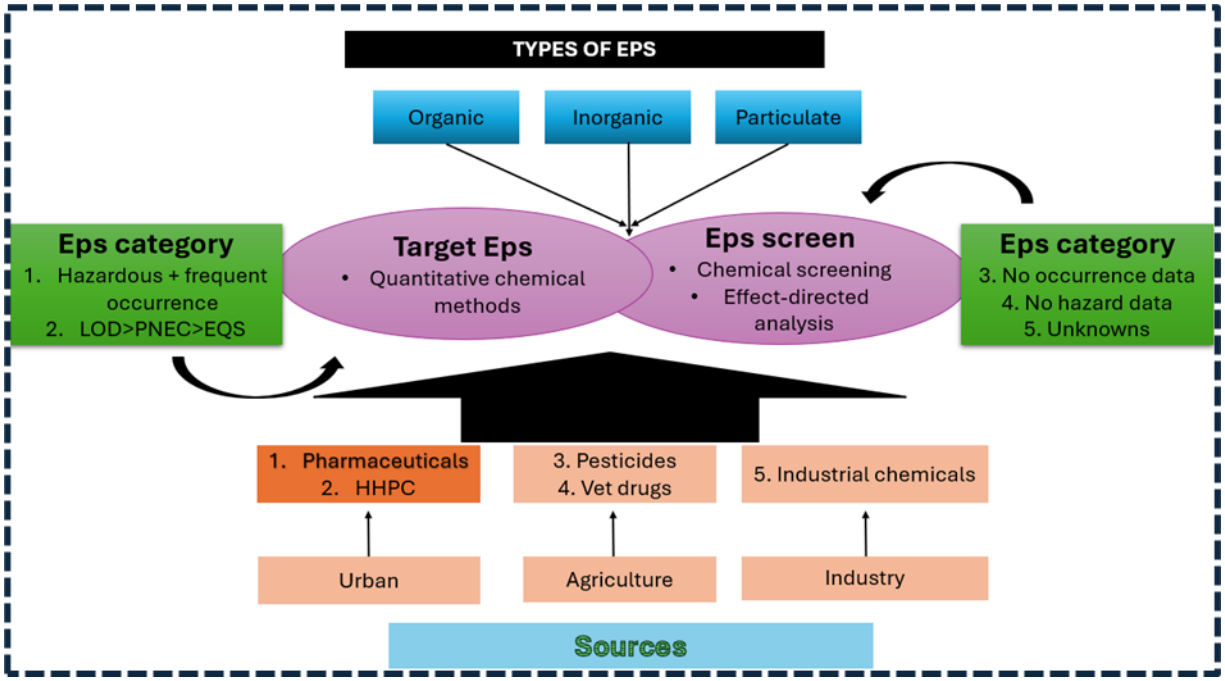

Figure 2.1 Types of EPs from various sources that can be monitored using targeted and screening approaches [9].

Recent studies have revealed that the current procedures for gathering precise information on the dynamics of emerging pollutants in water must be updated and modified to avoid hazards to water quality, vegetation, and fauna in river basins [12]. This is required because the Water Framework Directive requires member states to implement national programmes incorporating watch lists for emerging pollutants. These pollutants require additional attention because of their negative effects on aquatic and human life, which they can generate at any time [15]. According to the NORMAN database, more than 700 compounds are grouped into 20 classes of emerging pollutants. These include surfactants, steroid hormones, endocrine-disrupting compounds (EDCs), fire retardants, sunscreens, disinfection by-products, new pesticides, and pharmaceuticals [16]. In the last few decades, many classes of emerging pollutants have been detected in aquatic environments worldwide because of newly developed state-of-the-art analytical methods and growing concern about environmental preservation associated with the emergence of international guidelines and policies [13]. Among many, pharmaceutical pollutants have developed chemicals that are becoming a concern and one of the key concerns of global health authorities

[13]. Furthermore, these pharmaceutical pollutants are considered emerging contaminants in waterbodies because they remain unregulated or are currently undergoing a regularisation process [17].

2.2 Pharmaceuticals in the aquatic environment

In recent years, the significance of pharmaceuticals in human and veterinary use and their biologically active transformation products as environmental micropollutants has gained increasing attention due to the expanding awareness of their impact on water bodies [18]. Pharmaceuticals are several compounds designed to have therapeutic benefits on the body. They are typically active at low concentrations, and they can pass through biological membranes and survive in the body long enough to avoid being inactivated before having an effect [18]. Pharmaceutically active compounds have become emerging pollutants, and their presence in water bodies represents a significant environmental concern [19]. Various quantities of pharmaceutical pollutants have been reported globally across numerous environmental matrices, including drinking water, surface water, wastewater, sediments, and biota [20]. Pharmaceuticals persist in the environment because conventional water treatment processes do not completely remove them, and monitoring and regulation of these compounds in drinking water are limited [21]. The direct discharge of untreated and treated wastewater is the main source of pollutants in waterways. Secondary sources include terrestrial runoff from animal farms, agricultural areas, and aquaculture facilities [19]. Furthermore, these drugs are controlled and used differently; thus, a key source may not be as significant in another geographical region. These pollutants are transported through water channels, and their lipophilic nature promotes their bioaccumulation. However, lipophilicity is not the only metric used to understand bioaccumulation [22]. Recent studies have addressed different processes, including metabolism [22] and animal homeostasis, to better understand how these contaminants accumulate in aquatic life [23].

Multiple therapeutic classes of pharmaceuticals accumulate in aquatic environments, including anti-inflammatory agents, lipid regulators, beta-blockers, cancer therapeutics, steroids, numerous metabolites, transformation products, and antibiotics [24]. **Fig. 2.2** depicts the main types of human pharmaceuticals and the most commonly used products. Among these compounds, antibiotics are among the most

widely used pharmaceuticals. These drugs include ofloxacin, trimethoprim, penicillin, amoxycillin, flumequine, streptomycin, oxytetracycline, ciprofloxacin, and SMX.

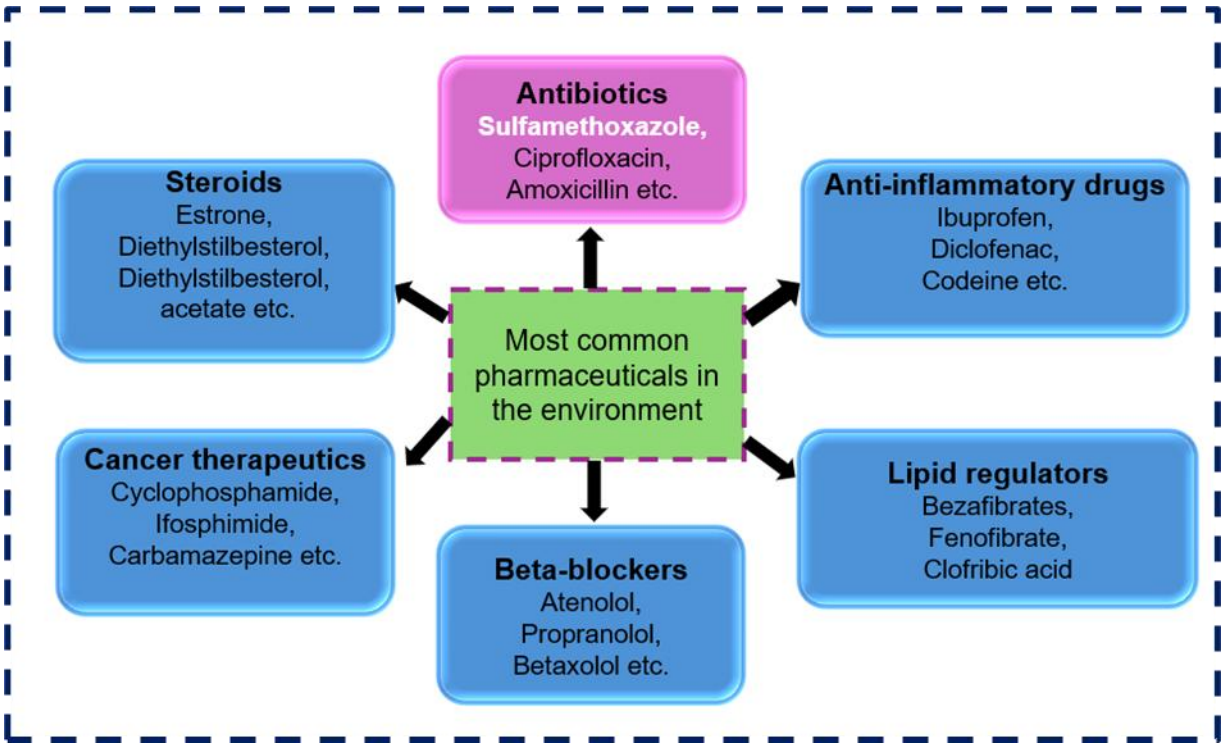

Figure 2.2 Several pharmaceutical compounds commonly found in the environment [25].

Antibiotics are an essential class of pharmaceuticals used in modern medicine. They are employed not only to treat human infections but also in veterinary medicine [26]. They can either suppress bacterial growth (bacteriostatic) or kill them (bactericidal) [27]. Approximately 200 000 tonnes of antibiotics are produced worldwide every year [28]. The global consumption of antibiotics is directly reflected in their presence in many environmental compartments, including the aquatic environment [29]. Specific antibiotic production rates have not been reported in the literature. However, in 1994, the output volume of antibiotics in Germany was 1831 tons, with penicillin alone accounting for 624 tons [30]. The use of antibiotics in veterinary medicine and as growth promoters is currently not under federal regulation. Consequently, no estimates for this area are available. However, the number of daily doses prescribed for humans is also available [31].

Although antibiotics provide significant therapeutic benefits, their excessive, inappropriate, and poorly regulated use has led to the release of their residual compounds and transformation products into the environment [28]. Owing to their

biological and physicochemical properties, antibiotics can remain in the environment for prolonged periods, potentially contaminating water sources [32]. Over the past two decades, there has been a growing concern regarding the contamination of water sources by antibiotics, with numerous studies highlighting wastewater treatment plant (WWTP) effluents as significant sources of this pollution [33]. A large percentage of antibiotics eventually make their way into wastewater, making them some of the most frequently detected pharmaceuticals in WWTPs globally [34]. The spread of antimicrobial resistance genes and resistant bacteria, which diminish the effectiveness of treatments for bacterial infections in both humans and animals, is the primary concern regarding antibiotics in the environment [34].

Many antibiotics have been detected in environmental waters due to their widespread use for treating human and animal infections. A marked increase in antibiotic consumption has been observed in many developing nations, including South Africa, where infectious diseases such as cholera, typhoid, meningitis, gonorrhoea, tuberculosis(TB), and malaria are increasingly associated with drug-resistant microorganisms [35]. The occurrence of antibiotics in many African water bodies has been linked to several factors including the discharge of untreated waste, the affordability and widespread availability of certain antibiotics, excretion by humans and animals, and the lack of effective drug return or disposal programmes. In South Africa, the presence of these contaminants has been reported in WWTPs as well as in surface waters [37]. For example, clozapine and ibuprofen antibiotics have been reported in the surface water and sediments of the Umgeni River in KwaZulu-Natal. Their levels ranged from 26.32 to 78.33 ug/L and from 16.29 to 62.0 g/L, respectively. A study by Agunbiade and Moodley reported ciprofloxacin concentrations of 27 µg/L and 14 µg/L in the influent and effluent of a WWTP in KwaZulu-Natal [38]. A recent study investigating antibiotic concentrations at two hospital WWTPs in the NW Province reported tetracycline levels as high as 45.38 µg/L in influent and 3.22 µg/L in effluent discharges [39]. Among all the detected antibiotics in the environment, SMX is one of the major detected antibiotics in South Africa. A few studies have reported the detection of SMX traces in the sediments of the Msunduzi River at concentrations up to 507.34 ng/g [40]. Similarly, SMX was detected in untreated sewage water in the Western Cape at concentrations of approximately 120 ng/L [41].

There are several pathways for the introduction of antibiotics into aquatic environments. Wastewater treatment plants handle a significant portion of the partially metabolised antibiotics from human waste through the sewer system, whereas the remainder is either discharged directly into nearby rivers and streams or leaks from sources such as landfill sites [42]. **Fig 2.3** presents a typical pathway describing the introduction of antibiotics into the environment. This study highlights the influence of societal activities, which lead to surface water contamination, which ultimately impacts the drinking water quality. Most WWTPs are not designed to eliminate antibiotics, resulting in their discharge into the aquatic environment through the final treated effluent. This makes WWTPs a significant source of antibiotic release [27,43].

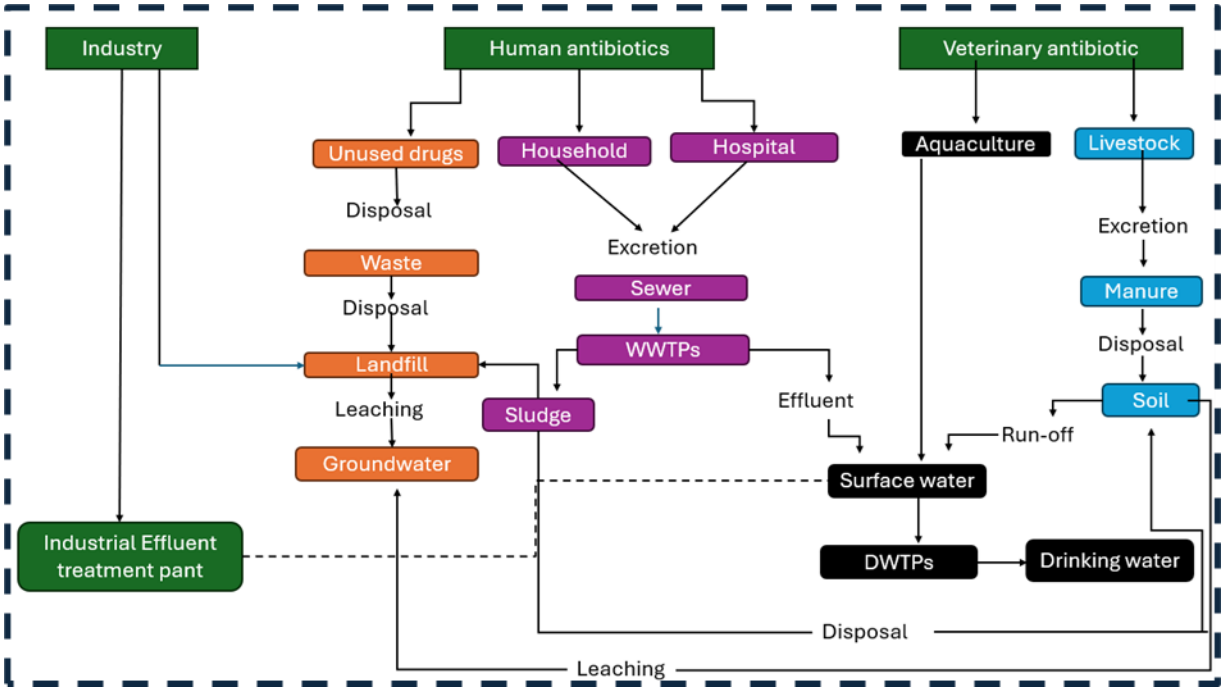

Figure 2.3 Different pathways of the introduction of antibiotics into the environment [32].

Conventional wastewater treatment plants (WWTPs) rely on a combination of physical, chemical, and biological processes to remove and break down organic contaminants, with treatment efficiency largely influenced by the physicochemical characteristics of the compounds [44,45]. However, most antibiotics are not fully mineralised in these systems, which typically include primary and secondary treatment stages. Although tertiary treatments, such as reverse osmosis, ultrafiltration, nanofiltration, and ozonation, are more effective at removing antibiotics, their high costs make them less

feasible in low- and middle-income countries like South Africa [44]. In conventional treatments, these substances may either be partially captured in the sludge or transformed into more hydrophilic but persistent forms, allowing them to pass through the WWTP and contaminate the surface and groundwater [46]. In animal husbandry, manure from livestock is often repurposed as organic fertiliser on agricultural land, and some of it can be washed into environmental waters through runoff. These waste products contain antibiotics, which contribute significantly to the rising levels of these substances in aquatic systems, posing various public health challenges [47,48]. Sulphonamides are among the antibiotic classes frequently found in water bodies.

2.2.1 Sulphonamides in freshwater systems

In recent years, researchers have depicted that sulphonamides (SAs) are amongst the most commonly used antibiotic classes and are frequently detected in aquatic environments [49]. However, they are primarily monitored in freshwater systems, with only a few studies on their prevalence in marine environments [49]. Sulphonamides are compounds derived from the ammonia benzene sulfonic group with a benzene ring, a para-amino group, and a sulphonamide functional group (**Fig. 2.4**). The chemical properties of SAs vary with their functional groups (denoted as R in **Fig. 2.4**), and their polarity is pH dependent [50].

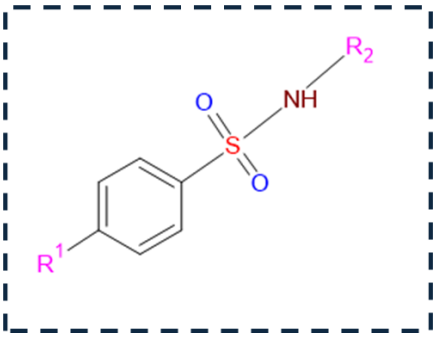

Figure 2.4 General structure of sulphonamide antibiotics [51].

One of the primary concerns regarding the widespread contamination of freshwater and other environmental compartments with SAs is the growing prevalence of microbial antibiotic resistance in these ecosystems. In addition to sulphaguanidine (SGM) and sulphasalazine (SSZ), most small-molecule SAs, including SMX, are water-soluble and have a low Henry's constant, allowing only minimal adsorption by soil. This makes them prone to environmental diffusion, although their properties

restrict significant accumulation in specific biological sites [52]. SMX is one of the most frequently detected groups of sulphonamides, with concentrations ranging from ng/L to mg/L in various aquatic environments, including rivers and wastewater treatment plant effluents [53,54]. On a global scale, SMX has been found in approximately 67% of the freshwater ecosystems examined, with a median concentration of 83 ng/L [55]. SMX (4-amino-N-(5-methyl-3-isoxazolyl) benzenesulphonamide) is a white, odourless, and tasteless antimicrobial agent and a broad-spectrum antibiotic that has been used in veterinary medicine and to treat various opportunistic infections in humans, such as Pneumocystis pneumonia caused by *Pneumocystis jirovecii*, toxoplasmosis caused by *Toxoplasma gondii*, malaria, and other diseases. Apart from its application in treating diseases and infections, SMX is also used as a feed additive to promote the growth and weight gain of food animals [56]. **Fig. 2.5** illustrates the molecular structure of SMX, which consists of an aniline moiety linked to a heterocyclic isoxazole ring through a sulphonamide functional group**.** The structure contains a para-aminobenzene ring ($–NH_2$) that contributes to the aromatic character and electron-donating properties of the molecule. The sulphonamide linkage ($–SO_2NH–$), characterised by two sulphonyl oxygen atoms, is a key functional group responsible for SMX's chemical stability and resistance to biodegradation.

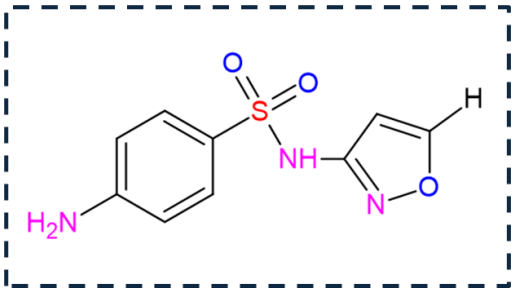

Figure 2.5 Structure of sulphamethoxazole [57].

Furthermore, SMX is a synthetic antibiotic that inhibits bacterial dihydrofolic acid synthesis, thereby hindering bacterial survival. The significance of this treatment stems from its extensive application in human and veterinary medicine. Often administered with trimethoprim to treat various diseases, limited data exist regarding the pharmacodynamics, dosage, withdrawal period, and turnover rate of SMX when used independently. SMX as an antimicrobial agent has been attracting serious attention worldwide, including in South Africa, due to its universality, persistence, and potential threats to aquatic life and human health [58]. A study in KwaZulu-Natal, South

Africa, reported the detection of SMX at concentrations up to 507.34 ng/g in the sediments of the Msunduzi River [40]. Similarly, SMX was detected in untreated sewage water in the Western Cape at a concentration of approximately 120 ng/L [41].

However, there is no enforcement of antibiotic regulations on wastewater and drinking water treatment before discharge in South Africa [59]. Consequently, this jeopardises the current wastewater system by spreading antibiotic-resistant bacteria and resistance genes into the nearby aquatic environment, which eventually reach the drinking water and pose a public health risk [59]. Even at low concentrations, SMX poses a serious environmental risk by altering the microbial community structure via the selection of antibiotic resistance [56]. In addition, SMX can affect aquatic ecosystems by inhibiting aquatic organisms' life activity. For example, the growth of the zooplankton *Ceriodaphnia dubia and the algae Pinnularia subcapitata* was limited when SMX concentrations reached 0.21 and 0.52 mg/L, respectively [56]. In this study, SMX was selected as the target antibiotic because it is frequently used for medical conditions prevalent in South Africa. This leads to recalcitrant behaviour during conventional wastewater treatment and persistence in the environment. This work was also conducted because of the major challenge facing the aquatic environment in the difficult removal of SMX residues, especially in WWTP effluents.

2.3 Environmental pollution

Water is an essential component of human life, and safe drinking water is crucial for maintaining good health [1,2]. Over the years, water pollution remediation has attracted global attention due to the continuous deterioration of water quality. Such a decline in water quality is due to the flooding of water sources by organic, inorganic, and microbial pollutants, which pose significant negative effects on human health and the social, cultural, and economic aspects of human existence [2]. A study by the US Environmental Protection Agency estimated that approximately 30% of the planet's water is contaminated [1]. Furthermore, the fatality rate from contaminated water has increased over the years, with more people dying every day from drinking unsafe water [3].

Several probable sources of human-made pollutants exist, some more significant than others. These materials fall into the point and diffuse sources category [4]. Discharges from industrial facilities and sewage treatment plants are point sources that are easier

to identify and control. Runoffs from agricultural land and hard surfaces, such as roadways, are less evident and difficult to control [5]. These sources can cause considerable variations in the pollutant loads over time. The dangers of chemical spills from industry and agriculture, as well as pathogen-containing slurries from intensive farming units (IFUs) [6]. Agricultural practices and industrial discharges into the aquatic environment have created various contaminants and disrupted the water cycle, raising global concerns about their eventual impact on wildlife and human health [7]. In recent decades, many studies have reported the presence of new compounds, called “emerging compounds,” in wastewater and aquatic environments [7]. These compounds have become a concern in the water sector owing to their persistence and bioaccumulation in natural aquatic environments. Constant exposure can lead to adverse effects, including aquatic toxicity and endocrine disruption, in livestock, aquatic life, and humans [8].

2.4 Removal of antibiotics from water

It is widely recognised that antibiotics must be eliminated from water; however, antibiotics are resistant to traditional treatment methods and purification technologies. The current conventional treatment processes for WWTPs, including adsorption, filtration, chlorination, coagulation, sedimentation, membrane technology, and biological treatment technologies, are not designed for effective and adequate removal of antibiotic residues because of their diverse chemical properties, stability, toxicity, and presence in ultra-low concentrations, leading to the uninterrupted entry of these pollutants into the environment, even at low concentrations [60]. This fact results in serious long-term risks, affecting the health and development of aquatic and/or terrestrial organisms and the availability of water around the world, aggravating the drinking water shortage in many countries, especially developing countries. According to the Food and Agriculture Organisation (2013), the global demand for drinking water is expected to increase by more than 40% by 2050 [61].

Conventional wastewater treatment involves a combination of physical, chemical, and biological stages to eliminate solids, organic pollutants, and emerging contaminants. The first step uses physical processes in a sedimentation tank to remove large particles. The secondary stage incorporates biological methods such as the activated sludge process, filter trickling, and oxidation ditches, and aerobic microorganisms are

used to degrade organic pollutants. Lastly, disinfection, commonly through chlorination, helps eliminate pathogens.

Physical treatment methods, such as membrane filtration, nanofiltration, reverse osmosis, and adsorption, are widely used for removing organic pollutants from water and wastewater. Membrane filtration is especially promising because it removes various organic pollutants, including bacteria and viruses, without using chemicals, thus producing high-quality water [61,62]. Nanofiltration combines adsorption, sieving, and electrostatic interactions, making it highly effective for pollutant elimination [64]. Similarly, AC adsorption captures pollutants by transferring them from liquid to solid phases. However, this generates toxic sludge and does not break down contaminants, which poses a challenge. The major limitations of physical treatment methods include their inability to fully degrade contaminants and high operational costs, which hinder their widespread application [64,65].

Biological treatment methods, such as percolation and activated sludge systems, effectively target nutrients such as N, P, and C in urban water and wastewater. The activated sludge process operates using aerobic granules containing spherical bacteria clusters enclosed in extracellular polymeric substances (EPS). These granules create oxygen gradients that allow the coexistence of various microbial communities responsible for nutrient removal in aerobic, anaerobic, and anoxic zones [66–68]. However, these biological systems are less effective at removing chemical pollutants, especially pharmaceuticals such as antibiotics, which are increasingly present in both domestic and industrial wastewaters [69]. The presence of such contaminants interferes with the performance of these systems, potentially disrupting the microbial communities essential for nutrient degradation [70]. This compromise in functionality makes it difficult for the system to effectively eliminate the pollutants that were originally designed to address, highlighting the challenges in treating antibiotics as emerging organic contaminants.

Chemical treatment methods, such as coagulation, chlorination, and oxidation, are other processes that are often used for water and wastewater treatment. Coagulation, which is typically performed with alum or ferric salts, produces a metal hydroxide flock. However, it has low efficiency in removing dissolved organic contaminants because these contaminants are often too small or chemically stable to be captured in the floc formation process [71,72]. Coagulation typically targets suspended particles and large

organic molecules rather than specific chemical structures of antibiotics, which reduces the overall effectiveness of these compounds [73]. Chlorination can oxidise a broad range of organic pollutants, including antibiotics. This process often leads to the creation of harmful disinfection by-products (DBPs), such as trihalomethanes and haloacetic acids, some of which are toxic and pose additional risks to human health and the environment [71]. In addition, chlorination may not fully degrade antibiotics, leading to the formation of antibiotic transformation products, some of which may retain biological activity or even become more toxic than the parent compounds. This incomplete degradation contributes to the proliferation of ARGs in aquatic environments [74]. Despite their potential, the practical use of these chemical methods often faces challenges such as operational costs, energy requirements, and the production of secondary waste or harmful by-products. Hence, advanced oxidation processes (AOPs) are promising methods that are widely used for the complete remediation of water contaminated with toxic, recalcitrant organic compounds such as antibiotics and microorganisms. AOPs aim for complete mineralisation and can be used either before or after other treatment steps to enhance overall efficiency [75]. Water treatment facilities can target various contaminants by utilising these treatment methods, but optimising the balance between efficiency, environmental safety and cost-effectiveness remains a significant challenge.

2.5 Advanced oxidation processes for removal of antibiotics

The development of advanced treatment technologies must be implemented to complement the current working technologies. These technologies are commonly referred to as AOPs. They are considered highly promising technologies because of their simplicity, high efficiency, and good reproducibility. Consequently, they have received considerable attention in the search for water treatment solutions [61]. The AOP was originally developed by Glaze et al. in 1987 as an innovative wastewater treatment technique and it was centred around the production of powerful oxidising agents, notably hydroxyl radicals ($HO^{\bullet}$), under ambient temperature and pressure conditions [76]. The principle of AOPs is generally based on the use of light irradiation, catalysts, and, in most cases, oxidants to produce highly reactive oxygen species, such as hydroxyl radicals ($HO^{\bullet}$), superoxide radicals ($O_2^{\bullet -}$), and sulphate radicals ($SO_4^{\bullet -}$) towards oxidation of recalcitrant organic pollutants, trace organic contaminants, or inorganic pollutants that are resistant to traditional biological

treatments [61,76]. **Fig. 2.6** demonstrates the basic mechanism of AOPs, where strong oxidising species are generated to degrade organic pollutants in water. In AOPs, oxidation leads to the formation of reactive oxygen species (ROS) such as hydroxyl radicals (•OH), superoxide radicals ($O_2^{\bullet -}$), and sulphate radicals ($SO_4^{\bullet --}$), which rapidly react with target pollutants. These reactions produce intermediate compounds that are progressively transformed into biodegradable species and ultimately mineralised into harmless end products such as carbon dioxide (CO_2), water (H_2O), and inorganic salts. The resulting products can then be removed through conventional physical, chemical, or biological water treatment processes.

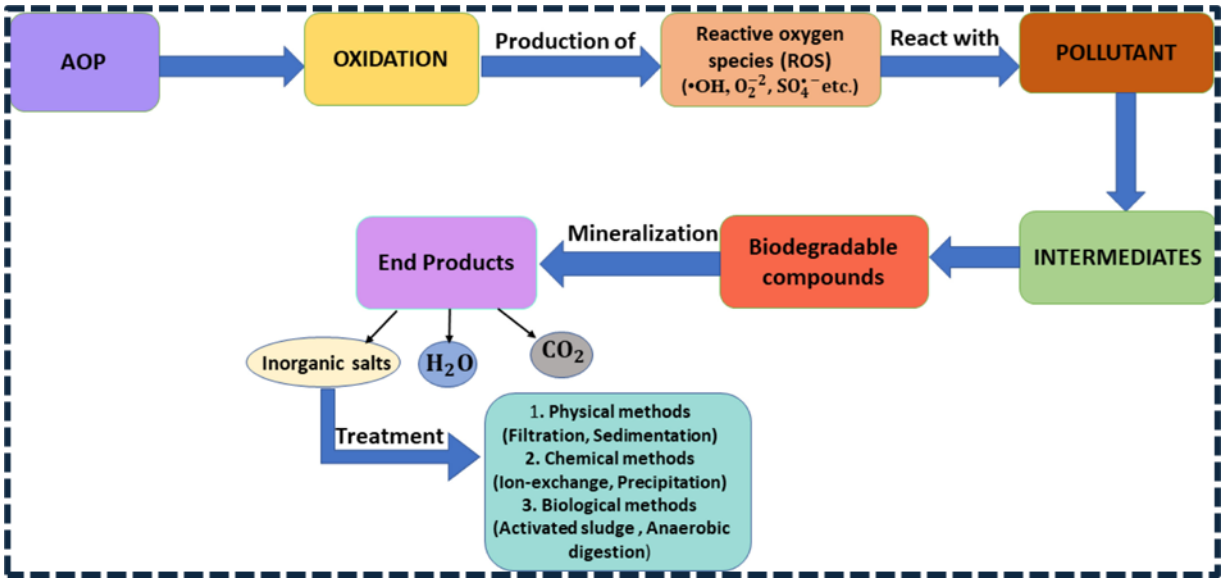

Figure 2.6 Working mechanism of the advanced oxidation process [78].

Advanced oxidation processes offer significant advantages over conventional wastewater treatment methods. They are highly effective in degrading low-concentration contaminants, such as pharmaceuticals and antibiotics, which conventional treatments often struggle to remove [79]. Additionally, AOPs do not produce chemical or biological sludge, minimising environmental concerns related to waste disposal. Unlike many biological or chemical methods that target specific pollutants, AOPs are non-selective and can achieve complete mineralisation of various organic compounds, breaking them down into non-toxic end products, such as carbon dioxide and water, which reduces the risk of secondary pollution [80]. The primary drawback of AOPs is their high operational costs, which significantly hinder their practical implementation on a larger scale. This is mainly due to the need for energy-

intensive processes, such as UV irradiation, the production of reactive agents, such as ozone or hydrogen peroxide, and the maintenance of specific reaction conditions [75]. These cost-related limitations reduce the feasibility of AOPs, particularly in settings where large volumes of wastewater must be treated continuously and in regions with limited financial resources for water treatment technologies [75]. As a result, AOPs are more suited for use in tertiary treatment than in earlier stages of wastewater treatment because they are highly efficient at degrading trace persistent organic pollutants that remain after primary and secondary treatments. Typical examples of AOPs include ozonation, sonolysis, photolysis, Fenton-based processes, and photocatalysis, which have both advantages and limitations.

2.5.1 Ozonation

Ozonation is an effective disinfection method for water and wastewater by targeting bacteria, viruses, algae, fungi, and organic matter. In AOPs, ozonation, along with various ozone-based combinations such as O_3/H_2O_2, O_3/UV, or O_3/H_2O_2/UV, and the use of catalysts (O_3/catalysts), has been extensively studied for the removal of antibiotics. Ozone's powerful oxidative properties help produce hydroxyl radicals ($HO^{\bullet}$), which play a crucial role in degrading antibiotics, particularly at elevated pH levels, to boost $HO^{\bullet}$ production. By combining ozone with hydrogen peroxide (H_2O_2), the generation of hydroxyl radicals increases, enhancing the system's ability to target a broad spectrum of pollutants in water and wastewater. However, several factors, such as pH, ozone dosage, and temperature, influence the overall efficiency of ozonation. The simple reaction mechanism of O_3 with water in an aqueous medium is given in **Eq. 2.1** as follows:

$$O_3 + H_2O \rightarrow 2HO^{\bullet} + 4O_2 \qquad 2.1$$

In ozone-based advanced oxidation processes, hydrogen peroxide may either be externally added to the aqueous system or generated in situ during ozone decomposition in water. In the peroxone (O_3/H_2O_2) process, the deliberate addition of hydrogen peroxide accelerates ozone decomposition, thereby enhancing the production of hydroxyl radicals ($HO^{\bullet}$), which are the dominant oxidising species responsible for pollutant degradation. This reaction occurs in an aqueous medium and is represented by **Eq. 2.2**:

$$H_2O_2 + 2O_3 \rightarrow 2HO^{\bullet} + 3O_3 \qquad 2.2$$

Typically, ozonation is used as a primary treatment method to improve the biodegradability of pollutants. It is particularly advantageous because of its low energy requirements and ability to recover up to 99% of water without creating additional waste. Nonetheless, ozonation has its limitations, such as high energy demand and significant implementation cost, which can hinder its widespread application in wastewater treatment plants.

2.5.2 Sonolysis

Sonolysis is performed by applying ultrasonic sound waves within a frequency range of 20 kHz to 10 MHz, causing cavitation bubbles to form in the liquid [81]. These bubbles grow and eventually violently collapse, releasing a large amount of energy that drives the degradation of organic molecules [82]. The process is considered environmentally safe because it does not involve hazardous chemicals. The formation of cavitation bubbles and their subsequent collapse play a pivotal role in this process, with the ultrasound frequency influencing the bubble formation efficiency [83]. Lower frequencies tend to produce fewer reactive bubbles due to the higher water vapour content within the collapsing bubbles, whereas higher frequencies may lead to reduced efficiency as the increased number of bubbles can result in collisions, decreasing the availability of reactive species. The collapse of cavitation bubbles during sonolysis results in extreme pressure (500–10,000 atm) and temperature (3,000–5,000 K) conditions, which drive the degradation of pollutants through pyrolysis [83,84]. This process also produces hydroxyl radicals ($HO^{\bullet}$) from water molecules, which react with pollutants to form their simplest forms. Degradation is concentrated at the bubble-liquid interface, where $HO^{\bullet}$ is highly active, and free radicals that migrate from this interface to the bulk liquid contribute to additional reactions. This process is a sludge-free method that does not generate secondary pollutants, making it favourable over other AOPs, such as photolysis and the Fenton process. Additionally, it can treat cloudy water and effectively degrade volatile and poorly soluble organic materials that increase turbidity [85,86]. However, this method is limited by its high energy requirements and relatively low mineralisation efficiency.

2.5.3 Fenton-based processes

The Fenton process is a widely recognised advanced oxidation process in which reactive oxygen species (mainly hydroxyl radicals $HO^{\bullet}$) are generated through the

reaction between hydrogen peroxide (H_2O_2) and ferrous ions (Fe^{2+}) [87]. These radicals are highly reactive and can degrade both organic and inorganic pollutants in aqueous environments. The foundation of Fenton chemistry was laid in 1894 by Henry J. Fenton demonstrated the oxidation of TA using H_2O_2 and iron salts [88]. In 1934, Haber and Weiss proposed that the Fenton reaction forms hydroxyl radicals with a high oxidation potential (2.73 V), making them among the most potent oxidants [88]. The classical Fenton reaction involves the catalytic decomposition of hydrogen peroxide by Fe^{2+}, leading to the generation of hydroxyl radicals and ferric ions, as shown in **Eq. 2.3**. The ferric ions produced can subsequently react with hydrogen peroxide to regenerate ferrous ions while forming hydroperoxyl radicals ($HO_2^{\bullet}$), as described in **Eq. 2.4.** Hydroxyl radicals may also participate in side reactions, including scavenging by excess hydrogen peroxide to form hydroperoxyl radicals, as illustrated in **Eq. 2.5.** Additionally, hydroxyl radicals can be consumed through reactions with Fe^{2+}, resulting in the regeneration of Fe^{3+}, as shown in **Eq. 2.6.** The hydroperoxyl radicals formed may further react with ferric ions to regenerate ferrous ions and molecular oxygen, as represented in **Eq. 2.7.** Further reactions between Fe^{2+} and hydroperoxyl radicals can also lead to the reformation of hydrogen peroxide, as shown in **Eq. 2.8.** Finally, hydroperoxyl radicals may undergo self-recombination to produce hydrogen peroxide and oxygen, as described in **Eq. 2.9.** Overall, these chain reactions describe the cyclic redox behaviour of iron and the continuous generation of reactive oxygen species under acidic conditions and in the absence of light, which are essential for effective contaminant degradation in aqueous solutions [89].

$$Fe^{2+} + H_2O_2 \rightarrow Fe^{3+} + OH^- + HO^{\bullet} \quad 2.3$$

$$Fe^{3+} + H_2O_2 \rightarrow Fe^{2+} + HO_2^{\bullet} + H^+ \quad 2.4$$

$$HO^{\bullet} + H_2O_2 \rightarrow HO_2^{\bullet} + H_2O \quad 2.5$$

$$HO^{\bullet} + Fe^{2+} \rightarrow Fe^{3+} + OH^- \quad 2.6$$

$$Fe^{3+} + HO_2^{\bullet} \rightarrow Fe^{2+} + O_2H^+ \quad 2.7$$

$$Fe^{2+}HO_2^{\bullet} + H^+ \rightarrow Fe^{3+} + H_2O_2 \quad 2.8$$

$$HO_2^{\bullet} + HO_2^{\bullet} \rightarrow H_2O_2 + O_2 \quad 2.9$$

The hydroxyl radical ($HO^{\bullet}$) can be consumed by both Fe^{2+} and H_2O_2, as shown in **Eqs. 2.5** and **2.6**, thereby reducing the overall efficiency of the Fenton reaction. To minimise

this scavenging, an optimal Fe^{2+}/H_2O_2 ratio is essential. As Fe^{3+} is produced during the reaction and can precipitate as ferric oxyhydroxides when the pH rises above its optimal range, resulting in undesirable sludge formation, which complicates practical applications [90]. Furthermore, the Fenton process has limitations in large-scale wastewater treatment, such as its dependency on pH (most effective between pH 2 and 5), sludge production, costly post-treatment requirements, and the need to neutralise the water before discharge [91]. Therefore, research into enhanced Fenton processes, such as the photo-Fenton method, is ongoing. This variation uses UV or visible light to increase the reaction rate and waste degradation efficiency by promoting the photolysis of Fe^{3+} complexes, which regenerate Fe^{2+} to react with H_2O_2, forming more $HO^{\bullet}$ radicals. The photo-Fenton reaction is optimal around pH 2.8, but challenges arise at higher pH due to the precipitation of Fe^{3+} as oxyhydroxides, while at lower pH, the concentration of $Fe(OH)^{2+}$ decreases [92]. Hydrogen peroxide photolysis occurs under UV light irradiation as shown in **Eq. 2.10**:

$$H_2O_2 + h\nu \quad 2HO^{\bullet} \qquad 2.10$$

Although the quantum yield of hydrogen peroxide during photolysis is relatively high, its overall activity during photo-Fenton reactions is limited due to poor light absorption. This reduces the efficiency of hydroxyl radical generation. Furthermore, similar to the traditional Fenton process, the photo-Fenton method shares some limitations, including the high costs associated with sludge management and the need for a very narrow pH range for optimal operation, which restricts its broader application in wastewater treatment [96,97]. To overcome these drawbacks, Fenton-like and photo-Fenton-like oxidation processes employing heterogeneous iron-based catalysts have been widely explored. In these systems, solid iron-containing materials activate hydrogen peroxide to generate reactive oxygen species under light irradiation, offering improved catalyst stability, reduced iron leaching, and broader pH applicability [95]. Such heterogeneous photo-Fenton-like systems are particularly attractive when coupled with visible-light-responsive catalysts, as they enable synergistic interactions between photocatalysis and H_2O_2 activation, thereby enhancing pollutant degradation efficiency.

2.5.4 Photocatalytic processes

Among the various AOPs mentioned above, the photocatalytic process has gained significant attention from researchers because of its numerous advantages. These benefits include the ability to degrade various organic pollutants, generate harmless end products, such as water and carbon dioxide, and the minimal production of secondary pollutants [96]. Photocatalysis is also energy efficient, requires fewer chemicals, and operates effectively under moderate conditions. Its versatility allows it to treat contaminants in different media (water, air, etc.) within a reasonable time, making it a promising green technology for environmental remediation [98,99]. Photocatalysis can be either homogeneous or heterogeneous. In homogeneous photocatalysis, the catalyst is dissolved in an aqueous medium to form a single-phase solution [61]. One of the major advantages of a homogeneous system is the low mass-transfer resistance between phases, which allows faster reaction rates for the generation of radical species and degradation of pollutants [99].

However, the recovery of homogeneous catalysts is a major challenge, often leading to secondary pollution [100]. In heterogeneous photocatalysis, the catalyst is usually dispersed in a solid form within the aqueous medium [101]. The heterogeneous photocatalysis offers advantages such as catalyst recyclability and reusability, flexibility for modification, and minimised secondary pollution. Furthermore, heterogeneous photocatalysis (HPC) stands out from other treatment methods by enabling both oxidation and reduction reactions simultaneously through light irradiation and the use of a light-absorbing photocatalyst. The process works by using semiconductors capable of absorbing light to catalyse photolytic reactions that produce redox processes [87]. These semiconductors generally exhibit a band structure that promotes an electron from the VB to the CB after photoexcitation with light of energy greater than the semiconductor's bandgap, leaving an electronic vacancy or hole (h^+) in the VB, as displayed in **Fig. 2.7** [88]. The hole is highly oxidative and quickly reacts with organic molecules adsorbed on the photocatalyst surface, leading to degradation. In addition, h^+ and e^- react with adsorbed water molecules and dissolved O_2, respectively, producing •OH and O_2•- that in turn degrade nearby organic molecules [89,99]. This separation facilitates redox reactions, making heterogeneous photocatalysis an effective and unique method for the degradation of various pollutants.

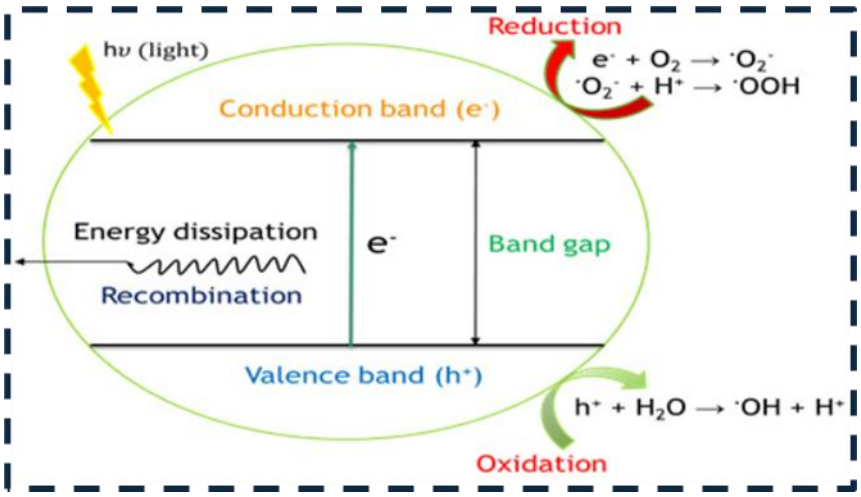

Figure 2.7 Schematic representation of the photocatalysis mechanism.

Some of the most widely used photocatalytic nanomaterials include magnetite (Fe_3O_4) [103], titanium dioxide (TiO_2) [104], zinc oxide (ZnO) [105], graphitic carbon nitride (g-C_3N_4) [106], and iron oxychloride (FeOCl) [107]. An ideal photocatalyst should possess several key properties, including strong light absorption within the solar spectrum, appropriate band-edge positions for redox reactions, efficient separation and transport of photogenerated charge carriers, chemical and structural stability, low toxicity, and cost-effectiveness. Semiconductor materials such as TiO_2 and ZnO are widely studied due to their high stability and strong oxidative potential [108,109], however, their wide band gaps restrict light absorption primarily to the ultraviolet region, and limiting solar utilization [110,111]. Graphitic carbon nitride has attracted attention because of its visible-light response and low cost, although its photocatalytic efficiency is often hindered by rapid charge recombination and low surface area [112]. Magnetite and other iron-based materials offer advantages such as earth abundance, redox flexibility, and magnetic recoverability, but may suffer from limited photocatalytic activity when used alone [113]. To overcome these limitations, material modification strategies such as nanostructuring, heterojunction construction, and support integration are commonly employed to enhance light harvesting, charge separation, and interfacial reaction kinetics.

Despite significant progress, several grand challenges continue to limit the large-scale application of photocatalysis in water treatment. These include inefficient utilization of visible light, rapid recombination of photogenerated electron–hole pairs, poor catalyst stability under operational conditions, low reaction rates in complex water matrices,

and difficulties associated with catalyst recovery and reuse [114]. In addition, laboratory-scale efficiencies often fail to translate to real wastewater systems due to the presence of competing species and natural organic matter. Addressing these challenges requires the rational design of composite photocatalysts that combine complementary materials to improve catalytic performance while maintaining stability, sustainability, and practical applicability. Recently, layered iron-based oxyhalides such as FeOCl have been explored as alternative photocatalysts because they combine visible-light activity with low cost and environmental compatibility.

2.5.5 Iron-oxychloride-based photocatalysts

Iron oxychloride (FeOCl) acts as a versatile heterogeneous catalyst, demonstrating high efficiency in breaking down organic contaminants in aqueous environments at various pH levels. The effectiveness of the catalyst stems from its stability and reactivity, which facilitate redox reactions that degrade pollutants. Owing to its wide operational pH range, FeOCl provides a flexible option for water treatment processes, allowing for adaptability in different wastewater conditions without the need for strict pH control, which can be a limitation in other treatment methods [115]. FeOCl is prepared using a partial pyrolysis method where $FeCl_3.6H_2O$ is used as a precursor and heated using a muffle furnace in the temperature range of 220°C–300°C, as shown in **Fig. 2.8**.



Figure 2.8 An illustration of the partial pyrolysis method for the synthesis of FeOCl.

FeOCl is a layered material with strong in-plane chemical bonds and weak out-of-plane Van der Waals bonds between the layers (**Fig. 2.9**). Its unique structure facilitates the rapid recycling of Fe(II) and Fe(III) through internal charge transfer [116].

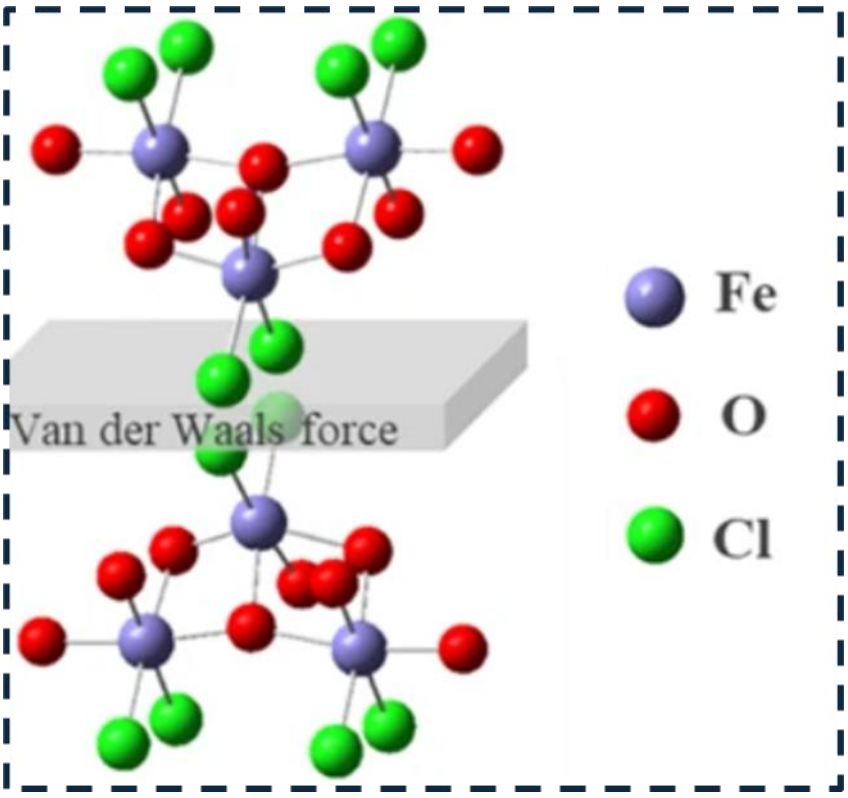

Figure 2.9 Molecular structure of FeOCl [117].

The abundance of Fe(II) within the FeOCl layered structure allows for the utilisation of FeOCl nanosheets as activators, resulting in significantly higher concentrations of •OH compared to other iron-containing activators, with an increase of approximately 2–4 times [118]. Furthermore, the exceptional photoelectric conversion performance and suitable energy band (~1.8 eV) structure of FeOCl enable its excitation by visible light [118]. In addition to its outstanding visible-light response, FeOCl is stable, has low toxicity, is simple to prepare, and is widely available. Despite its outstanding characteristics, FeOCl exhibits poor catalytic activity due to its small surface area and rapid charge-carrier recombination. Furthermore, FeOCl exhibits a low reduction potential (+0.91 eV) [119] but a high oxidation potential (+2.54 eV) [120]. To circumvent these shortcomings, it has been identified that coupling FeOCl with suitable materials through strategies such as elemental doping [121], construction of semiconductor heterojunctions [122], and integration with conductive carbon-based supports [123] has been shown to enhance its photocatalytic performance by promoting efficient charge separation and extending visible-light absorption.

For instance, Jinhuan Ma et al. synthesised a Z-scheme semiconductor heterojunction between FeOCl and g-C_3N_4, preventing the recombination of photogenerated

electrons and holes and improving the absorption efficiency of natural light on FeOCl, and 92% of RhB was degraded within 90 min [124]. Guo et al. constructed a BiOCl/FeOCl semiconductor heterojunction that facilitates the separation of photogenerated carriers and accelerates the photocatalytic degradation of RhB. The BiOCl/FeOCl heterostructures with an optimal composition of 15% BiOCl exhibited ~90 times higher visible-light photocatalytic activity than FeOCl alone [125]. Jianjun Song et al. successfully prepared an AgSCN/AgCl/FeOCl semiconductor heterojunction that degraded ibuprofen 40.7 times more than FeOCl alone (4.1 times) [126]. These semiconductor heterojunction structures help expose more active sites, thereby significantly improving the FeOCl photocatalytic efficiency. The presence of these junctions allows for better electron-hole separation and transfer, optimising the photocatalyst's overall performance in pollutant degradation. This improvement arises from the synergy between FeOCl and the additional materials, which enhances the ability of the catalyst to interact with light and generate reactive species.

Further research was conducted on other FeOCl modification routes. For example, metal-doped FeOCl, particularly with rare-earth elements such as lanthanum (La) and yttrium (Y), has emerged as an effective modification route that significantly enhances its catalytic performance [127]. Liu et al. successfully doped FeOCl with rare earth metals (La and Y), which showed efficient catalytic activity in degrading ibuprofen under stimulated solar light. The degradation constants of FeOCl/La and FeOCl/Y were 7.12 and 5.21 times higher than that of FeOCl, respectively [127]. Xuefeng Hu et al. also doped FeOCl with copper Cu(II) for phenol degradation. The introduction of Cu(II) resulted in lattice defects on the FeOCl surface and improved the separation efficiency of the photogenerated electron-hole pairs [128]. Despite the promising performance reported for modified FeOCl photocatalysts, several limitations remain unresolved. Most studies have focused on improving charge separation through semiconductor heterojunction construction or metal doping, often achieving high degradation efficiencies under laboratory conditions. However, these modification strategies frequently require expensive precursors, complex synthesis procedures, or rare-earth elements that may limit scalability and practical application. Furthermore, the reported enhancement mechanisms vary considerably among studies. Some researchers attribute the improved performance primarily to enhanced visible-light absorption, whereas others emphasise improved charge-carrier separation, increased

surface area, or accelerated PMS activation. The lack of agreement regarding the dominant performance-enhancing mechanism highlights the need for simpler and more sustainable modification approaches that can simultaneously improve charge separation, pollutant adsorption, and catalytic stability. Overcoming these challenges will enhance the photocatalytic efficiency and broaden the applicability of FeOCl in practical and industrial processes. These catalysts can be optimised for broader use by prioritising the synthesis of durable, sustainable and highly active materials. Carbon is one of nature's most prevalent elements. With advancements in science and technology, applications have expanded significantly, with the use of materials such as graphite/graphene [129], carbon nanotubes (CNTs) [130], carbon quantum dots (CQDs) [131], carbon nanodots [132], and biochar [113].

2.5.6 Carbon-based materials in photocatalysis

Carbon-based materials are being widely researched, particularly in environmental applications. Their remarkable chemical stability, mechanical strength, large surface area, high conductivity, and hydrophobicity make them ideal as metal oxide catalyst supports, enhancing their functionality in various environmental processes [134]. These attributes have drawn increasing attention to the use of carbon materials in fields such as pollution control and water and wastewater treatment [135]. The different synthesis methods have a significant influence on the photocatalytic activity of these compounds for water treatment. For example, graphite/graphene is mainly synthesised via a chemical vapour deposition (CVD) method, which produces high-quality graphite/graphene with minimal defects, allowing excellent charge transfer, which is critical for enhancing photocatalytic activity [136]. While, carbon nanotubes (CNTs) are prepared using the arc discharge method/laser ablation to produce CNTs with high surface area and controlled morphology, improving the dispersion of semiconductor particles and enabling better photocatalytic performance [137]. Meanwhile, carbon nanodots (CDs) are mainly prepared using hydrothermal or solvothermal methods. These green synthesis techniques produce CDs with tunable optical properties, strong light absorption, and emission characteristics, enhancing photocatalytic reactions [138].

Recently, researchers have focused a lot of their attention on semiconductor–carbon-material heterojunctions for the efficient removal of persistent organic compounds in

water. For example, Yang et al. synthesised a carbon-decorated FeOCl for the removal of tetracycline from water. Three actual states of carbon were identified, and their different roles in enhancing the FeOCl semiconductor performance were revealed. All carbon on/in FeOCl, including graphite carbon, carbon dots, and lattice carbon, enhanced visible light adsorption. More importantly, a homogeneous graphite carbon on the outer surface of FeOCl accelerated the transportation-separation of photo-excited electrons along the horizontal direction of FeOCl. Meanwhile, the interlayered carbon dots offered a Fe-O-C bridge to facilitate the transportation separation of photoexcited electrons along the vertical direction of FeOCl [139]. Mao et al. prepared novel carbon nitride-type polymers compounded with FeOCl for the efficient removal of tetracycline hydrochloride (TC-HCl), which reached 100% within 6 min [140]. Habibi-Yangjeh reported a novel g-C_3N_4/nanosheet/carbon dot/FeOCl nanocomposite for the removal of TC-HCl in water, which reached 99% in 45 min by photocatalytic reaction [112]. Although certain carbon-material-supported semiconductors, such as graphene and carbon nanotubes, offer remarkable advantages, they also face specific limitations. For instance, their synthesis can be costly, requiring high energy input and chemical-intensive processes. Such issues make certain carbon materials less practical for some large-scale, cost-sensitive, or environmentally focused applications, highlighting the potential of more sustainable alternatives, such as biochar-based composites, which are derived from waste biomass and are typically easier to produce and recover after.

2.5.7 Biochar-based nanocomposites photocatalysts

Biochar-based nanocomposites have gained attention as promising alternatives to certain conventional carbon-based nanocomposites, such as graphene- or carbon nanotube-supported materials, offering advantages in cost, sustainability, and ease of recovery [141]. Biochar is a porous carbon material derived through the pyrolysis of biomass waste in the temperature range of 300 °C – 800 °C (**Fig. 2.10**).

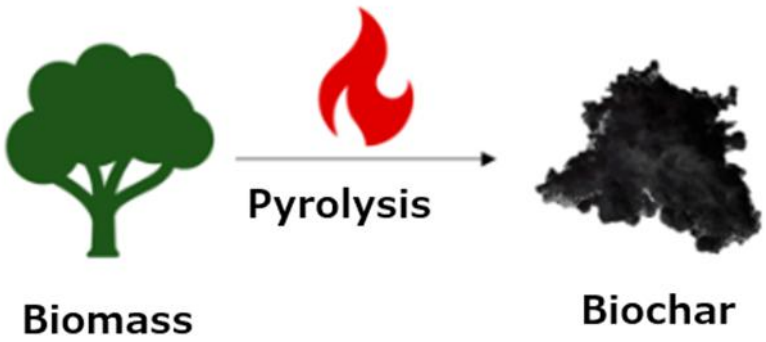

Figure 2.10 A basic illustration of biochar synthesis from biomass via pyrolysis.

Biochar can be produced from a wide range of abundant and low-cost biomass feedstocks, including agricultural residues (e.g., rice husks, corn stover, and sugarcane bagasse), forestry waste (e.g., wood chips and sawdust), and organic municipal waste [142]. As many of these feedstocks are organic wastes, biochar production indirectly contributes to waste management and resource recovery. Owing to its cost-effective synthesis, environmental sustainability, and broad availability, biochar has been extensively employed in water and wastewater treatment as a low-cost alternative to more expensive carbon materials such as activated carbon, carbon quantum dots, and carbon nanotubes [143] for the removal of diverse contaminants, including volatile organic compounds [144], heavy metal ions [145], pesticides [146], dyes [147], and pharmaceuticals [148]. The resulting biochar typically exhibits a high surface area, well-developed porous structure, stable carbon framework, and abundant surface functional groups (e.g., hydroxyl and carboxyl groups), which enhance its adsorption capacity and make it an effective support material in photocatalytic nanocomposites [149]. Consequently, biochar (BC) has gained increasing attention as a photocatalyst support due to its strong pollutant adsorption capability and ability to improve charge carrier dynamics.

In biochar-based photocatalytic systems, BC facilitates the separation of photoexcited electron–hole pairs generated by the semiconductor photocatalyst [150]. Upon light irradiation, electrons gain energy and move from the valence band to the conduction band and are subsequently transferred to biochar, which acts as an electron acceptor due to its high electron affinity [150]. These electrons react with adsorbed oxygen molecules on the biochar surface to generate reactive oxygen species, such as hydroxyl radicals ($HO^{\bullet}$) and superoxide radicals ($O_2^{\bullet -}$), which play a crucial role in the degradation of organic pollutants. By effectively trapping electrons and suppressing

electron–hole recombination, biochar significantly enhances the overall photocatalytic efficiency of the composite system.[150]. **Fig. 2.11** illustrates the electron photoexcitation and electron transfer to BC, leading to suppressed electron-hole recombination and improved pollutant degradation.

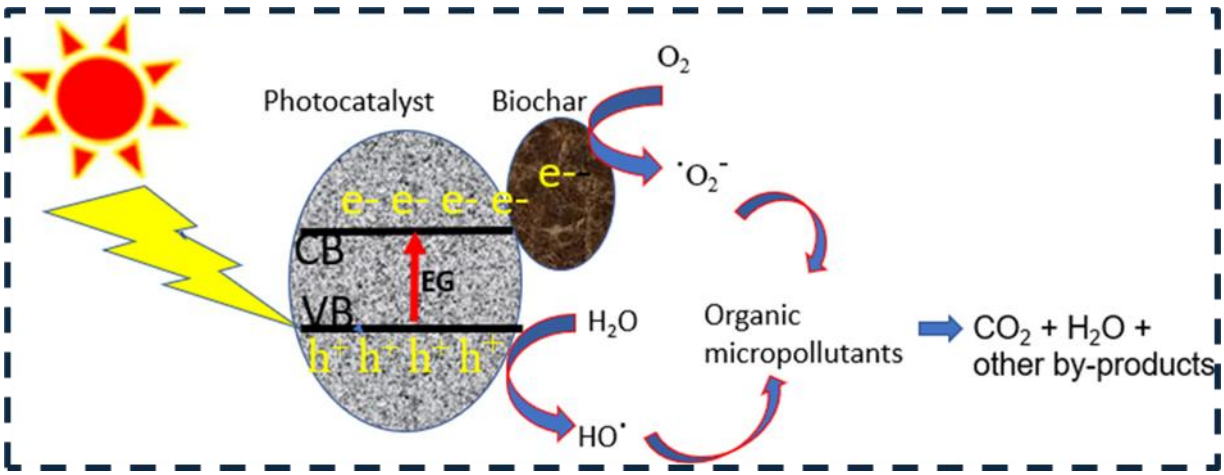

Figure 2.11 Typical degradation mechanism of the BC-supported photocatalyst for organic pollutants in water/wastewater [151].

As a result, the synergistic combination of strong pollutant adsorption by biochar and enhanced photocatalytic activity arising from improved charge carrier separation, BC-based nanocomposites exhibit more efficient pollutant degradation and improved overall water treatment performance. This dual functionality makes biochar-based nanocomposites a strong alternative to conventional carbon-supported photocatalysts. For example, Xie et al. reported approximately 80% removal of SMX within 3 h under simulated visible light irradiation using a Zn-TiO_2/biochar composite [111]. Li et al. studied carbamazepine (CBZ) photodegradation with magnetic Fe_3O_4/BiOBr/biochar and Fe_3O_4/BiOBr. At pH 6 Fe_3O_4/BiOBr/biochar (10% biochar, 0.05 g Fe_3O_4) was the best-performing photocatalyst, with 95%CBZ removal [152]. Khraisheh et al. assayed TiO_2/biochar with coconut shell powder char for CBZ photodegradation under UV light irradiation in the presence of O_2 flow [153]. Regardless of the amount of biochar, all composites exhibited higher adsorption and photocatalytic activity than bare TiO_2, biochar, and granular activated carbon, attaining 89.2%–94.4% CBZ removal. Furthermore, combining BC produced from waste materials or fast-growing invasive species, such as water hyacinth, with metallic oxides offers dual advantages, such as effective pollutant removal and environmental

waste management [154]. In the synthesised composites mentioned above, BC improved the nanoparticle dispersion and stability, while the nanoparticles themselves increased the surface area and provided more active sites for enhanced photocatalytic activity. Although biochar-supported photocatalysts have demonstrated enhanced degradation efficiencies for various organic pollutants, considerable variation exists in the reported performance of these materials. Several studies attributed the enhancement mainly to the improved adsorption capacity of biochar, whereas others reported that biochar primarily functioned as an electron acceptor that suppressed electron–hole recombination. Furthermore, photocatalytic performance is strongly influenced by factors such as biomass source, pyrolysis temperature, pore structure, and surface functionality, making direct comparisons between studies difficult. Consequently, the precise contribution of biochar to photocatalytic enhancement remains incompletely understood and requires further investigation, particularly when combined with FeOCl-based PMS activation systems [155]. The efficiency of these processes is often compromised in complex environmental conditions, particularly where there are high concentrations of dissolved organic matter (DOM) and inorganic anions, which tend to scavenge hydroxyl radicals, thus diminishing overall performance [156]. Given these limitations, sulphate radical-based AOPs (SR-AOPs) have emerged as a more effective alternative to SR-AOPs, offering improved selectivity and greater potential for organic pollutant degradation and mineralisation in such challenging conditions.

2.5.8 Sulphate radical-based advanced oxidation processes

Sulphate radical-based advanced oxidation processes (SR-AOPs) are a class of AOPs that primarily rely on sulphate radicals ($SO_4^{\bullet-}$) as the primary oxidising agents for degrading pollutants in water and wastewater [157]. Recently, they have become the most widely used advanced technologies. Their processes involve the gradual oxidation of organic pollutants into low-toxicity or nontoxic molecules, and eventually to complete mineralisation products of CO_2 and H_2O [158]. SR-AOPs have received considerable attention owing to their numerous activation methods, which promote their use in multiple effluent treatment and disinfection processes [155]. SR-AOPs rely on the generation of highly reactive sulphate radicals ($SO_4^{\bullet-}$), which cannot be efficiently produced by persulphate (PS, $S_2O_8^{2-}$) or peroxymonosulphate (PMS, HSO_5^-) alone under ambient conditions. Although PS and PMS are strong oxidants,

they exhibit relatively low reactivity toward most organic pollutants in their inactivated forms due to the high stability of the peroxide (O–O) bond [159]. Consequently, an activation step is required to cleave this bond and initiate the formation of reactive radical species. Upon activation, PMS generates both sulphate radicals ($SO_4^{\bullet-}$) and hydroxyl radicals ($HO^{\bullet}$), whereas PS activation predominantly yields sulphate radicals ($SO_4^{\bullet-}$) [160] shown in **Eqs. 2.11** and **2.12**. Persulphate is relatively inexpensive, highly soluble in water, and stable at ambient temperatures, making it particularly attractive for water treatment applications when combined with suitable activation strategies.

Persulphate (PS) and peroxymonosulphate (PMS) can be activated through several physical, chemical, and catalytic methods to generate sulphate radicals ($SO_4^{\bullet-}$). Common activation strategies include alkaline activation [161], thermal activation [162], radiation (UV or visible light) [163], electrochemical activation [164], ultrasound [165], and transition-metal-based catalysis [166]. Under alkaline conditions, PS and PMS can be activated via base-induced cleavage of the peroxide bond, however, this method often requires high pH, which limits practical application due to pH adjustment costs and potential secondary pollution [123]. Thermal activation promotes homolytic cleavage of the O–O bond [167], but its high energy demand restricts large-scale use [167]. Radiation-based activation (e.g., UV-vis light) is effective and controllable, yet its efficiency depends strongly on light penetration and reactor design [168]. Electrochemical activation allows in situ radical generation and good process control but is limited by electrode fouling and high operational costs [169]. Ultrasound activation enhances mass transfer and radical formation through cavitation effects, although it is energy-intensive and difficult to scale up [170].

Among these approaches, transition metal–based activation using metals or metal oxides (e.g., Fe, Co, and Mn) is widely regarded as one of the most promising strategies due to its high efficiency, mild operating conditions, and suitability over a relatively wide pH range [171]. These catalysts effectively activate PS or PMS to generate sulphate radicals ($SO_4^{\bullet-}$) with a high redox potential (2.5–3.1 V) [171], enabling the degradation of refractory organic pollutants. Compared to hydroxyl radicals, sulphate radicals exhibit longer lifetimes (30–40 μs versus ~20 μs for $HO^{\bullet}$), higher selectivity toward electron-rich organic compounds, and greater stability across a broader pH range, making SR-AOPs particularly attractive for water and wastewater treatment applications [172].

$$S_2O_8^{2-} \rightarrow 2SO_4^{2\bullet-} \quad 2.11$$

$$HSO_5^- \rightarrow SO_4^{\bullet-} + HO^\bullet \quad 2.12$$

In general, PMS is more easily activated by transition metals than PS because of its asymmetric structure [77], which is illustrated in **Fig. 2.12**.

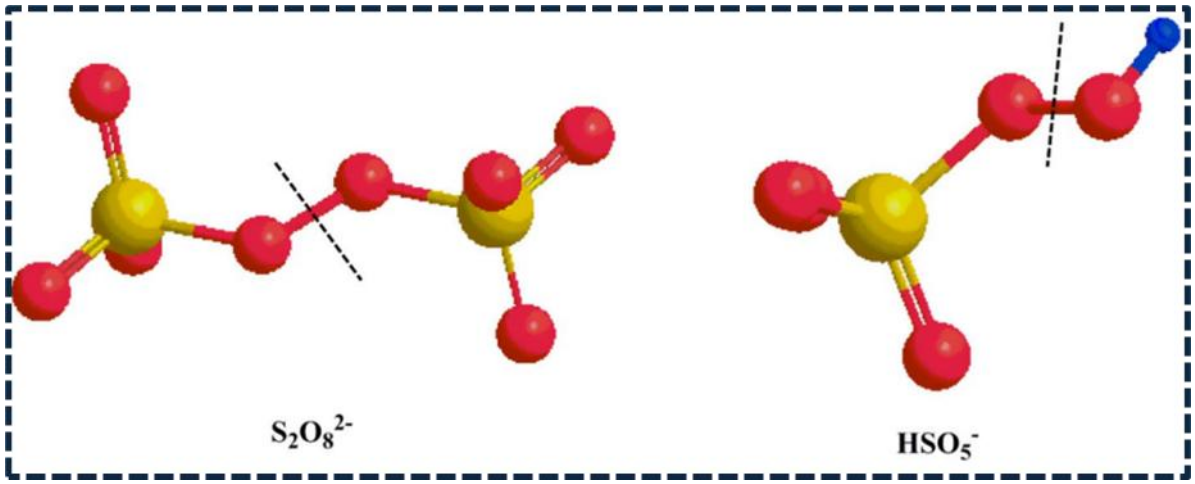

Figure 2.12 Structures of the PS and PMS. The yellow colour is the sulphur atom, and the red colour is the oxygen atom. The dashed line represents the fission position of O-O bond for the formation of sulphate radicals [155].

2.5.9 Peroxymonosulphate/persulphate catalytic/photo-catalytic activation

PMS and PS catalytic activation can be characterised as homogeneous or heterogeneous. In homogeneous catalytic activation, the catalyst is dissolved in an aqueous medium to form a single-phase solution [61]. One of the key advantages of a homogeneous system is the low mass-transfer resistance between phases, which allows for higher reaction rates for radical species formation and pollutant degradation. However, recovering the homogeneous catalyst is a significant challenge that frequently contributes to secondary contamination [99]. Meanwhile, catalysts for the activation of heterogeneous PMS and PS are often disseminated in solid form within aqueous media [173]. **Fig. 2.13** shows a typical mechanism example of the activation of PMS over FeOCl. Furthermore, the heterogeneous systems provide synergy between photocatalytic degradation and sulphate radical oxidation. In addition to sulphate radicals, other radical species, such as hydroxyl, superoxide, and holes, can be produced, enhancing the degradation kinetics.

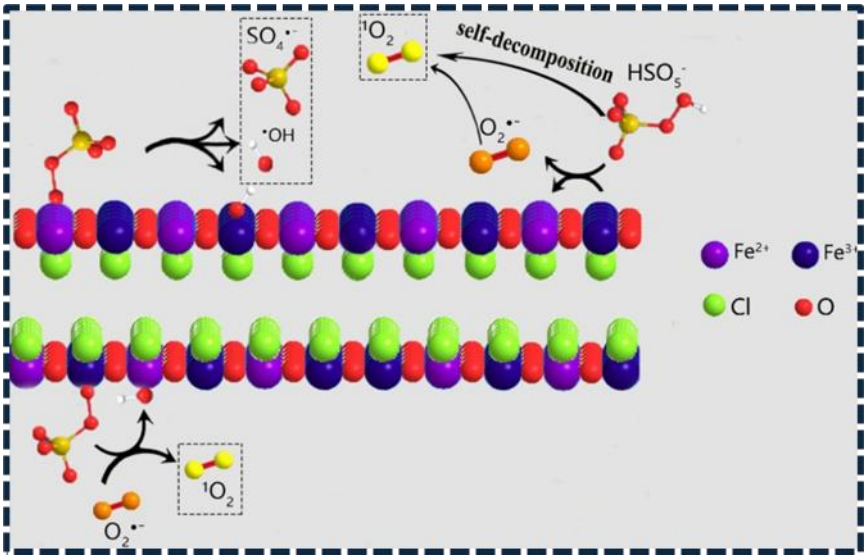

Figure 2.13 Typical example of a mechanism of PMS activation over FeOCl [174].

In heterogeneous catalytic systems, limitations such as low specific surface area, mass-transfer resistance, sluggish reaction kinetics, and potential leaching of active metal species must be carefully addressed [175]. To overcome these challenges, hybrid activation strategies combining thermocatalysis, sonocatalysis or sonophotocatalysis, piezocatalysis, and photocatalysis have been explored to enhance the activation efficiency of persulphate (PS) and peroxymonosulphate (PMS) [176]. Among these approaches, photocatalytic activation has emerged as a particularly promising strategy for sulphate radical–based advanced oxidation processes due to its ability to couple light-induced charge carrier generation with oxidant activation under mild conditions [177]. In photocatalytic PMS activation, photogenerated electrons and holes participate directly in PMS decomposition, leading to the formation of sulphate radicals ($SO_4^{\bullet-}$), hydroxyl radicals ($HO^{\bullet}$), and other reactive oxygen species that synergistically contribute to pollutant degradation [177].

Several studies have demonstrated the effectiveness of photocatalytic PMS activation for the degradation of antibiotics, including sulphonamides. For example, PMS activation by TiO_2- and g-C_3N_4-based photocatalysts under visible or simulated solar light has been shown to significantly enhance the degradation of SMX through dominant $SO_4^{\bullet-}$-driven pathways [178]. Li et al. reported accelerated SMX degradation using PMS activated by a modified TiO_2 photocatalyst, attributing the improved performance to efficient electron transfer from the photocatalyst to PMS, which suppressed charge recombination and promoted sulphate radical generation [179].

Similarly, PMS-assisted photocatalytic systems based on carbon-modified or Fe-containing photocatalysts have demonstrated high removal efficiencies for sulphonamide antibiotics such as sulfadiazine and sulfamethazine [180], benefiting from the combined effects of strong oxidant activation, extended light absorption, and improved charge separation. These studies highlight photocatalytic PMS activation as an effective and versatile route for enhancing sulphate radical–mediated oxidation of antibiotic contaminants in water.

Although numerous activation strategies have been reported for PMS and PS, there is still no consensus regarding the most effective approach for practical water treatment applications. For example, thermal and ultrasound activation can generate high concentrations of reactive radicals, but their large energy requirements limit large-scale implementation [170]. Similarly, homogeneous transition-metal activation often exhibits rapid reaction kinetics; however, concerns regarding metal leaching, catalyst recovery, and secondary contamination remain unresolved [171]. In contrast, heterogeneous photocatalytic activation offers improved catalyst stability and reusability while enabling simultaneous generation of sulphate radicals and photo-catalytically derived reactive oxygen species. Nevertheless, previous studies have reported conflicting observations regarding the dominant degradation pathways, with some attributing pollutant removal primarily to sulphate radicals ($SO_4^{\bullet -}$), while others suggest that hydroxyl radicals ($HO^{\bullet}$), superoxide radicals ($O_2^{\bullet -}$), or photogenerated holes contribute significantly to the degradation process. These inconsistencies indicate that the mechanisms governing PMS activation remain system-dependent and require further investigation, particularly for newly developed FeOCl-based photocatalysts. As a result, increasing emphasis has been placed on developing stable and recoverable photocatalytic systems by supporting semiconductor nanoparticles on functional carbon substrates that enhance visible-light utilization and interfacial charge transfer [181]. Overall, previous studies have demonstrated the effectiveness of advanced oxidation processes, PMS activation, FeOCl photocatalysts, and carbon-based support materials for the degradation of organic pollutants. However, significant challenges remain, including rapid charge-carrier recombination in FeOCl, uncertainty regarding dominant PMS activation pathways, high synthesis costs associated with many FeOCl modification strategies, and limited understanding of the synergistic interactions between biochar-supported FeOCl

composites and PMS activation. Furthermore, relatively few studies have investigated sustainable biomass-derived biochar as a low-cost support for FeOCl in photocatalytic PMS activation systems for the degradation of SMX. These unresolved limitations motivate the present study. In this study, a biochar-supported iron oxychloride photocatalyst (BC/FeOCl) was synthesised and investigated for the removal of SMX from aqueous solution. SMX removal occurred through a synergistic mechanism involving initial adsorption of SMX onto the porous biochar matrix, followed by photocatalytic degradation driven by FeOCl under visible-light irradiation. The surface functional groups and porous structure of biochar facilitate the pre-concentration of SMX at the catalyst interface, while FeOCl enables light-induced charge carrier generation and subsequent oxidative degradation of the adsorbed SMX molecules. To elucidate the influence of catalyst design and synthesis protocol on oxidative performance, the study then continued to investigate the activation of PMS using BC/FeOCl in order to establish a sulphate radical–based advanced oxidation process for enhanced SMX degradation. In this stage, BC/FeOCl nanocomposite was synthesised using two different methods: the wet impregnation and pyrolysis method as well as the ultrasonic-assisted mechanical mixing to assess the influence of synthesis protocol on catalyst structure, surface properties, and PMS activation efficiency. Under visible-light irradiation, the biochar-supported FeOCl served as a heterogeneous catalyst to activate PMS, generating reactive oxygen species dominated by sulphate radicals ($SO_4^{\bullet -}$), with contributions from hydroxyl radicals ($HO^{\bullet}$) and other oxidative species. The degradation efficiency of SMX was assessed through advanced oxidation experiments, and the photocatalytic activation mechanism, dominant reactive species, and degradation pathways were elucidated to understand the role of synthesis method and to validate the environmental applicability of the developed PMS/visible-light catalytic system

2.6 Chapter Summary

Chapter 2 outlined the fundamental aspects of environmental pollution, focusing specifically on emerging compounds such as pharmaceuticals in aquatic environments, with an emphasis on the challenges posed by antibiotics. The chapter reviewed conventional and advanced methods for removing these contaminants,

critically evaluating established treatment limitations and recent advances in oxidative processes, with particular attention to sulphonamide antibiotics like SMX and the catalytic role of biochar and iron oxychloride nanocomposites. The next chapter (**Chapter 3**) will present the experimental methodology adopted for synthesising and characterising the relevant nanomaterials, as well as the analytical procedures conducted in this study.

References

[1] M. Bruce, M. Limin, Recent advances on water pollution research in Africa: A critical review, Int. J. Sci. Adv. 2 (2021) 375–386. https://doi.org/10.51542/ijscia.v2i3.23.

[2] V. Matamoros, C.A. Arias, L.X. Nguyen, V. Salvadó, H. Brix, Occurrence and behavior of emerging contaminants in surface water and a restored wetland, Chemosphere. 88 (2012) 1083–1089. https://doi.org/10.1016/j.chemosphere.2012.04.048.

[3] F.B. Elehinafe, O. Agboola, A.D. Vershima, G.O. Bamigboye, Insights on the advanced separation processes in water pollution analyses and wastewater treatment – A review, South African J. Chem. Eng. 42 (2022) 188–200. https://doi.org/10.1016/j.sajce.2022.08.004.

[4] A.O. Fayiga, M.O. Ipinmoroti, T. Chirenje, Environmental pollution in Africa, Sprin. Netherl. 20 (2018) 41-73. https://doi.org/10.1007/s10668-016-9894-4.

[5] J. Robles-Molina, F.J. Lara-Ortega, B. Gilbert-López, J.F. García-Reyes, A. Molina-Díaz, Multi-residue method for the determination of over 400 priority and emerging pollutants in water and wastewater by solid-phase extraction and liquid chromatography-time-of-flight mass spectrometry, J. Chromat. 1350 (2014) 30–43. https://doi.org/10.1016/j.chroma.2014.05.003.

[6] R.R. Appannagari, Environmental pollution causes and consequences : a study, North Asian Int. Res. J. Soc. Sci. Humanit. 3 (2017) 2454–9827. https://doi.org/10.4172/2157-7625.1000225.

[7] T. Deblonde, C. Cossu-Leguille, P. Hartemann, Emerging pollutants in wastewater: A review of the literature, Int. J. Hyg. Environ. Health. 214 (2011) 442–448. https://doi.org/10.1016/j.ijheh.2011.08.002.

[8] M.S. de Ilurdoz, J.J. Sadhwani, J.V. Reboso, Antibiotic removal processes from water & wastewater for the protection of the aquatic environment - a review, J. Water Process Eng. 45 (2022) 102474. https://doi.org/10.1016/j.jwpe.2021.102474.

[9] V. Geissen, H. Mol, E. Klumpp, G. Umlauf, M. Nadal, M. van der Ploeg, S.E.A.T.M. van de Zee, C.J. Ritsema, Emerging pollutants in the environment:

A challenge for water resource management, Int. Soil Water Conserv. Res. 3 (2015) 57–65. https://doi.org/10.1016/j.iswcr.2015.03.002.

[10] H. Salazar, P.M. Martins, B. Santos, M.M. Fernandes, A. Reizabal, V. Sebastián, G. Botelho, C.J. Tavares, J.L. Vilas-Vilela, S. Lanceros-Mendez, Photocatalytic and antimicrobial multifunctional nanocomposite membranes for emerging pollutants water treatment applications, Chemosphere. 250 (2020). https://doi.org/10.1016/j.chemosphere.2020.126299.

[11] R.K. Mishra, S.S. Mentha, Y. Misra, N. Dwivedi, Emerging pollutants of severe environmental concern in water and wastewater: A comprehensive review on current developments and future research, Water-Energy Nexus. 6 (2023) 74–95. https://doi.org/10.1016/j.wen.2023.08.002.

[12] I.C. Vasilachi, D.M. Asiminicesei, D.I. Fertu, M. Gavrilescu, Occurrence and fate of emerging pollutants in water environment and options for their removal, Water (Switzerland). 13 (2021) 181. https://doi.org/10.3390/w13020181.

[13] F. Desbiolles, L. Malleret, C. Tiliacos, P. Wong-Wah-Chung, I. Laffont-Schwob, Occurrence and ecotoxicological assessment of pharmaceuticals: Is there a risk for the Mediterranean aquatic environment?, Sci. Total Environ. 639 (2018) 1334–1348. https://doi.org/10.1016/j.scitotenv.2018.04.351.

[14] C. Rimayi, L. Chimuka, A. Gravell, G.R. Fones, G.A. Mills, Use of the Chemcatcher passive sampler and time-of-flight mass spectrometry to screen for emerging pollutants in rivers in Gauteng province of South Africa, Environ. Monit. Assess. 191 (2019) 7515. https://doi.org/10.1007/s10661-019-7515-z.

[15] C. Teodosiu, A.F. Gilca, G. Barjoveanu, S. Fiore, Emerging pollutants removal through advanced drinking water treatment: A review on processes and environmental performances assessment, J. Clean. Prod. 197 (2018) 1210–1221. https://doi.org/10.1016/j.jclepro.2018.06.247.

[16] M. Petrović, S. Gonzalez, D. Barceló, Analysis and removal of emerging contaminants in wastewater and drinking water, TrAC - Trends Anal. Chem. 22 (2003) 685–696. https://doi.org/10.1016/S0165-9936(03)01105-1.

[17] J. Rivera-Utrilla, M. Sánchez-Polo, M.Á. Ferro-García, G. Prados-Joya, R. Ocampo-Pérez, Pharmaceuticals as emerging contaminants and their removal

from water. A review, Chemosphere. 93 (2013) 1268–1287. https://doi.org/10.1016/j.chemosphere.2013.07.059.

[18] P. Bottoni, S. Caroli, A.B. Caracciolo, Pharmaceuticals as priority water contaminants, Toxicol. Environ. Chem. 92 (2010) 549–565. https://doi.org/10.1080/02772241003614320.

[19] H.K. Khan, M.Y.A. Rehman, R.N. Malik, Fate and toxicity of pharmaceuticals in water environment: An insight on their occurrence in South Asia, J. Environ. Manage. 271 (2020) 111030. https://doi.org/10.1016/j.jenvman.2020.111030.

[20] T. Aus der Beek, F.A. Weber, A. Bergmann, S. Hickmann, I. Ebert, A. Hein, A. Küster, Pharmaceuticals in the environment-global occurrences and perspectives, Environ. Toxicol. Chem. 35 (2016) 823–835. https://doi.org/10.1002/etc.3339.

[21] H. Buser, M.D. Mu, C. Wa, Occurrence and fate of the pharmaceutical drug diclofenac in surface waters : Rapid photodegradation in a lake, Environ. Sci. Technol.32 (1998) 3449–3456. https://doi.org/10.1021/es980301x.

[22] B. Du, S.P. Haddad, A. Luek, W.C. Scott, G.N. Saari, L.A. Kristofco, K.A. Connors, C. Rash, J.B. Rasmussen, C.K. Chambliss, B.W. Brooks, Bioaccumulation and trophic dilution of human pharmaceuticals across trophic positions of an effluent-dependent wadeable stream, Philos. Trans. R. Soc. B Biol. Sci. 369 (2014) 58. https://doi.org/10.1098/rstb.2014.0058.

[23] C.F. Gomez, L. Constantine, M. Moen, A. Vaz, W. Wang, D.B. Huggett, Ibuprofen metabolism in the liver and gill of rainbow trout, Oncorhynchus mykiss, Bull. Environ. Contam. Toxicol. 86 (2011) 247–251. https://doi.org/10.1007/s00128-011-0200-8.

[24] M. Valdez-Carrillo, L. Abrell, J. Ramírez-Hernández, J.A. Reyes-López, C. Carreón-Diazconti, Pharmaceuticals as emerging contaminants in the aquatic environment of Latin America: a review, Environ. Sci. Pollut. Res. 27 (2020) 44863–44891. https://doi.org/10.1007/s11356-020-10842-9.

[25] A. Nikolaou, S. Meric, D. Fatta, Occurrence patterns of pharmaceuticals in water and wastewater environments, Anal. Bioanal. Chem. 387 (2007) 1225–1234. https://doi.org/10.1007/s00216-006-1035-8.

[26] R. Hirsch, T. Ternes, K. Haberer, K.L. Kratz, Occurrence of antibiotics in the aquatic environment, Sci. Total Environ. 225 (1999) 109–118. https://doi.org/10.1016/S0048-9697(98)00337-4.

[27] N. Milić, M. Milanović, N.G. Letić, M.T. Sekulić, J. Radonić, I. Mihajlović, M.V. Miloradov, Occurrence of antibiotics as emerging contaminant substances in aquatic environment, Int. J. Environ. Health Res. 23 (2013) 296–310. https://doi.org/10.1080/09603123.2012.733934.

[28] N.P. Ngqwala, P. Muchesa, Occurrence of pharmaceuticals in aquatic environments: A review and potential impacts in South Africa,. J. Sci. 116 (2020) 7-8. https://doi.org/10.17159/sajs.2020/5730.

[29] E. Felis, J. Kalka, A. Sochacki, K. Kowalska, S. Bajkacz, M. Harnisz, E. Korzeniewska, Antimicrobial pharmaceuticals in the aquatic environment - occurrence and environmental implications, Eur. J. Pharmacol. 866 (2020) 172813. https://doi.org/10.1016/j.ejphar.2019.172813.

[30] A.C. Faleye, A.A. Adegoke, K. Ramluckan, J. Fick, F. Bux, T.A. Stenström, Concentration and reduction of antibiotic residues in selected wastewater treatment plants and receiving waterbodies in Durban, South Africa, Sci. Total Environ. 678 (2019) 10–20. https://doi.org/10.1016/j.scitotenv.2019.04.410.

[31] M. Casewell, C. Friis, E. Marco, P. McMullin, I. Philips, The European ban on growth-promoting antibiotics and emerging consequences for human and animal health, J. Antimocrob. Chemo. 52 (2003) 159-161. https://doi.org/10.1093/jac/dkg313

[32] A.C. Faleye, A.A. Adegoke, K. Ramluckan, F. Bux, T.A. Stenström, Antibiotic residue in the aquatic environment: Status in Africa, Open Chem. 16 (2018) 890–903. https://doi.org/10.1515/chem-2018-0099.

[33] S.D. Costanzo, J. Murby, J. Bates, Ecosystem response to antibiotics entering the aquatic environment, Marin. Pollut. Bullet. 51 (2005) 218–223. https://doi.org/10.1016/j.marpolbul.2004.10.038.

[34] M.C. Ncibi, M. Sillanpää, Optimized removal of antibiotic drugs from aqueous solutions using single, double and multi-walled carbon nanotubes, J. Hazard. Mater. 298 (2015) 102–110. https://doi.org/10.1016/j.jhazmat.2015.05.025.

[35] N. G. Mbewana, Ntshaka, T. A. M. Msagati, Trends and progress on antibiotic-resistant *Mycobacterium tuberculosis* and genes in relation to human immunodeficiency virus, J. Infectious diseases. Med. Microbiol. 1 (2023) 1712-1819. https://doi.org/10.1155/2023/6659212.

[36] A.C. Faleye, A.A. Adegoke, K. Ramluckan, Faizal Bux, T. A. Stenström, Antibiotic residue in the aquatic environment: Status in Africa, Open. Chem. 16 (2018) 890-903. https://doi.org/10.1515/chem-2018-0099

[37] S. Matongo, G. Birungi, B. Moodley, P. Ndungu, Occurrence of selected pharmaceuticals in water and sediment of Umgeni River, KwaZulu-Natal, South Africa, Environ. Sci. Pollut. Res. 22 (2015) 10298–10308. https://doi.org/10.1007/s11356-015-4217-0.

[38] F.O. Agunbiade, B. Moodley, Occurrence and distribution pattern of acidic pharmaceuticals in surface water, wastewater, and sediment of the Msunduzi River, Kwazulu-Natal, South Africa, Environ. Toxicol. Chem. 35 (2016) 36–46. https://doi.org/10.1002/etc.3144.

[39] K.M. Kanama, A.P. Daso, L. Mpenyana-Monyatsi, M.A.A. Coetzee, Assessment of pharmaceuticals, personal care products, and hormones in wastewater treatment plants receiving inflows from health facilities in North West Province, South Africa, J. Toxicol. 2018 (2018). https://doi.org/10.1155/2018/3751930.

[40] S. Matongo, G. Birungi, B. Moodley, P. Ndungu, Pharmaceutical residues in water and sediment of Msunduzi River, KwaZulu-Natal, South Africa, Chemosphere 134 (2015) 133–140. https://doi.org/10.1016/j.chemosphere.2015.03.093.

[41] C.A. Magwira, N. Aneck-Hahn, M.B. Taylor, Fate, occurrence and potential adverse effects of antimicrobials used for treatment of tuberculosis in the aquatic environment in South Africa, Environ. Pollut. 254 (2019) 112990. https://doi.org/10.1016/j.envpol.2019.112990.

[42] R. K. Langbehn, C. Michels, H. M. Soares, Antibiotics in wastewater: From its occurrence to the biological removal by environmentally conscious technologies, Environ. Pollut. 275 (2021) 116603. https://doi.org/10.1016/j.envpol.2021.116603

[43] A. Jelic, M. Gros, A. Ginebreda, R. Cespedes-Sánchez, F. Ventura, M. Petrovic, D. Barcelo, Occurrence, partition and removal of pharmaceuticals in sewage water and sludge during wastewater treatment, Water Res. 45 (2011) 1165–1176. https://doi.org/10.1016/j.watres.2010.11.010.

[44] Y. Yang, Y.S. Ok, K.H. Kim, E.E. Kwon, Y.F. Tsang, Occurrences and removal of pharmaceuticals and personal care products (PPCPs) in drinking water and water/sewage treatment plants: A review, Sci. Total Environ. 596–597 (2017) 303–320. https://doi.org/10.1016/j.scitotenv.2017.04.102.

[45] M.J. García Galán, M.S. Díaz-Cruz, D. Barceló, Removal of sulfonamide antibiotics upon conventional activated sludge and advanced membrane bioreactor treatment, Anal. Bioanal. Chem. 404 (2012) 1505–1515. https://doi.org/10.1007/s00216-012-6239-5.

[46] Y. Li, G. Zhu, W.J. Ng, S.K. Tan, A review on removing pharmaceutical contaminants from wastewater by constructed wetlands: Design, performance and mechanism, Sci. Total Environ. 468–469 (2014) 908–932. https://doi.org/10.1016/j.scitotenv.2013.09.018.

[47] A.J. Baguer, J. Jensen, P.H. Krogh, Effects of the antibiotics oxytetracycline and tylosin on soil fauna, Chemosphere. 40 (2000) 751–757. https://doi.org/10.1016/S0045-6535(99)00449-X.

[48] N. Kemper, Veterinary antibiotics in the aquatic and terrestrial environment, Ecol. Indic. 8 (2008) 1–13. https://doi.org/10.1016/j.ecolind.2007.06.002.

[49] C.H. Johansson, L. Janmar, T. Backhaus, Toxicity of ciprofloxacin and sulfamethoxazole to marine periphytic algae and bacteria, Aquat. Toxicol. 156 (2014) 248–258. https://doi.org/10.1016/j.aquatox.2014.08.015.

[50] Z. Qiang, C. Adams, Potentiometric determination of acid dissociation constants (pKa) for human and veterinary antibiotics, Water Res. 38 (2004) 2874–2890. https://doi.org/10.1016/j.watres.2004.03.017.

[51] J. Zhou, X. Yun, J. Wang, Q. Li, Y. Wang, A review on the ecotoxicological effect of sulphonamides on aquatic organisms, Toxicol. Reports. 9 (2022) 534–540. https://doi.org/10.1016/j.toxrep.2022.03.034.

[52] M. Conde-Cid, G. Ferreira-Coelho, D. Fernández-Calviño, A. Núñez-Delgado,

M.J. Fernández-Sanjurjo, M. Arias-Estévez, E. Álvarez-Rodríguez, Single and simultaneous adsorption of three sulfonamides in agricultural soils: Effects of pH and organic matter content, Sci. Total Environ. 744 (2020) 140872. https://doi.org/10.1016/j.scitotenv.2020.140872.

[53] S.R. Hughes, P. Kay, L.E. Brown, Global synthesis and critical evaluation of pharmaceutical data sets collected from river systems, Environ. Sci. Technol. 47 (2013) 661–677. https://doi.org/10.1021/es3030148.

[54] G. Siedlewicz, A. Białk-Bielińska, M. Borecka, A. Winogradow, P. Stepnowski, K. Pazdro, Presence, concentrations and risk assessment of selected antibiotic residues in sediments and near-bottom waters collected from the polish coastal zone in the Southern Baltic Sea; Summary of 3 years of studies, Mar. Pollut. Bull. 129 (2018) 787–801. https://doi.org/10.1016/j.marpolbul.2017.10.075.

[55] C. Nguyen Dang Giang, Z. Sebesvari, F. Renaud, I. Rosendahl, Q. Hoang Minh, W. Amelung, Occurrence and dissipation of the antibiotics sulfamethoxazole, sulfadiazine, trimethoprim, and enrofloxacin in the Mekong Delta, Vietnam, PLoS. One. 10 (2015) 1–24. https://doi.org/10.1371/journal.pone.0131855.

[56] H. Gong, W. Chu, Photodegradation of sulfamethoxazole with a recyclable catalyst, Ind. Eng. Chem. Res. 54 (2015) 12763–12769. https://doi.org/10.1021/acs.iecr.5b03849.

[57] E. Scholar, Sulfonamide antibiotics, Primary. Care. Updates. OB/GYNS. 5 (1998) 32-35. https://doi.org/10.1016/S1068-607X(97)00121-2.

[58] T. Nguyen, C.P. Huang, R. Doong, C. Chen, C. Dong, Visible-light photodegradation of sulfamethoxazole (SMX) over AgP co-doped g-C_3 N_4 (Ag-P@UCN) photocatalyst in water, Chem. Eng. J. 384 (2020) 123383. https://doi.org/10.1016/j.cej.2019.123383.

[59] J. U. Okafor, U. U. Nwodo, Molecular characterization of antibiotic resistance determinants in Klebsiella pneumoniae isolates recovered from hospital effluents in the Eastern Cape province, South Africa, Nat. Lib. Med. 12 (2023) 01139. https://doi10.3390/antibiotics12071139.

[60] N. Bolong, A.F. Ismail, M.R. Salim, T. Matsuura, A review of the effects of emerging contaminants in wastewater and options for their removal, Desal. 239

(2009) 229–246. https://doi.org/10.1016/j.desal.2008.03.020.

[61] G. Lama, J. Meijide, A. Sanromán, M. Pazos, Heterogeneous advanced oxidation processes: Current approaches for wastewater treatment, Catal. 12 (2022) 344. https://doi.org/10.3390/catal12030344.

[62] N.Z. Arman, S. Salmiati, A. Aris, M.R. Salim, T.H. Nazifa, M.S. Muhamad, M. Marpongahtun, A review on emerging pollutants in the water environment: Existences, health effects and treatment processes, Water (Switzerland). 13 (2021) 1–31. https://doi.org/10.3390/w13223258.

[63] J.O. Tijani, O.O. Fatoba, G. Madzivire, L.F. Petrik, A review of combined advanced oxidation technologies for the removal of organic pollutants from water, Water. Air. Soil Pollut. 225 (2014) 2102. https://doi.org/10.1007/s11270-014-2102-y.

[64] Z. hua Liu, Y. Kanjo, S. Mizutani, Urinary excretion rates of natural estrogens and androgens from humans, and their occurrence and fate in the environment: A review, Sci. Total Environ. 407 (2009) 4975–4985. https://doi.org/10.1016/j.scitotenv.2009.06.001.

[65] O.M. Rodriguez-Narvaez, J.M. Peralta-Hernandez, A. Goonetilleke, E.R. Bandala, Treatment technologies for emerging contaminants in water: A review, Chem. Eng. J. 323 (2017) 361–380. https://doi.org/10.1016/j.cej.2017.04.106.

[66] S.S. Adav, D.J. Lee, K.Y. Show, J.H. Tay, Aerobic granular sludge: Recent advances, Biotechnol. Adv. 26 (2008) 411–423. https://doi.org/10.1016/j.biotechadv.2008.05.002.

[67] S. Tiglyene, A. Jaouad, L. Mandi, Treatment of tannery wastewater by infiltration percolation: Chromium removal and speciation in soil, Environ. Technol. 29 (2008) 613–624. https://doi.org/10.1080/09593330801983888.

[68] M. Bartolomeu, M.G.P.M.S. Neves, M.A.F. Faustino, A. Almeida, Wastewater chemical contaminants: remediation by advanced oxidation processes, Photochem. Photobiol. Sci. 17 (2018) 1573–1598. https://doi.org/10.1039/c8pp00249e.

[69] L.H.M.L.M. Santos, M. Gros, S. Rodriguez-Mozaz, C. Delerue-Matos, A. Pena, D. Barceló, M.C.B.S.M. Montenegro, Contribution of hospital effluents to the

load of pharmaceuticals in urban wastewaters: Identification of ecologically relevant pharmaceuticals, Sci. Total Environ. 461–462 (2013) 302–316. https://doi.org/10.1016/j.scitotenv.2013.04.077.

[70] M.K. De Kreuk, J.J. Heijnen, M.C.M. Van Loosdrecht, Simultaneous COD, nitrogen, and phosphate removal by aerobic granular sludge, Biotechnol. Bioeng. 90 (2005) 761–769. https://doi.org/10.1002/bit.20470.

[71] S. Weng, P. Sun, W. Ben, C.H. Huang, L.T. Lee, E.R. Blatchley, The Presence of pharmaceuticals and personal care products in swimming pools, Environ. Sci. Technol. Lett. 1 (2014) 495–498. https://doi.org/10.1021/ez5003133.

[72] N. Sutaswiriya, S. Homklin, T. Kreetachat, P. Vaithanomsat, N. Kreetachat, Monitoring estrogen and androgen residues from livestock farms in Phayao Lake, Thailand, Environ. Monit. Assess. 193 (2021) 10661. https://doi.org/10.1007/s10661-021-09607-9.

[73] N.A. Sabri, S. van Holst, H. Schmitt, B.M. van der Zaan, H.W. Gerritsen, H.H.M. Rijnaarts, A.A.M. Langenhoff, Fate of antibiotics and antibiotic resistance genes during conventional and additional treatment technologies in wastewater treatment plants, Sci. Total Environ. 741 (2020) 140199. https://doi.org/10.1016/j.scitotenv.2020.140199.

[74] T. Zhang, K. Lv, Q. Lu, L. Wang, X. Liu, Removal of antibiotic-resistant genes during drinking water treatment: A review, J. Environ. Sci. (China) 104 (2021) 415–429. https://doi.org/10.1016/j.jes.2020.12.023.

[75] G. Divyapriya, I.M. Nambi, J. Senthilnathan, Nanocatalysts in Fenton based advanced oxidation process for water and wastewater treatment, J. Bionanosci. 10 (2016) 356–368. https://doi.org/10.1166/jbns.2016.1387.

[76] J.A. Khan, M. Sayed, S. Khan, N.S. Shah, D.D. Dionysiou, G. Boczkaj, Advanced oxidation processes for the treatment of contaminants of emerging concern, Adv. Treat. Process. 45 (2020) 299-365. https://doi.org/10.1016/B978-0-12-813561-7.00009-2.

[77] Y. Chen, Y. Liu, L. Zhang, P. Xie, Z. Wang, A. Zhou, Z. Fang, J. Ma, Efficient degradation of imipramine by iron oxychloride-activated peroxymonosulfate process, J. Hazard. Mater. 353 (2018) 18–25.

https://doi.org/10.1016/j.jhazmat.2018.03.050.

[78] P. Kumari, A. Kumar, A remediation technique for organic and non-biodegradable pollutant, Res. Sur. Inter. 11 (2023) 100122. https://doi.org/10.1016/j.rsurfi.2023.100122.

[79] M.A. Oturan, J.J. Aaron, Advanced oxidation processes in water/wastewater treatment: Principles and applications. A review, Crit. Rev. Environ. Sci. Technol. 44 (2014) 2577–2641. https://doi.org/10.1080/10643389.2013.829765.

[80] A. Saravanan, V.C. Deivayanai, P.S. Kumar, G. Rangasamy, R. V. Hemavathy, T. Harshana, N. Gayathri, K. Alagumalai, A detailed review on advanced oxidation process in treatment of wastewater: Mechanism, challenges and future outlook, Chemosphere. 308 (2022) 136524. https://doi.org/10.1016/j.chemosphere.2022.136524.

[81] C.G. Joseph, G. Li Puma, A. Bono, D. Krishnaiah, Sonophotocatalysis in advanced oxidation process: A short review, Ultrason. Sonochem. 16 (2009) 583–589. https://doi.org/10.1016/j.ultsonch.2009.02.002.

[82] P. Chowdhury, T. Viraraghavan, Sonochemical degradation of chlorinated organic compounds, phenolic compounds and organic dyes - A review, Sci. Total Environ. 407 (2009) 2474–2492. https://doi.org/10.1016/j.scitotenv.2008.12.031.

[83] P. Sathishkumar, R.V. Mangalaraja, S. Anandan, Review on the recent improvements in sonochemical and combined sonochemical oxidation processes - A powerful tool for destruction of environmental contaminants, Renew. Sustain. Energy Rev. 55 (2016) 426–454. https://doi.org/10.1016/j.rser.2015.10.139.

[84] M.N. Patil, A.B. Pandit, Cavitation - A novel technique for making stable nano-suspensions, Ultrason. Sonochem. 14 (2007) 519–530. https://doi.org/10.1016/j.ultsonch.2006.10.007.

[85] M.H. Entezari, M. Mostafai, A. Sarafraz-Yazdi, A combination of ultrasound and a bio-catalyst: Removal of 2-chlorophenol from aqueous solution, Ultrason. Sonochem. 13 (2006) 37–41. https://doi.org/10.1016/j.ultsonch.2004.11.002.

[86] M.H. Sayadi, Water treatment using ultrasonic assistance : A review water treatment using ultrasonic assistance : A review, Environ. Civil. Eng. 2 (2016) 96–110. https://doi.org/10.1063/5.0013727

[87] B.H.J.H. Festos, Oxidation of tartaric acid in presence of iron, J. Chem. Soc. 65 (1894) 899–910. https://doi.org/10.1039/CT8946500899

[88] F. Haber, J. Weiss, J.O. Seph, W. Eiss, The catalytic decom position of hydrogen peroxide by Iron salts, J. Chem. Phys. 153 (2020) 332–351. https://doi.org/10.1063/5.0013727

[89] Walling C., Fenton's reagent revisited, American. J. Anal. Chem. 7 (2016) 125–131. https://doi.org/10.1021/ar50088a003

[90] A. Khataee, F. Salahpour, M. Fathinia, B. Seyyedi, B. Vahid, Iron rich laterite soil with mesoporous structure for heterogeneous Fenton-like degradation of an azo dye under visible light, J. Ind. Eng. Chem. 26 (2015) 129–135. https://doi.org/10.1016/j.jiec.2014.11.024.

[91] J.A. Giroto, A.C.S.C. Teixeira, C.A.O. Nascimento, R. Guardani, Photo-Fenton removal of water-soluble polymers, Chem. Eng. Process. Process Intensif. 47 (2008) 2361–2369. https://doi.org/10.1016/j.cep.2008.01.014.

[92] H. Hansson, F. Kaczala, M. Marques, W. Hogland, Photo-Fenton and Fenton oxidation of recalcitrant industrial wastewater using nanoscale zero-valent Iron, Inter. J. Photo. 6 (2012) 531076. https://doi.org/10.1155/2012/531076

[93] J.J. Pignatello, E. Oliveros, A. MacKay, Advanced oxidation processes for organic contaminant destruction based on the Fenton reaction and related chemistry, Crit. Rev. Environ. Sci. Technol. 36 (2006) 1–84. https://doi.org/10.1080/10643380500326564.

[94] N. De la Cruz, J. Giménez, S. Esplugas, D. Grandjean, L.F. De Alencastro, C. Pulgarín, Degradation of 32 emergent contaminants by UV and neutral photo-Fenton in domestic wastewater effluent previously treated by activated sludge, Water Res. 46 (2012) 1947–1957. https://doi.org/10.1016/j.watres.2012.01.014.

[95] C. Adán, J. Carbajo, A. Bahamonde, I. Oller, S. Malato, A. Martínez-Arias, Solar light assisted photodegradation of phenol with hydrogen peroxide over iron-doped titania catalysts: Role of iron leached/reabsorbed species, Appl. Catal. B

Environ. 108–109 (2011) 168–176. https://doi.org/10.1016/j.apcatb.2011.08.026.

[96] H. Sheng, Q. Li, W. Ma, H. Ji, C. Chen, J. Zhao, Photocatalytic degradation of organic pollutants on surface anionized TiO_2: Common effect of anions for high hole-availability by water, Appl. Catal. B Environ. 138–139 (2013) 212–218. https://doi.org/10.1016/j.apcatb.2013.03.001.

[97] W. Buchanan, F. Roddick, N. Porter, M. Drikas, Fractionation of UV and VUV pretreated natural organic matter from drinking water, Environ. Sci. Technol. 39 (2005) 4647–4654. https://doi.org/10.1021/es048489+.

[98] Z.H. Jabbar, S. Esmail Ebrahim, Recent advances in nano-semiconductors photocatalysis for degrading organic contaminants and microbial disinfection in wastewater: A comprehensive review, Environ. Nanotechnol. Monit. Manag. 17 (2022) 100666. https://doi.org/10.1016/j.enmm.2022.100666.

[99] Y. Deng, R. Zhao, Advanced oxidation processes (AOPs) in wastewater treatment, Curr. Pollut. Reports 1 (2015) 167–176. https://doi.org/10.1007/s40726-015-0015-z.

[100] G. Mamba, P.J. Mafa, V. Muthuraj, A. Mashayekh-Salehi, S. Royer, T.I.T. Nkambule, S. Rtimi, Heterogeneous advanced oxidation processes over stoichiometric ABO_3 perovskite nanostructures, Mater. Today Nano 18 (2022). https://doi.org/10.1016/j.mtnano.2022.100184.

[101] V. Hasija, V.H. Nguyen, A. Kumar, P. Raizada, V. Krishnan, A.A.P. Khan, P. Singh, E. Lichtfouse, C. Wang, P. Thi Huong, Advanced activation of persulfate by polymeric g-C_3N_4 based photocatalysts for environmental remediation: A review, J. Hazard. Mater. 413 (2021) 125324. https://doi.org/10.1016/j.jhazmat.2021.125324.

[102] W.G. Barb, J.H. Baxendale, P. George, K.R. Hargrave, Reactions of ferrous and ferric ions with hydrogen peroxide. Part II. - The ferric ion reaction, Trans. Faraday Soc. 47 (1951) 591–616. https://doi.org/10.1039/TF9514700591.

[103] F. Luo, C. Wei, Preparation of heterogeneous Fenton catalyst with residual carbon separated from coal gasification slag as carrier, Energy sources, Part A recover. Util. Environ. Eff. 45 (2023) 1747–1758.

https://doi.org/10.1080/15567036.2023.2179691.

[104] C.P. Silva, D. Pereira, V. Calisto, M.A. Martins, M. Otero, V.I. Esteves, D.L.D. Lima, Biochar-TiO_2 magnetic nanocomposites for photocatalytic solar-driven removal of antibiotics from aquaculture effluents, J. Environ. Manage. 294 (2021). https://doi.org/10.1016/j.jenvman.2021.112937.

[105] M.R. Abukhadra, A.A. AlHammadi, J. Seong Khim, J.S. Ajarem, A.A. Allam, Enhanced decontamination of Levofloxacin residuals from water using recycled glass based a green zinc oxide/mesoporous silica nanocomposite; adsorption and advanced oxidation studies, J. Clean. Prod. 356 (2022) 131836. https://doi.org/10.1016/j.jclepro.2022.131836.

[106] S. Jiang, H. Zheng, X. Sun, M. Zhu, Y. Zhou, D. Wang, D. Zhang, L. Zhang, New and highly efficient Ultra-thin g-C_3N_4/FeOCl nanocomposites as photo-Fenton catalysts for pollutants degradation and antibacterial effect under visible light, Chemosphere 290 (2022) 133324. https://doi.org/10.1016/j.chemosphere.2021.133324.

[107] N.A. Simamane, P.J. Mafa, N. Chaukura, T.T.I. Nkambule, T.J. Malefetse, G. Mamba, Leveraging biochar/iron oxychloride heterostructures for sulfamethoxazole pollution mitigation in water: Influential factors, environmental relevance, and mechanistic insights, Sur. Inter. 72 (2025). 107351. https://doi.org/10.1016/j.surfin.2025.107351.

[108] J. Gao, J. Xue, Q. Shen, T. Liu, X. Zhang, X. Liu, H. Jia, Q. Li, Y. Wu, A promoted photocatalysis system trade-off between thermodynamic and kinetic via hierarchical distribution dual-defects for efficient H_2 evolution, Chem. Eng. J. 431 (2022) 133281. https://doi.org/10.1016/j.cej.2021.133281.

[109] K.H. Tam, C.K. Cheung, Y.H. Leung, A.B. Djurišić, C.C. Ling, C.D. Beling, S. Fung, W.M. Kwok, W.K. Chan, D.L. Phillips, L. Ding, W.K. Ge, Defects in ZnO nanorods prepared by a hydrothermal method, J. Phys. Chem. B 110 (2006) 20865–20871. https://doi.org/10.1021/jp063239w.

[110] M. Sabri, A. Habibi-yangjeh, H. Chand, V. Krishnan, Activation of persulfate by novel TiO_2/FeOCl photocatalyst under visible light : Facile synthesis and high photocatalytic performance, Sep. Purif. Technol. 250 (2020) 117268. https://doi.org/10.1016/j.seppur.2020.117268.

[111] X. Xie, S. Li, H. Zhang, Z. Wang, H. Huang, Promoting charge separation of biochar-based Zn-TiO_2/pBC in the presence of ZnO for efficient sulfamethoxazole photodegradation under visible light irradiation, Sci. Total Environ. 659 (2019) 529–539. https://doi.org/10.1016/j.scitotenv.2018.12.401.

[112] S. Asadzadeh-Khaneghah, A. Habibi-Yangjeh, D. Seifzadeh, H. Chand, V. Krishnan, Visible-light-activated g-C_3N_4 nanosheet/carbon dot/FeOCl nanocomposites: Photodegradation of dye pollutants and tetracycline hydrochloride, Colloids Surfaces A Physicochem. Eng. Asp. 617 (2021) 126424. https://doi.org/10.1016/j.colsurfa.2021.126424.

[113] M. Liu, Y. Ye, J. Ye, T. Gao, D. Wang, G. Chen, Z. Song, Recent Advances of Magnetite (Fe_3O_4)-Based Magnetic Materials in Catalytic Applications, Magnetochemistry. 9 (2023) 110. https://doi.org/10.3390/magnetochemistry9040110.

[114] S.B. Beil, S. Bonnet, C. Casadevall, R.J. Detz, F. Eisenreich, S.D. Glover, C. Kerzig, L. Næsborg, S. Pullen, G. Storch, N. Wei, C. Zeymer, Challenges and future perspectives in photocatalysis: Conclusions from an Interdisciplinary workshop, JACS Au. 4 (2024) 2746–2766. https://doi.org/10.1021/jacsau.4c00527.

[115] C. Revilla Pacheco, M.R. Riveros Cruz, J. Cárdenas Garcia, R. Terán Hilares, G. de J. Colina Andrade, D.A. Pacheco Tanaka, A. Mogrovejo-Valdivia, Adsorption and degradation of rhodamine B and bromocresol green by FeOCl under advanced oxidation process, Arab. J. Chem. 16 (2023). https://doi.org/10.1016/j.arabjc.2023.105049.

[116] J. Zhang, X.L. Jiao, Y.G. Xia, F.F. Liu, Y.P. Pang, X.F. Zhao, D.R. Chen, Enhanced catalytic activity in liquid-exfoliated FeOCl nanosheets as a Fenton-like catalyst, Chem. - A Eur. J. 22 (2016) 9321–9329. https://doi.org/10.1002/chem.201600172.

[117] X. Zhao, Z. Zhang, FeOCl in advanced oxidization processes for water purification: A critical review, Curr. Pollut. Reports 9 (2023) 143–164. https://doi.org/10.1007/s40726-023-00256-9.

[118] J. Zhang, G. Zhang, Q. Ji, H. Lan, J. Qu, H. Liu, Carbon nanodot-modified FeOCl for photo-assisted Fenton reaction featuring synergistic in-situ H_2O_2 production

and activation, Appl. Catal. B Environ. 266 (2020) 118665. https://doi.org/10.1016/j.apcatb.2020.118665.

[119] B. Zhang, M. Chen, D. Li, H. Xu, D. Xia, Quantitative investigation into the enhancing utilization efficiency of H_2O_2 catalyzed by FeOCl under visible light, J. Photochem. Photobiol. A Chem. 386 (2020) 112072. https://doi.org/10.1016/j.jphotochem.2019.112072.

[120] F. Wen, S. Liu, X. Huang, L. Pang, C. Li, H. Liu, Photocatalytic synthesis of ammonia from hollow coral-like graphitic carbon nitride/FeOCl loaded with Fe-1T MoS_2 nanosheets as Co-catalysts, Langmuir. 40 (2024) 12207–12215. https://doi.org/10.1021/acs.langmuir.4c01283.

[121] T. Zhu, X. Shi, Z. Yan, Z. Sun, Tailored electronic modulation driven by Co-O-Fe bridge bonds: the key role of charge redistribution in boosting electrocatalytic oxidation of co-doped FeOCl Fenton catalysts, Sep. Purif. Technol. 380 (2026) 135387. https://doi.org/10.1016/j.seppur.2025.135387.

[122] J. Zhang, M. Zhan, L. Zheng, C. Zhang, G. Liu, J. Sha, S. Liu, S. Tian, FeOCl/POM heterojunctions with excellent Fenton catalytic performance via different mechanisms, Inorg. Chem. 58 (2019) 250–258. https://doi.org/10.1021/acs.inorgchem.8b02329.

[123] S. Zhong, Z.S. Zhu, P. Zhou, L. Shi, X. Duan, B. Lai, S. Wang, FeOCl nanoparticles loaded onto oxygen-enriched carbon nanotubes and nickel-foam-based cathodes for the electro-Fenton degradation of pollutants, ACS Appl. Nano Mater. 5 (2022) 12095–12106. https://doi.org/10.1021/acsanm.2c01413.

[124] Z. Vilamova1, M.J. Sampaio, L. Svoboda, J. Bednar, Z. Simonova, R. Dvorsky, C.G. Silva, J. L. Faria, Enhancing photocatalytic g-C_3N_4/PVDF membranes through new insights into the preparation methods, J. Alloys. Comp. 931 (2023) 167469. https://doi.org/10.1016/j.jallcom.2022.167469

[125] H. Guo, Y. Deng, H. Yin, J. Liu, S. Zou, Fabricating BiOCl nanoflake/FeOCl nanospindle heterostructures for efficient visible-light photocatalysis, Molecules. 28 (2023) 6949. https://doi.org/10.3390/molecules28196949.

[126] J. Song, M. Zhang, C. Yan, X. Zhao, G. Liu, J. Zhang, AgSCN/AgCl/FeOCl nanosheets heterojunction with novel interface structure and excellent

photocatalytic performance, J. Alloys Compd. 836 (2020) 155544. https://doi.org/10.1016/j.jallcom.2020.155544.

[127] X. Shi, C. Cui, L. Zhang, J. Zhang, G. Liu, FeOCl/Ln (Ln = la or Y): Efficient photo-Fenton catalysts for ibuprofen degradation, New J. Chem. 43 (2019) 16273–16280. https://doi.org/10.1039/c9nj03746b.

[128] J. Wei, X. Feng, X. Hu, J. Yang, C. Yang, B. Liu, Cu(II) doped FeOCl as an efficient photo-Fenton catalyst for phenol degradation at mild pH, Colloids Surfaces A Physicochem. Eng. Asp. 631 (2021) 127754. https://doi.org/10.1016/j.colsurfa.2021.127754.

[129] A. K. Worku, D. W. Ayele, Recent advances of graphene-based materials for emerging technologies, Results Chem. 5 (2023) 100971. https://doi.org/10.1016/j.rechem.2023.100971.

[130] Z. Tao, Y. Zhao, Y. Wang, G. Zhang, Recent advances in carbon nanotube technology: Bridging the gap from fundamental science to wide applications, J. Carbon Res. 10 (2024). https://doi.org/10.3390/c10030069.

[131] F. Zhao, Y. Rong, J. Wan, Z. Hu, Z. Peng, B. Wang, High photocatalytic performance of carbon quantum dots/TNTs composites for enhanced photogenerated charges separation under visible light, Catal. Today. 315 (2018) 162–170. https://doi.org/10.1016/j.cattod.2018.02.019.

[132] V.S. Sivasankarapillai, A. Vishnu Kirthi, M. Akksadha, S. Indu, U. Dhiviya Dharshini, J. Pushpamalar, L. Karthik, Recent advancements in the applications of carbon nanodots: Exploring the rising star of nanotechnology, Nanoscale Adv. 2 (2020) 1760–1773. https://doi.org/10.1039/c9na00794f.

[133] H. Luo, Y. Zeng, D. He, X. Pan, Application of iron-based materials in heterogeneous advanced oxidation processes for wastewater treatment: A review, Chem. Eng. J. 407 (2021) 127191. https://doi.org/10.1016/j.cej.2020.127191.

[134] J. Scaria, A. V. Karim, G. Divyapriya, P. V. Nidheesh, M. Suresh Kumar, Carbon-supported semiconductor nanoparticles as effective photocatalysts for water and wastewater treatment, Nanomater. Photocatal. Environ. Poll. 2 (2020) 245-278. https://doi.org/10.1016/B978-0-12-818598-8.00013-4.

[135] X. Hu, B. Liu, Y. Deng, H. Chen, S. Luo, C. Sun, P. Yang, S. Yang, Adsorption and heterogeneous Fenton degradation of 17α-methyltestosterone on nano Fe_3O_4/MWCNTs in aqueous solution, Appl. Catal. B Environ. 107 (2011) 274–283. https://doi.org/10.1016/j.apcatb.2011.07.025.

[136] M.A. Hossain, Synthesis of carbon nanoparticles from kerosene and their characterization by SEM, EDX, XRD and FTIR, Am. J. Nanosci. Nanotechnol. 1 (2013) 52. https://doi.org/10.11648/j.nano.20130102.12.

[137] S. Iijima, Helical microtubules of graphitic carbon, Mat. Sci. 354 (1991) 56-58. https://doi.org/10.1038/354056a0.

[138] A.L. Cazetta, L. Spessato, S.A.R. Melo, K.C. Bedin, T. Zhang, T. Asefa, T.L. Silva, V.C. Almeida, Sugarcane vinasse-derived nanoporous N-S-doped carbon material decorated with Co: A new and efficient multifunctional electrocatalyst, Int. J. Hydrogen Energy. 45 (2020) 9669–9682. https://doi.org/10.1016/j.ijhydene.2020.01.205.

[139] L. Wang, H. Yang, Y. Yang, Z. He, A novel scheme to improve the photo-Fenton performance of iron oxychloride by carbon: Three existent states and roles of carbon in the degradation of tetracycline in water, J. Colloid Interface Sci. 641 (2023) 916–928. https://doi.org/10.1016/j.jcis.2023.03.113.

[140] Y. Jiang, K. Mao, J. Ran, J. Su, G. Huang, X. Zheng, K. Zhang, H. Guan, C. Yang, H. Zhang, Carbon nitride-type polymers compounded with FeOCl to enhance the catalytic removal of antibiotics over a wide pH range: Performance and mechanism, J. Water Process Eng. 53 (2023) 103601. https://doi.org/10.1016/j.jwpe.2023.103601.

[141] P. Borpujari, S. Khan, J. Dutta, D. Borah, Biochar-metal nanocomposites for azo dye removal: advancements, mechanisms, and future prospects, Discov. Appl. Sci. 7 (2025). https://doi.org/10.1007/s42452-025-07706-7.

[142] A. El-Naggar, A.H. El-Naggar, S.M. Shaheen, B. Sarkar, S.X. Chang, D.C.W. Tsang, J. Rinklebe, Y.S. Ok, Biochar composition-dependent impacts on soil nutrient release, carbon mineralization, and potential environmental risk: A review, J. Environ. Manage. 241 (2019) 458–467. https://doi.org/10.1016/j.jenvman.2019.02.044.

[143] K.P. Gopinath, D.V.N. Vo, D. Gnana Prakash, A. Adithya Joseph, S. Viswanathan, J. Arun, Environmental applications of carbon-based materials: a review, Environ. Chem. Lett. 19 (2021) 557–582. https://doi.org/10.1007/s10311-020-01084-9.

[144] X. Zhang, B. Gao, Y. Zheng, X. Hu, A.E. Creamer, M.D. Annable, Y. Li, Biochar for volatile organic compound (VOC) removal: Sorption performance and governing mechanisms, Bioresour. Technol. 245 (2017) 606–614. https://doi.org/10.1016/j.biortech.2017.09.025.

[145] Z. Liu, Z. Xu, L. Xu, F. Buyong, T.C. Chay, Z. Li, Y. Cai, B. Hu, Y. Zhu, X. Wang, Modified biochar: synthesis and mechanism for removal of environmental heavy metals, Carbon Res. 1 (2022) 1–21. https://doi.org/10.1007/s44246-022-00007-3.

[146] S.K. Manikandan, P. Pallavi, K. Shetty, D. Bhattacharjee, D.A. Giannakoudakis, I.A. Katsoyiannis, V. Nair, Effective usage of biochar and microorganisms for the removal of heavy metal ions and pesticides, Molecules. 28 (2023). https://doi.org/10.3390/molecules28020719.

[147] L. Goswami, A. Kushwaha, S.R. Kafle, B.S. Kim, Surface modification of biochar for dye removal from wastewater, Catal. 12 (2022) 817. https://doi.org/10.3390/catal12080817.

[148] S. Chauhan, T. Shafi, B.K. Dubey, S. Chowdhury, Biochar-mediated removal of pharmaceutical compounds from aqueous matrices via adsorption, Waste Dispos. Sustain. Energy. 5 (2023) 37–62. https://doi.org/10.1007/s42768-022-00118-y.

[149] Y. Liu, X. Dai, J. Li, S. Cheng, J. Zhang, Y. Ma, Recent progress in TiO_2-biochar-based photocatalysts for water contaminants treatment: strategies to improve photocatalytic performance, RSC Adv. 14 (2024) 478–491. https://doi.org/10.1039/d3ra06910a.

[150] T.G. Ambaye, M. Vaccari, E.D. van Hullebusch, A. Amrane, S. Rtimi, Mechanisms and adsorption capacities of biochar for the removal of organic and inorganic pollutants from industrial wastewater, Int. J. Environ. Sci. Technol. 18 (2021) 3273–3294. https://doi.org/10.1007/s13762-020-03060-w.

[151] J. Fito, K.K. Kefeni, T.T.I. Nkambule, The potential of biochar-photocatalytic nanocomposites for removal of organic micropollutants from wastewater, Sci. Total Environ. 829 (2022) 154648. https://doi.org/10.1016/j.scitotenv.2022.154648.

[152] S. Li, Z. Wang, X. Zhao, X. Yang, G. Liang, X. Xie, Insight into enhanced carbamazepine photodegradation over biochar-based magnetic photocatalyst Fe_3O_4/BiOBr/BC under visible LED light irradiation, Chem. Eng. J. 360 (2019) 600–611. https://doi.org/10.1016/j.cej.2018.12.002.

[153] M. Khraisheh, J. Kim, L. Campos, A.H. Al-Muhtaseb, G.M. Walker, M. Alghouti, Removal of carbamazepine from water by a novel TiO_2-coconut shell powder/UV process: Composite preparation and photocatalytic activity, Environ. Eng. Sci. 30 (2013) 515–526. https://doi.org/10.1089/ees.2012.0056.

[154] E. Weidner, E. Karbassiyazdi, A. Altaee, T. Jesionowski, F. Ciesielczyk, Hybrid metal oxide/biochar materials for wastewater treatment technology: A review, ACS. Omega. 7 (2022) 27062–27078. https://doi.org/10.1021/acsomega.2c02909.

[155] J. Wang, S. Wang, Activation of persulfate (PS) and peroxymonosulfate (PMS) and application for the degradation of emerging contaminants, Chem. Eng. J. 334 (2018) 1502–1517. https://doi.org/10.1016/j.cej.2017.11.059.

[156] J. Adusei-Gyamfi, B. Ouddane, L. Rietveld, J.P. Cornard, J. Criquet, Natural organic matter-cations complexation and its impact on water treatment: A critical review, Water Res. 160 (2019) 130–147. https://doi.org/10.1016/j.watres.2019.05.064.

[157] G.D. Fang, D.D. Dionysiou, Y. Wang, S.R. Al-Abed, D.M. Zhou, Sulfate radical-based degradation of polychlorinated biphenyls: Effects of chloride ion and reaction kinetics, J. Hazard. Mater. 227–228 (2012) 394–401. https://doi.org/10.1016/j.jhazmat.2012.05.074.

[158] H. Dai, N. Li, J. Ye, J. Zhao, X. He, X. Duan, B. Yan, Engineering ohmic contact interfaces via oxygen-deficient oxide layers toward uniform Zn^{2+} flux and deposition, Chem. Eng. J. 472 (2023) 173216. https://doi.org/10.1016/j.cej.2023.144861.

[159] R. Xiao, Z. Luo, Z. Wei, S. Luo, R. Spinney, W. Yang, D.D. Dionysiou, Activation of peroxymonosulfate/persulfate by nanomaterials for sulfate radical-based advanced oxidation technologies, J. Chem. Eng. 19 (2018) 51–58. https://doi.org/10.1016/j.coche.2017.12.005.

[160] S. Guerra-Rodríguez, E. Rodríguez, D.N. Singh, J. Rodríguez-Chueca, Assessment of sulfate radical-based advanced oxidation processes for water and wastewater treatment: A review, Water (Switzerland) 10 (2018). https://doi.org/10.3390/w10121828.

[161] S. Wacławek, H. V. Lutze, V.K. Sharma, R. Xiao, D.D. Dionysiou, Revisit the alkaline activation of peroxydisulfate and peroxymonosulfate, Curr. Opin. Chem. Eng. 37 (2022) 100854. https://doi.org/10.1016/j.coche.2022.100854.

[162] A. Senthilkumar, M. Ganeshbabu, J. Karuppiah Lazarus, S. Sevugarathinam, J. John, S.K. Ponnusamy, P. V. Chellam, M. Sillanpää, Thermal and radiation based catalytic activation of persulfate systems in the removal of micropollutants: A review, Ind. Eng. Chem. Res. 62 (2023) 4554–4572. https://doi.org/10.1021/acs.iecr.2c02419.

[163] F. Chen, G.X. Huang, F.B. Yao, Q. Yang, Y.M. Zheng, Q.B. Zhao, H.Q. Yu, Catalytic degradation of ciprofloxacin by a visible-light-assisted peroxymonosulfate activation system: Performance and mechanism, Water Res. 173 (2020) 115559. https://doi.org/10.1016/j.watres.2020.115559.

[164] H. Song, L. Yan, Y. Wang, J. Jiang, J. Ma, C. Li, G. Wang, J. Gu, P. Liu, Electrochemically activated PMS and PDS: Radical oxidation versus nonradical oxidation, Chem. Eng. J. 391 (2020) 123560. https://doi.org/10.1016/j.cej.2019.123560.

[165] L. Zhang, M. Zhang, G. Kang, Z. Xu, Ultrasonically activated peroxymonosulfate oxidation for advanced water treatment: Cavitation mechanism, free radical generation and process simulation, Ultrason. Sonochem. 122 (2025) 107601. https://doi.org/10.1016/j.ultsonch.2025.107601.

[166] M. Kumari, M. Pulimi, Sulfate radical-based degradation of organic pollutants: A review on application of metal-organic frameworks as catalysts, ACS Omega. 8 (2023) 34262–34280. https://doi.org/10.1021/acsomega.3c02977.

[167] X. Xia, F. Zhu, J. Li, H. Yang, L. Wei, Q. Li, J. Jiang, G. Zhang, Q. Zhao, A review study on sulfate-radical-based advanced oxidation processes for domestic/industrial wastewater treatment: Degradation, efficiency, and mechanism, Front. Chem. 8 (2020) 592056. https://doi.org/10.3389/fchem.2020.592056.

[168] A. Buthiyappan, A.R. Abdul Aziz, W.M.A. Wan Daud, Recent advances and prospects of catalytic advanced oxidation process in treating textile effluents, Rev. Chem. Eng. 32 (2016) 1–47. https://doi.org/10.1515/revce-2015-0034.

[169] X. Wang, M. Sun, Y. Zhao, C. Wang, W. Ma, M.S. Wong, M. Elimelech, In situ electrochemical generation of reactive chlorine species for efficient ultrafiltration membrane self-cleaning, Environ. Sci. Technol. 54 (2020) 6997–7007. https://doi.org/10.1021/acs.est.0c01590.

[170] V. V. Banakar, S.S. Sabnis, P.R. Gogate, A. Raha, Saurabh, Ultrasound assisted continuous processing in microreactors with focus on crystallization and chemical synthesis: A critical review, Chem. Eng. Res. Des. 182 (2022) 273–289. https://doi.org/10.1016/j.cherd.2022.03.049.

[171] B. Su, Z.C. Cao, Z.J. Shi, Exploration of earth-abundant transition metals (Fe, Co, and Ni) as catalysts in unreactive chemical bond activations, Acc. Chem. Res. 48 (2015) 886–896. https://doi.org/10.1021/ar500345f.

[172] C. Dong, W. Fang, Q. Yi, J. Zhang, A comprehensive review on reactive oxygen species (ROS) in advanced oxidation processes (AOPs), Chemosphere 308 (2022) 136205. https://doi.org/10.1016/j.chemosphere.2022.136205.

[173] G. Mamba, P.J. Mafa, V. Muthuraj, A. Mashayekh-Salehi, S. Royer, T.I.T. Nkambule, S. Rtimi, Heterogeneous advanced oxidation processes over stoichiometric ABO_3 perovskite nanostructures, Mater. Today Nano 18 (2022) 100184. https://doi.org/10.1016/j.mtnano.2022.100184.

[174] C. Tan, Q. Xu, T. Sheng, X. Cui, Z. Wu, H. Gao, H. Li, Reactive oxygen species generation in FeOCl nanosheets activated peroxymonosulfate system: Radicals and non-radical pathways, J. Hazard. Mater. 398 (2020). https://doi.org/10.1016/j.jhazmat.2020.123084.

[175] I. Gul, M. Sayed, N.S. Shah, F. Rehman, J.A. Khan, S. Gul, N. Bibi, J. Iqbal, A

novel route for catalytic activation of peroxymonosulfate by oxygen vacancies improved bismuth-doped titania for the removal of recalcitrant organic contaminant, Environ. Sci. Pollut. Res. 28 (2021) 23368–23385. https://doi.org/10.1007/s11356-020-11497-2.

[176] D. Zhao, X. Liao, X. Yan, S.G. Huling, T. Chai, H. Tao, Effect and mechanism of persulfate activated by different methods for PAHs removal in soil, J. Hazard. Mater. 254–255 (2013) 228–235. https://doi.org/10.1016/j.jhazmat.2013.03.056.

[177] S. Li, M. Qi, Q. Yang, F. Shi, C. Liu, J. Du, Y. Sun, C. Li, B. Dong, State-of-the-art on the sulfate radical-advanced oxidation coupled with nanomaterials: biological and environmental applications, J. Funct. Biomater. 13 (2022). https://doi.org/10.3390/jfb13040227.

[178] R. Shakeel, A. Ahmad, H. Mushtaq, T. Haider, M. Javeria, A. Asif, K. Zia, H. Zafar, B. Ishaque, W.Z. Khan, Multifunctional nanomaterials in materials chemistry: A cross-disciplinary review of applications in energy, environment, catalysis, and biomedicine, Sch. J. Eng. Technol. 13 (2025) 673–707. https://doi.org/10.36347/sjet.2025.v13i08.007.

[179] J. Li, X. Jiang, H. Guan, Z. Liu, J. Li, Z. Lin, F. Li, W. Xu, Visible-light-driven peroxymonosulfate activation by robust TiO_2-base nanoparticles for efficient removal of sulfamethoxazole, Environ. Pollut. 334 (2023) 122150. https://doi.org/10.1016/j.envpol.2023.122150.

[180] R. Aali, H. Azari, H. Pasalari, K. Yaghmaeian, M. Yousefi, A. Azari, A.R. Yari, N. Sharifi, H. Kamani, M. Dowlati, Enhanced sulfadiazine degradation through synergistic visible light assisted peroxymonosulfate activation using a magnetic Fe_3O_4-$ZnIn_2S_4$ catalyst, Sci. Rep. 15 (2025) 25013. https://doi.org/10.1038/s41598-025-10973-4.

[181] I.F. Teixeira, E.C.M. Barbosa, S.C.E. Tsang, P.H.C. Camargo, Carbon nitrides and metal nanoparticles: From controlled synthesis to design principles for improved photocatalysis, Chem. Soc. Rev. 47 (2018) 7783–7817. https://doi.org/10.1039/c8cs00479j.

CHAPTER 3

EXPERIMENTAL METHODOLOGY

3.1 Introduction

This work comprised two interconnected studies, which together aimed to evaluate the synthesis, photocatalytic performance, and PMS activation capability of BC/FeOCl for SMX degradation from water. In the first part, the BC/FeOCl nanocomposite was synthesised via an ultrasonic-assisted wet impregnation followed by calcination method and subsequently evaluated for visible light-driven photocatalytic degradation of SMX in aqueous solution. The findings of the first part of this work and corresponding discussion are presented in **Chapter 4.** This first phase established the baseline photocatalytic performance of the nanocomposite and confirmed its suitability as a photocatalyst for antibiotic removal. Building on the outcomes of the first phase (**Chapter 4**), the second part of the work focused on the heterogeneous activation of PMS over BC/FeOCl nanocomposites obtained using two different synthesis methods to establish a sulphate radical–based advanced oxidation process for enhanced SMX degradation, and the findings are presented in **Chapter 5**. The wet impregnation and pyrolysis method was used to prepare WP-BC/FeOCl, and ultrasonic-assisted mechanical mixing was used to produce MM-BC/FeOCl, where WP and MM denote wet impregnation and mechanical mixing, respectively. The two composite materials were systematically compared to elucidate the influence of their different synthesis routes on physico-chemical properties, catalyst–oxidant interactions, and PMS activation efficiency. Based on the comparative performance, further PMS activation and photo-Fenton-like experiments were conducted using the more effective materials, namely WP-BC/FeOCl, under visible-light irradiation to evaluate SMX degradation kinetics, reactive species generation, and process efficiency.

This chapter presents the procedures employed for the synthesis and characterisation of the prepared nanomaterials, namely biochar, nano-sized FeOCl photocatalyst, and BC/FeOCl nanocomposites. Biochar was synthesised via a pyrolysis method, while FeOCl and BC/FeOCl were synthesised using two different preparation routes depending on the objectives of the study. In the first approach, an ultrasonic-assisted wet impregnation followed by calcination was used to obtain a well-integrated

BC/FeOCl nanocomposite for photocatalytic experiments. In the second approach, an ultrasonic-assisted mechanical mixing method was employed to prepare BC/FeOCl nanocomposites for comparative evaluation during PMS activation studies. These synthesis routes enabled the assessment of the influence of preparation method on material properties and catalytic performance.

Finally, the analytical techniques applied are outlined below, with a brief explanation of each approach and the expected outcomes. This research was conducted at the Institute for Nanotechnology and Water Sustainability (iNanoWS), University of South Africa.

3.2 Materials and reagents

Sodium nitrate ($NaNO_3$, 99%), sodium hydroxide pellets (NaOH, 98%), sodium chloride (NaCl, 99%), sodium bicarbonate ($NaHCO_3$, 99.7%), sodium phosphate (Na_3PO_4, 99%), Iron(III) chloride hexahydrate ($FeCl_3.6H_2O$, 97%), methanol (CH_3CH_2OH, 99 %), polyvinylpyrrolidone ($(C_6H_9NO)_n$, 99%), potassium peroxymonosulphate ($KHSO_5$, 99%), sulphamethoxazole (SMX, ≥ 98%), hydrochloric acid (HCl, 37%), benzoquinone (BQ ≥ 98%), and ethylene diamine tetra-acetic acid sodium salt (EDTA, 98.5 %) were purchased from Sigma Aldrich (South Africa). All reagents used in this study were of analytical grade and were used without any further purification. In addition, all aqueous solutions were prepared with deionised water (18.2 MΩ cm resistivity at 20 °C) obtained from a Mili-Q water purification system (Merk Millipore, Burlington, MA, USA).

3.3 Overview of synthesis methods for supported metal-based photocatalysts

3.3.1 Ultrasound-assisted wet impregnation

The ultrasonic-assisted wet impregnation method is an innovative technology for material synthesis and catalyst preparation [1]. It integrates wet impregnation with ultrasonication to enhance the dispersion and penetration of active components onto or within a support material. This leads to improved uniformity and overall performance. The active phase (catalyst, metal precursor, or other functional material) is dissolved in a solution, which is commonly an aqueous or organic solvent, during wet impregnation. Subsequently, this solution is placed into a porous support (such as biochar, silica, activated carbon, zeolites, or alumina) [2]. The solution then infiltrates

the support's pores, depositing the active substance. The solvent is then removed by drying or calcination, leaving the active component bound to the substrate. However, ultrasonication is performed using ultrasonic waves between 20 kHz and a few MHz [3]. Pressurised cavitation occurs as these high-frequency sound waves generate small bubbles that form and then rapidly collapse in the liquid. This produces localised hotspots of high pressure and temperature and creates strong agitation in the solution. This energy reduces agglomeration, improves mass transfer, and speeds up the penetration of the active material into the support pores [4]. **Fig. 3.1** displays an example of the ultrasonic-assisted wet impregnation method.

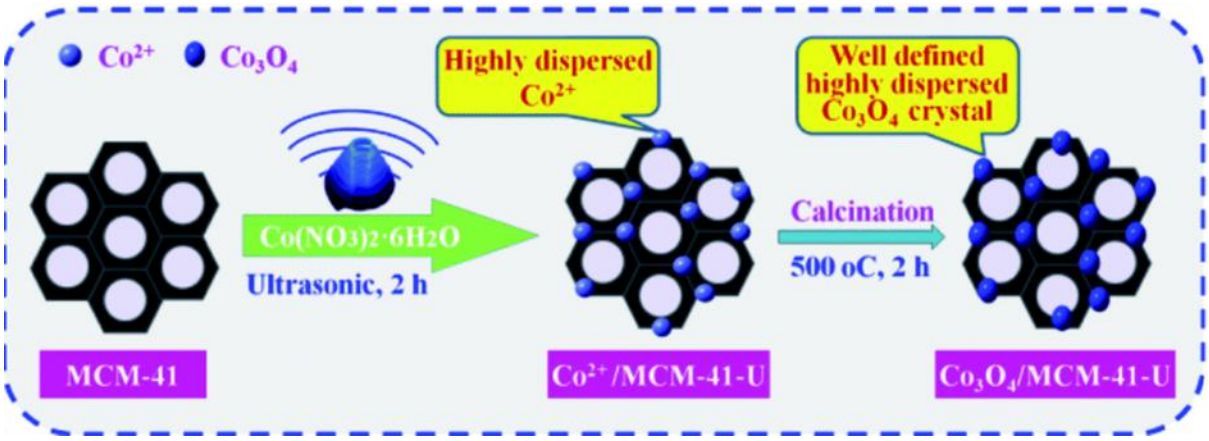

Figure 3.1 The synthesis of Co3O4/MCM-41-U using an ultrasonic-assisted wet impregnation [5].

3.3.2 Calcination

The calcination method involves heating a substance at a controlled temperature in a monitored environment, typically in the absence of air or a limited supply of oxygen. This process plays a critical role in tailoring the phase composition, crystallinity, morphology, and surface chemistry of synthesised materials [6]. In addition to inducing phase transformation and improving structural stability, calcination is particularly attractive because it promotes the removal of residual solvents, organic species, and precursor ligands, leading to purer and more thermally stable materials [7]. Furthermore, controlled calcination can enhance interfacial contact between supported phases and substrates, which is essential for improving catalytic and photocatalytic performance. **Fig. 3 .2** illustrates the calcination procedure employed in this study, in which a furnace was used to thermally treat the materials of interest [8]

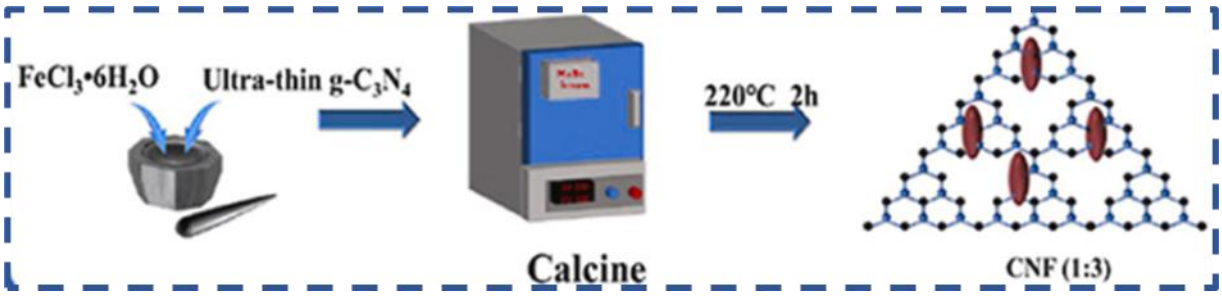

Figure 3.2 The calcination method for the synthesis of ultrathin g-C_3N_4/FeOCl material [8].

3.3.3 Synthesis of biochar/iron oxychloride heterojunctions

For the first part of the work (presented in **Chapter 4**), the preparation of the BC/FeOCl nanocomposite entailed ultrasonic-assisted wet impregnation of pre-synthesised biochar using aqueous ferric chloride hexahydrate and subsequent calcination. For the second part of the work (presented in **Chapter 5**), preparation of the BC/FeOCl nanocomposites proceeded via two methods: wet impregnation and pyrolysis, and ultrasonic-assisted mechanical mixing.

3.3.3.1 Synthesis of biochar

The synthesis of biochar was adopted from the literature with slight modifications [9]. Biochar (BC) was prepared via pyrolysis of dry blue gum pine wood trees found in the Savannah of Kimberly, Northern Cape, South Africa. The blue gum pine wood was first cut into slabs, which were further chopped into smaller pieces, before pyrolysis synthesis. Typically, the biomass pieces were transferred into a crucible that was closed with a lid, and the crucible was wrapped in heavy-duty aluminium foil to deprive the sample of free-flowing air. Subsequently, the sample was heated in a laboratory muffle furnace up to 750 °C at 10 °C min^{-1} and held for 2 h to complete the pyrolysis reaction. Finally, the furnace was allowed to cool naturally to room temperature before removing BC. Biochar was collected and washed sequentially with deionized water and ethanol, then dried overnight in a vacuum oven at 80 °C. The biochar was stored in air-tight sample vials for characterisation and further use.

3.3.3.2 Synthesis of BC/FeOCl via ultrasonic-assisted wet impregnation and pyrolysis

Furthermore, the ultrasonic-assisted wet impregnation and pyrolysis synthesis route of the BC/FeOCl nanocomposite was adopted from the literature with slight modifications, and the summary is shown in **Fig. 3.3a** [10]. Ferric chloride hexahydrate ($FeCl_3$. $6H_2O$, 3 g, 0.0111 mol) was poured into a 50 mL beaker containing 20 mL of deionised water/ethanol mixture (60 vol% water and 40 vol% ethanol) and sonicated for 30 min. A pre-weighed amount of BC was added to the solution and sonicated for another 30 min. The mixture was then stirred for 1 h and dried in an oven at 80 °C for 12 h. The resultant dried product was manually ground using an agate mortar and pestle to obtain a fine powder, transferred into a porcelain crucible, and heated to 230 °C in a muffle furnace at 3 °C/min for 3 h. The furnace was then allowed to cool to room temperature, and the powdered nanoparticles were collected and washed several times using deionised water and ethanol, then dried in an oven at 80 °C for 12 h. The final product was denoted as X-BC/FeOCl (where X = 3, 6, 9, and 12, representing the wt% ratio of BC relative to hexahydrate $FeCl_3$). The samples were stored in air-tight sample vials for characterisation and further use. Pristine FeOCl was prepared by calcining 3 g of $FeCl_3$. $6H_2O$ at 230 °C in a muffle furnace at 3 °C/min and held for 3 h (**Fig. 3.3b**)**.** The washing and drying of FeOCl followed the same order as the BC/FeOCl composite.

NB- In **Chapter 4**, the BC percentage was defined relative to the mass of the ferric chloride hexahydrate ($FeCl_3 \cdot 6H_2O$) precursor during the wet impregnation stage. However, upon calcination, $FeCl_3 \cdot 6H_2O$ thermally decomposes to form FeOCl, resulting in a substantial reduction in mass. Based on molar mass relationships, only approximately 39.3% of the original $FeCl_3 \cdot 6H_2O$ mass is retained as FeOCl in the final material. As a result, the BC loading initially expressed relative to $FeCl_3 \cdot 6H_2O$ in **Chapter 4** effectively corresponds to a BC: FeOCl mass ratio in the calcined composite. Accordingly, the optimal 6 wt% BC identified in **Chapter 4** is equivalent to approximately 6 wt% BC relative to FeOCl in the final material (6-BC/FeOCl). This equivalence forms the basis for fixing the BC content at 6 wt% relative to FeOCl in the synthesis of WP-BC/FeOCl and MM-BC/FeOCl in **Chapter 5**, thereby ensuring compositional consistency and meaningful comparison between the two parts of the study.

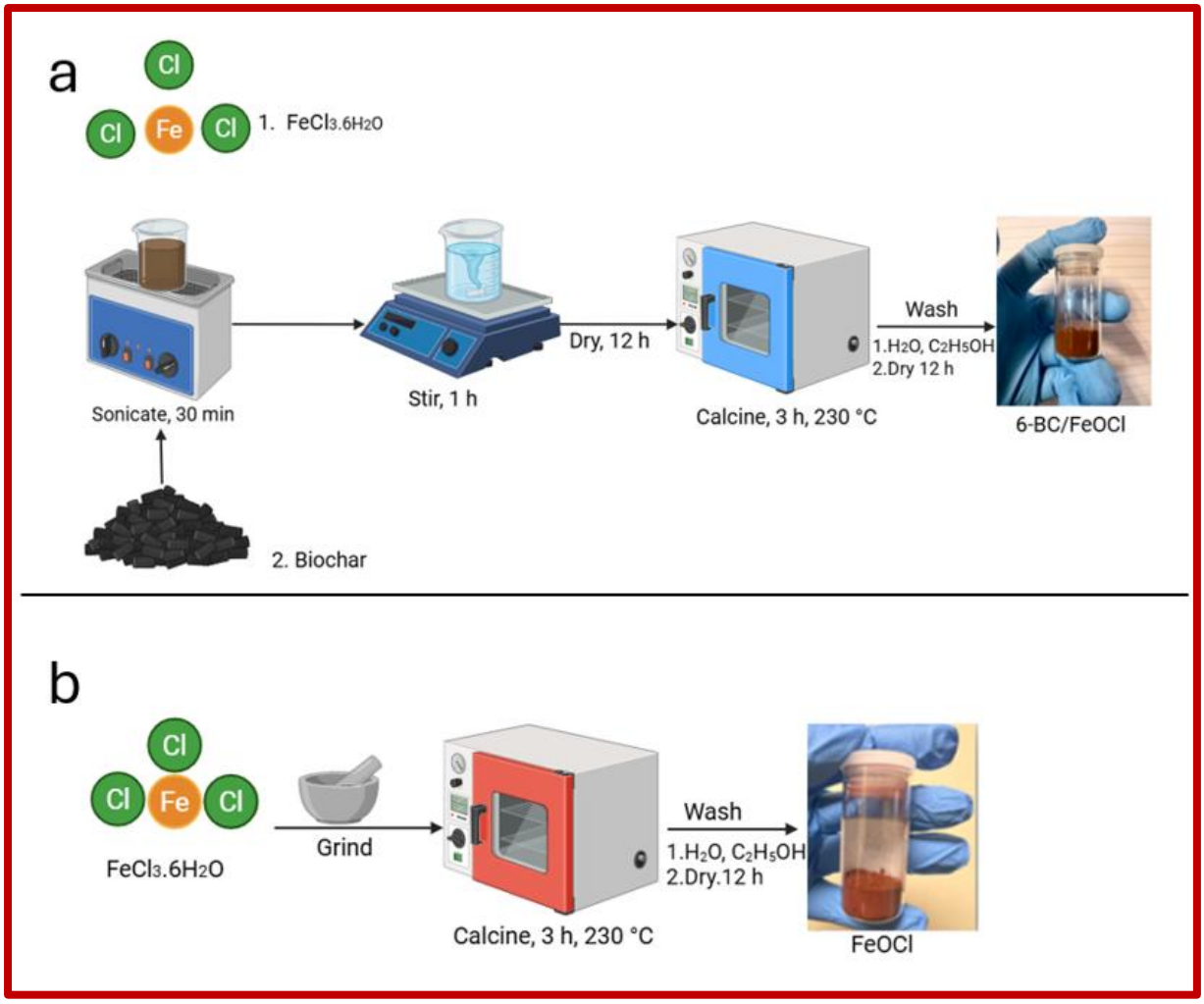

Figure 3.3 (a) Summary schematic illustration of 6-BC/FeOCl nanocomposite via ultrasonic-assisted wet impregnation and calcination method, (b) FeOCl synthesis via calcination of $FeCl_3 \cdot 6H_2O$.

3.3.3.3 Synthesis of WP-BC/FeOCl and MM-BC/FeOCl composites

In the second phase of the work (presented in **Chapter 5**), preparation of the BC/FeOCl nanocomposites via wet impregnation and pyrolysis was employed for the fabrication of WP-BC/FeOCl, and ultrasonic-assisted mechanical mixing for preparing MM-BC/FeOCl. In both composite materials, the biochar content was fixed at 6 wt% relative to FeOCl, which was established as the optimal loading in the first part (**Chapter 4**). In WP-BC/FeOCl, the "WP" denotes the wet impregnation and pyrolysis synthesis method, and the "MM" represents the mechanical mixing method in MM-BC/FeOCl. Firstly, WP-BC/FeOCl was prepared as outlined in **Section 3.3.3.2**. Meanwhile, MM-BC/FeOCl was prepared by mechanically mixing pre-synthesised BC (**Section 3.3.3.1**) and FeOCl prepared as outlined in **Section 3.3.3.2** at a mass ratio

of 0.14 g to 2.2 g, corresponding to approximately 6 wt% biochar (BC:FeOCl). The preparation of the MM-BC/FeOCl nanocomposite was adopted from the literature with slight modifications [11] and summarised in **Fig. 3.4**. Previously synthesised FeOCl (2.2 g) was placed into a 50 mL beaker containing a mixture of deionised water and ethanol (60 vol% water and 40 vol% ethanol). An amount of 0.14 g of BC was then added to the mixture, which was subjected to sonication for 30 min. Afterward, the mixture was stirred for 1 h and dried overnight in an oven at 80 °C. The dried product was manually ground using an agate mortar and pestle to obtain a fine powder, transferred into a porcelain crucible, and heated to 230 °C in a muffle furnace at a rate of 3 °C/min, maintaining the temperature for 3 h. The furnace was then allowed to cool to room temperature, and the resulting powdered nanoparticles were collected, thoroughly washed multiple times with deionised water and ethanol, and dried overnight at 80 °C. The final product, labelled as MM-BC/FeOCl, was stored in air-tight vials for further characterisation and applications.

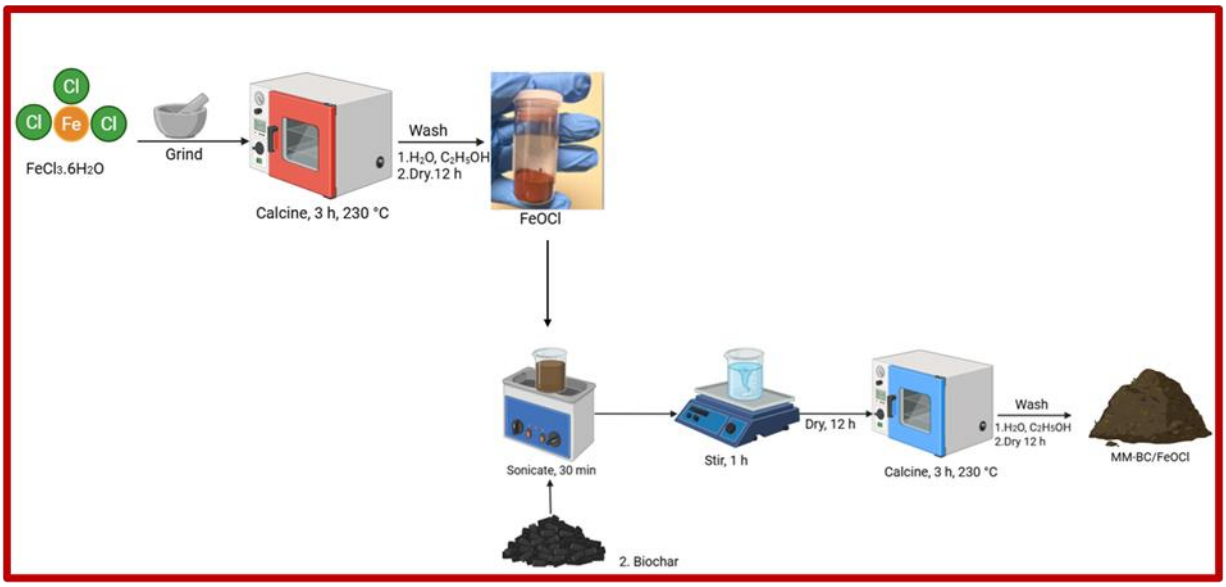

Figure 3.4 Summary schematic illustration of MM-BC/FeOCl synthesis via ultrasonic-assisted mechanical mixing.

3.4 Characterisation of the prepared materials

The prepared BC/FeOCl nanocomposites prepared via the different methods were analysed using various techniques to study their physical, chemical, and optical properties. X-ray diffraction (XRD) was performed using a PANalytical PW3040/60

X'Pert Pro powder X-ray diffractometer, with Cu Kα radiation (45 kV, 40 mA) with a wavelength λ=1.54 Å. The scan angle ranged from $5^o < 2\theta < 90^o$ at a scan rate of 2 degrees min^{-1}. FT-IR spectroscopy was employed to analyse the functional groups of the prepared materials using a Perkin-Elmer Infrared 100 spectrometer with a KBr background. The samples were scanned at wavenumbers ranging from 500 to 4000 cm^{-1} at 4 cm^{-1} resolution. The optical properties of the materials were examined using a Perkin-Elmer UV-vis diffuse reflectance spectrometer (Lambda 650 S) fitted with deuterium and tungsten halogen light sources. The morphologies and microstructures of the prepared materials were observed using a Zeiss Field Emission Scanning Electron Microscope (FE-SEM) coupled with EDS with an Oxford detector and a JEOL JEM 2100 (TEM) operated at 200 kV, respectively. Brunauer-Emmett-Teller (BET) analysis was performed using an Autosorb iQ3 (Quantachrome Instruments) after a degassing temperature of 200 °C for 6 h. The Thermo ESCAlab 250Xi spectrometer with Al kα (1486.7 eV) monochromatic radiation source was used for XPS analysis.

For the electrochemical characterisation, an Autolab potentiostat/galvanostat (PGSTAT 302 N model, Metrohm, Swiss instrument) was used. The Ag/AgCl (3M KCl) and platinum wires were used as reference and counter electrodes, respectively. The working electrodes were fabricated by blending the photocatalytic materials with poly (vinylidene fluoride) (PVDF) and polyvinylpyrrolidone (PVP), working as binders in 3 mL of N-Methyl-2-pyrrolidinone (NMP) solvent. The weight ratios of PVDF: PVP were 1:1 in the NMP solution, and they were sonicated for 1 h. Thereafter, the prepared slurry was used to construct the working electrodes using the clean FTO glasses. The cyclic voltammetry curves were measured using a sweep rate of 50 mV s^{-1} and a potential window of -0.5 to 1.2 V. The linear sweep voltammetry was measured along with Tafel polarisation curves at a sweep rate of 50 mV s^{-1} and a potential window of -0.2 to 2 V. Electrochemical impedance spectroscopy (EIS) was performed at a frequency range of 100 kHz to 100 MHz and 10 mV RMS amplitude. The 0.5 mM $[Fe(CN)_6]^{3-/4-}$ prepared in 0.1 M KCl was used as an active redox electrolyte throughout the electrochemical experiments.

3.4.1 Zeiss Field Emission Scanning Electron Microscope

Zeiss Field Emission Scanning Electron Microscope (FE-SEM) is used to observe the surface or internal structure of a particle and obtain information such as the size and

shape of nanoparticles embedded in a bulk sample focusing from a highly energised electron beam [12]. Due to its utility in studying organic and inorganic materials within nanometre to micrometre (μm) regions, FE-SEM finds applications in many branches of science. Most of the SEMs operate at very high magnifications, some attaining a maximum of 300,000 times, with the latest models getting up to one million times magnification, which allows imaging of various materials with high accuracy and clarity [13]. In addition, as part of scanning electron microscope systems, energy-dispersive X-ray spectroscopy (EDS) provides insights into the material's composition, offering critical details beyond the capabilities of standard lab tests [13]. As shown in **Fig. 3.5**, the SEM equipment features advanced Quanta SEM technology tailored for materials science applications.

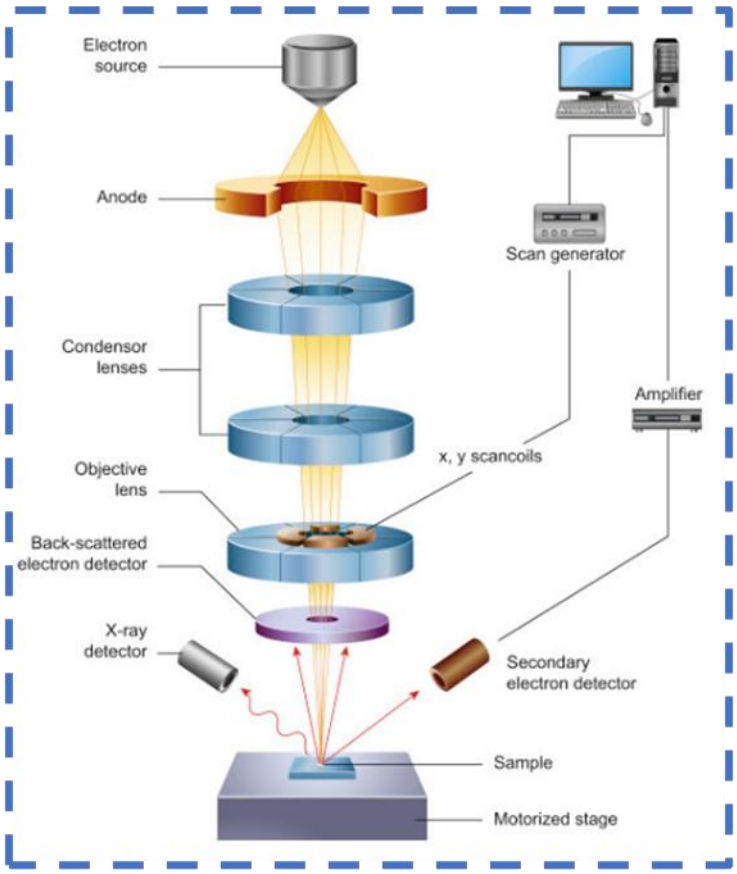

Figure 3.5 Schematic of the scanning electron microscope [14].

Electrons are generated at the top of the column in the electron gun and accelerated down the column at a predetermined accelerating voltage, which normally ranges between 1 and 30 keV [14]. Condenser lenses and apertures narrow the beam diameter. The objective lens, which is the final lens in the column, focuses on the

electron beam onto the sample surface [14]. In an SEM, the beam diameter can vary from less than 1 to 20 nm, depending on factors such as the electron gun type, accelerating voltage, and lens configuration [15]. The sample is positioned on a stage within the chamber, where both the chamber and the column are kept under vacuum using a pump system [15]. The vacuum level is determined by the design of the microscope, with some allowing for adjustable pumping. This enables the sample chamber to be maintained at a lower vacuum level than the column, facilitating low-vacuum imaging when necessary [16]. The electron beam position on the sample is managed by scan coils located above the objective lens. These coils enable the beam to sweep across the sample surface in the X-Y plane. The scanned beam interacts with the sample and produces various signals, including secondary electrons, backscattered electrons, and elastic scattering. Then, these signals are captured by specific detectors for analysis. Elastic scattering can provide valuable insights into the SEM image, revealing important details about the nanoparticles' topology and morphology [16]. In this study, SEM was employed to capture microscale images of the synthesised materials. These images were used to illustrate the surface microstructure, which helped predict the particle arrangement. Additionally, scanning electron microscopy (SEM) provided valuable insights into the morphology and particle aggregation of the synthesised material.

3.4.2 High-resolution transmission electron microscopy

High-resolution transmission electron microscopy (HRTEM) in **Fig. 3.6** is a mode of transmission electron microscopy (TEM) that enables direct imaging of the atomic structure of the sample [17]. It is an essential tool for characterising nanostructures, offering various imaging modes and high-sensitivity insights into elemental composition and electronic structure [17]. As materials research increasingly targets optimisation at the nanoscale, precise information at this level becomes crucial. HRTEM provides the most detailed structural insights, allowing for the fundamental characterisation of samples at the atomic level. This detail is vital in nanomaterials research, as even minor structural inconsistencies can significantly change the properties of materials.

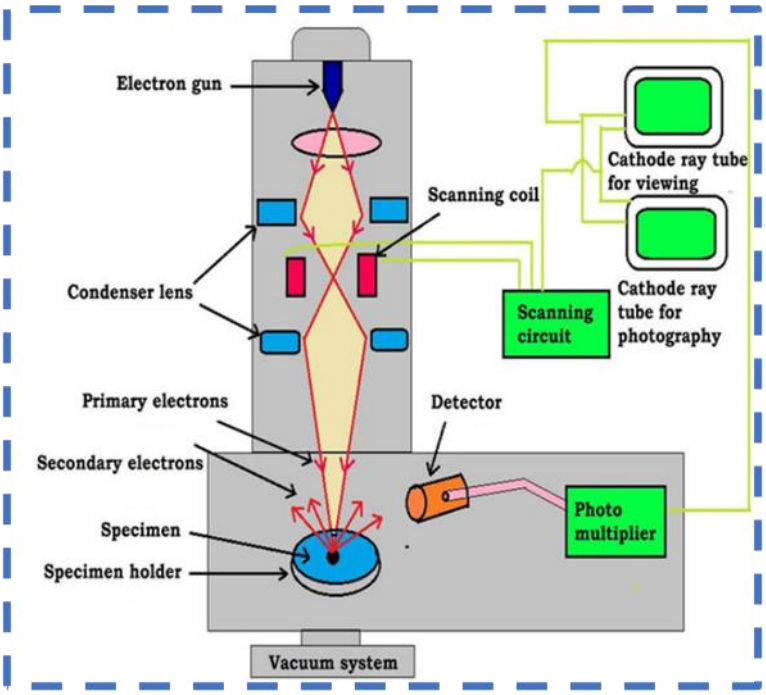

Figure 3.6 Schematic illustration of HR-TEM [18].

In this technique, electrons are generated in the electron gun through thermionic emission (using tungsten or lanthanum hexaboride filaments), Schottky emission, or field emission (using tungsten filaments) [18]. The two-stage condenser lens system allows for control over both the illumination aperture and the illumination area of the specimen. The primary function of the objective lens is to form either an image or a specimen diffraction pattern [19]. These EDS patterns are instrumental in determining the crystallographic structure of the sample. The resulting image can be captured using a photographic plate or through a digital fluorescence screen, which is coupled to a charge-coupled device (CCD) camera via a fibre-optic plate [19]. In this study, transmission electron microscopy (TEM) was employed to analyse the crystal structure, particle sizes, and shapes, as well as the morphology and aggregation of the synthesised nanomaterials.

3.4.3 Energy dispersive spectroscopy

Energy dispersive spectroscopy (EDS) operates by detecting and analysing the energy and intensity of X-rays emitted from a sample when it is bombarded by an electron beam in an electron microscope [20]. Depending on whether SEM or a TEM is used, the technique is referred to as SEM-EDS or TEM-EDS, respectively. During EDS analysis, the high-energy electron beam of the microscope interacts with the

sample's atoms. This interaction causes several effects, including the ejection of an electron from the inner shell of the atom, creating a vacancy [21]. A higher energy outer-shell electron fills this vacancy quickly. As the outer electron transitions to the lower energy shell, it releases excess energy in the form of X-rays [22]. An energy-dispersive spectrometer can detect and measure the energy and number of X-rays emitted from a specimen [11]. Thus, EDS experiments were conducted to verify the presence of various elements in all the synthesised nanomaterials.

3.4.4 Fourier-transform infrared spectroscopy

Fourier-transform infrared (FT-IR) spectroscopy (**Fig. 3.7**) is a technique that is used to investigate molecular vibrations and identify specific functional groups within a molecule. The IR region (10–14,000 cm^{-1}) of the electromagnetic spectrum is divided into three sections: near, mid, and far IR. The mid-IR range (400–4,000 cm^{-1}) is most commonly used for analysis because all molecules have characteristic absorbance frequencies and primary molecular vibrations within this range. Mid-IR spectroscopy is based on the interaction between IR radiation and samples [23]. Certain wavelengths are absorbed as IR radiation passes through a sample, causing the chemical bonds in the material to vibrate through stretching, bending, and contracting [23]. IR radiation is consistently absorbed by functional groups in a molecule at specific wavenumbers, regardless of other molecular structures, and the spectral peaks result from these vibrational energy changes [24].

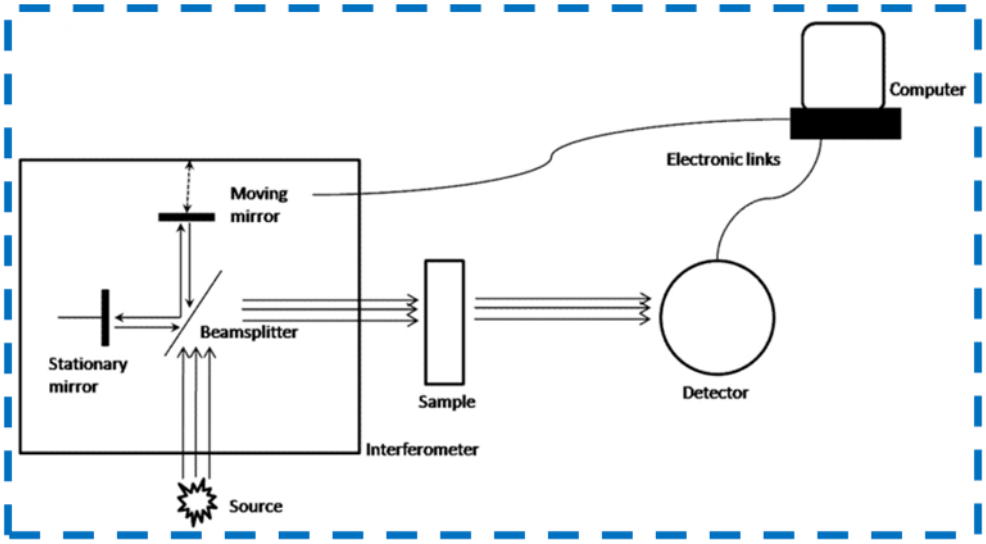

Figure 3.7 Basic components of the FT-IR spectrometer [23].

The general schematic of the FT-IR spectrometer shows that the IR source emits radiation that passes through an interferometer, typically a Michelson interferometer, that includes a beam splitter (a semi-reflecting film, usually made of KBr), a fixed mirror, and a moving mirror [25]. The interferometer employs interference patterns to precisely measure light wavelengths. A portion of the IR radiation is absorbed when it passes through a sample, while the remaining radiation is transmitted to the detector [25]. The detector captures the total interferogram from all IR wavelengths. The interferogram (intensity versus time spectrum) is converted into an IR spectrum (intensity versus frequency spectrum) by a mathematical operation known as the Fourier transform [23,25]. FT-IR was employed in this study to confirm the molecular fingerprints of the synthesised nanomaterials.

3.4.5 X-ray diffraction analysis

X-ray diffraction (XRD) is one of the useful techniques for structural analysis to study the crystal structure, namely employed to determine atomic arrangement in a para-crystalline phase and information about electronic distribution, bond length, bond angle, and so forth [26]. XRD is a non-destructive process that is generally used in day-to-day analysis. It is based on monochromatic X-rays and relies on the constructive interference between the X-rays and a crystalline sample [27]. The X-rays are generated through a cathode-ray tube, monochromatized by passing through different filters, and then directed towards the sample [28]. When X-rays strike a crystalline solid, the scattered beams are intensified in coherent directions because of the ordered structure of crystalline atoms. This constructive interference manifests diffraction patterns when the conditions follow Bragg's Law ($n\lambda = 2d \sin \theta$), which depends on the wavelength (λ) of electromagnetic radiation, the angle of diffraction (θ), and lattice spacing (d) in a crystalline material [27]. The random orientation of crystals causes the diffraction peaks in nanocrystalline materials. XRD is an indispensable characterisation method and is commonly employed in nanoparticle studies to determine essential properties such as crystallographic phase, crystallite size, and strain [29]. In this work, XRD was used to determine the crystallinity of the material to ascertain the phases or forms that correspond to the synthesis produced. Moreover, by analysing the diffraction peaks in the XRD spectra, an average particle size was obtained.

3.4.6 Brunauer-Emmet-Teller analysis

The Brunauer-Emmett-Teller (BET) theory is employed to measure the surface area of solid or porous materials, providing valuable insight into their physical structure. Since the surface area of a material influences its interactions with the environment, it plays a key role in properties such as catalytic activity, shelf life, moisture retention, and dissolution rates [30]. Surface area analysis, which is essential for the design and production of solids, is one of the commonly used methods in material characterisation. The surface area of a material can change during synthesis and processing. When a particle is broken down (grounded) into smaller particles, the surface area is extended, increasing the overall surface area. Similarly, the creation of pores within the particle's interior through dissolution, decomposition, or other physical or chemical methods also expands the surface area [30]. Materials with numerous narrow pores, such as activated carbon, have surface areas that can reach up to 2000 m^2 per gram [31]. To measure the BET-specific surface area of a sample, an inert gas is adsorbed onto its surface. Nitrogen is the most used gas adsorbate for surface probing in the BET analysis. As a result, the measurements are typically conducted just above the boiling point of nitrogen (77 K) and under controlled pressure [31].

Adsorption occurs when gas molecules are attracted to the surface of a solid sample and form physical bonds with it. The amount of gas adsorbed is determined at various pressure points and used to generate the adsorption isotherm. The BET analysis is performed at the starting points of the isotherm, reflecting the monolayer adsorption of gas molecules on the sample's surface [32]. Before measuring the specific surface area of the sample, any gases or vapours that may have physically adsorbed onto the surface during synthesis, treatment, handling, or storage should be eliminated [32]. The data is then collected by either introducing (for adsorption) or removing (for desorption) a known quantity of gas from a specified amount of material in a sample cell, which is kept at a constant temperature just above 77 K [33]. BET analysis was used in this research to obtain the specific surface area of the synthesised nanomaterials, pore volume, and pore size distribution. The data show the BET adsorption isotherm type the material represents.

3.4.7 X-ray photoelectron spectroscopy

X-ray photoelectron spectroscopy (XPS) is a surface analysis technique that bombards the sample with photons/electrons/ions and measures the electrons/photons/ion emitted. XPS uses low-energy (~1.5 keV) X-rays to irradiate the sample to induce a photoelectric effect. A high-resolution electron spectrometer detects the energy spectrum of fine photoelectrons. XPS experiments require the highest available vacuum conditions. The high vacuum helps transport photoelectrons from the sample to the analyser and prevents recontamination of cleaned samples. Since XPS is a surface-sensitive technique and typically has a sampling depth of a few nm [34], surface analysis conducted through XPS entails irradiation of the sample by low-energy (or mono-energetic) X-rays and subsequent analysis of the energy of emitted electrons. The X-rays commonly used are Kα lines of Mg (1.2536 keV) and Al (1.4866 keV). These photons penetrate the solid sample by only a few microns. Therefore, the incident photons interact with the surface atoms and cause electron photoelectric emission (**Eq. 3.1**) [34].

$$K.E = h\nu - B.E - \varphi s \qquad 3.1$$

In this equation, hv is the photon energy, B.E. is the binding energy of the atomic orbital from which the electron is released, and φs, is the spectrometer's work function. Binding energy (B.E.) is the energy difference between an atom's initial and final states when an electron is ejected. The electrons emitted from an ion exhibit varying kinetic energies due to the potential for different final states of the ion, depending on the specific atom. In addition, each of these final states has a distinct probability or cross-section [35].

Because the core-level binding energy is characteristic of a particular element or atom, XPS can reveal both the elemental composition and chemical bonding of a material's surface [36]. The XPS peaks are closely connected to the electronic structure of the atom, with spectral peaks corresponding to the specific energy levels from which photoelectrons are emitted. Because the intensity of specific electron transitions in an element is directly related to the amount of that element in the sample, XPS is an efficient method for performing quantitative chemical analysis. The strength of the XPS signals is influenced by the atomic concentration of the element being analysed within

the sample [37]. In this project, XPS analysis was used to determine the surface chemistry of the synthesised nanomaterials.

3.4.8 Ultraviolet-visible spectroscopy

Ultraviolet-visible spectroscopy (UV-vis) utilises light from the ultraviolet and visible regions of the electromagnetic spectrum to excite electrons from their ground state to higher energy levels. This process results in absorption at wavelengths unique to each molecule or material. Molecules or semiconductors that contain π-electrons or nonbonding electrons can absorb ultraviolet or visible light energy, causing these electrons to move to higher anti-bonding molecular orbitals [38]. Molecules with easily excitable electrons, i.e., those with a smaller energy gap between the highest occupied molecular orbital (HOMO) and the lowest unoccupied molecular orbital (LUMO), absorb light at longer wavelengths within the UV-vis spectrum [39]. UV-vis is a widely used and well-established analytical method because it is simpler, more versatile, faster, more accurate, and more cost-effective than many other techniques.

In a UV-vis spectrophotometer, the light source emits light across all wavelengths in the UV and visible spectra [40]. This light is then collimated, directed through an entrance slit, and passed through a monochromator, which separates the light into individual wavelengths. The selected light is transmitted through the sample and then detected by a photocell that measures the intensity at each wavelength. The intensity is recorded as absorbance (A) or transmission (T or %T). UV-vis is a qualitative and quantitative technique. The absorption peaks observed at specific wavelengths provide qualitative insights into the types of bonds within a molecule, thereby identifying the functional groups in a sample. On the quantitative side, the Beer-Lambert law states that the absorbance (A) is directly proportional to the concentration (c) of the absorbing species and the path length (L) of the sample (**Eq. 3.2**) [41].

$$A = \varepsilon \mathrm{c} \mathrm{L} \qquad 3.2$$

Here, $\boldsymbol{\varepsilon}$ represents the absorption coefficient, and A is calculated using the formula A = log10 (I_0/I), where I_0 is the initial light intensity before passing through the sample, and I is the light intensity after passing through it. Therefore, with a fixed path length, UV-vis spectroscopy can be used to determine the analyte concentration in a solution [41].

Qualitative analysis of semiconductor materials through UV-vis is performed using the diffuse reflectance spectrum to determine the reflectance (R) of the material. This data can then be transformed into the Kubelka-Munk function, F(%R), derived from the %R values, or the UV-vis instrument may directly provide the Kubelka–Munk function values. The electronic structure of semiconductor crystallites exhibits a three-dimensional size effect at the nanoscale, which can be assessed using UV-vis absorption spectroscopy. The optical bandgap can be calculated using the Tauc relationship, as expressed by the following equation (**Eq. 3.3**) [42]:

$$\alpha \mathrm{hv} = (hv - Eg)^n \qquad 3.3$$

In this context, α represents the absorption coefficient, h is Planck's constant, v is the photon frequency, A is a constant, and Eg denotes the optical bandgap. In crystalline semiconductors, where the crystal momentum is conserved and the electron transitions follow specific selection rules, the value of n is 1/2, 3/2, 2, or 3 for the direct-allowed, direct-forbidden, indirect-allowed, and indirect-forbidden transitions, respectively. On a Tauc plot, which graphs $(\alpha hv)^n$ on the y-axis against photon energy (hv) on the x-axis, the bandgap of the material is determined by extrapolating the linear portion of the plot to the x-axis at Y = 0 [43].

UV-vis spectroscopy was used to assess whether the synthesised nanomaterials absorb energy within the visible spectrum, as the wavelength of absorption typically indicates that they absorb light in the 200–700 nm range. The wavelength of maximum absorption was identified, and the absorption edge was used to calculate the band gap of the nanocomposites for qualitative analysis. The technique was further applied for quantitative analysis in degradation experiments to assess the remaining amount of pollutant at a specific time. Additionally, UV-vis helped determine the rate constant in the degradation experiments.

3.5 Advanced oxidation experiments

The visible light-induced photocatalytic decomposition and PMS-assisted photocatalytic degradation of SMX experiments were performed in a 500 mL Lelesil Innovation Systems photochemical glass reactor equipped with a 250 W sodium vapour lamp and a magnetic stirrer to ensure the agitation of the reaction medium during the degradation experiments. The lamp was enclosed in a jacketed quartz tube

connected to a 4 L cold-water circulation tank to help maintain the reaction system temperature. The photoreactor includes a sampling tube to facilitate sampling without interfering with the progress of the reaction.

3.5.1 Photocatalytic oxidation of sulphamethoxazole

In a typical experiment, the photocatalyst (0.05 g) was mixed with the SMX solution (10 ppm, 250 mL), and under dark conditions, the mixture was continuously stirred for 20 min to attain adsorption-desorption equilibrium. The mixture was exposed to visible light for 120 min, while 5 mL aliquots of the solution were withdrawn at regular intervals (20 min) and filtered through 0.45 µm polytetrafluoroethylene syringe filters. The residual concentration of SMX was measured using a PerkinElmer Lambda 650S UV–vis spectrometer at 266 nm (wavelength of maximum absorption). Various reaction conditions, such as catalyst composition, SMX concentration, catalyst dosage, and pH, were studied individually to establish the optimum degradation conditions. The SMX degradation efficiency (η) and rate constant (k) were computed using **Eqs. 3.4** and **3.5**, respectively:

$$\eta.(\%) = \frac{C0-Ct}{C0}\ X\ 100 \qquad 3.4$$

$$\ln\left(\frac{C0}{Ct}\right) = kt \qquad 3.5$$

where C_0, C_t, and t refer to the initial concentration, concentration at time t, and reaction time, respectively. The reactive species responsible for SMX degradation were confirmed by conducting scavenging experiments using EDTA, Tert-butyl, and p-BQ as trapping agents for h^+, $HO^\bullet$ and $^\bullet O_2^-$ radicals, respectively. Furthermore, five cycles of degradation tests were conducted to assess the reusability and stability of the BC/FeOCl photocatalyst. For reusability assessment, the photocatalyst was centrifuged after each cycle, followed by sequential washing with deionised water and ethanol, drying, and preparation for the next cycle. In addition, parallel experiments were conducted to maintain sufficient catalyst and compensate for catalyst losses during sampling and washing.

3.5.2 PMS-assisted photocatalytic degradation of SMX

The PMS-assisted degradation experiments followed a procedure similar to that described in **Section 3.5.1**, with the inclusion of peroxymonosulphate (PMS) as an external oxidant to promote sulphate radical formation. All experiments were

conducted in a 500 mL Lelesil Innovation Systems photochemical glass reactor equipped with a 250 W sodium vapour lamp (light intensity = 27.1 x 10^2 lux) as the visible-light source. Prior to irradiation, the initial pH of the SMX solution (10 ppm, 250 mL) was adjusted using 0.1 M NaOH or HCl, as pH strongly influences PMS speciation, Fe^{2+}/Fe^{3+} redox cycling, and reactive oxygen species generation. The photocatalyst (50 mg of either WP-BC/FeOCl or MM-BC/FeOCl) was added to the solution and magnetically stirred in the dark for 20 min to establish adsorption–desorption equilibrium, as described previously. Subsequently, PMS was introduced into the system, and the suspension was irradiated under visible light for 120 min. At regular intervals (20 min), 5 mL aliquots were withdrawn, filtered through 0.45 µm PTFE syringe filters, and immediately quenched with 1 mL methanol to terminate further radical reactions before analysis. The residual SMX concentration was measured using a PerkinElmer Lambda 650S UV–vis spectrophotometer at 266 nm. The degradation efficiency (η) and pseudo-first-order rate constant (k) were calculated using **Eqs. 3.4 and 3.5** presented in **Section 3.5.1.**

To evaluate performance under environmentally relevant conditions, the PMS-assisted degradation of SMX was further examined in different water matrices, including deionised water, tap water, wastewater effluent, and river water. Changes in dissolved organic matter and fluorophoric species during treatment were monitored using two-dimensional fluorescence excitation–emission matrix spectroscopy (2D-FEEM). The reactive species responsible for SMX degradation were confirmed by conducting scavenging experiments using EDTA, methanol, tert-butyl, furfuryl alcohol, and p-BQ as trapping agents for h^+, $SO_4^{\bullet -}$, $HO^{\bullet}$, $^1O_2$ and $^{\bullet}O_2^-$ radicals, respectively. Furthermore, five cycles of degradation tests were conducted to assess the reusability and stability of the BC/FeOCl photocatalyst. For reusability assessment, the photocatalyst was centrifuged after each cycle, followed by sequential washing with deionised water and ethanol, drying, and preparation for the next cycle. In addition, parallel experiments were conducted to maintain sufficient catalyst and compensate for catalyst losses during sampling and washing.

3.5.3 Degradation kinetics

The empirical understanding of reaction kinetics is crucial in photocatalysis, as it plays a key role in designing and optimising large-scale photocatalytic applications for

maximum efficiency. Factors such as reaction temperature, the physical state of the reactants (whether gas, liquid, or solid), the presence of a catalyst, and the available surface area of the reactants influence the rates of chemical reactions [44]. The law of mass action describes these reactions, which mathematically represents how the reaction rate depends on the concentration of reactants through a rate law. The proportionality factor in this relationship is referred to as the rate constant [41]. The rate law for elementary reactions can be directly derived from the equation of balanced reactions. However, for multi-step reactions, the rate law is the result of the sequence of elementary steps that define the reaction mechanism, offering the most effective approach for uncovering an unknown mechanism [45]. In multi-step reactions, the rate law, rate constant, and reaction order are experimentally determined by observing how the reactant concentration changes over time. The reaction orders typically do not correspond to the stoichiometric coefficients in the reaction equation and must be determined experimentally. The overall rate laws for a reaction can include reactant, product, and catalyst concentrations. The rate of organic degradation is determined by the change in reactant concentration over time, and various kinetic models, such as the Eley–Rideal model, Alberty-Hammes-Eigen model, Langmuir-Hinshelwood model, Deal–Grove model, laminar finite rate model, eddy dissipation and dissipation concept models, Chou's model, and others, have been employed to describe this process. The Langmuir-Hinshelwood (L-H) model is widely used for organic degradation because it provides an effective and efficient way to express rate constants in most degradation experiments [46]. Moreover, it connects the degradation rate (r) to the reactant concentration (C) at a specific time (t) (**Eq. 3.6)**, accounting for the various degradation rates [47].

$$\boldsymbol{r} = -\frac{dc}{dt} = -\frac{KradC}{1+Kad} \qquad 3.6$$

Here, Kr is the rate constant, and Kad is the adsorption equilibrium constant. According to the L-H model, infinitely small initial concentrations are often experienced in photocatalytic experiments [48], KadC <<1 and the reaction follows the pseudo-first-order equation (**Eq. 3.7**):

$$\mathrm{In}\left(\frac{\mathrm{C0}}{\mathrm{Ct}}\right) = \mathrm{KrKadt} = \mathrm{Kappt} \qquad 3.7$$

In this context, Kapp represents the apparent rate constant, C_0 is the initial concentration (mM), and Ct is the concentration at a given time during the degradation process. A plot of $\ln(C_0/C_t)$ against time produces a straight line, with the slope obtained through linear regression corresponding to the pseudo first order observed rate constant (K_{obs}). The term "pseudo-" is used because one reactant remains constant, functioning as a catalyst, and its concentration does not change during the reaction. This classification results in the reaction being classified as pseudo-first-order or pseudo-second-order rather than true second- or third-order [47,49].

3.6 Chapter Summary

Chapter 3 detailed the materials, reagents, and synthesis methods deployed, including wet impregnation and calcination, and the ultrasonic-assisted mechanical mixing for the preparation of biochar and BC/FeOCl heterojunctions. The chapter described comprehensive characterisation approaches, including FE-SEM, HRTEM, EDS, FT-IR, XRD, BET, XPS, and UV-vis spectroscopy. These techniques were explained in terms of their respective contributions to understanding the physical, chemical, and optical properties of the prepared materials. Finally, the chapter summarised the experimental procedures for photocatalytic oxidation and degradation kinetics relevant to SMX removal. The next chapter discusses the application of the synthesised nanocomposites for the mitigation of SMX pollution in water, constituting the first part of this study.

References

[1] Z. Zhang, X. Liu, D. Li, Y. Lei, T. Gao, B. Wu, J. Zhao, Y. Wang, G. Zhou, H. Yao, Sonochemistry mechanism of ultrasonic impregnation on porosity of activated carbons in non-cavitation and cavitation regimes, Ultrason. Sonochem. 51 (2019) 206–213. https://doi.org/10.1016/j.ultsonch.2018.10.024.

[2] T.A. Zepeda, Ultrasonic-assistance influence on the impregnation method for high metal loading CoMo/Ti-HMS catalysts, Appl. Catal A. Gen. 693 (2025) 120135. https://doi.org/10.1016/j.apcata.2025.120135.

[3] R. Feng, Y. Zhao, C. Zhu, T.J. Mason, Enhancement of ultrasonic cavitation yield by multi-frequency sonication, Ultrason. Sonochem. 9 (2002) 231–236. https://doi.org/10.1016/S1350-4177(02)00083-4

[4] M. Janer, X. Plantà, D. Riera, Ultrasonic moulding : Current state of the technology, Ultrason. 102 (2020) 106038. https://doi.org/10.1016/j.ultras.2019.106038.

[5] B. Jiang, J. Zhang, Y. Chen, H. Song, T. Hao, J. Kuang, Ultrasonic-assisted preparation of highly active CO_3O_4/MCM-41 adsorbent and its desulfurization performance for low H_2S concentration gas, RSC Adv. 10 (2020) 30214–30222. https://doi.org/10.1039/d0ra05606e.

[6] S. Rondinini, S. Ardizzone, G. Cappelletti, A. Minguzzi, A. Vertova, Physico-chemical characterization of IrO_2–SnO_2 sol-gel nanopowders for electrochemical applications, J. Appl. Electrochem. 39 (2009) 2093-2105. https://doi.org/10.1007/s10800-009-9895-1

[7] F. Kleitz, W. Schmidt, F. Sch, Evolution of mesoporous materials during the calcination process : structural and chemical behavior, Micropo. Mesopo. Mater. 44-45 (2001) 95-109. https://doi.org/10.1016/S1387-1811(01)00173-1

[8] S. Jiang, H. Zheng, X. Sun, M. Zhu, Y. Zhou, D. Wang, D. Zhang, L. Zhang, New and highly efficient Ultra-thin g-C_3N_4/FeOCl nanocomposites as photo-Fenton catalysts for pollutants degradation and antibacterial effect under visible light, Chemosphere. 290 (2022) 133324. https://doi.org/10.1016/j.chemosphere.2021.133324.

[9] B. Handson, P. Timo, Effect of pyrolysis temperature on the physical and

chemical characteristics of pine wood biochar, Waste. Manag. Bul. 2 (2024) 281–287. https://doi.org/10.1016/j.wmb.2024.11.008.

[10] C. Shao, J. Zhang, Z. Wang, L. Zhang, B. Wang, J. Ren, X. Zhang, W. He, Photo-Fenton degradation of tetracycline on nitrogen vacancy and potassium-doped Z-scheme FeOCl/NvCN heterojunction with low H_2O_2 consumption : Activity and mechanism, J. Alloys Compd. 970 (2024) 172532. https://doi.org/10.1016/j.jallcom.2023.172532.

[11] J. Meng, J. Han, Z. Wang, C. Yang, X. Lu, J. Wang, The coordination bond reinforced FeOCl/C_3N_4 heterostructure for photocatalytic degradation of persistent organic pollutants, J. Environ. Chem. Eng. 12 (2024) 114404. https://doi.org/10.1016/j.jece.2024.114404.

[12] R.P. Jaya, 14. Porous concrete pavement containing nanosilica from black rice husk ash, INC, New Mater. Civil Eng. 22 (2020) 493-527. https://doi.org/10.1016/B978-0-12-818961-0.00014-4.

[13] A. Mohammed, A. Abdullah, Mineral characterization using scanning electron microscopy (SEM): A review of the fundamentals, advancements, and research directions, Appl. Sci. 13 (2023) 12600. https://doi.org/10.3390/app132312600

[14] M. Lam, C. Schwarz, R. Sharma, J. Donnelly, An Introduction to scanning electron microscopy and science communication skills for undergraduate chemistry students, J. Chem. Edu. 100 (2023) 2802-2808. https://doi.org/10.1021/acs.jchemed.3c00076.

[15] F. Ahmad, M. Mohammed, A. Mohammed, P.R. Kareem, M.A. Al-jubbori, Revolutionizing scanning electron microscopy with compound lenses : a comprehensive review, Russ. Phys. J. 68 (2025) 64–70. https://doi.org/10.1007/s11182-025-03401-7.

[16] E.M.S. Bex, M. Webb, Fast elemental analysis of heavy mineral suites by scanning electron microscopy (SEM-Unity BEX), Minerals.14 (2024) 950. https://doi.org/10.3390/min14090950

[17] L. Bijeli, F. Ruiz-zepeda, The role of high-resolution transmission electron microscopy and aberration corrected scanning transmission electron microscopy in unraveling the structure, property relationships of Pt-based fuel

cells electrocatalysts, Inorg. Chem. Front.11 (2024) 323–341. https://doi.org/10.1039/d3qi01998e.

[18] A. Khurshid, A. Saeed, Z. Ashraf, Q. Abbas, M. Hassan, Green synthesis of silver nanoparticles using plant extracts: A comprehensive review of physicochemical properties and multifunctional applications, Int. J. Mol. Sci. 26 (2025) 6222. https://doi.org/10.3390/ijms26136222

[19] J.P. Horwath, Understanding important features of deep learning models for segmentation of high-resolution transmission electron microscopy images, Npj Comput. Mater. 6. (2020) 108. https://doi.org/10.1038/s41524-020-00363-x.

[20] J. Yuan, X. Li, Y. Chen, Z. Zhang, X. Li, S. Komarneni, Rapid recognition and quantitative analysis of niobium minerals by scanning electron microscopy/energy dispersive X-ray spectroscopy, J. Anal. At. Spectrom. 37 (2022) 2392–2400. https://doi.org/10.1039/d2ja00274d.

[21] M. Procop, V.D. Hodoroaba, R. Terborg, D. Berger, Determination of the effective detector area of an energy-dispersive x-ray spectrometer at the scanning electron microscope using experimental and theoretical x-ray emission yields, Microsc. Microanal. 22 (2016) 1360–1368. https://doi.org/10.1017/S1431927616011788.

[22] A.T. Raghavender, N. Hoa Hong, K. Joon Lee, M.H. Jung, Z. Skoko, M. Vasilevskiy, M.F. Cerqueira, A.P. Samantilleke, Nano-ilmenite $FeTiO_3$: Synthesis and characterization, J. Magn. Magn. Mater. 331 (2013) 129–132. https://doi.org/10.1016/j.jmmm.2012.11.028.

[23] R. Davis, L. Mauer, Fourier transform infrared (FT-IR) spectroscopy: a rapid tool for detection and analysis of foodborne pathogenic bacteria, Curr. Res. Technol. 22 (2010) 1582–1594. http://www.formatex.info/microbiology2/1582-1594.pdf.

[24] Y. Chen, C. Zou, M. Mastalerz, S. Hu, C. Gasaway, X. Tao, Applications of micro-fourier transform infrared spectroscopy (FTIR) in the geological sciences; A Review, Int. J. Mol. Sci. 16 (2015) 30223–30250. https://doi.org/10.3390/ijms161226227.

[25] C. Berthomieu, R. Hienerwadel, Fourier transform infrared (FTIR) spectroscopy, Photosynth. Res. 101 (2009) 157–170. https://doi.org/10.1007/s11120-009-

9439-x.

[26] J. Epp, X-Ray diffraction (XRD) techniques for materials characterization, Elsevier Ltd, 2 (2016).222-226. https://doi.org/10.1016/B978-0-08-100040-3.00004-3.

[27] A.A. Bunaciu, E. gabriela Udriştioiu, H.Y. Aboul-Enein, X-Ray diffraction: instrumentation and applications, Crit. Rev. Anal. Chem. 45 (2015) 289–299. https://doi.org/10.1080/10408347.2014.949616.

[28] H. Khan, A.S. Yerramilli, A. D'Oliveira, T.L. Alford, D.C. Boffito, G.S. Patience, Experimental methods in chemical engineering: X-ray diffraction (XRD), Can J Chem Eng (2020) 1255–1266. https://doi.org/10.1002/cjce.23747

[29] C. Series, Dislocation, Crystallite size distribution and lattice strain of magnesium oxide nanoparticles, J. Phys. 979 (2018) 012021. https://doi.org/10.1088/1742-6596/979/1/012021

[30] R. Bardestani, G.S. Patience, experimental methods in chemical engineering : specific surface area and pore size distribution measurements; BET, Can. J. Chem. Eng. 97 (2019) 2781–2791. https://doi.org/10.1002/cjce.23632

[31] S. Reza, C.S. Yun, S. Afroze, N. Radenahmad, M.S.A. Bakar, R. Saidur, J. Taweekun, K. Abul, Preparation of activated carbon from biomass and its ' applications in water and gas purification, a review, Arab J. Basic Appl. Sci. 27 (2020) 208–238. https://doi.org/10.1080/25765299.2020.1766799.

[32] D. Dollimore, P. Spooner, A. Turner, D. dollimore, The bet method of analysis of gas adsorption data and its relevance to the calculation of surface areas, Sur. Technol. 4 (1976) 121-160. https://doi.org/10.1016/0376-4583(76)90024-8

[33] K.S.W. Sing, The use of gas adsorption for the characterization of porous solids, Colloi. Sur. 38 (1989) 113–124. https://doi.org/10.1016/0166-6622(89)80148-9

[34] F. A. Stevie, C. L. Donley, XPS principle and instrumentation introduction, J. Vac. Sci. Technol. 38 (2020) 063204. https://doi.org/10.1116/6.0000412

[35] D. W. Bahnemann, A. O. T. Patrocinio, Introduction to X-ray photoelectron spectroscopy, Inorg. Photochem. 11 (2022) 249-271. https://doi.org/10.1007/978-3-030-63713-2_10

[36] A.L. Cazetta, L. Spessato, S.A.R. Melo, K.C. Bedin, T. Zhang, T. Asefa, T.L. Silva, V.C. Almeida, Sugarcane vinasse-derived nanoporous N-S-doped carbon material decorated with Co: A new and efficient multifunctional electrocatalyst, Int. J. Hydrogen Energy 45 (2020) 9669–9682. https://doi.org/10.1016/j.ijhydene.2020.01.205.

[37] M.S.P. Francisco, V.R. Mastelaro, P.A.P. Nascente, A.O. Florentino, Activity and characterization by XPS, HR-TEM, Raman spectroscopy, and bet surface area of CuO/CeO_2-TiO_2 catalysts, J. Phys. Chem. B. 105 (2001) 10515–10522. https://doi.org/10.1021/jp0109675.

[38] J.A. Torres-Luna, N.R. Sanabria, J.G. Carriazo, Powders of iron(III)-doped titanium dioxide obtained by direct way from a natural ilmenite, Powder Technol. 302 (2016) 254–260. https://doi.org/10.1016/j.powtec.2016.08.056.

[39] Z. Ye, S. Hung, B. Chen, M. Tsai, Assessment of predicting frontier orbital energies for small organic molecules using knowledge-based and structural information, ACS. Eng. 2 (2022) 360-368. https://doi.org/10.1021/acsengineeringau.2c00011.

[40] P. Parthasarathy, S.K. Narayanan, Effect of hydrothermal carbonization reaction parameters on, Environ. Prog. Sustain. Energy. 33 (2014) 676–680. https://doi.org/10.1002/ep.11974

[41] E. Kim, Z.T. Jiang, K. No, Measurement and calculation of optical band gap of chromium aluminum oxide films, Japanese J. Appl. Physics, Part 1 Regul. 39 (2000) 4820–4825. https://doi.org/10.1143/jjap.39.4820.

[42] Y. Chen, K. Liu, Fabrication of Ce/N co-doped TiO_2/diatomite granule catalyst and its improved visible light-driven photoactivity, J. Hazard. Mater. 324 (2017) 139–150. https://doi.org/10.1016/j.jhazmat.2016.10.043.

[43] Y. Chen, A. Li, Z.H. Huang, L.N. Wang, F. Kang, Porphyrin-based nanostructures for photocatalytic applications, Nanomater. 6 (2016) 51. https://doi.org/10.3390/nano6030051.

[44] A. Kotarba, Demonstration of the influence of specific surface area on reaction rate in heterogeneous catalysis, J. Chem. Edu. 98 (2021) 935-940. https://doi.org/10.1021/acs.jchemed.0c01101.

[45] G. Chambashi, M.S. Ishaq, M. Shahzad, Analyzing multi-step reaction mechanisms: Unveiling non-linear dynamics with advanced reduction techniques, AIP. Adv. 14 (2024) 045338. https://doi.org/10.1063/5.0197019.

[46] P. Chen, Q. Zhang, Y. Su, L. Shen, F. Wang, H. Liu, Y. Liu, Z. Cai, W. Lv, G. Liu, Accelerated photocatalytic degradation of diclofenac by a novel CQDs/BiOCOOH hybrid material under visible-light irradiation: Dechloridation, detoxicity, and a new superoxide radical model study, Chem. Eng. J. 332 (2018) 737–748. https://doi.org/10.1016/j.cej.2017.09.118.

[47] B. Ntsendwana, S. Sampath, B.B. Mamba, O.S. Oluwafemi, O.A. Arotiba, Photoelectrochemical degradation of eosin yellowish dye on exfoliated graphite–ZnO nanocomposite electrode, J. Mater. Sci. Mater. Electron. 27 (2016) 592–598. https://doi.org/10.1007/s10854-015-3793-6.

[48] Z. Wang, C. Chen, F. Wu, B. Zou, M. Zhao, J. Wang, C. Feng, Photodegradation of rhodamine B under visible light by bimetal co-doped TiO_2 nanocrystals, J. Hazard. Mater. 164 (2009) 615–620. https://doi.org/10.1016/j.jhazmat.2008.08.041.

[49] A.T. Kuvarega, N. Khumalo, D. Dlamini, B.B. Mamba, Polysulfone/N,Pd co-doped TiO_2 composite membranes for photocatalytic dye degradation, Sep. Purif. Technol. 191 (2018) 122–133. https://doi.org/10.1016/j.seppur.2017.07.064.

CHAPTER 4

BIOCHAR/IRON OXYCHLORIDE PHOTOCATALYTIC DEGRADATION OF SULPHAMETHOXAZOLE IN WATER

4.1 Introduction

Antibiotic contamination, especially by sulphonamides such as sulphamethoxazole (SMX) are a major challenge for conventional water treatment technologies. Therefore, there is a need to develop more effective and innovative strategies for the removal of these contaminants from wastewater. Although the literature review in chapter 2 has outlined the importance of advanced oxidation processes (AOPs) in the removal of persistent pharmaceuticals from water, there is still limited understanding of how tailored nanocomposite materials can be optimised for real-world water matrices.

This chapter addresses the limitations of conventional FeOCl systems by examining biochar/iron oxychloride (6-BC/FeOCl) nanocomposite prepared using ultrasonic-assisted wet impregnation and calcination for the photocatalytic degradation of SMX under visible light irradiation. The prepared composite material was systematically characterised to elucidate its structural and physicochemical properties. The preparation methods and characterisation techniques of the prepared nanomaterials are described in **Chapter 3**, **Sections 3.3.2, 3.3.3.3,** and **3.4**. The photocatalytic investigation of SMX is also explained in **Section 3.5.1**. Several key reaction conditions, such as photocatalyst dosage, SMX concentration, solution pH, organic and inorganic species, and water matrix, were investigated. By combining biochar's adsorption properties with the visible light-driven photocatalytic activity of FeOCl, this approach enhances SMX removal from water.

4.2 Results and Discussion

4.2.1 Surface morphology and microstructural analysis

The surface architecture and internal microstructure were investigated using FE-SEM and HRTEM, respectively. The SEM image of FeOCl (**Fig. 4.1a**) shows microspheres of varying irregular shapes and sizes composed of aggregated FeOCl nanoparticles. The SEM image of BC (**Fig. 4.1b**) shows irregular sheet-like structures with undefined edges and relatively smooth surfaces. Meanwhile, the morphology of the composite (6-BC/FeOCl) resembled that of pristine FeOCl with less clustering of the rod-like nanostructures, which have disordered orientation (**Fig. 4.1c**). The slight change in the morphology of the composite could be attributed to the incorporation of BC. Compared with pristine FeOCl, the BC/FeOCl composite exhibited a modified surface morphology characterised by less densely packed FeOCl domains and the presence of elongated features distributed throughout the composite structure. These observations suggest that the incorporation of biochar influenced the growth and assembly of FeOCl during synthesis.

The internal microstructures of the synthesised materials were analysed using TEM and HR TEM. The short, rod-like nanostructures of FeOCl with a certain level of aggregation were confirmed (**Fig. 4.1d**). The characteristic sheet-like structure of BC (**Fig. 4.1e**) appeared to consist of multiple layers stacked together in an orderly manner. **Fig. 4.1f** shows that the BC sheet-like structures were coupled with the FeOCl nanorods, suggesting interfacial interaction. Intimate contact between the two materials is essential in ensuring synergy between FeOCl and BC, which is anticipated to improve the composite's catalytic properties. Moreover, the TEM image of the composite confirmed a significant reduction in clustering, indicating the important role of BC in inhibiting aggregation. HR-TEM was used to gain further insight into the internal microstructure of the prepared materials. The high-resolution image of the FeOCl nanostructures (**Fig. 4.1g**) shows lattice fringes with an interlayer distance of 0.27 nm, which is assigned to the (110) lattice plane. Similar results were observed for 6-BC/FeOCl (**Fig. 4.1h**), indicating the presence of crystalline FeOCl in the composite [1]. EDS spectroscopy (**Fig. 4.1i**) was used to clarify the qualitative elemental composition of the 6-BC/FeOCl nanocomposite photocatalyst. The expected elements (Fe, O, Cl, and C) were found to be present, of which Fe, O, and Cl can be associated with FeOCl, and C with BC [2]. Furthermore, EDS elemental mapping of Fe, O, Cl,

and C (**Fig. 4.2a–e**) confirmed the presence of these elements throughout the analyzed region of the 6-BC/FeOCl composite, with no obvious elemental segregation observed at the microscale, suggesting a relatively homogeneous elemental distribution. Quantitative EDS analysis (**Fig. 4.2i**) revealed Fe (40.82 wt.%, 32.23 at.%) and Cl (48.56 wt.%, 60.40 at.%) as the dominant elements, consistent with the FeOCl phase, while a Cu signal (10.62 wt.%, 7.37 at.%) originated from the copper support grid used during TEM analysis. Although C and O were observed in the elemental maps, their concentrations were not reliably quantified by EDS and were therefore reported as negligible in the compositional analysis. This limitation can be attributed to the reduced sensitivity of EDS toward light elements, as the low-energy characteristic X-rays emitted by carbon and oxygen are readily absorbed or attenuated during TEM/STEM-EDS measurements. Similar limitations in the quantification of light elements by EDS have been reported in previous studies [3]. Therefore, the presence of carbon and oxygen in the 6-BC/FeOCl composite was further verified using complementary characterisation techniques, including XPS (**Fig 4.4b**) and FTIR (**Fig. 4.4a**), which confirmed the incorporation of biochar-derived carbon and oxygen-containing functional groups within the composite structure.

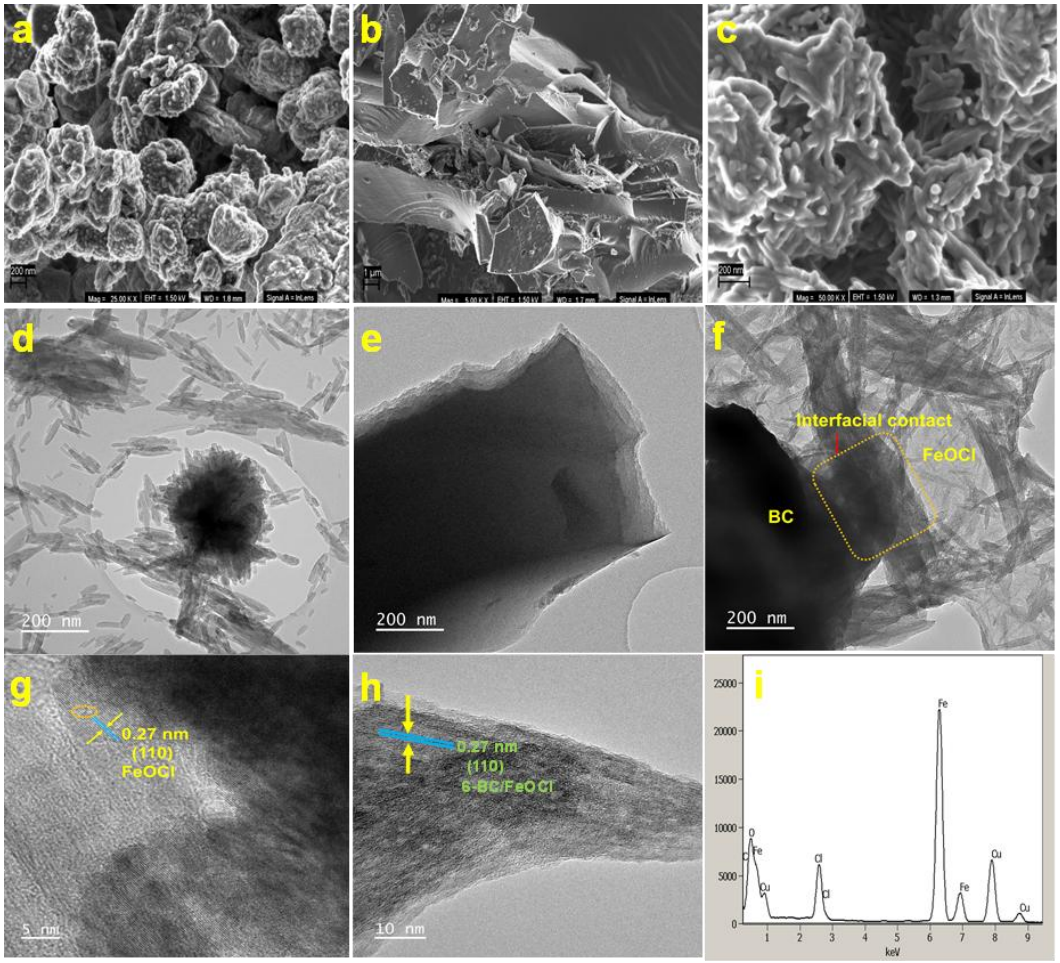

Figure 4.1 SEM images of (a) FeOCl, (b) BC, and (c) 6-BC/FeOCl; TEM images of (d) FeOCl, (e) BC, and (f) 6-BC/FeOCl; HR-TEM image of (g) FeOCl and (h) 6-BC/FeOCl, and (i) EDS spectra of 6-BC/FeOCl.

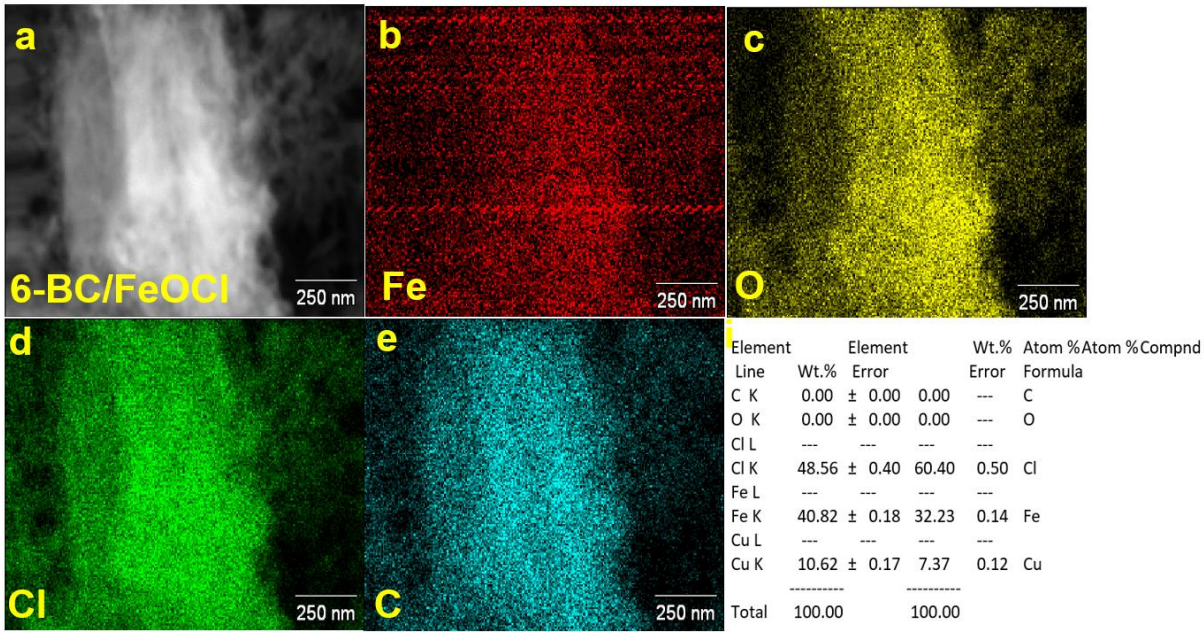

Figure 4.2 (a-e) EDS elemental mapping images of 6-BC/FeOCl. (i) Quantitative EDS data.

4.2.2 X-ray diffraction and textural properties

The phase composition and purity of the FeOCl, BC, and 6-BC/FeOCl composites were studied using X-ray diffraction (XRD), and the results are shown in **Fig. 4.3a**. A broad diffraction peak around 23.0° is ascribed to the C (002) crystal plane, which corresponds to the orientation of the aromatic and carbonised structures both in parallel and azimuthal alignment [3]. Another broad feature at approximately 43.1° is linked to C (100) reflections, associated with graphitic and hexagonal carbon arrangements, indicating the size of the aromatic layers [4]. The broadening of these peaks is indicative of the amorphous structure of biochar. FeOCl displayed distinctive diffraction peaks at 11.2, 26.0, 32.7, 35.4, and 37.7° corresponding to (010), (110), (120), (021), and (111) crystal facets, respectively, confirming its pure orthorhombic lattice phase, JCPDS no. 24-1005 and JCPDS no. 72-0619 [20, 36]. Meanwhile, the XRD pattern recorded for 6-BC/FeOCl demonstrates mostly similar peaks to those of FeOCl but with relatively weak intensity. The decreased peak intensity on the 6-BC/FeOCl composite may be due to the addition of the noncrystalline biochar material on FeOCl. This observation indicates the coexistence of FeOCl and BC in the composite and the absence of any foreign peaks, indicating the purity of the prepared materials. This is important in the photocatalytic application of materials, especially in the remediation of water pollution.

The Brunauer–Emmett–Teller (BET) analysis was used to evaluate the specific surface areas and pore size distributions of the as-prepared materials, and the results are displayed in **Fig. 4.3b**. The pore characteristics were examined by measuring the N_2 adsorption-desorption isotherms. Consistent with the IUPAC standards, all the materials revealed a similar trend, showing type-IV isotherm with H3 hysteresis loop, confirming their mesoporous structure [6]. The surface area values of FeOCl, BC, and 6-BC/FeOCl were 5.034, 70.038, and 13.846 $m^2\ g^{-1}$, respectively. The smaller surface area of FeOCl could be attributed to the large particle sizes viewed as clustered microspheres observed in the SEM (**Fig. 4.1a**) and TEM (**Fig. 4.1d**) results. Although the specific surface area of 6-BC/FeOCl (13.846 $m^2\ g^{-1}$) being lower than that of BC (70.038 $m^2\ g^{-1}$), it is more than twice that of pristine FeOCl (5.034 $m^2\ g^{-1}$), indicating

the positive influence of the introduction of BC. Ultimately, the increase in the surface area of 6-BC/FeOCl translates to an increase in the number of available active sites for an elevated interaction with SMX during the catalytic degradation process. The average pore size distribution was 3.056, 30.68, and 0.060 nm for FeOCl, BC, and 6-BC/FeOCl, respectively. The mesoporous volumes were measured at 0.012, 0.306, and 0.040 $cm^3\ g^{-1}$ for the respective pore size distributions.

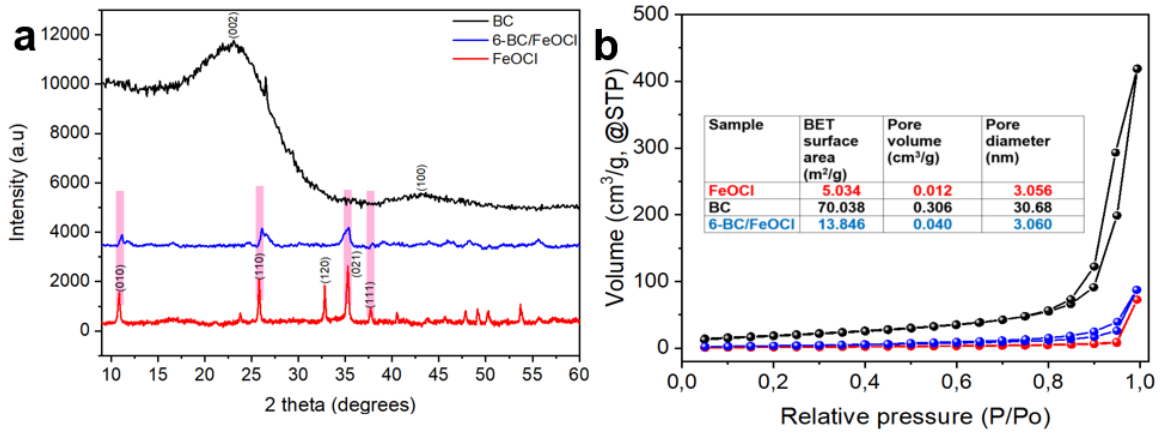

Figure 4.3 (a) XRD patterns and (b) BET surface area, pore volume, pore diameter, and N2 adsorption-desorption isotherms of FeOCl, BC, and 6-BC/FeOCl.

4.2.3 Functional groups and chemical analysis

FT-IR analysis was employed to reveal insights into the chemical bonds and functional groups present in the synthesised FeOCl, BC, and binary nanocomposite. **Fig. 4.4a** shows that all three materials have an O-H stretching mode peak observed approximately at 3487 cm^{-1} belonging to the O-H group of adsorbed H_2O bonded molecules on the surface of the materials [7]. The characteristic FeOCl peaks at 574 cm^{-1} and 887 cm^{-1} were attributed to the stretching and vibration of the Fe-O bond, respectively [8]. Meanwhile, the peak around 1601.23 cm^{-1} can be primarily attributed to the vibration of Fe–Cl, which also appeared in the spectrum of the 6-BC/FeOCl composite, indicating the presence of FeOCl [9]. Notably, the pristine BC spectrum shows a C=O/C-O stretching vibration around 1596 cm^{-1} originating from the oxygenated carbon functional groups, which are essential in catalysis reactions and could function as reactive sites for eliminating organic contaminants [10]. The peak observed at 2852 cm^{-1} emanates from the stretching vibration mode of the

aromatic rings of BC, and the same peak is observed in the spectrum of the 6-BC/FeOCl composite. However, in the composite, the peak is significantly shifted to 2906 cm^{-1}, which may be due to the coordination with the FeOCl structure.

X-ray photoelectron spectroscopy (XPS) was used to study the surface chemical states and composition of FeOCl and 6-BC/FeOCl composite. **Fig. 4.4b** shows the XPS survey spectra of the pristine FeOCl and 6-BC/FeOCl composite. Both materials are composed of the elements C, Fe, Cl, and O, which are in accordance with the theoretical expectation. In the case of FeOCl, the observed carbon peak is attributed to adventitious carbon, which is inherent to all air-exposed samples. Compared with the adventitious carbon peak of FeOCl, the carbon peak in 6-BC/FeOCl is significantly more intense due to the presence of the carbonaceous BC structure. Furthermore, Cl 2p of 6-BC/FeOCl has a lower intensity than that of FeOCl, which may indicate a partial substitution of Cl atoms with carbon atoms due to the weak Fe-Cl bond [5]. **Fig. 4.4c** shows the high-resolution Fe 2p spectra of FeOCl and 6-BC/FeOCl, which were deconvoluted into four distinctive Fe peaks separated by a satellite peak. For Fe 2p from 6-BC/FeOCl, the peaks appearing at 727.5 eV and 711.4 eV are linked to the $2p_{1/2}$ and $2p_{3/2}$ states of Fe^{2+}, respectively, and the peaks at 725.0 eV and 713.3 eV can be attributed to the $2p_{1/2}$ and $2p_{3/2}$ states of Fe^{3+}, respectively [42, 34]. The presence of the Fe^{2+}/Fe^{3+} redox pair is crucial for the acceleration of charge separation and the formation of reactive species responsible for pollutant degradation. Compared with pristine FeOCl, all the Fe peaks in 6-BC/FeOCl are significantly shifted to higher binding energies, indicating a decline in the electron density around Fe owing to the interfacial interaction with the incorporated BC.

The O 1s high-resolution spectra in **Fig. 4.4d** from both FeOCl and 6-BC/FeOCl could be deconvoluted to three peaks corresponding to several chemical states of oxygen: lattice oxygen (530.6 eV) corresponding to the Fe-O bond of the metal oxide in the FeOCl lattice [2], adsorbed oxygen (531.8 eV) allocated to adsorbed water molecules (O-H), and chemically bound oxygen (533.2 eV) for C-O bonds in BC [11]. Obviously, the O 1s spectra are comparable with the 6-BC/FeOCl peaks, slightly shifted to higher binding energies compared to FeOCl oxygen, which signifies a level of interaction between the BC and FeOCl, resulting in a change in the chemical environment of the oxygen atoms. **Fig. 4.4e** shows that the Cl 2p peak has two distinctive peaks at 200.6 and 199.0 eV and 199.6 and 198.0 eV, corresponding to the Cl $2p_{1/2}$ and Cl $2p_{3/2}$

doublets in 6-BC/FeOCl and FeOCl, respectively. The incorporation of BC reduced the electron density around Cl, which increased the binding energy of the Cl electrons in the composite. The C 1s spectrum of 6-BC/FeOCl (**Fig. 4.4f**) was deconvoluted into three peaks at 285.0, 286.6, and 289.2 eV, corresponding to C-C, C-O, and Fe-C bonds, respectively, further confirming the partial replacement of lattice Cl by carbon atoms [12]. Overall, the XPS findings confirmed the intimate interactions between FeOCl and BC, indicating that the generated pathway favours charge separation and photocatalytic activity.

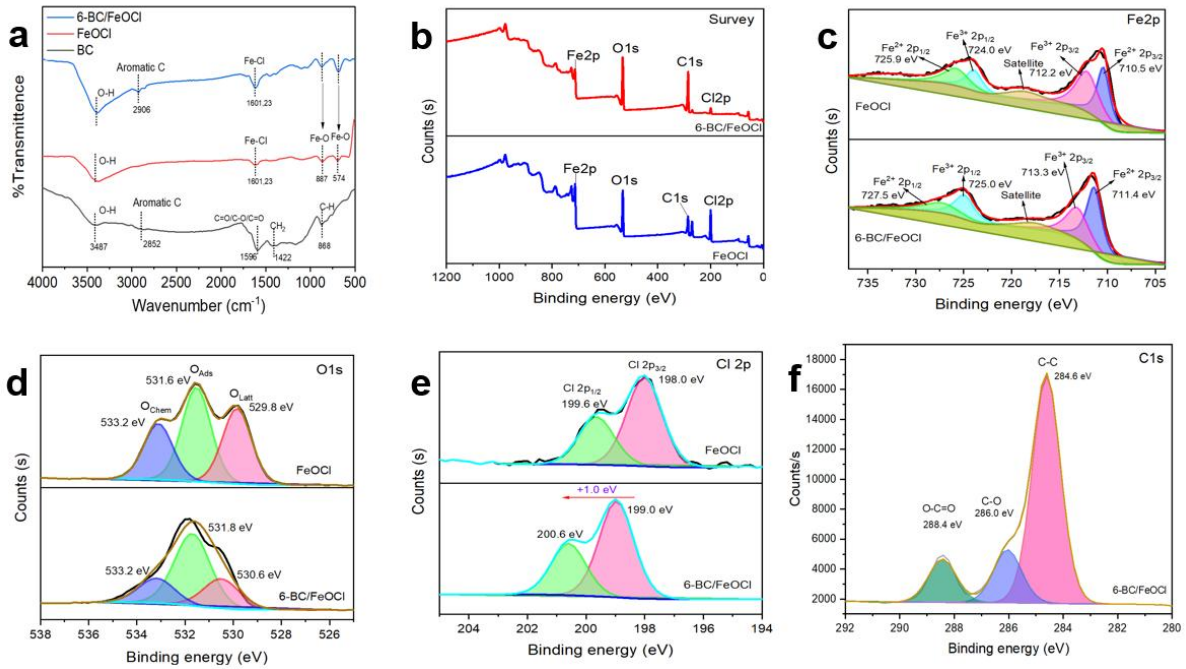

Figure 4.4 (a) FT-IR spectra, (b) X-ray photoelectron spectroscopy (XPS) survey scan for FeOCl and 6-BC/FeOCl, high-resolution XPS of (c) Fe 2p, (d) O 1s, (e) Cl 2p of FeOCl, and 6-BC/FeOCl, respectively, and (f) C 1s of 6-BC/FeOCl.

4.2.4 Optical properties and electrochemical measurements

The synthesised material's optical properties were examined using UV–Vis diffusive reflectance spectroscopy (UV-vis-DRS), as shown in **Fig. 4.5a**. The visible light region starts from 400 to 700 nm. Pristine FeOCl is known to be a good visible light absorption semiconductor. As expected, FeOCl (**Fig. 4.5a)** absorbed almost the entire visible light region, with a wavelength edge of approximately 639 nm. The DRS spectrum of BC in **Fig. 4.5a** displayed an intense, wide-ranging absorption band, suggesting that the BC-

containing composites would effectively harness solar energy. Compared with FeOCl, 6-BC/FeOCl exhibited enhanced visible light absorption at around 682 nm, confirming the incorporation of BC into FeOCl. Under these illumination conditions, enhanced photocatalytic performance would be observed, resulting in higher photocatalytic efficiency. In photocatalysis, the energy band gap of a material is crucial because it dictates the energy required for the generation of charge carriers (electrons and holes) when electrons transition from the VB to the CB, forming electron-hole pairs. The distinct absorption properties of different catalysts indicate varying band gaps, which can be calculated from the absorption spectrum by employing the relationship between energy (hv) and wavelength: he (eV)=1239.8/λ. This method provides insights into the efficiency of the material in absorbing light and facilitating photocatalytic reactions. The band gap energies (E_g) of the synthesised materials were determined using the Tauc plot (**Fig. 4.5b**).

$$Ahv = A\,(hv - Eg)^2 \qquad 4.1$$

where α, h, v, Eg, and A are the absorption coefficient, Planck's constant, light frequency, bandgap energy, and proportionality constant, respectively. The optical band gap was determined through Tauc plot analysis where $(\alpha hv)^2$ vs. hv estimated the band gap after extrapolating with the best possible fit to the baseline at y = 0.

The peak at approximately 639 nm (**Fig. 4.4a**) had the best possible fit, which depicted a band gap of 1.97 eV for FeOCl, and the peak at approximately 682 nm (**Fig. 4.4a**) had the best possible fit, which depicted a band gap of 1.80 eV for 6-BC/FeOCl (**Fig. 4.4b**). Notably, the band gap of the 6-BC/FeOCl composite was reduced compared to that of FeOCl (**Fig. 4.4b**). This observation suggests that the 6-BC/FeOCl composite generated photoinduced electrons and holes at a lower energy threshold than pristine FeOCl. Therefore, BC could further shift the absorbance of FeOCl to the visible region.

The energy band positions of FeOCl and 6-BC/FeOCl were conducted using the Mott–Schottky method, and the results are shown in the **Appendix (A1).** The flat band potential (E_{fb}) values were obtained from the intercept fixed at $1/C^2 = 0$ and found to be 0.61 and 0.51 V (vs. Ag/AgCl) for FeOCl and 6-BC/FeOCl, respectively. The measured potentials vs. Ag/AgCl were then transformed to the NHE scale using the relation $E_{NHE} = E_{Ag/AgCl} + 0.2$ [13]. After changing to NHE scale, the E_{fb} values became 0.81 V and 0.71 V for FeOCl and 6-BC/FeOCl, respectively. Both the pristine FeOCl

and 6-BC/FeOCl composites showed positive slopes in the Mott–Schottky curves, demonstrating that they are both n-type semiconductors. The flat band level of an n-type semiconductor is located 0.1 V below its CB. Therefore, the CB positions of FeOCl and 6-BC/FeOCl are 0.91 and 0.81 eV vs. NHE, respectively [14]. There is a slight shift in the conduction band potential towards the electronegative direction compared to pristine FeOCl, which underpins the influence of BC in altering the electrochemical properties of FeOCl. Using the equation $Eg = Evb - Ecb$, 2.61 eV is NHE was calculated to be the valence band (E_{Vb}) of 6-BC/FeOCl. The oxidation potential for $H_2O/^{\bullet}OH$ (2.4 eV) or $OH^-/^{\bullet}OH$ (1.99 eV) is lower than that of 6-BC/FeOCl (2.61 eV). Hence, under visible irradiation, it is feasible and thermodynamically favourable for H_2O oxidation to produce $^{\bullet}OH$ via the holes (h^+) in the VB of the 6-BC/FeOCl catalyst, resulting in SMX degradation [15].

Furthermore, the electrochemical measurements were evaluated to investigate the catalysts' electron transfer capacity, which is critical for determining their SMX decontamination ability. CV measurements (**Fig. 4.5c**) were examined at a scan rate of 0.02 V s^{-1} and a potential rate of -0.50 V - 1.2 V to measure the electron storage capacity and redox potential of the catalysts. The results show that 6-BC/FeOCl has better electron transfer efficiency than pure FeOCl or BC. As expected, the redox current response was substantially higher in 6-BC/FeOCl than in FeOCl. All the catalysts confirmed both reversible oxidation and reduction peaks, while an extra oxidation peak was observed in FeOCl. The LSV curves of FeOCl and 6-BC/FeOCl are shown in **Fig. 4.5d.** The current density of 6-BC/FeOCl increased significantly , suggesting that the addition of BC increases the conductivity of FeOCl, indicating that 6-BC/FeOCl has a high catalytic activity. Additionally, EIS was employed to investigate the charge transfer efficiency at the electrode-electrolyte interface, and the results are displayed in **Fig. 4.5e**. The EIS Nyquist plots reveal that 6-BC/FeOCl has a smaller semicircular diameter, revealing that the resistance to charge transfer in the composite interface is lower, and the coupling of FeOCl and BC results in higher conductivity, obtaining higher electron transfer efficiency [16]. From **Fig. 4.5f**, the order of free corrosion potentials at the most positive one was as follows: 0.2760 V (6-BC/FeOCl) and 0.1588 V (FeOCl). Because 6-BC/FeOCl had the most positive free corrosion potential, a high electron transfer rate was verified, combined with good photostability [17].

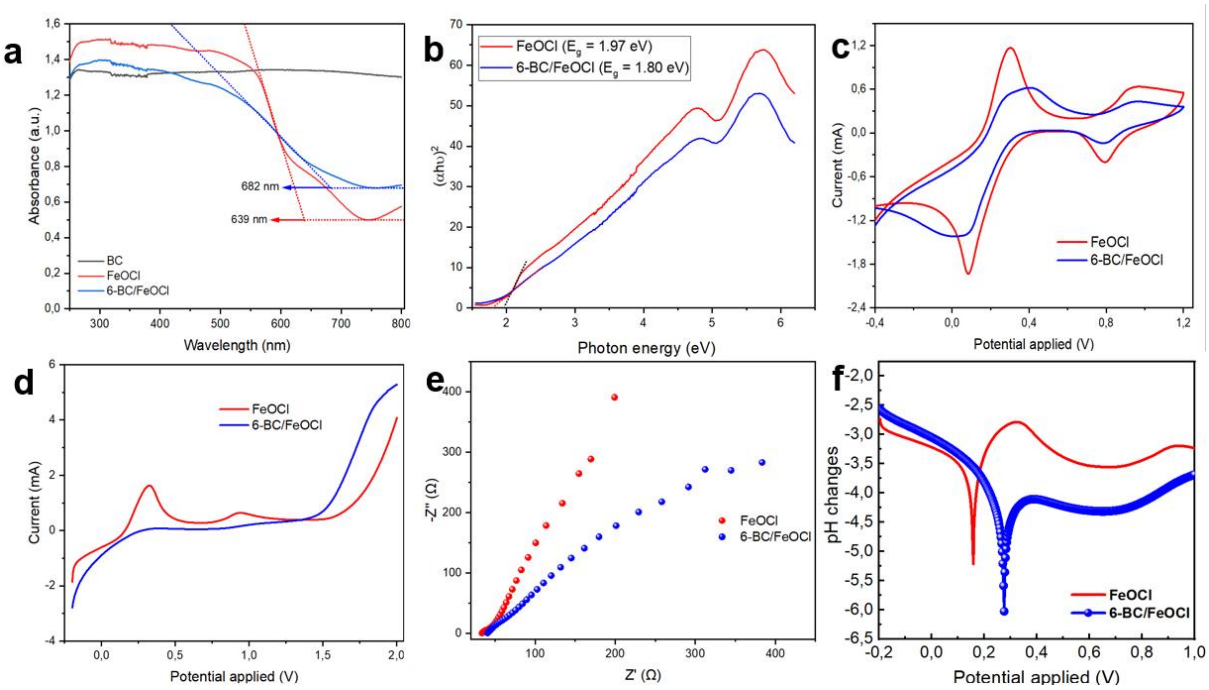

Figure 4.5 (a) UV-vis DRS spectra, (b) Tauc plots, (c) CV curve plots, (d) LSV curve plots, (e) EIS Nyquist plots, and (f) Tafel polarisation plots of FeOCl and 6-BC/FeOCl.

4.2.5 Photocatalytic degradation of sulphamethoxazole

The degradation of SMX was performed in triplicate using 3-BC/FeOCl, 6-BC/FeOCl, 9-BC/FeOCl, and 12-BC/FeOCl to evaluate the influence of the biochar loadings on the catalyst activity. In addition, degradation experiments were conducted in the dark using BC, FeOCl, and 6-BC/FeOCl as controls. Prior to visible light irradiation, the SMX solution mixture and all the catalysts were stirred in the dark for 20 min to achieve an adsorption-desorption equilibrium state. **Fig. 4.6a** shows that the adsorption of SMX was below 20% for all the catalysts, implying a low contribution of adsorption to the overall removal of SMX. Sulphamethoxazole (SMX) adsorption on the catalyst surface is an essential step in the photocatalytic process. The photolysis experiment revealed that SMX is relatively stable and resistant to visible light degradation, as evidenced by the minimal changes in the SMX levels recorded. In the presence of BC and FeOCl as catalysts, SMX degradation reached 43% and 70%, respectively. Despite BC having a higher surface area (70.04 m^2/g, it typically lacks significant photocatalytic active sites required to generate hydroxyl or superoxide reactive species, which can degrade organic contaminants. Additionally, it has been reported that biochar lacks the semiconductor characteristics required for efficient light

absorption and electron-hole pair production, both of which are critical for photodegradation processes [18]. Although biochar does not possess semiconductor characteristics or inherent photocatalytic activity, it was still able to remove 43% of SMX from water through adsorption. Its large surface area, porous structure (**Fig. 4.3b**), and numerous functional groups (**Fig. 4.4a**) promote organic molecule adsorption on the functionalised biochar through π–π interactions, H-bonding, Coulombic attraction, and ion exchange [19]. Resulted in a certain amount of SMX removal (43%). Meanwhile, FeOCl showed better photocatalytic activity owing to its remarkable visible light activity emanating from its narrow band gap (1.97 eV) and its unique "van der Waals layer," which promotes good intercalation ability. The interlayer spacing of FeOCl can easily accommodate guest molecules, enhancing pollutant adsorption and even influencing the charge transfer dynamics. This intercalation ability supports and improves the photocatalytic degradation of water pollutants [20]. However, its small surface area (5.03 m^2 g^{-1}) limits the number of adsorbed SMX molecules on the surface, and the rapid recombination of the charge carriers (e^-/h^+) reduces the radicals produced for efficient degradation of SMX.

All the BC/FeOCl nanocomposites have improved catalytic activity for SMX degradation compared to FeOCl, indicating that the addition of BC increased the catalytic activity of the composite materials. After 120 min of photocatalysis, the optimal 6-BC/FeOCl exhibited the highest photocatalytic activity of 89.8%, which was significantly higher than that of 3-BC/FeOCl (78.1%), 9-BC/FeOCl (79.33%), and 12-BC/FeOCl (78.8%). Evidently, increasing the BC concentration from 3% to 6% also increases SMX removal degradation from 78 1 to 89.8%; however, further increasing the BC loading to 9% results in a slight decrease in SMX removal to 79.3% and then 78.8% when the BC loading reaches 12%. It is widely reported that at lower biochar contents, the active sites of the photocatalyst remain more exposed, allowing efficient light absorption for the activation of charged carriers and enhancing pollutant degradation. Meanwhile, excessive BC introduction blocks the active sites of FeOCl and may mask the light absorption of FeOCl. At high concentrations, biochar acts as an optical shield that significantly decreases the photon flux throughout the reaction solution, thereby shielding some parts of the reactor from accessing the light. Ultimately, this shielding effect results in poor catalyst activation and lower overall photocatalytic activity [21]. The kinetics of SMX degradation were investigated using

the Langmuir-Hinshelwood model and fitted to the pseudo-first-order equation shown in **Eq. 4.2** and the results are illustrated in the **Appendix (A2).**

$$kt = \ln(\frac{C0}{Ct}) \quad 4.2$$

where k is the pseudo-first-order rate constant (min^{-1}), C_0 is the initial concentration, and C_t is the SMX concentration at time t.

The rate constants k (**Fig. 4.6b**) were 0.01435, 0.01646, 0.01183, 0.01091, 0.00855, and 0.01058 min^{-1} for 3-BC/FeOCl, 6-BC/FeOCl, 9-BC/FeOCl, 12-BC/FeOCl, FeOCl, and BC, respectively. The optimal 6-BC/FeOCl ratio exhibited the highest rate constant, which was 1.9 and 2.8 times higher than that of FeOCl and BC, respectively. Therefore, supporting FeOCl with BC resulted in enhanced photocatalytic activity. However, the yield of incorporated BC must be carefully controlled to ensure augmented catalytic activity and minimal side effects.

Fig. 4.6c shows the UV–vis absorption spectra for SMX degradation as a function of contact time using 6-BC/FeOCl as the photocatalyst. Evidently, the absorption peak of SMX decreased at 266 nm, suggesting the destruction of the chromophore responsible for the absorbance. Additionally, the SMX absorption peak shifts to the left after 20 min of visible light irradiation. As the SMX is further degraded over time, the absorption peak shifts further to the left. This observation suggests that as the photocatalytic reaction progresses, SMX molecules are broken down into smaller byproducts. Therefore, the newly formed intermediate species have different electronic structures than the parent compound. These intermediates absorb light at different wavelengths, resulting in a shift in the absorption peak [22].

4.2.6 Effect of the initial sulphamethoxazole concentration and the photocatalyst dosage

Using the optimal 6-BC/FeOCl as the most effective photocatalyst, SMX degradation was investigated at different pollutant concentrations (5 ppm–20 ppm) and photocatalyst loading (0.1 to 0.8 g L^{-1}). **Fig. 4.6d** indicates that the SMX removal efficiency first increased with increasing pollutant concentration from 5 ppm (85.4%) to 10 ppm (90.2%) and subsequently decreased with increasing initial concentration from 15 ppm (71.0%) to 20 ppm (48.6%). Usually, the lowest pollutant concentrations degrade the fastest with high removal efficiency because, when SMX concentrations

are low, fewer molecules of SMX are available for adsorption, and there are abundant active radicals to efficiently break down and mineralise each SMX molecule into simpler molecules, allowing a higher percentage of the SMX molecules to interact with the generated radicals [23]. However, in the case at 5 ppm (85.3%), the SMX degradation was slightly lower than that at 10 ppm (90.1%), possibly because the generated reactive species might not have adequate interaction with enough SMX molecules to react with, leading to scavenging or recombination of these reactive species. Ultimately, this reduces the overall degradation efficiency. As the SMX concentration increased to 10 ppm, more SMX molecules were adsorbed onto the photocatalyst surface for complete saturation. This suggested that the available SMX molecules were directly proportional to the available active sites on the photocatalyst; therefore, sufficient active radicals are required for the efficient breakdown and mineralisation of SMX into smaller molecules [23]. When the initial concentration of SMX increased further to 15 and 20 ppm, the degradation efficiency of SMX started to decrease. This is because at high concentrations of SMX, the existing reactive radicals are insufficient to remove the excess SMX molecules. Excess intermediates are formed as the SMX molecules are degraded. These intermediates compete with undegraded SMX molecules for active sites on the photocatalyst surface, thus inhibiting the overall adsorption and degradation of SMX molecules. Inevitably, this leads to a reduction in the photocatalytic efficiency [51,49].

Different photocatalyst dosages of the optimal 6-BC/FeOCl ratio were selected to assess the photocatalytic activity using 10 ppm SMX. The results are displayed in **Fig. 4.6e**. As the catalyst dosage increased from 0.1 to 0.2 g L^{-1}, the degradation efficiency of SMX also steadily increased from 80.0% to 89.7%. Thereafter, an increase in the photocatalyst concentration was accompanied by a decrease in the SMX removal efficiency, with the lowest removal recorded when a concentration of 0.8 g L^{-1} (66.2%) was used. Typically, increasing the photocatalyst dosage increases degradation efficiency because of the provision of abundant active sites that could rapidly oxidise pollutants [11]. However, when the catalyst dosage was increased further, the degradation efficiency was hampered, possibly because the excess catalyst increased the opacity of the solution. Ultimately, this lowers the photocatalyst light absorption efficiency and generates the reactive species responsible for SMX degradation. In addition, it is noted that adsorption efficiency worsens at higher catalyst dosages (0.8

g L^{-1}), which might be due to the fact that increasing the catalyst dosage beyond the optimal threshold leads to an excessive catalyst in the solution, which may encourage the clustering of the photocatalyst particles, reducing the active surface area and leading to blockages of the active sites, thereby reducing the overall degradation efficiency [21].

4.2.7 Influence of the initial pH of the pollutant solution

The pH is a critical parameter that significantly affects SMX removal in a solution. To investigate the impact of pH on SMX degradation, photocatalytic degradation experiments were conducted over the 6-BC/FeOCl composite at pH 5, 6.5, 7.5, 8.5, and 10. Different pH values were obtained by adjusting the SMX solution with 0.1 M NaOH and 0.1 M HCl for basic and acidic conditions, respectively. The results shown in **Fig. 4.6f** show that the removal rate of SMX decreases with increasing solution pH. At a pH of 5, the SMX removal rate was relatively high, reaching 90.2%. As the pH further increased from pH 5 to pH 8.5, the degradation efficiency of SMX decreased from 90.2% to 76.7%. At pH 10, the efficiency decreased even further (43.2%). Previous studies have shown that SMX exists in various forms at different pH values. When the pH of the solution is less than the second pKa value (5.81) of the compound, SMX exists in a positively charged form, and when it is around the pKa value (5.81), SMX exists in both positively and negatively charged forms. As the pH of the solution increases beyond this pKa value, SMX can be deprotonated slowly, and the fraction of negatively charged species increases [24]. Consequently, the removal of SMX will depend on the interaction between the surface of the charged catalyst and the SMX molecules present. Therefore, **Fig. 4.6g** shows that the photocatalyst's point of zero charge is 2.1, indicating that the catalyst was mostly negatively charged in the selected pH range investigated. These results imply that SMX was mostly protonated at pH 5 and could interact with the negatively charged catalyst via the electrostatic force of attraction, thereby increasing the catalytic SMX removal (90.2%). As the pH increased from 5 to 8.5, the SMX removal slowly decreased from 90.2% to 76.7%, indicating a slow deprotonation of SMX with more negatively charged species present, causing a repulsion force between the photocatalyst and SMX. Under highly alkaline conditions (pH 10), many negatively charged species in the solution prevented SMX from adsorbing onto the catalyst surface, resulting in a substantial decline in the catalytic

efficiency (43.0% SMX removal). The change in degradation rate confirmed that pH is an essential factor for the degradation of SMX.

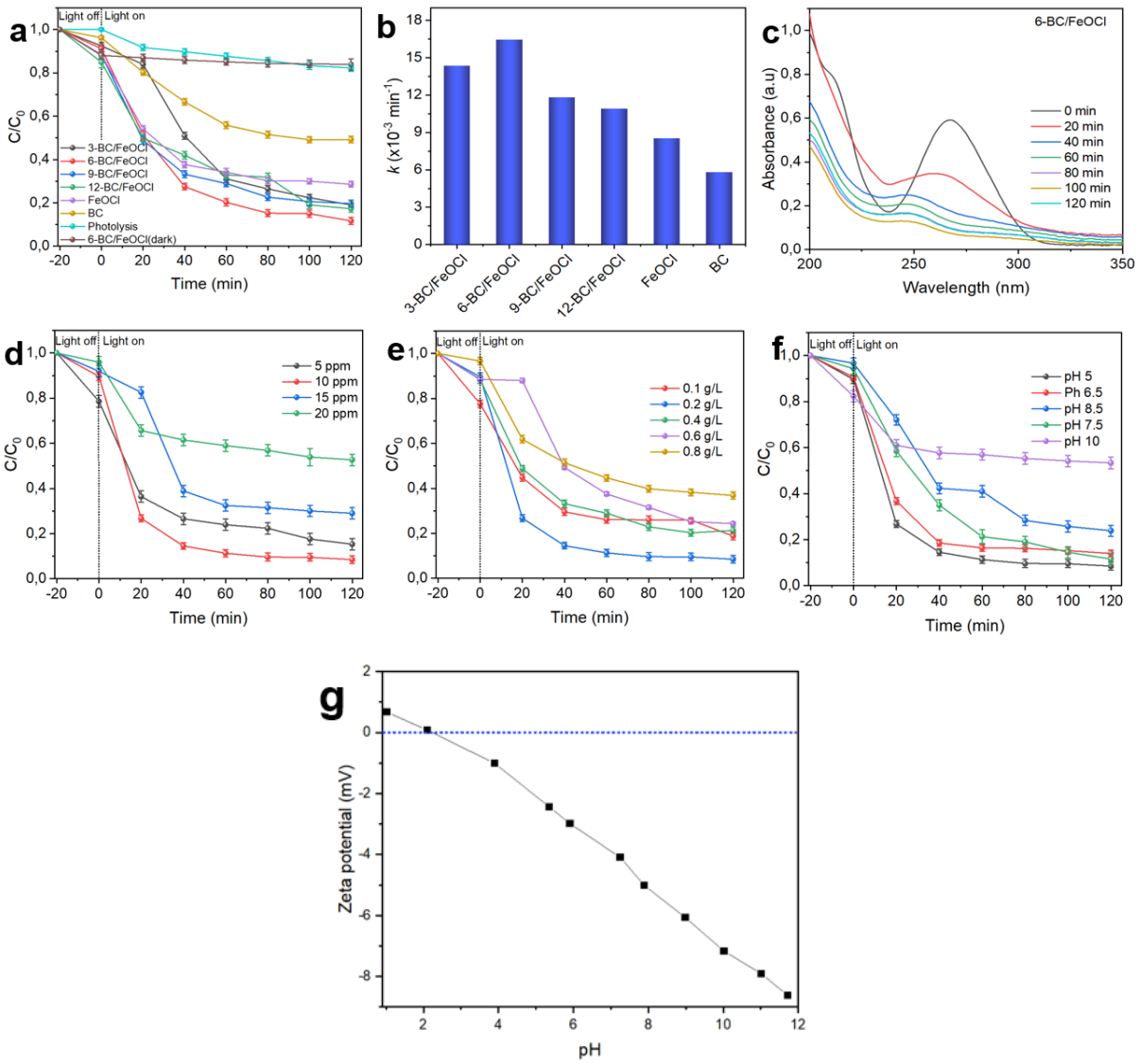

Figure 4.6 (a) SMX degradation using different catalysts, (b) SMX degradation rate constants of the different catalysts, (c) UV-vis spectra for SMX degradation over 6-BC/FeOCl, (d) SMX concentration, (e) catalyst dosage, (f) initial solution pH, and (g) 6-BC/FeOCl zeta potential. Optimum conditions (SMX =10 ppm, catalyst = 0.2 g/L, pH = 5).

4.2.8 Effects of organic matter and inorganic anions

Dissolved organic matter present in the aqueous environment and different ions (cations and anions) can influence the removal of antibiotics from water in various ways. Different water matrices contain various inorganic anions (Cl^-, NO_3^-, SO_4^{2-}, $H_2PO_4^-$, HCO_3^-), that may compete with the target pollutants. In this work, 10 mM of each inorganic anion was prepared and introduced separately to study its influence on SMX degradation using 6-BC/FeOCl in the presence of visible light irradiation, and the results are shown in **Fig. 4.7a**. The presence of sulphate (SO_4^{2-}), and bicarbonate (HCO_3^-) anions reduced the removal of SMX from 90.8% to 78.2% and 22.4%, respectively. This is because generally, both SO_4^{2-} and HCO_3^- ions are effective radical scavengers and lead to the formation of less powerful reactive species [60, 61]. Therefore, when they are present in a photocatalytic reaction, they tend to react with both hydroxyl radicals ($^{\bullet}OH$) and holes (h^+), reducing the availability of these reactive species for attacking and breaking down SMX molecules (**Eqs. 4.3 - 4.6**) [27]. This competition significantly decreases the SMX removal efficiency. In addition, bicarbonate ions act as a pH buffer, which can shift the pH of the solution to more basic conditions [28]. The negatively charged SMX molecules may experience repulsion from the negatively charged 6-BC/FeOCl photocatalyst surface as the pH increases, further reducing degradation efficiency.

Interestingly, no major changes in the SMX degradation pattern were detected in the presence of Cl^- anions compared with the control sample (DI water). Previous studies have reported the suppressive effects of Cl^- ions on the photocatalytic degradation of some antibiotics in water, and it was presumed that these ions behaved as hydroxyl radical (•OH) scavengers, slowing down the degradation [29,30]. However, in this work, the presented experimental conditions showed a slight improvement for SMX degradation (91.8%), which may be attributed to the production of inorganic radical anions such as $Cl^{\bullet}$ and $Cl_2^{\bullet-}$, which increased SMX photodegradation (**Eq. 4.7**) [29]. For the first 60 min, a slight decrease in the SMX efficiency was observed in the presence of NO_3^- . The NO_3^- anions likely reacted with $^{\bullet}OH$ and h^+ to form $NO_3^{\bullet}$, which has a lower oxidation potential (2.3 V) relative to 2.8 V of $^{\bullet}OH$ (**Eqs. 4.8** and **4.9**), thereby decreasing the overall reaction efficiency [25]. However, the overall SMX degradation efficiency nearly matched that observed in the presence of Cl^- and the control sample, indicating an increase in the degradation kinetics. This may be

attributed to the generation of hydroxyl radicals (•OH) in addition to the $NO_3^{\bullet}$, which collectively participate in the degradation of SMX [31,32]. Among the natural organic substances present in aquatic environments, humic acid (HA) is one of the most abundant forms of friction in NOM [25,26]. The results show that HA inhibits SMX removal, which declined from 90.8% to 75.2%. Humic acid can scavenge ROS, including •OH and $^{\bullet}O_2^-$, which are essential for photocatalytic pollutant breakdown. By reacting with these reactive species, HA reduces their ability to interact with the target pollutant (SMX), ultimately lowering the degradation efficiency [33].

$$SO_4^{2-} + HO^{\bullet} \rightarrow SO_4^{\bullet -} + HO^- \quad 4.3$$

$$SO_4^{2-} + h^+ \rightarrow SO_4^{\bullet -} \quad 4.4$$

$$HCO_3^- + HO^{\bullet} \rightarrow CO_3^{\bullet -} + H_2O \quad 4.5$$

$$HCO_3^- + h^+ \rightarrow CO_3^{\bullet -} + h^+ \quad 4.6$$

$$Cl^- + HO^{\bullet} \leftrightarrow HOCl^{\bullet -} \xleftrightarrow{H+(-H_2O)} Cl^{\bullet -} \xleftrightarrow{Cl-} Cl_2^{\bullet -} \quad 4.7$$

$$NO_3^- + HO^{\bullet} \rightarrow NO_3^{\bullet} + HO^- \quad 4.8$$

$$NO_3^- + h^+ \rightarrow NO_3^{\bullet} \quad 4.9$$

4.2.9 Probing the Influential Reactive Species

Semiconductor photocatalysis initiates the degradation of organic molecules through the absorption of photons by ground-state electrons in the semiconductor, which initiates the formation of charge carriers and subsequently, various reactive species for the complete mineralisation of pollutants [33]. Active species trapping experiments were performed in the photocatalytic reaction of SMX degradation over 6-BC/FeOCl in the presence of visible light to examine the different reactive oxygen species responsible for the degradation of SMX by 6-BC/FeOCl. Disodium ethylenediamine (EDTA-2Na), methanol, and benzoquinone (BQ) were used to capture photogenerated holes (h^+), hydroxyl radical (•OH), and superoxide radical ($^{\bullet}O_2^-$), respectively. **Fig. 4.7b** reveals that the addition of EDTA-2Na, methanol, and BQ suppressed the photocatalytic degradation efficiency to different degrees. Specifically, the degradation efficiency of SMX reduced significantly with the addition of EDTA-2Na (18.1%) and methanol (19.3%), indicating that h^+ and •OH served as the dominant factors in the photocatalytic process. Meanwhile, $^{\bullet}O_2^-$ was not the principal factor in SMX

degradation because the addition of BQ yielded a moderate decline in SMX degradation compared with EDTA and methanol. Nearly 60% SMX removal was recorded in the presence of BQ (superoxide radical scavenger).

4.2.10 Degradation of sulphamethoxazole in different water matrices

To further evaluate the effectiveness of the 6-BC/FeOCl composite in treating environmental water samples, three water samples, namely, tap, wastewater effluent, and river water, were collected, spiked with 10 mg/L SMX, and subjected to photocatalytic degradation. **Fig. 4.7c** shows that after 120 min of visible irradiation, the degradation efficiencies of SMX in tap water, wastewater effluent, and river water were 86.1%, 79.2%, and 68.1%, respectively. The degradation efficiency in these samples is significantly lower than the SMX degradation efficiency in deionised water (92.7%). This observation suggests that the 6-BC/FeOCl composite has strong adaptability to complex water matrices. Evidently, the percentage of SMX removal in the river water was the lowest (68.1%), which may be ascribed to the complexity of the river water generally characterised by the presence of multiple competitive substances, such as organic and inorganic ions, that may compete with SMX in the consumption of reactive species. Overall, the results demonstrated that the 6-BC/FeOCl photocatalyst can be further investigated in natural waters with organic contaminants over extended periods of visible light irradiation, especially in wastewater effluents, which are hotspots for pharmaceuticals and their metabolites. The corresponding rate constants are presented in **Fig. 4.7d**. The degradation of SMX in DI water was the fastest (0.01705 min^{-1}) followed by degradation in tap water (0.01366 min^{-1}), wastewater effluent (0.01018 min^{-1}), and river water (0.006430 min^{-1}). Despite the relatively low degradation efficiency of SMX in the various matrices compared to DI water, the composite photocatalyst still displayed appreciable activity, which signalled its importance as a potential remediation tool for environmental pollution.

Several materials have been explored for SMX degradation under various reaction conditions. The variation in terms of the reactors used and reaction conditions present a prevalent challenge in terms of achieving reliable comparison across reported research. Despite this challenge, a crude comparison can still be drawn between similar or different materials for the same application. The photocatalytic activity of 6-BC/FeOCl against SMX was compared with other photocatalysts for the same

application (**Table 4.1)**. The photocatalytic removal of SMX in our study was competitive compared to the highlighted reports. Substantial amounts of SMX were degraded over 6-BC/FeOCl within a shorter reaction time.

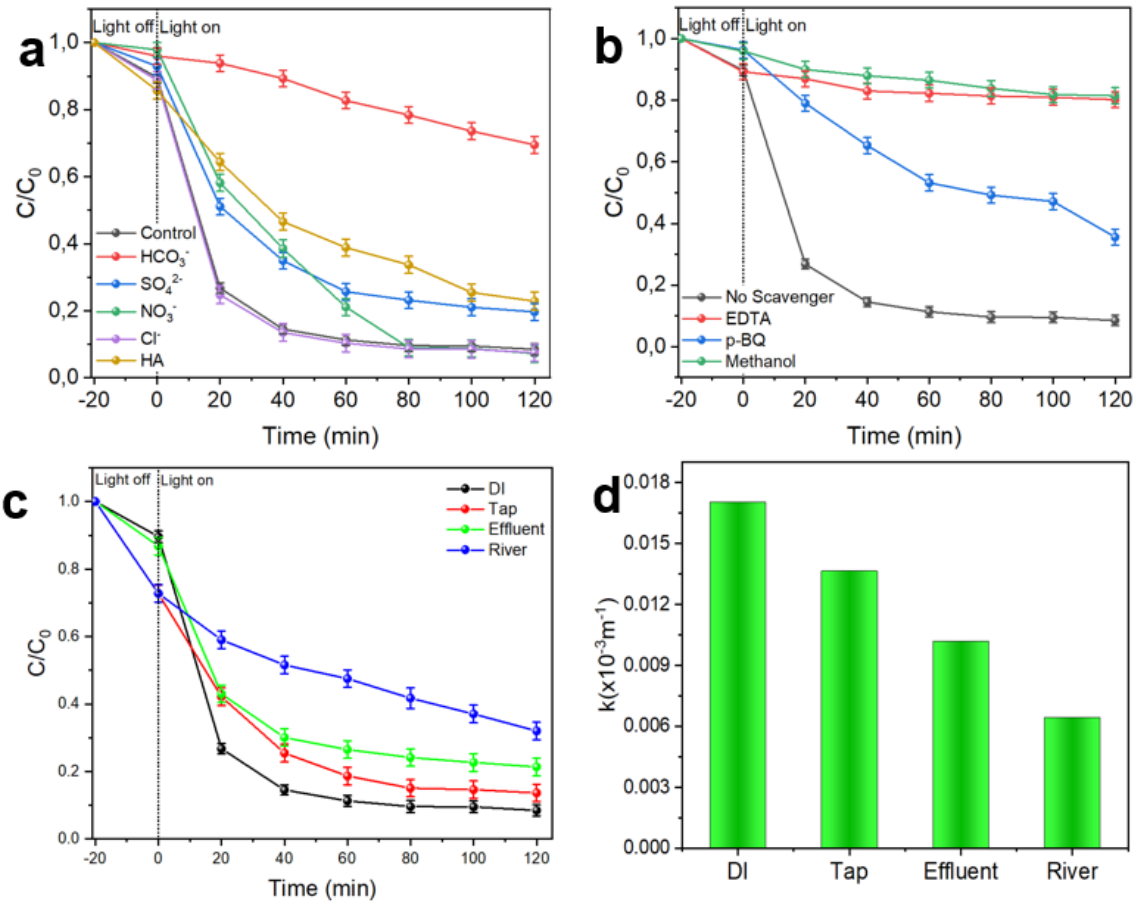

Figure 4.7 (a) Effect of different environmental inorganic ions and HA; (b) identification of predominant reactive species; (c) SMX degradation in various surface water and wastewater effluent matrices; (d) corresponding reaction rate constants for SMX removal in different surface water matrices and wastewater effluent. Optimum conditions (SMX =10 ppm, catalyst = 0.2 g/L, pH = 5).

Table 4.1: Comparison of SMX degradation in water using 6-BC/FeOCl with other photocatalysts.

Catalyst	Catalyst dosage (g/L)	SMX conc. (ppm)	Irradiation type	Kinetic constant(min^{-1})	Time (min)	SMX removal efficiency (%)	Refs
6-BC/FeOCl	0.2	10	Visible light (250 W)	0.01646	120	90.1	Current work
Biochar/TiO_2	0.5	10	UV (15W)	0.03833	360	91.0	[34]
$FeCl_3$-activated biochar	0.1	100	Visible light (300 W)	0.1733	720	99.9	[35]
ZnO/Biochar	0.2	10	Visible light (50 W)	0.0087	180	81.2	[36]
BC/Cu_2O	0.3	20	Visible light (500 W)	0.01425	270	93.0	[37]

4.2.11 SMX degradation analysis using fluorescence excitation-emission matrix

The photodegradation processes of SMX in all water samples (DI, tap, wastewater effluent, and river) were further investigated using two-dimensional fluorescence excitation-emission matrices (2D FEEMs), as shown in **Fig. 4.8.** In all 4 waters, before visible light irradiation (0 min), SMX exhibited five independent fluorescence components: less aromatic humic-like, more aromatic humic-like, marine-like, tyrosine-like, and protein-like, which showed different excitation-emission peaks at 260/380-460 nm, 320-360/420-460 nm, 290-310/370-410 nm, 260/280 nm, and 250-300/410-355 nm, respectively (**Table 4.2**). Under visible light irradiation, the degradation of SMX across various water matrices was confirmed through the

changes in the intensity of the observed colours which then resulted in degradation by-products with different EX and EM regions after 120 min. In DI water (**Fig. 4.8a-c**) after 120 min of irradiation, 99, 55, 97, 88, and 96% of humic-like (less aromatic), more aromatic humic-like, marine, tyrosine, and protein-like organic compounds, respectively, were removed using 6-BC/FeOCl under visible light exposure. The excitation-emission matrix peak intensities which serve as distinct fingerprints of the presence of the SMX in the samples, progressively diminished with the extended degradation time. A significant reduction in peak fluorescence was observed within 120 min, suggesting near complete degradation of SMX. In addition, SMX removal was highly favoured in DI water compared to the other matrices due to less interference and competition since it is a much simpler matrix with most of the organic and inorganic species removed. However, only 55.2% of the aromatic humic-like substances were removed from the water, indicating inertness to catalytic oxidation.

SMX degradation in tap water is shown in **Fig. 4.9a-c** to be 92.1%, 46.3%, 90.0%, 86.6%, and 91.0 % of less aromatic humic-like, more aromatic humic-like, marine, tyrosin, and protein-like substances, respectively, which also indicated a high removal of NOM indicated by SMX. The same results were observed for aromatic humic-like substances in tap water. In both wastewater effluent (**Fig. 4.9d-f)** and river water (**Fig. 4.9g-i)**, the FSI of SMX slightly decreased from 0 to 120 min. Even after 120 min of visible light irradiation, there is still a resemblance of SMX FSI before visible light irradiation. This observation agrees with the percentage removal of the different organic substances found in SMX in water. Various organic substances found in wastewater, such as humic-like, protein-like, and tyrosine-like compounds, exhibit different oxidation reactivities toward oxidation due to their distinct molecular structures and interactions with catalysts [38]. Catalytic oxidation struggles to fully break down these stable molecules, resulting in low removal efficiency in this region of the matrix. In wastewater effluent, where most of these non-biodegradable organics are found, only 49.2%, 47.7%, 38.1%, 69.6%, and 35.0 % of less aromatic humic-like, more aromatic humic-like, marine, tyrosine, and protein-like substances, respectively, were removed (**Fig. 4.9d-f)**. This observation suggests that substances from industrial sources often contain non-biodegradable organic components that are less susceptible to oxidative degradation, contributing to the overall low removal efficiency during catalytic oxidation. FEEM analysis proved the behaviour of these organic

substances across different regions of the fluorescence matrix, helping to highlight which types of organic matter are most susceptible or resistant to oxidation [39]. In river water (**Fig. 4.9g-i)**, the removal of less aromatic humic-like, more aromatic humic-like, marine, tyrosine, and protein-like substances was observed at 36.9%, 1.5%, 56.7%, 69.4%, and 9.2%, respectively. The removal percentage is even lower in river water, possibly because SMX is hardly photodegraded because of the competing various inorganic and organic compounds that are normally highly present in surface water. Overall, the obtained results suggest that 6-BC/FeOCl greatly removes SMX in DI and tap water under visible light illumination. However, the removal efficiency of SMX in wastewater effluent and river water was lower because of the presence of competing organics in water, hindering the degradation of SMX. Therefore, a pretreatment step will need to be implemented to reduce the complexity of the matrix to effectively apply this photocatalytic process in environmental samples.

A specific ultraviolet absorbance at 254 nm (UV_{254}) examination was also performed to further assess the degradation of the aromatic components of SMX. The results are presented in **Fig. 4.8d**. Notably, UV_{254} removal reached 92.5 % (DI), 84.8 % (Tap), 78.2 % (WW effluent), and 67.9 % (River), indicating that the aromatic molecules in SMX and the resultant intermediates were converted to aliphatic compounds [40]. Although the removal efficiency was lower in river water than in all the other matrices, it was still significantly high considering the complexity of the river water. UV_{254} is often used as an indicator of the quantity of aromatic compounds present in water. The observed high UV_{254} removal in almost all the water matrices suggests that the aromatic backbone of SMX and its degraded intermediates were largely aliphatic molecules. Aliphatic molecules are more susceptible to photodegradation than aromatic compounds [41]. These results demonstrate the successful breakdown of the SMX structure into simpler intermediates through the 6-BC/FeOCl photocatalytic process.

Table 4.2: Different organic compounds found in water and detected in five different regions on the fluorescence excitation-emission matrix [42].

Description	**Excitation max (nm)**	**Emission max (nm)**

UV humic-like, less aromatic	<260	380-460
Visible humic-like, more aromatic	320-360	420-460
Marine humic-like	290-310	370-410
Tyrosine-like substances	260	280
Protein-like Tryptophan	250-300	305-355

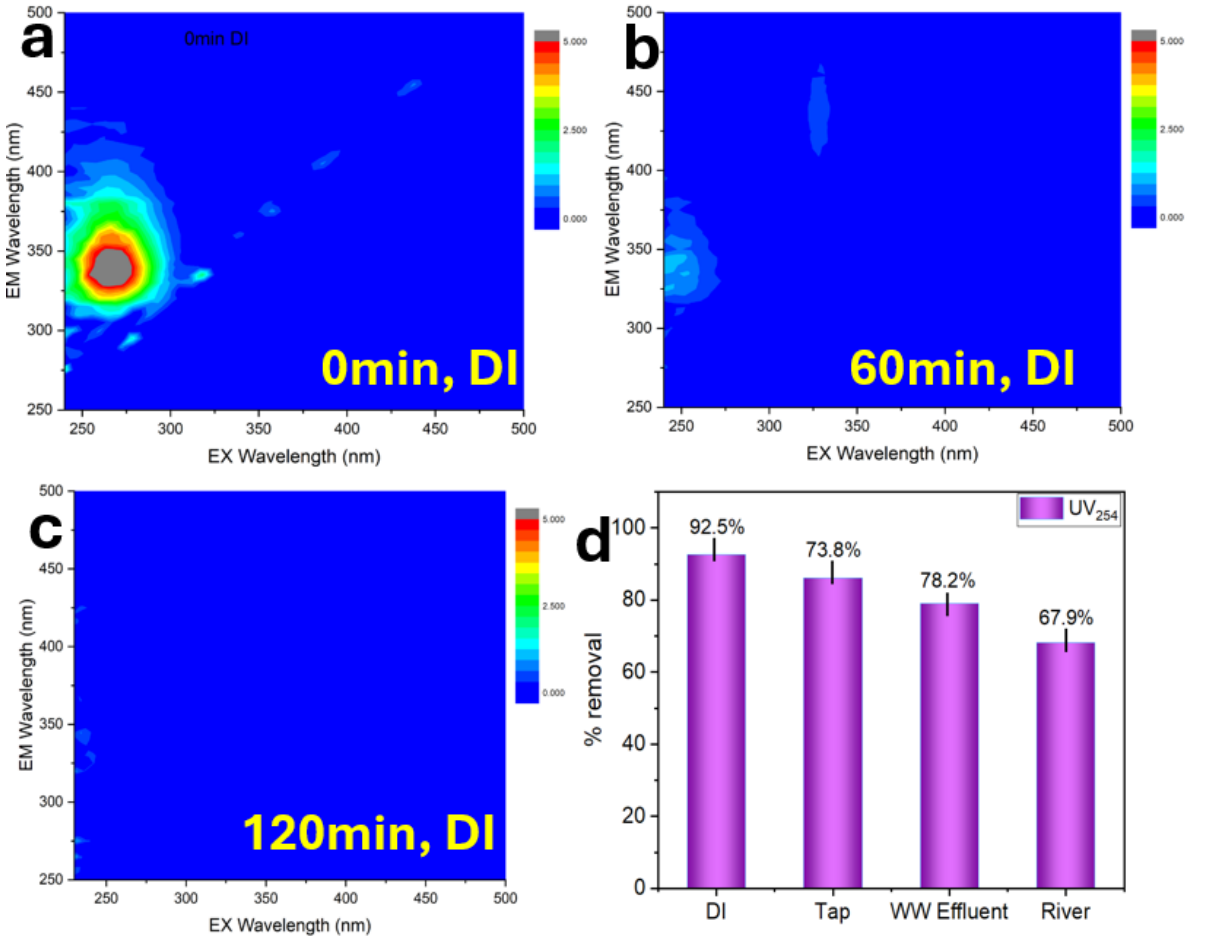

Figure 4.8 FEEM spectra of sulphamethoxazole degradation in DI water (a) at 0 min, (b) after 60 min, and (c) after 120 min using 6-BC/FeOCl under visible light irradiation, and (d) specific ultraviolet absorbance at 254 nm (UV_{254}) removal during SMX degradation in DI, tap, wastewater effluent, and river water.

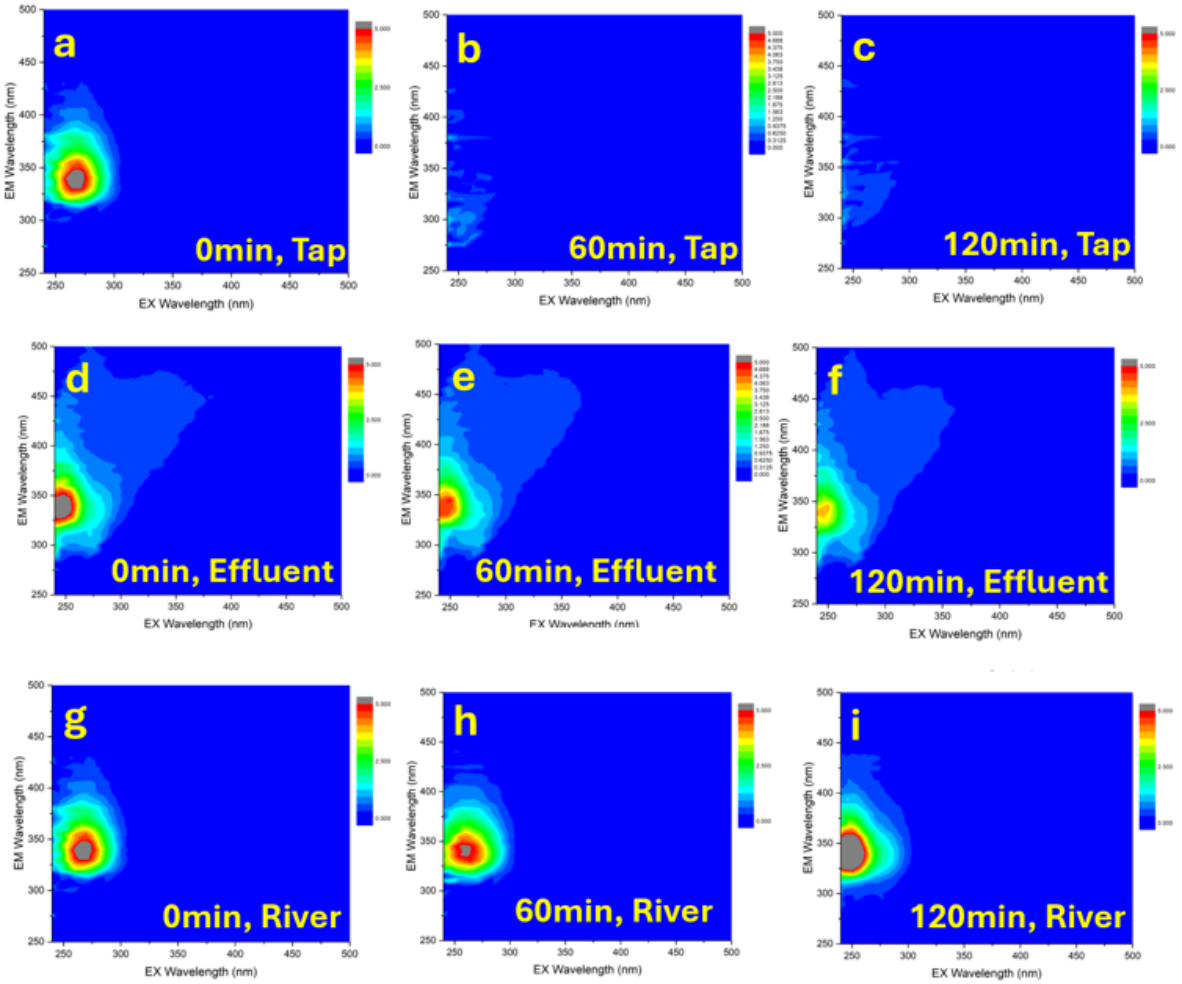

Figure 4.9 Sulphamethoxazole degradation fluorescence spectra for tap water (a - c), wastewater effluent (d - f), and river water (g – i) before and after photodegradation using 6-BC/FeOCl photocatalyst under visible light irradiation.

Table 4.3: Physicochemical properties of the water matrices used in the SMX degradation experiments.

Parameter	Tap water	WW Effluent	River water
pH	6.86	7.88	7.95
DO (ug/L)	1.66	3.09	2.90
Conductivity (us/cm)	251	744.00	677.00

TDS (ug/L)	127.00	373.00	338.00
Salinity (psu)	0.12	0.37	0.33

4.2.12 Investigation of the stability of the photocatalyst

The reusability and stability of the catalyst are essential for its practical implementation. Cyclic degradation experiments were performed to determine the reusability of 6-BC/FeOCl. The catalyst was reused five times under identical optimised conditions (SMX = 10 ppm, 6-BC/FeOCl = 0.2 g L^{-1}, pH = 5). After each SMX photodegradation reaction, the catalyst was washed multiple times with both water and ethanol and centrifuged for recovery. The mixture was then dried in an oven at 80 °C for 12 h and used again for the next photocatalytic reaction for 5 cycles. The results are shown in **Fig. 4.10a**. After the first round of photocatalysis, 90.2% of SMX was removed. Thereafter, there was a gradual decrease in the SMX degradation efficiency with an increasing number of cycles, probably attributed to competition between residual SMX and degradation intermediates for the catalyst surface, thereby reducing the amount of SMX degraded [21]. The experiments revealed that the 6-BC/FeOCl composite had favourable stability and reusability (at least for the first three cycles with SMX removal above 75%) for application in removing SMX in aqueous medium. Moreover, the reused catalyst was characterised using XRD (**Fig. 4.3a**) and FT-IR (**Fig. 4.4b**) to probe changes in the crystal structure and its functional groups. Evidently, XRD analysis confirmed that the crystalline structure was largely retained, but an intensity loss at the (010) plane was observed. FTIR showed some functional group changes (e.g., Fe–O weakening), suggesting the participation of the catalyst in SMX degradation. These slight changes in the 6-BC/FeOCl ratio might also be the reason for the decreased SMX removal (68.1%) after 5 cycles. This is particularly crucial for ensuring sustainable water treatment methods.

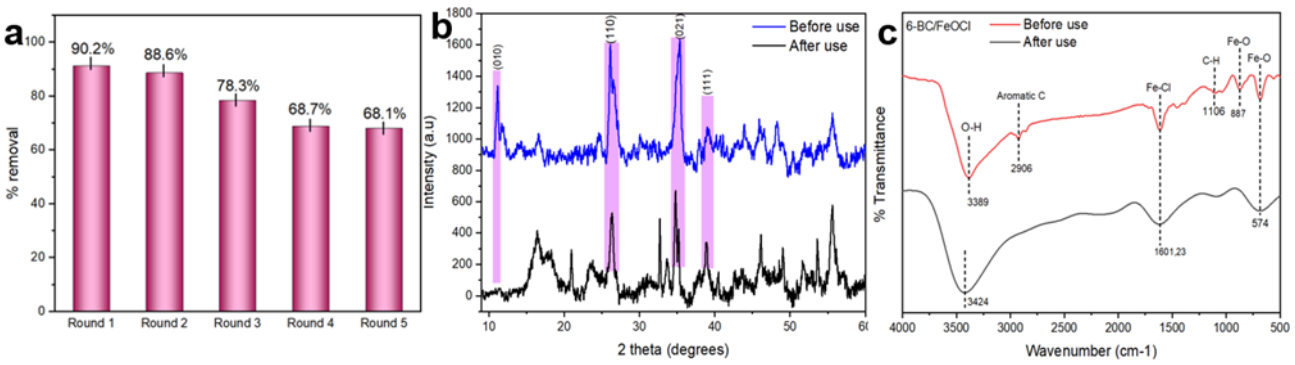

Figure 4.10 (a) Reusability test and (b, and c) XRD and FT-IR spectra of 6-BC/FeOCl before and after use.

4.2.13 Possible charge generation and transfer pathways

Based on the optical response analyses, electrochemical measurements, and reactive species trapping experiments, the most feasible charge generation and transfer pathway was proposed (**Fig. 4.11**). When 6-BC/FeOCl is illuminated with visible light, light absorption occurs and photoexcitation occurs, resulting in electron transfer from the VB to the CB of FeOCl while generating positive holes in the VB. The electrons moved freely from the CB of FeOCl to the BC due to the potential difference. The electrons in BC then react with adsorbed O_2 to form $^{\bullet}O_2^-$ radicals, which have been shown through trapping experiments to play a role in the degradation of SMX. Meanwhile, the electrons in the CB of FeOCl have a more electropositive potential (+0.81 V vs NHE) compared to that of $O_2/^{\bullet}O_2^-$ redox couple (−0.33 eV vs NHE), reducing O_2, thermodynamically unfavourable [43]. Therefore, the incorporation of BC and intimate interaction with FeOCl is crucial for generating reactive species and directing electrons away from the CB of FeOCl, ultimately improving charge separation. Furthermore, the possible Fe^{2+}/Fe^{3+} redox cycle contributes to charge separation and improved reactive species formation. Meanwhile, the holes in the VB of FeOCl have a higher oxidation potential (+2.61 eV vs. NHE) compared to $H_2O/^{\bullet}OH$ (+2.40 eV vs. NHE) and $OH^-/^{\bullet}OH$ (+1.99 eV vs. NHE) [44], making it feasible to react with water and hydroxide ions to form highly reactive and powerful $^{\bullet}OH$ radicals (2.72 V). In addition, the holes can also directly attack and oxidise SMX molecules to form degradation by-products. Both the holes and $^{\bullet}OH$ were identified as the predominant reactive species responsible for SMX degradation through the trapping experiments. Overall, the generation of charge carriers, transfer, and degradation of SMX is a result

of the existence of synergy between BC and FeOCl. Therefore, this simple material can be scaled up and explored in pilot-scale systems.

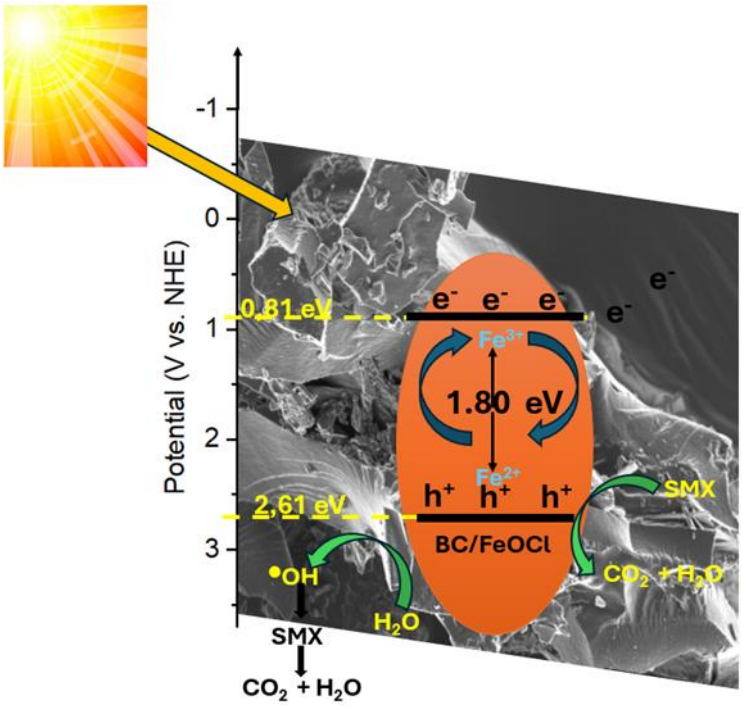

Figure 4.11 Proposed mechanism for SMX degradation over the 6-BC/FeOCl catalyst under visible light irradiation.

4.3 Chapter summary

A newly developed composite catalyst (6-BC/FeOCl) exhibiting remarkable catalytic activity was successfully prepared by ultrasonic-assisted wet impregnation and a one-step calcination method for the photocatalytic oxidation of SMX in water. The characterisation of the physicochemical properties of 6-BC/FeOCl was conducted by TEM, SEM, XPS, XRD, FT-IR, and BET. The photocatalytic capacity of 6-BC/FeOCl was significantly improved compared with that of FeOCl. The SMX photocatalytic efficiency of 6-BC/FeOCl was increased by 2.9 times compared with that of FeOCl. When the initial SMX concentration was 10 ppm (0.2 g L^{-1} catalyst dosage and pH = 5), the degradation rate to SMX reached 90.1%. The presence of BC increased the conductivity and provided chemical stability on FeOCl while also acting as an electron acceptor, forming a heterojunction and inhibiting e^-/h^+ fast recombination, which then increased the 6-BC/FeOCl catalytic efficiency. The scavenging tests performed

revealed that $^{\bullet}OH$ and h^{+} served as key reactive species in the photocatalytic process of SMX. Furthermore, the 6-BC/FeOCl composite showed no significant loss in either stability or catalytic efficiency after the first three cycles of testing. Therefore, this work has demonstrated the potential of using BC/FeOCl nanocomposites for the mitigation of sulphonamide pollution in surface water, which is a meaningful approach for environmental protection. Also, due to the possession of Fe^{2+}/Fe^{3+} cycles and abundant groups on biochar, the photocatalyst can be further explored for photo-Fenton and activation of persulphate for pollutant degradation.

The next chapter extends this study by investigating the heterogeneous activation of peroxymonosulphate (PMS) using the BC/FeOCl nanocomposite synthesised via wet impregnation and pyrolysis method and the ultrasonic-assisted mechanical mixing method. The chapter focuses on evaluating the effectiveness of this PMS-based advanced oxidation process for the degradation of SMX in aqueous systems under environmentally relevant conditions.

References

[1] R.F. Biocl, N. Room temperature synthesis and photocatalytic activity of magnetically recovarable Fe_3O_4/BiOCl nanocomposites and photocatalysts, J. Clust. Sci. 24 (2013) 1115–1126. https://doi.org/10.1007/s10876-013-0602-3.

[2] Y. Jiang, K. Mao, J. Ran, J. Su, G. Huang, X. Zheng, K. Zhang, H. Guan, C. Yang, H. Zhang, Carbon nitride-type polymers compounded with FeOCl to enhance the catalytic removal of antibiotics over a wide pH range: Performance and mechanism, J. Water Process Eng. 53 (2023) 103601. https://doi.org/10.1016/j.jwpe.2023.103601.

[3] H. Ohfuji, M. Yamamoto, EDS quantification of light elements using osmium surface coating, 110 (2015) 189–195. https://doi.org/10.2465/jmps.141126.

[4] M. Xie, B. Pan, N. Li, S. Zhao, J. Yan, S. Guo, Z. Chen, H. Wang, 2D graphene/FeOCl heterojunctions with enhanced tribology performance as a lubricant additive for liquid paraffin, RSC Adv. 12 (2022) 2759–2769. https://doi.org/10.1039/d1ra06650a.

[5] L. Wang, H. Yang, Y. Yang, Z. He, A novel scheme to improve the photo-Fenton performance of iron oxychloride by carbon: Three existent states and roles of carbon in the degradation of tetracycline in water, J. Colloid Interface Sci. 641 (2023) 916–928. https://doi.org/10.1016/j.jcis.2023.03.113.

[6] F. Luo, C. Wei, Preparation of heterogeneous Fenton catalyst with residual carbon separated from coal gasification slag as carrier, Energy sources, part A Recover. Util. Environ. Eff. 45 (2023) 1747–1758. https://doi.org/10.1080/15567036.2023.2179691.

[7] J. Zhao, G. Liu, Y. Zhang, J. Dong, Y. Wang, Y. Liu, H. Li, J. Xia, Physicochemical and engineering aspects fabrication of MoS_2/FeOCl composites as heterogeneous photo-fenton catalysts for the efficient degradation of water pollutants under visible light irradiation, Colloids Physicochem. Eng. Asp. 648 (2022) 129357. https://doi.org/10.1016/j.colsurfa.2022.129357.

[8] T. Yu, A. Xing, S. Wang, D. Zhao, S. Liang, Well-dispersed FeOCl nanosheets

as high-performance chloride ion battery cathode material, Euro. Chem. Soc. 7 (2022) 2454. https://doi.org/10.1002/slct.202202454.

[9] Y. Zeng, F. Wang, D. He, J. Li, H. Luo, X. Pan, Insight into iron oxychloride composite bone char for peroxymonosulphate activation: Mechanism of singlet oxygen evolution for selective degradation of organic pollutants, Chemosphere. 326 (2023) 138471. https://doi.org/10.1016/j.chemosphere.2023.138471.

[10] Z. Mo, Z. Tan, J. Liang, Z. Guan, X. Liao, J. Jian, H. Liu, Y. Li, W. Dai, S. Sun, Iron-rich sludge biochar triggers sodium percarbonate activation for robust sulphamethoxazole removal: Collaborative roles of reactive oxygen species and electron transfer, Chem. Eng. J. 457 (2023) 141150. https://doi.org/10.1016/j.cej.2022.141150.

[11] Y. Ding, S. Zuo, D. Li, Z. Guan, F. Yang, Regulating interlayer confinement FeOCl for accelerating polymerization of pollutants to reduce carbon emission in water purification, ACS Appl. Mater. Interfaces 15 (2023) 5058–5070. https://doi.org/10.1021/acsami.2c16396.

[12] J. Zhang, G. Zhang, Q. Ji, H. Lan, J. Qu, H. Liu, Carbon nanodot-modified FeOCl for photo-assisted Fenton reaction featuring synergistic in-situ H_2O_2 production and activation, Appl. Catal. B Environ. 266 (2020) 118665. https://doi.org/10.1016/j.apcatb.2020.118665.

[13] L. Zhang, Y. Gao, X. Ding, Z. Yu, L. Sun, High-performance photoelectrochemical cells based on a binuclear ruthenium catalyst for visible light-driven water oxidation, ChemSusChem. 7 (2014) 2801–2804. https://doi.org/10.1002/cssc.201402561.

[14] J. Gao, J. Xue, Q. Shen, T. Liu, X. Zhang, X. Liu, H. Jia, Q. Li, Y. Wu, A Promoted photocatalysis system trade-off between thermodynamic and kinetic via hierarchical distribution dual-defects for efficient H_2 evolution, Chem. Eng. J. 431 (2022) 133281. https://doi.org/10.1016/j.cej.2021.133281.

[15] S. Asadzadeh-Khaneghah, A. Habibi-Yangjeh, D. Seifzadeh, H. Chand, V. Krishnan, Visible-light-activated g-C_3N_4 nanosheet/carbon dot/FeOCl nanocomposites: Photodegradation of dye pollutants and tetracycline hydrochloride, Colloids Surfaces A Physicochem. Eng. Asp. 617 (2021) 126424.

https://doi.org/10.1016/j.colsurfa.2021.126424.

[16] M. Li, D. Xia, H. Xu, Z. Guan, D. Li, Iron oxychloride composite sludge-derived biochar for efficient activation of peroxymonosulphate to degrade organic pollutants in wastewater, J. Clean. Prod. 329 (2021) 129656. https://doi.org/10.1016/j.jclepro.2021.129656.

[17] P.J. Mafa, M.E. Malefane, F. Opoku, A. Sacko, A.O. Oladipo, S.L. Lebelo, D. Liu, J. Gui, B.B. Mamba, A.T. Kuvarega, Experimental and theoretical confirmation of CeFeCu trimetal oxide/Bi_2O_3 S-scheme heterojunction for boosted photocatalytic degradation of sulphamethoxazole and toxicity evaluation, J. Clean. Prod. 429 (2023) 139519. https://doi.org/10.1016/j.jclepro.2023.139519.

[18] B. Li, C. Wang, N. Li, C. Chen, Z. Zhu, X. Tang, Y. Cui, T. Liu, C. Kwashie, X. Wang, Partially oxidized mackinawite/biochar for photo-Fenton organic contaminant removal : Synergistically improve interfacial electron transfer, Environ. Pollut. 346 (2024) 123660. https://doi.org/10.1016/j.envpol.2024.123660.

[19] Y. Lu, Y. Cai, S. Zhang, L. Zhuang, B. Hu, S. Wang, J. Chen, X. Wang, Application of biochar-based photocatalysts for adsorption-(photo)degradation/reduction of environmental contaminants: mechanism, challenges and perspective, Biochar. 4 (2022) 45. https://doi.org/10.1007/s42773-022-00173-y.

[20] H. Li, C. Shan, B. Pan, Fe(III)-Doped g-C_3N_4 mediated peroxymonosulphate activation for selective degradation of phenolic compounds via high-valent Iron-oxo species, Environ. Sci. Technol. 52 (2018) 2197–2205. https://doi.org/10.1021/acs.est.7b05563.

[21] W. Song, J. Zhao, X. Xie, W. Liu, S. Liu, H. Chang, C. Wang, Novel BiOBr by compositing low-cost biochar for efficient ciprofloxacin removal: The synergy of adsorption and photocatalysis on the degradation kinetics and mechanism insight, RSC Adv. 11 (2021) 15369–15379. https://doi.org/10.1039/d1ra00941a.

[22] W. Zhu, F. Sun, R. Goei, Y. Zhou, Facile fabrication of RGO-WO_3 composites for effective visible light photocatalytic degradation of sulphamethoxazole, Appl.

Catal. B Environ. 207 (2017) 93–102. https://doi.org/10.1016/j.apcatb.2017.02.012.

[23] J. Dang, W. Pei, F. Hu, Z. Yu, S. Zhao, J. Hu, J. Liu, D. Zhang, Z. Jing, X. Lei, Photocatalytic degradation and toxicity analysis of sulphamethoxazole using TiO_2/BC, Toxics. 11 (2023) 818. https://doi.org/10.3390/toxics11100818.

[24] A. Simon, W. Price, L.D. Nghiem, Implications of membrane fouling toward the removal of the pharmaceutical sulphamethoxazole by nanofiltration processes, J. Zhejiang Univ. Sci. A 12 (2011) 575–582. https://doi.org/10.1631/jzus.A1000469.

[25] L.A. Tercero Espinoza, M. Neamţu, F.H. Frimmel, The effect of nitrate, Fe(III) and bicarbonate on the degradation of bisphenol A by simulated solar UV-irradiation, Water Res. 41 (2007) 4479–4487. https://doi.org/10.1016/j.watres.2007.06.060.

[26] R. Andreozzi, R. Marotta, N. Paxéus, Pharmaceuticals in STP effluents and their solar photodegradation in the aquatic environment, Chemosphere. 50 (2003) 1319–1330. https://doi.org/10.1016/S0045-6535(02)00769-5.

[27] H. Sheng, Q. Li, W. Ma, H. Ji, C. Chen, J. Zhao, Photocatalytic degradation of organic pollutants on surface anionised TiO_2: Common effect of anions for high hole-availability by water, Appl. Catal. B Environ. 138–139 (2013) 212–218. https://doi.org/10.1016/j.apcatb.2013.03.001.

[28] H.Y. Chen, O. Zahraa, M. Bouchy, Inhibition of the adsorption and photocatalytic degradation of an organic contaminant in an aqueous suspension of TiO_2 by inorganic ions, J. Photochem. Photobiol. A Chem. 108 (1997) 37–44. https://doi.org/10.1016/S1010-6030(96)04411-5.

[29] A.G. Trovó, R.F.P. Nogueira, A. Agüera, A.R. Fernandez-Alba, C. Sirtori, S. Malato, Degradation of sulphamethoxazole in water by solar photo-Fenton. Chemical and toxicological evaluation, Water Res. 43 (2009) 3922–3931. https://doi.org/10.1016/j.watres.2009.04.006.

[30] X. Gao, Q. Guo, G. Tang, W. Peng, Y. Luo, D. He, Effects of inorganic ions on the photocatalytic degradation of carbamazepine, J. Water Reuse Desalin. 9

(2019) 301–309. https://doi.org/10.2166/wrd.2019.001.

[31] E. Shang, Y. Li, J. Niu, Y. Zhou, T. Wang, J.C. Crittenden, Relative importance of humic and fulvic acid on ROS generation, dissolution, and toxicity of sulfide nanoparticles, Water Res. 124 (2017) 595–604. https://doi.org/10.1016/j.watres.2017.08.001.

[32] X.X. Peng, S. Gai, K. Cheng, F. Yang, Roles of humic substances redox activity on environmental remediation, J. Hazard. Mater. 435 (2022) 129070. https://doi.org/10.1016/j.jhazmat.2022.129070.

[33] E.T. Saka, Y. Çağlar, New Co(II) and Cu(II) Phthalocyanine Catalysts reinforced by long alkyl chains for the degradation of organic pollutants, Catal. Letters. 147 (2017) 1471–1477. https://doi.org/10.1007/s10562-017-2054-0.

[34] J.R. Kim, E. Kan, Heterogeneous photocatalytic degradation of sulphamethoxazole in water using a biochar-supported TiO_2 photocatalyst, J. Environ. Manage. 180 (2016) 94–101. https://doi.org/10.1016/j.jenvman.2016.05.016.

[35] S. Zeng, E. Kan, $FeCl_3$-activated biochar catalyst for heterogeneous Fenton oxidation of antibiotic sulphamethoxazole in water, Chemosphere. 306 (2022) 135554. https://doi.org/10.1016/j.chemosphere.2022.135554.

[36] X. Xie, S. Li, H. Zhang, Z. Wang, H. Huang, Promoting charge separation of biochar-based Zn-TiO_2/pBC in the presence of ZnO for efficient sulphamethoxazole photodegradation under visible light irradiation, Sci. Total Environ. 659 (2019) 529–539. https://doi.org/10.1016/j.scitotenv.2018.12.401.

[37] M.W. Zheng, S.J. Yang, Y.C. Pu, S.H. Liu, Mechanisms of biochar enhanced Cu_2O photocatalysts in the visible-light photodegradation of sulphamethoxazole, Chemosphere 307 (2022) 135984. https://doi.org/10.1016/j.chemosphere.2022.135984.

[38] H.K. Shon, S. Vigneswaran, S.A. Snyder, Effluent organic matter (EfOM) in wastewater: Constituents, effects, and treatment, Crit. Rev. Environ. Sci. Technol. 36 (2006) 327–374. https://doi.org/10.1080/10643380600580011.

[39] Y.Y. Choi, S.R. Baek, J.I. Kim, J.W. Choi, J. Hur, T.U. Lee, C.J. Park, B.J. Lee,

Characteristics and biodegradability of wastewater organic matter in municipal wastewater treatment plants collecting domestic wastewater and industrial discharge, Water (Switzerland). 9 (2017) 409. https://doi.org/10.3390/w9060409.

[40] M.E. Malefane, U. Feleni, A.T. Kuvarega, Cobalt (II/III) oxide and tungsten (VI) oxide p-n heterojunction photocatalyst for photodegradation of diclofenac sodium under visible light, J. Environ. Chem. Eng. 8 (2020) 103560. https://doi.org/10.1016/j.jece.2019.103560.

[41] T.I. Nkambule, R.W.M. Krause, J. Haarhoff, B.B. Mamba, A three step approach for removing organic matter from South African water sources and treatment plants, Phys. Chem. Earth. 50–52 (2012) 132–139. https://doi.org/10.1016/j.pce.2012.08.009.

[42] M. Sgroi, P. Roccaro, G. V Korshin, F.G.A. Vagliasindi, Monitoring the behavior of emerging contaminants in wastewater- impacted rivers based on the use of fluorescence excitation emission matrices (EEM), Environ. Sci. Technol.51 (2017) 4306-4316. https://doi.org/10.1021/acs.est.6b05785.

[43] Fundamentals, (n.d.). https://doi.org/10.1039/9781782620389-00001.

[44] O.A. Zelekew, H.H. Haitosa, L. He, H. Ma, J. Cai, Z. Wang, Y. nan Wu, Boosted visible light-induced photo-Fenton degradation of organic pollutants over a novel direct Z-scheme NH_2-MIL-125(Ti)@FeOCl heterojunction catalyst, Chemosphere. 365 (2024) 143347. https://doi.org/10.1016/j.chemosphere.2024.143347.

CHAPTER 5

DEGRADATION OF SULPHAMETHOXAZOLE USING PMS-ASSISTED BIOCHAR/FEOCL NANOCOMPOSITE

5.1 Introduction

Antibiotic contamination, particularly by sulphonamides such as sulphamethoxazole (SMX), remains challenging for conventional water treatment technologies. While advanced oxidation processes (AOPs) have demonstrated potential for degrading persistent pharmaceuticals, hydroxyl radical–based systems often exhibit reduced efficiency in complex water matrices. In contrast, SR-AOPs driven by peroxymonosulphate (PMS) activation offer greater stability and broader operational applicability. This chapter builds on earlier investigations of biochar-supported catalysts (**Chapter4**) by exploring SR-AOPs through the activation of PMS using a biochar/iron oxychloride (BC/FeOCl) nanocomposite prepared via wet impregnation and pyrolysis method, and an ultrasonic-assisted mechanical mixing method for the activation of PMS to degrade SMX in water under visible light irradiation. The synthesis procedures and physicochemical characterisation of the prepared materials are presented in **Sections 3.3.3.2, 3.3.3.3, and 3.4**, followed by an evaluation of their catalytic performance for SMX degradation in the presence of PMS in **Section 3.5.2**. By integrating the adsorption capacity and electron-transfer properties of biochar with the catalytic activity of FeOCl, this approach aimed to enhance PMS activation and improve SMX removal efficiency compared to conventional FeOCl systems.

5.2 Results and discussion

5.2.1 Morphological and microstructural characterisation

The morphology of the prepared materials was examined using FESEM and TEM/HR-TEM analyses (**Fig. 5.1**). FESEM was coupled with energy-dispersive X-ray spectroscopy (EDS) for qualitative chemical analysis (**Fig**. **5.2**). The SEM image of the WP-BC/FeOCl nanocomposite (**Fig. 5.1a**) reveals an irregular, highly textured surface composed of interconnected, plate-like, and elongated nanosprindles with no uniform orientation. These structures are densely aggregated, forming a compact structure

with visible pores and gaps between particles. The rough and heterogeneous morphology suggests intimate interfacial contact between FeOCl and the biochar matrix, which facilitates surface reactions and enhances mass transfer during photocatalytic processes [1]. **Fig. 5.2b** shows that the SEM image of the MM-BC/FeOCl nanocomposite is consists of aggregated, near-spherical particles lacking well-defined long-range order. The SEM and TEM images in the **Appendix (A3)** further reveal that these particles exhibit morphologies characteristic of FeOCl, whereas the biochar phase serves primarily as a supporting matrix rather than a dominant structural feature. In conjunction with the synthesis ratios and complementary structural analyses, this observation suggests that FeOCl constitutes the primary surface-exposed phase in both nanocomposites.

The TEM image of the WP-BC/FeOCl nanocomposite showed long rods that were scattered in different directions and aggregated (**Fig. 5.2c**). Further, high-resolution TEM (HRTEM) showed clear lattice fringes with an interplanar spacing of approximately 0.27 nm (**Fig. 5.2d**), which can be indexed to the (110) crystal plane of FeOCl. The presence of well-defined lattice fringes indicates good FeOCl phase crystallinity and confirms its incorporation within the biochar-supported composite [2]. Meanwhile, MM-BC/FeOCl (**Fig. 5.2e**) showed clustered and aggregated spherical particles, as observed in FESEM (**Fig. 5.2b**). The HR-TEM (**Fig. 5.2f**) further supported the formation of the spheres while revealing the lattice fringes characteristic of FeOCl. **Fig. 5.2f** shows that the observed interplanar spacing of approximately 1.10 nm for MM-BC/FeOCl matched well with the (010) reflection, suggesting partial exposure of the layered FeOCl structure [3]. In contrast, the WP-BC/FeOCl composite exhibited a lattice spacing of 0.27 nm **(Fig. 5.2d)**, consistent with the (110) plane of FeOCl in the XRD pattern [4]. The difference in lattice orientation indicates that the synthesis route influences the crystal growth direction and surface-exposed facets. Furthermore, the less distinct lattice fringes in MM-BC/FeOCl and the slight broadening of its XRD peaks (**Fig. 5.3a**) indicate smaller crystallite domains or mild structural disorder, likely introduced during the mechanical blending process. These variations may affect charge mobility and surface reactivity during catalytic processes [5]. The different methods resulted in the formation of differently shaped nanoparticles, which may result in different degradation efficiencies.

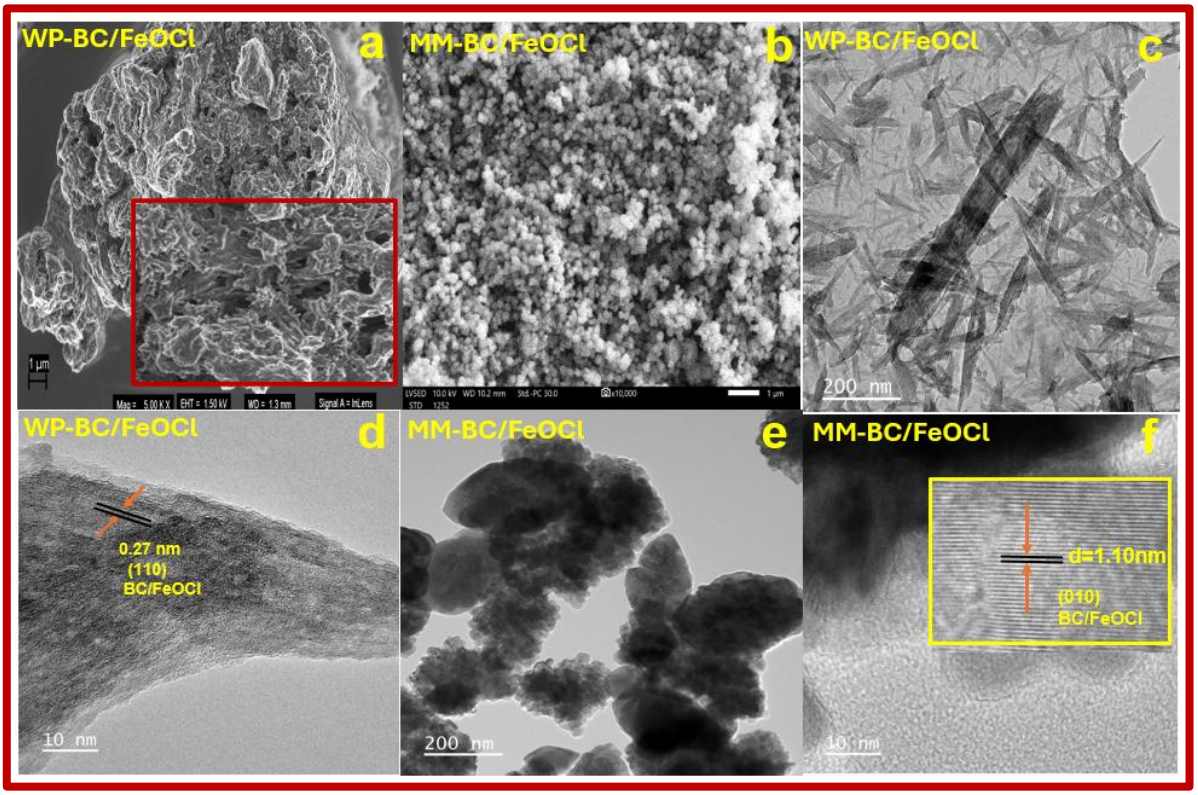

Figure 5.1 SEM micrographs of (a) WP-BC/FeOCl and (b) MM-BC/FeOCl, along with TEM and HR-TEM images of (c, d) WP-BC/FeOCl and (e, f) MM-BC/FeOCl.

The EDS analysis (**Fig. 5.2a**) qualitatively confirmed the presence and distribution of C, O, Cl, and Fe in the WP-BC/FeOCl composite. The corresponding elemental mapping images show a relatively uniform distribution of C, Fe, O, and Cl across the analysed region, indicating the homogeneous dispersion of the FeOCl phase incorporated with the biochar support. The Cu signals observed in the EDS spectrum are attributed to the copper TEM grid used as the sample support and do not originate from the catalyst itself. The EDS spectrum of the mechanically mixed (MM-BC/FeOCl) composite (**Fig. 5.2b**) confirms the presence of Fe, O, and Cl, indicating that FeOCl is the dominant phase. In MM-BC/FeOCl, the carbon signal could not be clearly resolved in the EDS spectrum and elemental mapping, likely due to the use of carbon coating and the low sensitivity of EDS towards light elements in the presence of FeOCl. This discrepancy could also be attributed to the inherently low X-ray emission efficiency and detection sensitivity for light elements such as carbon in SEM-EDS systems, where heavier elements such as Fe and Cl produce stronger X-ray signals that

dominate elemental mapping. SEM-EDS is known to have reduced capability for reliably detecting and mapping low atomic number elements due to their weak X-ray generation and absorption effects [6]. Furthermore, EDS elemental mapping of Fe, O, Cl, and C (**Fig. 5.2b**) confirmed the presence of these elements throughout the analyzed region, with no obvious elemental segregation observed at the microscale, suggesting a relatively homogeneous elemental

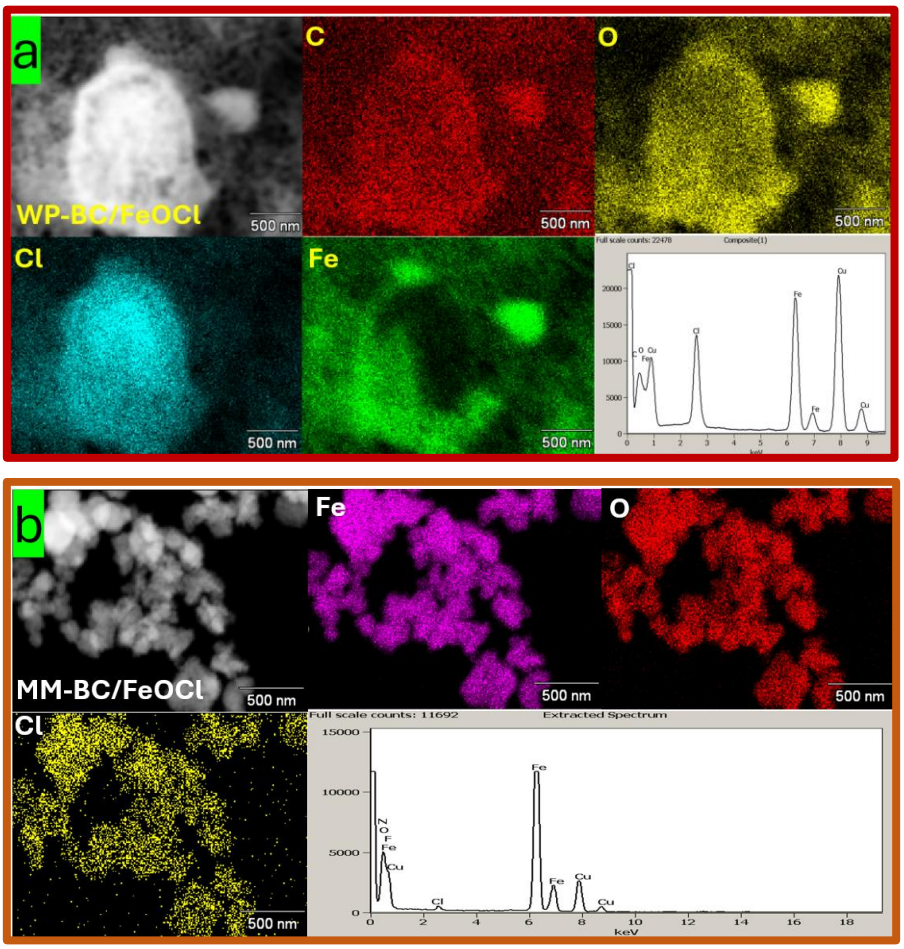

Figure 5.2 EDS elemental mapping images of (a) WP-BC/FeOCl and (b) MM-BC/FeOCl.

5.2.2 XRD and functional group analysis

The crystalline phases and structural purity of both WP-BC/FeOCl and MM-BC/FeOCl composites were examined using XRD, and the resulting patterns are shown in **Fig. 5.3a**. Distinct diffraction peaks for the BC/FeOCl composites were observed at 2θ values of approximately 10.8°, 26.3°, 35.0°, and 38.1°, which correspond to the (010), (110), (021), and (111) crystal planes, respectively. These patterns can be assigned to

the pure orthorhombic phase of FeOCl, confirming that the FeOCl phase remained intact after the formation of the composite in the **Appendix (A4)**. The XRD results for both WP-BC/FeOCl and MM-BC/FeOCl composites perfectly matched JCPDS no. 24-1005 and JCPDS no. 72-0619 [3,7]. Overall, the diffraction patterns and their 2θ values are similar between WP-BC/FeOCl and MM-BC/FeOCl, suggesting a successful synthesis of the crystalline BC/FeOCl nanocomposite. Nevertheless, the peaks recorded for the MM-BC/FeOCl material appeared to be slightly broader than those of the WP-BC/FeOCl material. Generally, peak broadening reflects smaller crystallite domains, lattice strain, or partial loss of structural order introduced during the grinding and ultrasonic-assisted blending steps [8]. In contrast, WP-BC/FeOCl exhibited sharper diffraction peaks, indicating a higher degree of crystallinity and a more uniform distribution of FeOCl particles on the biochar surface. The in situ growth of FeOCl on the carbon framework during synthesis likely enhanced interfacial coupling and directed the formation of well-ordered crystalline domains. These structural differences may influence the photocatalytic performance, as well-crystallised and uniformly distributed FeOCl domains facilitate more efficient charge separation and visible light absorption [9].

The functional groups present in the synthesised materials were matched using FTIR vibrational frequencies (**Fig. 5.3b)**. The stretching and vibration of the Fe-O bond appeared below 1000 cm^{-1} and shows two pronounced peaks in WP-BC/FeOCl at 682 and 866 cm^{-1} while this bond was observed only at 674 cm^{-1} in MM-BC/FeOCl. These characteristic peaks are attributed to FeOCl [10] Additionally, the Fe-Cl bond peak appears in the spectrum of both materials, and they are observed at 1612 and 1710 cm^{-1} for WP-BC/FeOCl and MM-BC/FeOCl, respectively, also coming from FeOCl [11]. The O-H stretching mode peak (2856 cm^{-1}) also appeared in both composites, indicating adsorbed H_2O-bonded molecules on the surface of the materials [12]. It was noted to be broad and more shifted to the right for MM-BC/FeOCl but sharp, intense, and more shifted to the left (3382 cm^{-1}) for WP-BC/FeOCl. Relatively, the peaks of WP-BC/FeOCl were more intense and pronounced than those of MM-BC/FeOCl. This could be because there is a stronger interfacial interaction and a higher availability of surface functional groups when the wet impregnation and pyrolysis (WP-BC/FeOCl) was used compared to the ultrasonic assisted mechanical mixing (MM-BC/FeOCl). The improved dispersion of FeOCl on the biochar matrix in WP-BC/FeOCl promotes

a more effective interaction between FeOCl and oxygen-containing and aromatic carbon functional groups, thereby enhancing the vibrational responses associated with O–H, aromatic carbon, Fe–Cl, and Fe–O bonds [13]. In contrast, the mechanically mixed MM-BC/FeOCl composite exhibited weaker interfacial contact, resulting in reduced vibrational intensity and less distinct FT-IR features. The existence of the aromatic carbon peaks (2924cm^{-1}) for WP-BC/FeOCl and 1642 cm^{-1} for MM-BC/FeOCl demonstrated the presence of biochar in both composites.

Fig. 5.3c shows the optical absorption characteristics of the synthesised WP-BC/FeOCl and MM-BC/FeOCl composites, as well as the pristine FeOCl obtained using UV–Vis DRS. Pristine FeOCl is a well-known visible light-responsive semiconductor, and the FeOCl sample (**Fig. 5.3c**) exhibited strong absorption across nearly the entire visible region (400–700 nm), with an absorption edge at approximately 639 nm. Both composites displayed broad absorption within the visible light region, confirming their potential for visible light-driven photocatalysis. However, there are clear differences in their absorption behaviour and edge positions. The WP-BC/FeOCl composite exhibited a red-shifted absorption edge at approximately 679 nm, whereas the mechanically mixed MM-BC/FeOCl composite exhibited a slightly black-shifted edge near 648 nm. The absorption shifts of both composites increased in the visible light region compared to the FeOCl catalyst, indicating enhanced visible light absorption, confirming the incorporation of biochar into the FeOCl matrix. The red shift in WP-BC/FeOCl indicates a stronger interaction between FeOCl and the biochar matrix formed during synthesis, resulting in improved electronic coupling and charge transfer efficiency. In contrast, the MM-BC/FeOCl composite, which was prepared through physical mixing, exhibited a relatively weaker interfacial contact, leading to less efficient visible light absorption.

The Tauc plots presented in the **Appendix (A5)** further support these optical band-gap trends, where the optical band gaps were determined to be 1.79, 1.78, and 1.59 eV for FeOCl, MM-BC/FeOCl, and WP-BC/FeOCl, respectively. The band gaps of both WP-BC/FeOCl and MM-BC/FeOCl were reduced after biochar incorporation compared to the pristine FeOCl. However, the WP-BC/FeOCl material was greatly reduced to 1.59 eV. The smaller band gap of the WP-BC/FeOCl composite indicates

that it requires less photon energy for electron excitation from the valence band (VB) to the conduction band (CB), implying more effective utilisation of visible light for photoinduced charge generation [14]. The narrowing of the band gap in WP-BC/FeOCl can be attributed to the strong Fe–O–C interfacial bonding and the partial hybridisation of Fe 3d and C 2p orbitals introduced by the biochar framework, which enhances delocalised electron mobility and extends light absorption into the visible range [15].

The Mott-Schottky plots indicated that all materials have a positive slope, which is characteristic of n-type semiconductors (**Fig. 5.3d** and **5.3e**). The values for MM-BC/FeOCl and WP-BC/FeOCl were 0.41 and 0.51 V Vs Ag/AgCl, respectively, which were then converted to NHE (using ENHE = EAg/AgCl + 0.2) to give 0.61 V vs NHE and 0.71 V vs NHE, respectively. The flat band potential of n-type semiconductors is located 0.1 V below their CB, such that the CB of MM-BC/FeOCl and WP-BC/FeOCl are 0.71 and 0.81 eV, respectively [3]. The VB positions obtained from the relationship of $E_{VB} = E_{CB} + Eg$ were 2.60 eV for both catalysts. This showed that while WP-BC/FeOCl resulted in a low energy band gap, the conduction band potential of MM-BC/FeOCl was 0.1 eV more negative than that of WP-BC/FeOCl. However, the conduction band potentials of both catalysts were still more positive than the redox potential required for superoxide radical formation from dissolved oxygen (E0 = -0.33 eV). This could be the reason for the minor contribution of this ROS, as its presence may be due to indirect processes. The equal VB positions of MM-BC/FeOCl and WP-BC/FeOCl demonstrate that $HO^{\bullet}$ could be formed by both materials, which excludes their involvement in the observed difference in degradation processes.

In our previous study [16], we showed that the wet impregnation and pyrolysis method increased the electronegativity of the WP-BC/FeOCl sample to enhance its performance compared to pristine FeOCl. However, comparisons between MM-BC/FeOCl and WP-BC/FeOCl showed that the band structure had little effect on the observed difference. Overall, the WP-BC/FeOCl composite exhibits superior optical characteristics compared with the mechanically mixed MM-BC/FeOCl counterpart, as evidenced by its red-shifted absorption edge and reduced band gap energy. These findings suggest that the wet impregnation and pyrolysis approach promotes more intimate heterojunction formation and better electronic contact between biochar and FeOCl, facilitating enhanced light harvesting and improved photoinduced charge

separation efficiency. Consequently, WP-BC/FeOCl is expected to exhibit higher photocatalytic activity under visible light than MM-BC/FeOCl.

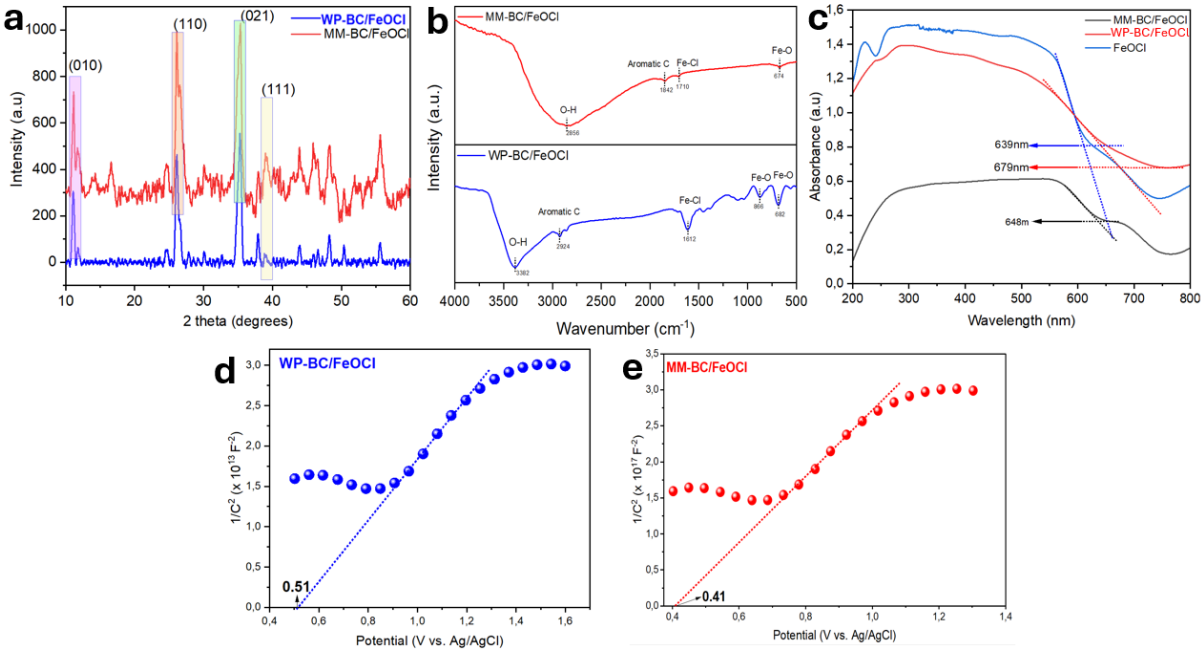

Figure 5.3 (a) XRD, (b) FTIR, and (c) UV-vis DRS for FeOCl, WP-BC/FeOCl, and MM-BC/FeOCl. Mott-Schottky curve of (d) WP-BC/FeOCl and (e) MM-BC/FeOCl.

XPS survey analysis was conducted to identify the elemental composition of the synthesised nanocomposites. As shown in **Fig. 5.4a**, the spectra of WP-BC/FeOCl and MM-BC/FeOCl exhibit distinct peaks corresponding to carbon (C 1s), oxygen (O 1s), chlorine (Cl 2p), and iron (Fe 2p), confirming the presence of these expected elements in the composites. No additional peaks were observed, indicating the absence of extraneous elements and the high purity of the prepared materials. The presence of C and O peaks is consistent with the incorporation of biochar, which typically contains oxygenated carbon structures, such as carboxyl, hydroxyl, and carbonyl groups [17], thus improving the separation of electrons and holes.

The high-resolution C 1s spectra (**Fig. 5.4b**) of both composites were deconvoluted into three components located at approximately 284.87 eV (C–C/C=C), 286.22 eV (C–O), and 288.76 eV (C=O), which are characteristic of biochar-derived carbon materials. In both samples, C–C/C=C is the dominant carbon species, confirming that the aromatic carbon framework of the biochar was also observed in the FT-IR (**Fig.**

5.3b). Minor binding energy shifts between MM-BC/FeOCl and WP-BC/FeOCl are observed, which are attributed to differences in electronic interaction between FeOCl and surface oxygen-containing carbon groups arising from the synthesis route, rather than changes in elemental composition. For example, the C–C/C=C (284.87 eV), C–O (286.22 eV), and C=O (288.76 eV) peaks for MM-BC/FeOCl shifted to a lower band energy (BE) compared to WP-BC/FeOCl. Despite these shifts, the relative intensity of the peaks — C–C/C=C > C–O > C=O — remained consistent across both samples, suggesting that the surface functional group distribution is similar in both catalysts. **Fig. 5.4c** depicts the O 1s spectra, which show peaks due to metal-oxygen (M-O) bond, C-O, and C=O occurring at high binding energies (BE) of 530.46, 531.96, and 533.70 eV in WP-BC/FeOCl compared to 529.98, 531.90, and 533.50 eV, respectively, in MM-BC/FeOCl. The slightly lower BE of the M–O component in MM-BC/FeOCl indicates a subtle change in the electronic environment of Fe–O bonds, likely due to synthesis-induced interfacial interactions with biochar. Based on peak areas, MM-BC/FeOCl displays a higher relative contribution of M–O, whereas WP-BC/FeOCl shows a higher fraction of C–O, reflecting differences in surface composition rather than bulk elemental ratios [18]. These interfacial variations may influence PMS activation and CT.

Fig. 5.4d shows the Cl 2p spectra deconvoluted into Cl $2p_{3/2}$ and Cl $2p_{1/2}$ components with distinct BE in the two materials. Peaks were observed at 198.22 and 200.16 eV in MM-BC/FeOCl, consistent with Fe–Cl bonding environments [19]. An additional feature at 202.13 eV might indicate the presence of an organic chlorine in a higher BE state, which may be associated with surface heterogeneity introduced during mechanical mixing [20]. In contrast, the WP-BC/FeOCl spectrum was deconvoluted into two peaks at 198.95 and 200.53 eV, both attributable to Fe–Cl bonds from FeOCl. The absence of higher-energy chlorine features suggests that the wet impregnation and pyrolysis synthesis method results in a more uniform chemical environment [[21]. However, the WP-BC/FeOCl peaks still appeared at higher BE values. This result suggests a slight increase in the electron binding energy of Cl atoms. This shift generally indicates stronger electronic interactions between chlorine and the surrounding lattice, which can arise from charge redistribution at the FeOCl–biochar interface [22]. The Fe 2p peak was deconvoluted to four peaks (**Fig. 5.4e**). In MM-BC/FeOCl, the peaks at BE of 709.95 and 723.53 eV emanate from Fe^{2+}, and those

at 711.01 and 724.95 eV show the existence of Fe^{3+} [23]. Meanwhile, in WP-BC/FeOCl, the Fe^{2+} peaks were observed at BE of 711.57 and 725.11 eV, while the Fe^{3+} peaks appeared at BE of 713.19 and 727.04 eV. WP-BC/FeOCl showed positively shifted peaks along with satellite features at 713.19 and 727.04 eV, indicating a more oxidised Fe environment and stronger Fe^{3+} character. These shifts suggest enhanced interfacial electronic interactions between FeOCl and biochar, which can influence the redox cycling of Fe species during PMS activation. Fe^{2+} plays a critical role in initiating PMS activation via one-electron transfer, generating sulphate radicals $SO_4^{\bullet-}$ [24].

In addition, valence band XPS (VB-XPS (**Fig. 5.4f**) shows the oxidation potential of the catalyst, where a high VB-XPS can be related to the catalyst's high oxidation potential [25]. Since the VB-XPS of WP-BC/FeOCl is slightly more positive than that of MM-BC/FeOCl, the WP-BC/FeOCl composite likely exhibits stronger interfacial contact between FeOCl and biochar, allowing the carbon component to influence the overall VB position more effectively. In contrast, MM-BC/FeOCl exhibits a slightly lower VB edge, suggesting weaker interfacial electronic interactions and less pronounced modification of the intrinsic VB structure of FeOCl. Therefore, the difference arises from the synthesis-dependent interfacial contact and highlights how the preparation route influences the electronic structure of the composites [26]. Therefore, the wet impregnation and pyrolysis method improves the oxidative capability of the WP-BC/FeOCl nanocomposite compared to MM-BC/FeOCl. This high oxidative potential could enhance ROS formation for enhanced photocatalytic degradation performance.

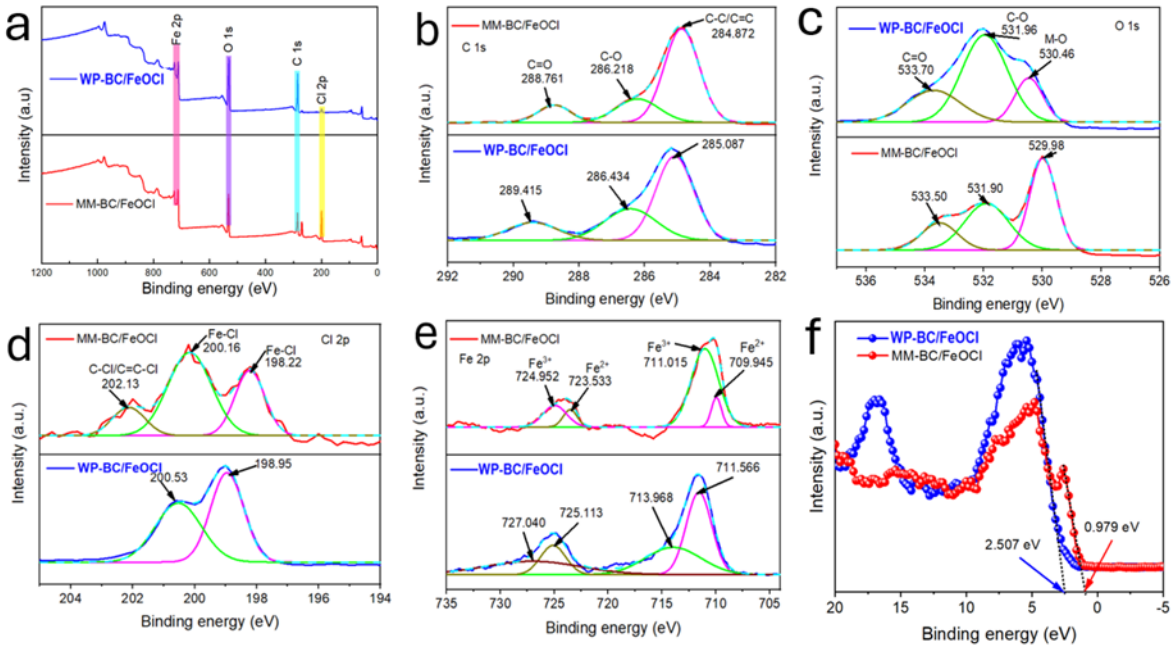

Figure 5.4 (a) XPS survey scan and high-resolution XPS of (b) C 1s, (c) O 1s, (d) Cl 2p, (e) Fe 2p, and (f) VB-XPS of WP-BC/FeOCl and MM-BC/FeOCl.

Tables A6 and **A7** in the **Appendix** section show the atomic weight compositions of WP-BC/FeOCl and MM-BC/FeOCl, respectively. Based on the XPS-derived atomic percentages, WP-BC/FeOCl exhibits a higher surface atomic concentration of Fe than MM-BC/FeOCl. The Fe weight ratio relative to C is 1:6 for MM-BC/FeOCl and 1:4 for WP-BC/FeOCl. While the Fe:C ratio is higher in WP-BC/FeOCl than in MM-BC/FeOCl, the overall ratios are higher than those of other high-performing Fe/C-based catalysts for PMS activation [27–29]. The O ratio is the highest in the MM-BC/FeOCl nanocomposite. Generally, MM-BC/FeOCl gave the highest amount of all atoms except Fe and Cl. This further supports the fact that the FeOCl content in WP-BC/FeOCl is higher than that in the MM-BC/FeOCl composite. The observed difference may be due to the potential loss of FeOCl by adhering to the mortar and pestle during mechanical mixing.

5.2.3 Sulphamethoxazole photocatalytic degradation

This study evaluated the performance of WP-BC/FeOCl and MM-BC/FeOCl photocatalysts in activating PMS under visible light to degrade SMX in spiked water samples. Several control experiments were conducted, including PMS alone, BC with PMS, FeOCl with PMS, and photocatalysis, and the results are shown in **Fig. 5 .5a**.

Before adding PMS and initiating visible light irradiation, the SMX solution and each catalyst were stirred in the dark for 20 min to reach adsorption-desorption equilibrium. During the initial dark period, negligible SMX removal was observed for PMS-only and FeOCl-containing systems, confirming minimal adsorption (>10%). In contrast, BC + PMS exhibited an even lower adsorption efficiency of approximately ~2%, indicating weak physical SMX adsorption on the BC surface. This limited adsorption slightly enhanced the initial degradation rate upon light irradiation but did not contribute to the effective activation of PMS. PMS alone under visible light resulted in limited SMX degradation (67.1%), indicating that direct PMS photolysis only marginally contributes to SMX removal. The BC + PMS system exhibited a degradation efficiency comparable to PMS alone (69.6%), within experimental error, demonstrating that pristine BC does not possess sufficient active sites to effectively activate PMS [30]. The slight enhancement in the initial degradation rate under light irradiation can be attributed to weak PMS adsorption on the biochar surface rather than catalytic activation.

In contrast, the FeOCl + PMS system exhibited a markedly higher SMX degradation efficiency (77.5%), confirming that FeOCl functions as an active PMS activator under visible light through iron-mediated redox reactions [31]. This highlights the essential role of Fe species in generating reactive oxygen species (ROS) for SMX degradation. When FeOCl was combined with biochar, the photocatalytic performance was clearly improved (90.1%). Both MM-BC/FeOCl + PMS and WP-BC/FeOCl + PMS exhibited enhanced SMX degradation compared with FeOCl + PMS alone, indicating that BC promotes catalyst dispersion and interfacial charge transfer. Notably, WP-BC/FeOCl + PMS achieved the highest SMX degradation efficiency of 94.9% within 120 min, significantly outperforming MM-BC/FeOCl + PMS (82.3%). This superior activity is attributed to the wet impregnation and pyrolysis synthesis method, which enables stronger interfacial coupling between FeOCl and biochar, increased surface-exposed Fe active sites, and more efficient PMS activation under visible light. Overall, these results demonstrate that while biochar alone is catalytically inactive towards PMS activation, its integration with FeOCl, particularly through wet impregnation and pyrolysis synthesis, substantially enhances photocatalytic efficiency by improving active site accessibility and charge separation.

The apparent first-order rate constants were determined and demonstrated that WP-BC/FeOCl + PMS gave the highest degradation efficiency and the highest rate constant, as shown in **Fig. 5.5b**. The rate constants for PMS only, BC + PMS, FeOCl + PMS, MM-BC/FeOCl + PMS, WP-BC/FeOCl, and WP-BC/FeOCl + PMS were 0.00864 min^{-1}, 0.00922 min^{-1}, 0.0117 min^{-1}, 0.0129 min^{-1}, 0.0135 min^{-1}, and 0.0139 min^{-1}, respectively. The enhanced activity of the FeOCl-containing systems demonstrates that surface-exposed Fe sites act as the primary active centres for PMS activation, consistent with iron-mediated redox reactions [32]. Comparing the catalytic performance of WP-BC/FeOCl + PMS and MM-BC/FeOCl, XPS analysis (**Fig. 5.4e**) revealed that WP-BC/FeOCl possesses a higher surface Fe atomic percentage and a larger Fe^{2+}/Fe^{3+} ratio than MM-BC/FeOCl. These Fe^{2+} species are widely recognised as the dominant active sites for PMS activation, as Fe^{2+} reacts directly with PMS to generate sulphate and hydroxyl radicals while being oxidised to Fe^{3+}.

Although WP-BC/FeOCl exhibits slightly higher Fe exposure than MM-BC/FeOCl, the difference in catalytic performance between photocatalysis alone and PMS-assisted photocatalysis remains relatively small (~4.8% after 120 min). This limited enhancement can be attributed to the already high intrinsic activity of FeOCl under visible light, where photogenerated charge carriers substantially contribute to SMX degradation. Under these conditions, PMS acts mainly as an auxiliary oxidant rather than the dominant reaction pathway, leading to only a modest increase in the overall degradation efficiency. Furthermore, the high FeOCl loading in both composites may restrict PMS accessibility to some surface Fe^{2+} sites due to partial site occupation or diffusion limitations, thereby limiting the additional benefit of PMS introduction. Similar behaviour has been reported for iron-based photocatalysts operating under strong light-driven oxidation conditions. [33]. The UV–vis spectral evolution of SMX degradation over WP-BC/FeOCl + PMS + visible light (**Fig. 5.5c**) shows a rapid decrease in the characteristic SMX absorption band within the first 20 min, indicating the destruction of SMX chromophoric functional groups rather than complete mineralisation. In 120 min, the results showed that some SMX by-products existed as the graph was not flat. This observation suggests the presence of intermediate by-products, which is consistent with the incomplete (<100%) SMX removal observed in the degradation experiments.

5.3 Key reaction parameters

5.3.1 Sulphamethoxazole, PMS, and photocatalyst dosage

To evaluate the photocatalytic performance of WP-BC/FeOCl as the optimal composite in the presence of PMS under visible light irradiation, the degradation behaviour of SMX was investigated at initial concentrations ranging from 5 to 20 ppm. Experiments were conducted using WP-BC/FeOCl as the catalyst, PMS as the oxidant, and visible light as the energy source. As shown in **Fig. 5.5d**, the SMX removal efficiency initially improved with increasing concentration, rising from 79.2% at 5 ppm to 95.1% at 10 ppm. However, further increases in SMX concentration led to a decline in degradation performance, with efficiencies dropping to 78.2% at 15 ppm and 75.6% at 15 and 20 ppm, respectively. This reduction is attributed to the saturation of active sites by excess SMX molecules, which not only prolongs the degradation process but also hinders the catalyst's ability to absorb light [34]. Diminished light penetration reduces the generation of reactive oxygen species (ROS), thereby slowing the reaction rate. These findings suggest that optimal SMX removal occurs at moderate concentrations, where sufficient active sites and light absorption are maintained for efficient ROS production.

The influence of PMS concentration on the degradation efficiency of SMX using the WP-BC/FeOCl under visible light irradiation was systematically evaluated, as shown in **Fig. 5.5e**. The influence of the investigated PMS concentration ranged from 0.1 to 0.8 mM. Notably, increasing the PMS concentration from 0.1 to 0.6 mM enhanced the degradation rate from 78.2% to 95.1%, attributed to the elevated generation of ROS, such as sulphate radicals ($SO_4^{-\bullet}$) and hydroxyl radicals ($HO^{\bullet}$), which are primarily responsible for SMX oxidation. However, further increasing the PMS concentration to 0.8 mM resulted in a marked reduction in degradation efficiency (76.2%). This phenomenon is likely due to the self-scavenging effect of excess PMS, wherein the surplus oxidant reacts with the generated ROS, forming less reactive species such as $SO_5^{-\bullet}$ shown in **Eqs. 5.1** and **5.2** [35]. These side reactions illustrate the competitive consumption of potent radicals by PMS, ultimately limiting the availability of ROS for SMX degradation.

$$SO_4^{-\bullet} + HSO_5^- \rightarrow HSO_4^- + SO_5^{-\bullet} \quad 5.1$$

$$HO^{\bullet} + HSO_5^- \rightarrow SO_5^{-\bullet} + H_2O \quad 5.2$$

The influence of different photocatalyst dosages on the degradation of SMX (10 ppm) in the presence of 0.6 mM PMS under visible light irradiation was then systematically investigated in the range of 0.1–0.8 g/L. Increasing the concentration of WP-BC/FeOCl from 0.1 to 0.2 g/L resulted in a significant increase in SMX degradation efficiency from 82.6% to 95.1% (**Fig. 5.5f**). This improvement is attributed to the greater availability of active sites on the catalyst surface, which facilitates PMS activation and promotes ROS generation. These ROS are responsible for the oxidative degradation of SMX. Additionally, the increased surface area enhances SMX adsorption, allowing a more effective interaction with the generated ROS. However, further increasing the catalyst dosage from 0.4 to 0.8 g/L led to a decline in degradation efficiency (76.1%–73.3%). This reduction is likely due to excessive catalyst loading, which causes light scattering and opacity in the reaction medium, limiting light penetration and reducing the photoactivation of the catalyst [36]. Consequently, ROS generation is suppressed, resulting in lower photocatalytic performance. These findings highlight the importance of optimising catalyst dosage to balance active site availability and light utilisation for efficient SMX removal.

5.3.2 Effect of solution pH

Sulphate radicals ($SO_4^{\bullet-}$) maintain high oxidative stability over a broad pH range, making PMS an effective oxidant under diverse environmental conditions [37]. Nevertheless, the pH of the solution remains a critical parameter in PMS-assisted photocatalytic systems because it influences PMS speciation, catalyst surface charge, and pollutant speciation. Since photocatalytic reactions predominantly occur at or near the catalyst surface, the interplay between these factors directly affects the degradation efficiency. SMX degradation was evaluated over a pH range of 5–10, which is representative of natural waters and wastewater effluents, to assess the influence of pH [38–40]. As shown in **Fig. 5.5g**, the highest SMX degradation efficiency was achieved under mildly acidic conditions, with a pH of 6.5 yielding approximately 95.0% removal. When the pH was increased to slightly alkaline values (pH 7.5 and 8.5), a moderate decline in degradation efficiency of 83.6% and 82.1%, respectively, was observed; however, the overall removal remained high, indicating that the catalyst retains activity across a broad pH window. In contrast, a pronounced decrease in performance was recorded at pH 10, with only 56.2% degradation after 120 min. To

elucidate the observed pH-dependent behaviour, the surface charge properties of WP-BC/FeOCl were investigated by determining its point of zero charge (P_{ZC}). As shown in **Fig. 5.5h**, the P_{ZC} of the composite was approximately pH 1.5, indicating that the catalyst surface was negatively charged throughout the pH range investigated. This suggests that the electrostatic attraction between the catalyst surface and anionic PMS species is not the primary factor governing PMS activation in this system.

Instead, the enhanced degradation observed at pH 6.5 is attributed to more favourable redox interactions between surface Fe^{2+} sites and PMS, which promote efficient radical generation [41]. Although SMX exists predominantly in its anionic form above pH 5.7 [25], degradation efficiency does not strictly follow SMX speciation, indicating that adsorption is not the rate-limiting step. Rather, the degradation process is dominated by radical-mediated oxidation, with surface-bound Fe^{2+} species playing a central role. Under highly alkaline conditions (pH 10), PMS predominantly exists as SO_5^{2-} due to deprotonation of HSO_5^- (pKa_{a2} ~ 9.5), which is less reactive towards radical formation. This shift in PMS speciation suppresses reactive oxygen species generation, leading to the significantly reduced degradation efficiency observed. Therefore, the superior performance of the WP-BC/FeOCl/PMS/Vis system under mildly acidic to neutral conditions can be attributed to the efficient activation of PMS in its HSO_5^- form via surface Fe^{2+}/Fe^{3+} redox cycling

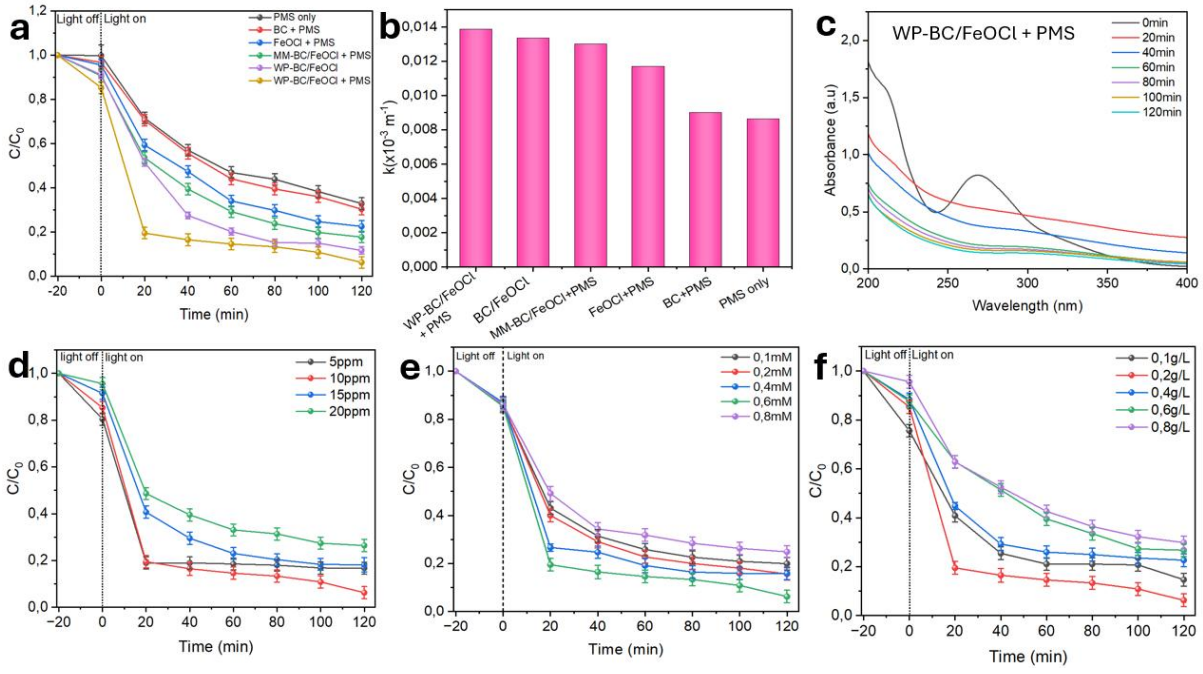

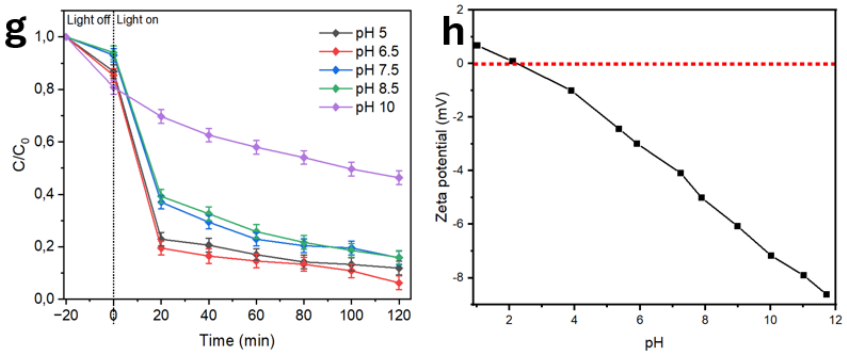

Figure 5.5 SMX degradation under (a) different catalyst compositions and (b) corresponding rate constants. (c) Variation in SMX absorbance in the WP-BC/FeOCl/PMS/Vis system. Optimisation of (d) initial SMX concentration, (e) PMS concentration, (f) catalyst dosage, (g) pH, and (h) catalyst charge in the WP-BC/FeOCl system under PMS and visible light activation.

5.3.3 Effect of coexisting inorganic ions and natural organic matter

Various anions and natural organic matter (NOM) commonly present in water can influence the activation of PMS. Therefore, the influence of humic acid (HA) as a representative NOM, and chloride (Cl^-), bicarbonate (HCO_3^-), nitrate (NO_3^-) ions, on PMS activation was investigated, and the results are depicted in **Fig. 5.6a**. When 10 mM of HCO_3^-, HA, NO_3^-, and Cl^- was added to the WP-BC/FeOCl/PMS/vis light system, the degradation efficiencies of SMX were 43.4%, 77.6%, 82.9%, and 84.7%, respectively. The addition of HCO_3^-/CO_3^{2-} largely reduces the activity of AOPs by generating free radicals with a decreased redox potential. Specifically, HCO_3^- could easily react with $SO_4^{-\bullet}$ and $HO^\bullet$ to form less reactive carbonate radicals, according to **Eqs. 5.3** and **5.4**. In addition, HCO_3^- tends to raise the pH of the solution more than other coexisting anions, and the removal of SMX decreases at higher pH [42]. Anions like NO_3^- and Cl^- also exhibit inhibitory effects on the degradation efficiency of SMX in the following order: $Cl^- < NO_3^- < HCO_3^-$. This suggests that the pH variations caused by these anions are not the primary factor. Instead, the inhibition may be attributed to the competition between the anions and SMX for active sites and their radical quenching effects. The minor inhibition by Cl^- and NO_3^- is due to their scavenging effect on the highly oxidative species responsible for SMX degradation·[43]. Specifically,NO_3^- anions react with $SO_4^{-\bullet}$ and $HO^\bullet$ ROS with a higher redox potential to produce $NO_3^\bullet$ radicals (**Eqs. 5.5** and **5.6**) with lower redox potential (2.0 to 2.2 V). When

Cl^- is added to the reaction, it reacts with both $SO_4^{\bullet-}$ and $HO^\bullet$ radicals to produce less oxidising chlorine radicals such as $Cl^\bullet$, $Cl_2^{\bullet-}$, and $HOCl^{\bullet-}$ (**Eqs. 5.7 – 5.9)**. For example, $Cl^\bullet$ (2.4 V) and $Cl_2^{\bullet-}$ (2.1 V) have lower redox potentials compared to $SO_4^{\bullet-}$ (2.5-3.1 V) and $HO^\bullet$ (2.8 V) [35]. The inhibitory effect of HA, which reduced the SMX degradation efficiency from 95.1% to 77.6%, may be due to several factors. This could be due to HA and SMX competing for the active sites on the surface of the WP-BC/FeOCl catalyst [44,45]. Second, HA can swiftly scavenge $SO_4^{\bullet-}$ with a rate constant of 2.35 x 10^7 M^{-1} s^{-1}, which further diminishes the availability of these reactive species for pollutant oxidation. However, the dominant reactive oxygen species in this system are singlet oxygen, which maintains the high SMX degradation efficiency.

$$SO_4^{\bullet-} + HCO_3^- \rightarrow CO_3^{\bullet-} + SO_4^{2-} + H^+ \quad 5.3$$

$$HO^\bullet + HCO_3^- \rightarrow CO_3^{\bullet-} + H_2O \quad 5.4$$

$$SO_4^{\bullet-} + NO_3^- \rightarrow NO_3^\bullet + SO_4^{2-} \quad 5.5$$

$$HO^\bullet + NO_3^- \rightarrow NO_3^\bullet + HO^- \quad 5.6$$

$$SO_4^{\bullet-} + Cl^- \rightarrow Cl^\bullet + SO_4^{2-} \quad 5.7$$

$$Cl^\bullet + Cl^- \rightarrow Cl_2^{\bullet-} + SO_4^{2-} \quad 5.8$$

$$HO^\bullet + Cl^- \rightarrow HOCl^{\bullet-} \quad 5.9$$

5.3.4 Identification of reactive species

To study the role of ROS in PMS-assisted SMX decomposition, different scavengers, including ethylenediaminetetraacetic acid (EDTA), p-benzoquinone (p-BQ), tert-butyl alcohol (TBA), methanol, and furfuryl (FFA) alcohol, were used to trap h^+, $O_2^{\bullet-}$, $HO^\bullet$, $SO_4^{\bullet-}$, and $^1O_2$, respectively. **Fig. 5.6b** shows the inhibition of SMX degradation efficiency in the following order: FFA > methanol > EDTA > TBA > p-BQ. This implies that $^1O_2$ is the main ROS responsible for SMX degradation. The SMX degradation efficiency decreased from 95.1% in the absence of any scavenger to 33.6% when FFA was introduced into the reaction. PMS activation using carbon-supported catalysts often results in the formation of $^1O_2$. Methanol is known to react rapidly with both ($SO_4^{\bullet-}$) and ($HO^\bullet$), but it exhibits a significantly higher rate constant with $HO^\bullet$ (k ~ 9.7 x 10^8 M^{-1} s^{-1}) than with $SO_4^{\bullet-}$ (k ~ 3.2 x 10^6 M^{-1} s^{-1}) [46]. Therefore, methanol preferentially quenches $HO^\bullet$, while still partially inhibiting $SO_4^{\bullet-}$. In this study, the addition of methanol

reduced SMX degradation efficiency to 69.2%, which was a more pronounced inhibition than that observed with TBA, a selective scavenger for $HO^{\bullet}$. This greater suppression suggests that $SO_4^{-\bullet}$ contributed more significantly to SMX degradation than $HO^{\bullet}$, as methanol's dual scavenging effect impacted both radicals, while TBA primarily targeted $HO^{\bullet}$. Meanwhile, h^+ and $O_2^{\bullet-}$ also had some contribution effects as the introduction of EDTA and p-BQ slightly decreased the degradation of SMX. Considering the VB-XPS, WP-BC/FeOCl showed the most positive VB with a value above 2. Therefore, the holes in this catalyst possess sufficient oxidative potential to degrade SMX.

5.3.5 Sulphamethoxazole degradation in different water matrices

The PMS-assisted SMX degradation was conducted using WP-BC/FeOCl across different water sources (deionized water, tap water, wastewater effluent, and river water) to assess the environmental relevance of the treatment process. Among these matrices, SMX degradation efficiency declined in all cases, with river water exhibiting the most pronounced in removal efficiency (**Fig. 5.6c**). The decline in SMX degradation in the environmental water matrices compared to DI water arises from the complex matrix of the environmental samples. Furthermore, the different water matrices show variable interferences with SMX removal, largely due to differences in quality parameters [77]. **Table 5.1** shows the physicochemical properties of the water matrices affecting the degradation of SMX. River water exhibited the highest conductivity (744 µS/cm) and TDS (388 µg/L) among the environmental samples, indicating a high concentration of dissolved ions. These ions, particularly inorganic anions such as bicarbonate, chloride, and nitrate, can act as radical scavengers, competing with SMX for reactive oxygen species (ROS) generated during PMS activation, as shown in **Fig. 5.6a**. Additionally, river water showed elevated salinity (0.39 psu), which further contributes to ionic strength and radical quenching. Furthermore, bicarbonate anions are known to increase the pH of the solution, and the pH of river water is 7.95, confirming that the ionic load is higher, which likely suppresses the formation and activity of sulphate and hydroxyl radicals. In this work, $SO_4^{\bullet-}$ radicals play a role in SMX removal. The lower dissolved oxygen (2.90 µg/L) compared with effluent WW (**3**.09 µg/L) may also limit oxidative degradation pathways. Therefore, the reduced SMX removal in river water is primarily due to its higher ionic

content and conductivity, which interfere with PMS activation and radical-mediated degradation [47] These findings highlight the importance of matrix composition when applying advanced oxidation processes in real-world water treatment scenarios.

The apparent rate constants (**Fig. 5.6d**) demonstrate that the degradation occurred faster in DI water, and the order can be summarised as 0.01645 min^{-1} > 0.01006 min^{-1} > 0.00915 min^{-1} > 0.00714 min^{-1} for SMX degradation in DI, tap, wastewater effluent, and river water, respectively. To confirm the degradation of SMX in the different water matrices, UV_{254} was used to measure the TOC removal in the different water matrices (**Fig. 5.6e**). In all water types, the WP-BC/FeOCl/PMS/Vis system achieved lower UV_{254} removal than the WP-BC/FeOCl/Vis system alone. This indicates that while PMS activation enhances SMX degradation, it does not necessarily improve mineralisation efficiency under the tested conditions. The reduced UV_{254} removal in the PMS-assisted system may be attributed to the composite's non-optimal Fe loading. Although the Fe content was optimised for SMX degradation, excessive Fe can lead to radical self-quenching or non-productive, PMS decomposition, limiting the formation of reactive oxygen species (ROS) required for complete mineralisation [48]. In contrast, the photocatalytic system (without PMS) may favour direct photodegradation pathways that more effectively break down aromatic structures contributing to UV_{254} absorbance. Another reason could be the poor activity of the main ROS ($^1O_2$) towards efficient mineralisation of the formed intermediate by-products. Since $^1O_2$ ROS did not play a significant role during photocatalysis, the h^+ and $HO^\bullet$ (predominant reactive species in photocatalysis) have better degradation efficiency for both SMX and the formed intermediates, resulting in high UV_{254} removal [16].

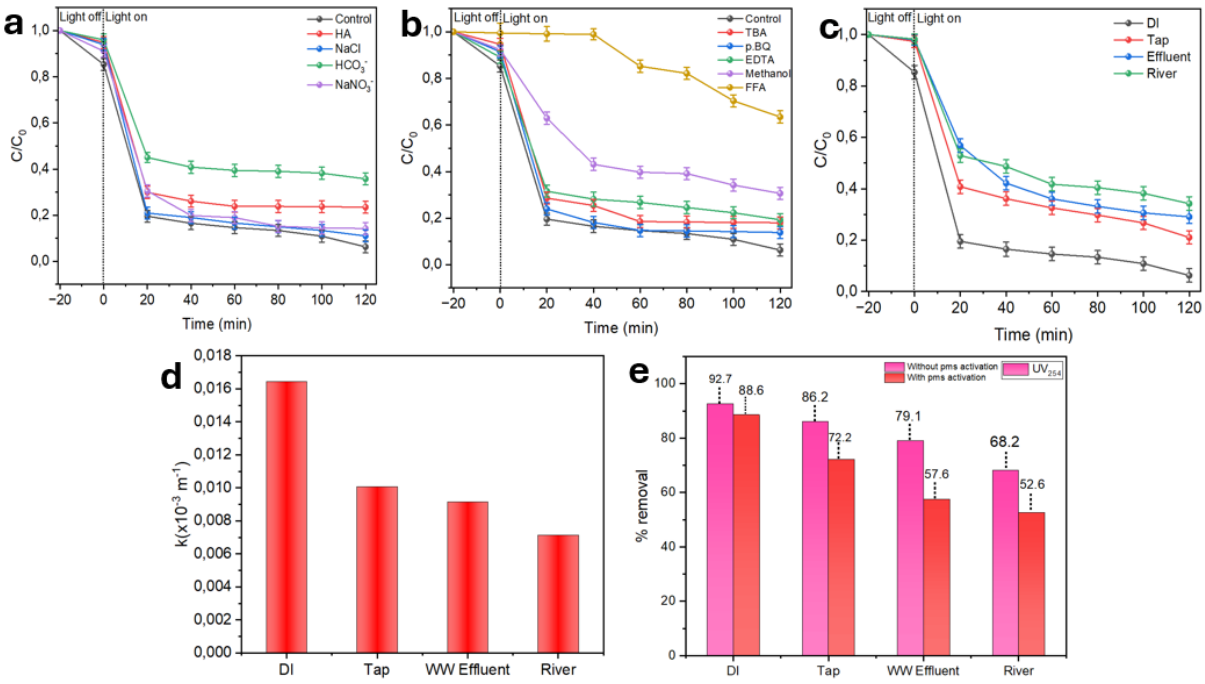

Figure 5.6 WP-BC/FeOCl + PMS analysis of (a) Effects of humic acid + coexisting anions, (b) radical trapping experiments, (c) Effect of different water matrix, (d) corresponding rate constants, and (e) UV254 removal of WP-BC/FeOCl during SMX degradation with and without PMS.

Table 5.1: Physicochemical properties of water matrices used for the effectiveness of the WP-BC/FeOCl/PMS/Vis system over SMX degradation.

Parameter	**Tap water**	**WW Effluent**	**River water**
pH	6.86	7.88	7.95
DO (ug/L)	1.66	3.09	2.90
Conductivity (us/cm)	251	677.00	744.00
TDS (ug/L)	127.00	373.00	388.00
Salinity (psu)	0.12	0.37	0.39

The degree of SMX mineralisation using the WP-BC/FeOCl/PMS/Vis was analysed using 3D-fluorescence excitation-emission matrix (FEEM) across all four water matrices (**Fig. 5.7**). SMX displayed five distinct fluorescence components at 0 min

(before visible light exposure). These were identified as less aromatic humic-like, more aromatic humic-like, marine-like, tyrosine-like, and protein-like substances, each characterised by specific excitation–emission peaks at 260/380–460, 320–360/420–460, 290–310/370–410, 260/280, and 250–300/410–355 nm, respectively, in the **Appendix** (**A9**) [49]. SMX degradation in the different water matrices was evidenced by variations in fluorescence intensity when exposed to visible light, leading to the generation of by-products with distinct excitation and emission regions after 120 min. **Fig. 5.7a** depicts the intense SMX peak with greyish, red, yellow, and lime colours from the core in respective order which is centred at EM wavelengths of 300–400 nm and EX wavelengths of 250–300 nm. After 60 min, the matrix displayed faint colours which further declined in 120 min to demonstrate the destruction of SMX and intermediates. The colour intensity is minimal in DI water after 60 and 120 min (**Fig 5.7b-c**) compared with the 3D-FEEM in tap water (**Fig. 5.7d-f**), river water (**Fig. 5.7g-i**), and WW effluent (**Fig. 5.7j-l**). This supported the degradation results that SMX degradation efficiency is high in DI water. The FEEM images of the tap water closely mirror the trends observed in DI water. An intense SMX-related fluorescence band is present at 0 min and substantially attenuates by 60 min, with only a trace signal remaining at 120 min. The rapid loss of fluorescence in tap water likely reflects the low organic background and modest ionic strength, which minimise radical scavenging and light attenuation and permit efficient SMX adsorption and oxidation on the WP-BC/FeOCl surface. These observations are consistent with the kinetic data showing that most degradation occurs within the first hour of the reaction. River water FEEM images reveal a more complex pattern. Although the primary SMX band decreases over time, humic-like features and some redistributed fluorescence persist at 60–120 min. This behaviour is attributed to the elevated DOM and natural humic substances in the river matrix, which compete for reactive species (scavenging) and cause inner-filter attenuation of excitation/emission light. Consequently, obvious fluorescence removal is slower, and intermediate by-products with different EX/EM signatures are more evident than in tap or DI water. The wastewater effluent maps show the strongest and most persistent background fluorescence, with a reduced SMX band but a substantial residual signal even after 120 min. High DOM, colloidal material, and other constituents in effluent (i) provide alternative sinks for reactive oxygen species and (ii) shield SMX from direct photoreaction (inner-filter effect and light scattering). These

combined effects reduce the apparent degradation rate and lead to detectable transformation products with distinct excitation–emission regions. Accordingly, the effluent matrix demonstrates the greatest inhibition of complete mineralisation under the same conditions [50].

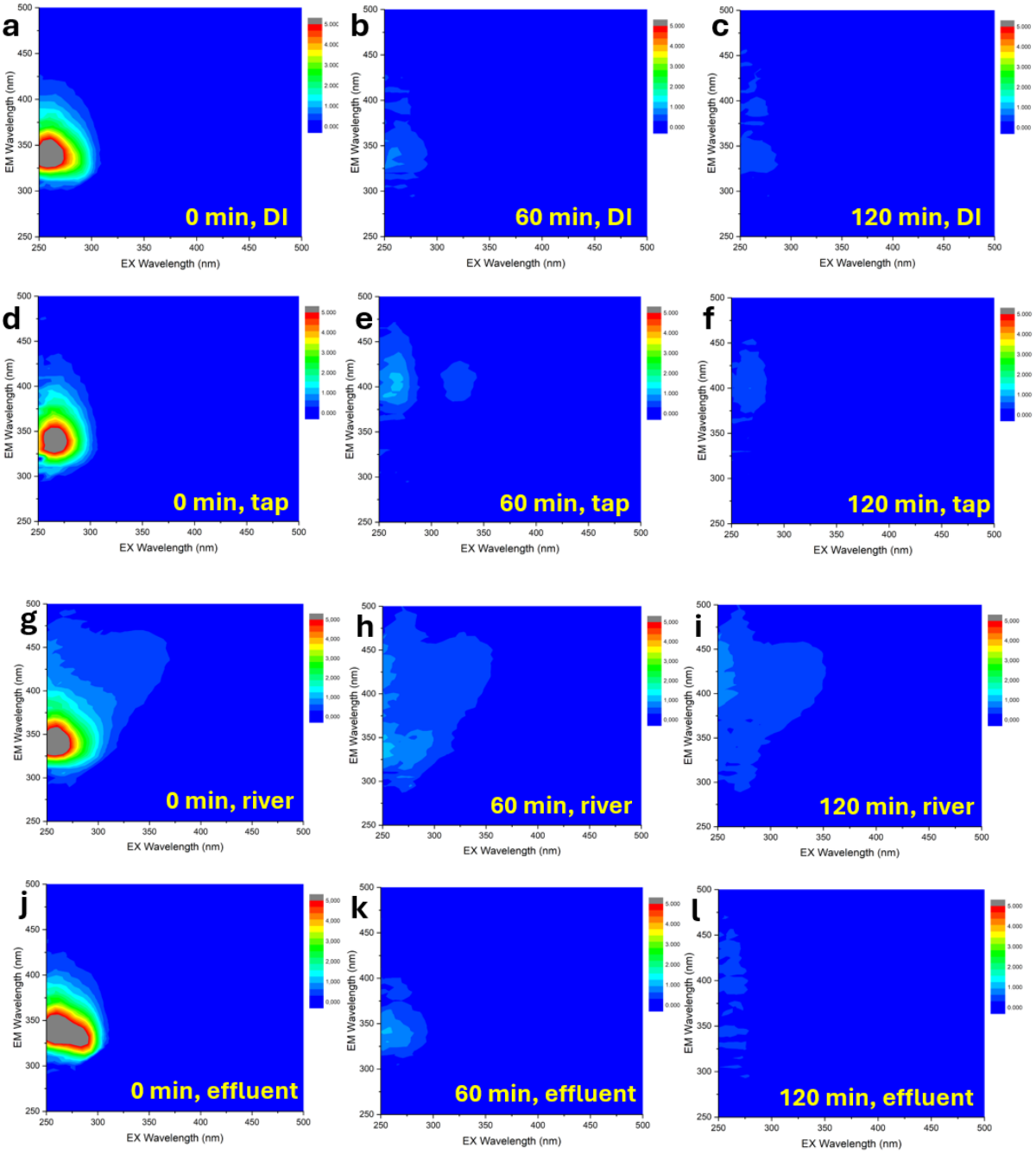

Figure 5.7 Sulphamethoxazole degradation 3D fluorescence spectra for DI water (a - c), tap water (e - f), river water (g - i), and wastewater effluent (j – l) before and after photodegradation using the WP-BC/FeOCl/PMS/Vis system.

5.3.6 Photo-Fenton-like sulphamethoxazole degradation

The versatility of WP-BC/FeOCl for H_2O_2-mediated degradation of SMX in a photo-Fenton-like reaction was further investigated. **Fig. 5.8a** demonstrates that the degradation of SMX by H_2O_2, WP-BC/FeOCl, and WP-BC/FeOCl + H_2O_2 had different degradation efficiencies of 47.0%, 83.7%, and 91.8%, respectively. The degradation of SMX by WP-BC/FeOCl in the presence of H_2O_2 started with a high initial rate in the first 20 min compared to H_2O_2 and photocatalysis alone, demonstrating the synergy of the catalyst and H_2O_2 in SMX degradation. The concentration of H_2O_2 was then varied from 1 to 7 mM (**Fig. 5.8b**), and the degradation efficiency increased from 1 to 3 mM and then decreased with increasing concentration between 4 and 7 mM. The increase in efficiency from 1 to 3 mM can be attributed to an increase in the number of oxidant molecules, which enhanced the generation of ROS. As the oxidant further increases, there is a lack of adequate active sites towards increased generation of ROS. Another reason may be the H_2O_2 self-scavenging effect, which results in H_2O_2 scavenging ROS (especially hydroxyl radicals), resulting in a low concentration of ROS that participate in SMX degradation [51]. **Fig. 5.8c** shows that SMX degradation efficiency increased from pH 3 to pH 5 under acidic conditions and then started decreasing when the pH approached alkaline conditions (pH 6.5 to 7.5). The results collate with previous reports that highlighted that photo-Fenton and Fenton-like degradation favour acidic conditions [52].

To assess the oxidant activation performance of WP-BC/FeOCl under visible light, SMX degradation was compared across three systems: photocatalysis alone, PMS activation, and H_2O_2 activation (**Fig. 5.8d**).

The reaction was monitored over 60 min, as most SMX degradation occurred within this period. After 20 min, the photo-Fenton-like reaction achieved the highest SMX removal (89%), followed by PMS (77%) and photocatalysis (51%). This finding indicates that both oxidants substantially enhanced the initial degradation rate compared to photocatalysis alone. Although the degradation efficiency of all systems continued to increase between 20 and 60 min, the rate of improvement slowed. After 60 min, the photo-Fenton-like reaction remained the most effective (90%), while PMS and photocatalysis reached 83% and 80%, respectively. The small difference between PMS and photocatalysis in 60 min suggests that PMS activation did not significantly

outperform photocatalysis under the tested conditions. This finding implies that while PMS and H_2O_2 both accelerate early-stage SMX degradation, H_2O_2 is more effective overall. The extended surface area of the FeOCl nanosheets by biochar incorporation, along with enhanced electron mobility facilitated by Fe–O and Fe–Cl linkages, encourages more efficient H_2O_2 decomposition and subsequent hydroxyl radical production. In addition, pollutant molecules can adsorb onto FeOCl surfaces, effectively minimising the diffusion path of hydroxyl radicals and thereby improving degradation efficiency [53]. The limited improvement with PMS may be due to suboptimal activation dynamics or radical quenching, despite the composite being optimised for SMX removal. The catalytic mechanism of H_2O_2 decomposition facilitated by Fe(II)/Fe(III) redox cycling within the FeOCl nanocatalyst can be illustrated by **Eqs. 5.10–4.12**.

$$Fe^{2+} + H_2O_2 \rightarrow Fe^{3+} + HO^{\bullet} + HO^{-} \quad 5.10$$

$$Fe^{3+} + H_2O_2 \rightarrow Fe^{2+} + HO_2^{\bullet} + H^{+} \quad 5.11$$

$$H_2O_2 + HO_2^{\bullet} \rightarrow HO^{\bullet} + O_2^{-\bullet} + H_2O \quad 5.12$$

The reason for the different behaviours was not investigated by experiments.

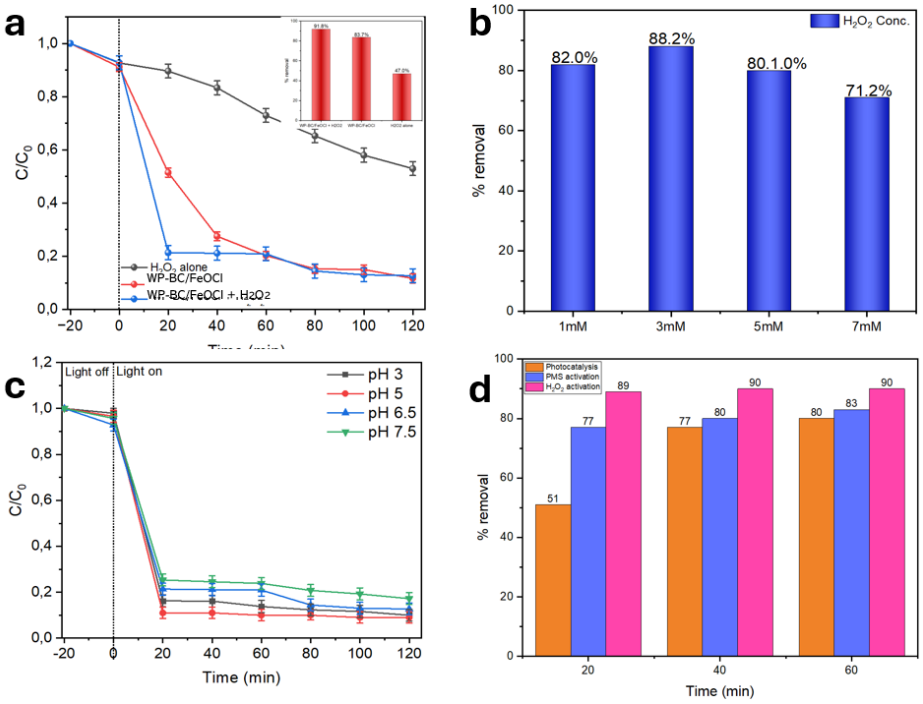

Figure 5.8 SMX degradation under (a) different catalyst compositions, (b) optimized H_2O_2 dosage, (c) varying pH conditions, and (d) comparison of photocatalysis, PMS activation, and Fenton-like reactions at an initial pH of 5.

5.3.7 Mechanism of SMX degradation by the WP-BC/FeOCl/PMS system

To investigate the charge transfer and redox behaviour of the catalysts, three electrochemical techniques were employed: Electrochemical Impedance Spectroscopy (EIS), Bode phase angle analysis, and cyclic voltammetry (CV). **Fig. 5.9a** presents the Bode phase angle plot, which reflects the capacitive behaviour and frequency response of the materials. Both WP-BC/FeOCl and MM-BC/FeOCl exhibit similar phase angle trends, indicating comparable capacitive characteristics and charge storage behaviour. The absence of a sharp phase drop suggests that both materials maintain stable interfacial charge dynamics across the frequency range. **Fig. 5.9b** shows the Nyquist plot from EIS, which evaluates the CTR and interfacial conductivity. Although the overall impedance profiles are similar, the inset reveals a slightly smaller semicircle diameter for WP-BC/FeOCl, indicating lower CTR and faster electron transfer kinetics compared to MM-BC/FeOCl. This subtle improvement in conductivity may contribute to enhanced catalytic activity, especially under visible light activation. **Fig. 5.9c** shows the CV curves, where WP-BC/FeOCl exhibits more pronounced redox peaks than MM-BC/FeOCl. This suggests a higher density of

electroactive sites and stronger redox capability, which is consistent with the higher oxidation potential observed in the XPS valence band analysis. The enhanced redox behaviour supports the superior performance of WP-BC/FeOCl in activating oxidants and facilitating SMX degradation. The high redox potential of WP-BC/FeOCl results in efficient ROS generation for efficient SMX degradation. Therefore, the obtained results were used to propose the degradation pathway of the WP-BC/FeOCl + PMS system, as shown in **Fig. 5.10**. BC has no effect on SMX degradation in the presence of PMS therefore, its involvement is believed to increase the surface area of the FeOCl, increasing the number of active sites for further SMX degradation.

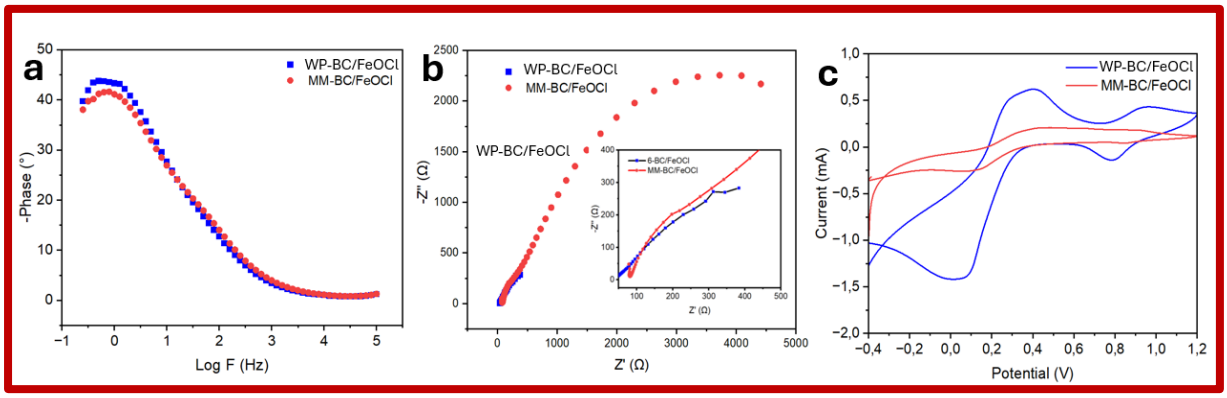

Figure 5.9 Electrochemical properties of the materials: (a) Bode phase angle, (b) EIS, and (c) CV. (d) Proposed mechanism of SMX degradation by WP-BC/FeOCl in the presence of PMS.

From the results of the optical properties measurements, radical-scavenging experiments and XPS characterisation, it can be inferred that SMX degradation through PMS activation by WP-BC/FeOCl under visible light proceeds via both radical and non-radical mechanisms. **Fig. 5.10** illustrates the proposed mechanism for SMX degradation under visible light. Upon illumination, FeOCl absorbs photons, excitation electrons from the VB to the CB, leaving behind photoinduced holes in the VB. To suppress electron–hole recombination, the excited electrons migrate to the conductive BC support, where they facilitate the reduction of molecular oxygen to generate superoxide radicals ($O_2^{\bullet -}$). Meanwhile, the holes (h^+) remaining in the VB can oxidise water or hydroxide ions to form hydroxyl radicals ($HO^{\bullet}$) or directly oxidise SMX molecules and their intermediates. However, radical scavenging experiments revealed

that $HO^{\bullet}$ and $O_2^{\bullet-}$ were not the dominant reactive species in this system. At the catalyst surface, redox cycling between Fe^{2+} and Fe^{3+} species plays a crucial role in peroxymonosulphate (PMS) activation. As shown in **Eq. 5.13**, Fe^{2+} reacts with HSO_5^- to yield Fe^{3+} and sulphate radicals ($SO_4^{\bullet-}$), while Fe^{3+} can be reduced back to Fe^{2+} through interaction with PMS, forming peroxymonosulphate radicals ($SO_5^{\bullet-}$) (**Eq. 5.14**). The generated $SO_4^{\bullet-}$ may further react with water or hydroxide ions to produce $HO^{\bullet}$ (**Eq. 5.15**). Additionally, $SO_5^{\bullet-}$ species can undergo self-decomposition or disproportionation, forming sulphate ions and molecular oxygen (**Eqs. 5.16** and **5.17**) [54].

Given the reversible Fe^{3+}/Fe^{2+} cycle and the abundance of PMS species ($HSO_5^{\bullet-}$) under near-neutral pH conditions, PMS primarily adsorbs on the catalyst surface and participates in electron transfer with Fe^{2+}, initiating a cascade of radical and nonradical reactions. Although both $SO_4^{\bullet-}$ and $HO^{\bullet}$ radicals contributed to SMX degradation, the major pathway was driven by the generation of singlet oxygen ($^1O_2$), which dominated the oxidation process. The high yield of $^1O_2$ is attributed to the self-decomposition of PMS and surface-mediated electron transfer processes accelerated under visible light, resulting in a predominantly nonradical oxidation mechanism (**Eqs. 5.17 – 5.19**) [55]. When these ROS are generated, they interact with surface-adsorbed SMX, resulting in the formation of degradation by-products. These by-products are further broken down into CO_2 and H_2O.

$$Fe^{2+} + HSO_5^- \rightarrow Fe^{3+} + SO_4^{\bullet-} + OH^- \quad 5.13$$

$$Fe^{3+} + HSO_5^- \rightarrow Fe^{2+} + SO_5^{\bullet-} + H^+ \quad 5.14$$

$$SO_4^{\bullet-} + OH^-/H_2O \rightarrow SO_4^{2-} + HO^{\bullet} \quad 5.15$$

$$SO_5^{\bullet-} + SO_5^{\bullet-} \rightarrow 2SO_4^{2-} + H^+ \quad 5.16$$

$$2SO_5^{\bullet-} \rightarrow 2SO_4^{\bullet-} + O_2 \quad 5.17$$

$$O_2 + e^- \quad 5.18$$

$$HSO_5^- + SO_5^{2-} \rightarrow HSO_4^- + SO_4^{2-} + {}^1O_2 \quad 5.19$$

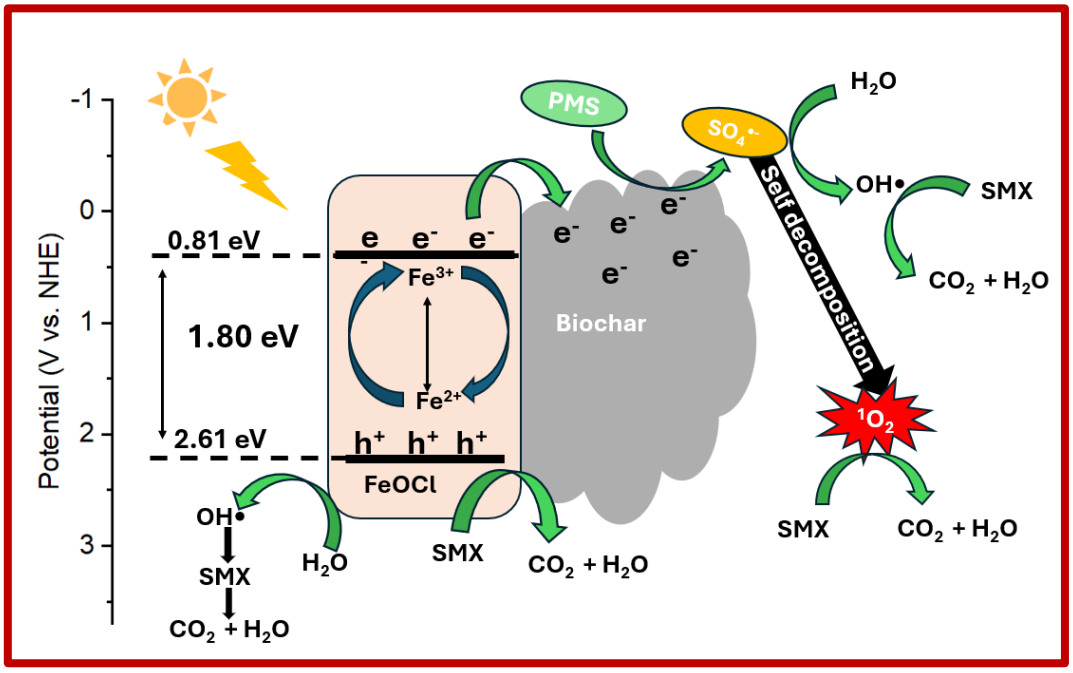

Figure 5.10 Proposed mechanism for SMX degradation over the WP-BC/FeOCl/PMS/Vis system.

5.3.8 Recyclability studies

The catalyst stability during reuse studies is an important parameter during AOPs to determine the potential applicability of the system. In this study, the WP-BC/FeOCl/PMS/VL system was reused over 5 cycles, and the efficiency was reduced from 94.9% to 80.7% (**Fig. 5.11a**). This demonstrated that the catalyst is stable and can provide potential for large-scale applications with an overall decrease in efficiency of 14.2% after five cycles. **Fig. 5.11b** displays the comparison of the FTIR spectra of the fresh and the used catalysts to determine if any changes occurred. The results demonstrated that the spectra look the same except that the OH (around 3500 cm^{-1}) and C-H (around 2500 cm^{-1}) groups in the used catalyst merged into one broad peak. This can be concluded to occur from the interaction of the catalyst and the pollutant or its degradation by-products through hydrogen bonding using OH and CH terminal functional groups. Therefore, it can be inferred that the pollutant or intermediates adsorbed on the surface of the catalyst through bonding and reduced the degradation as the catalysts were reused.

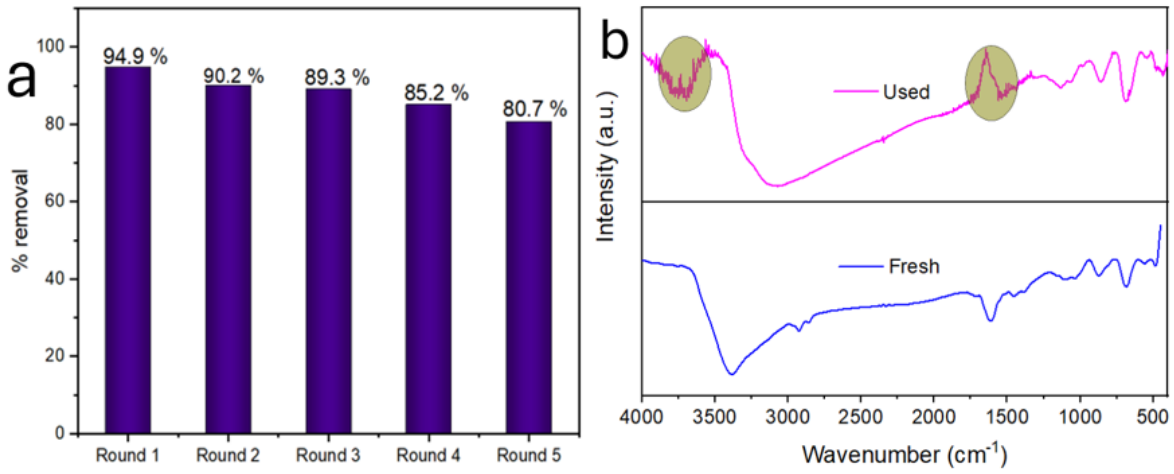

Figure 5.11 (a) Reusability studies of WP-BC/FeOCl/PMS/vis system and (b) FTIR spectra of fresh and used catalysts.

5.4 Chapter summary

BC/FeOCl nanocomposites were successfully synthesised via the wet impregnation and pyrolysis and the ultrasonic-assisted and mechanical mixing routes for peroxymonosulphate (PMS) activation in sulphamethoxazole (SMX) degradation. XRD revealed similar crystalline structures for both WP-BC/FeOCl and MM-BC/FeOCl, although the MM-BC/FeOCl composite exhibited broader peaks, suggesting smaller crystallites and minor lattice disorder induced during grinding. These structural variations directly influenced the catalytic activity and degradation efficiency of the composites. Morphological and surface analyses (SEM, TEM/HRTEM, and XPS) confirmed distinct particle geometries and a higher Fe^{2+}/Fe^{3+} ratio in the WP-BC/FeOCl composite, enabling enhanced Fe redox cycling and interfacial charge transfer. FeOCl acted as the main active component, while biochar improved dispersion and electron conduction. Although the WP-BC/FeOCl + PMS system exhibited superior degradation performance, limited mineralisation was attributed to its higher FeOCl content. Radical quenching experiments identified singlet oxygen ($^1O_2$) as the dominant reactive species responsible for SMX degradation. The findings of this study demonstrate that the synthesis strategy critically determines the physicochemical structure, redox behaviour, and reactive oxygen species pathway of

BC/FeOCl catalysts. The strong oxidant activation achieved by WP-BC/FeOCl, particularly for H_2O_2 conditions, highlights its potential for advanced oxidation processes and warrants further investigation for sustainable wastewater treatment applications.

References

[1] H. Guo, Y. Deng, H. Yin, J. Liu, S. Zou, Fabricating BiOCl nanoflake/FeOCl nanospindle heterostructures for efficient visible-light photocatalysis, Molecules. 28 (2023). https://doi.org/10.3390/molecules28196949.

[2] Z. Hao, X. Lv, W. Hou, X. Liu, Facile synthesis of BiOCl single-crystal photocatalyst with high exposed (001) facets and its application in photocatalytic degradation, Inorg. Chem. Commun. 134 (2021) 109038. https://doi.org/10.1016/j.inoche.2021.109038.

[3] L. Wang, H. Yang, Y. Yang, Z. He, A novel scheme to improve the photo-Fenton performance of iron oxychloride by carbon: Three existent states and roles of carbon in the degradation of tetracycline in water, J. Colloid Interface Sci. 641 (2023) 916–928. https://doi.org/10.1016/j.jcis.2023.03.113.

[4] R.F. Biocl, N. Photocatalysts, room temperature synthesis and photocatalytic activity of magnetically room temperature synthesis and photocatalytic, J. Clust. Sci. 24 (2013) 1115–1126. https://doi.org/10.1007/s10876-013-0602-3.

[5] D. Chaira, B.K. Mishra, S. Sangal, Efficient synthesis and characterisation of iron carbide powder by reaction milling, Powder Technol. 191 (2011) 107–113. https://doi.org/10.1016/j.powtec.2008.09.020

[6] D.E. Newbury, N.W.M. Ritchie, Is scanning electron microscopy/energy dispersive X-ray spectrometry (SEM/EDS) quantitative?, Scanning. 35 (2013) 141–168. https://doi.org/10.1002/sca.21041.

[7] S. Geng, J. Yao, L. Wang, Y. Wang, X. Wang, J. Li, Electrochemical degradation of sulphamethoxazole enhanced by bio-inspired iron-nickel encapsulated biochar particle electrode, Int. J. Mol. Sci. 25 (2024) 13579. https://doi.org/10.3390/ijms252413579.

[8] X. Zhao, Q. Li, T. Yu, M. Yang, K. Fink, X. Shen, Carbon incorporation effects and reaction mechanism of FeOCl cathode materials for chloride ion batteries, Sci. Reports. 6 (2016) 19448. https://doi.org/10.1038/srep19448.

[9] Y. Zeng, Z. Wang, P. Xu, C. Lai, H. Qin, Y. He, Y. Li, X. Huo, Q. Tian, C. Wang, Fenton chemistry rising star: Iron oxychloride, Coord. Chem. Rev. 518 (2024)

216051. https://doi.org/10.1016/j.ccr.2024.216051.

[10] T. Yu, A. Xing, S. Wang, D. Zhao, S. Liang, Well-dispersed FeOCl nanosheets as high-performance chloride ion battery cathode material, Euro. Chem. Soc. 202202454 (2022) 2454. https://doi.org/10.1002/slct.202202454.

[11] Y. Zeng, F. Wang, D. He, J. Li, H. Luo, X. Pan, Insight into iron oxychloride composite bone char for peroxymonosulphate activation: Mechanism of singlet oxygen evolution for selective degradation of organic pollutants, Chemosphere. 326 (2023) 138471. https://doi.org/10.1016/j.chemosphere.2023.138471.

[12] J. Zhao, G. Liu, Y. Zhang, J. Dong, Y. Wang, Y. Liu, H. Li, J. Xia, Fabrication of MoS_2/FeOCl composites as heterogeneous photo-Fenton catalysts for the efficient degradation of water pollutants under visible light irradiation, Colloids Surfaces A Physicochem. Eng. Asp. 648 (2022) 129357. https://doi.org/10.1016/j.colsurfa.2022.129357.

[13] K. Al-Amin, M. Kawsar, M.T.R.B. Mamun, M. Sahadat Hossain, Fourier transform infrared spectroscopic technique for analysis of inorganic materials: a review, Nanoscale Adv. 7 (2025) 6677–6702. https://doi.org/10.1039/d5na00522a.

[14] S. Chandra, P. Jagdale, I. Medha, A.K. Tiwari, M. Bartoli, A. De Nino, F. Olivito, Biochar-supported TiO_2-based nanocomposites for the photocatalytic degradation of sulphamethoxazole in water—A review, Toxics 9 (2021) 313. https://doi.org/10.3390/toxics9110313.

[15] P.A. Ajibade, A.E. Oluwalana, Photocatalytic degradation of single and binary mixture of brilliant green and rhodamine B dyes by zinc sulfide quantum dots, Molecules. 26 (2021) 23588–23606. https://doi.org/10.3390/molecules26247686.

[16] N.A. Simamane, P.J. Mafa, N. Chaukura, T.T.I. Nkambule, T.J. Malefetse, G. Mamba, Leveraging biochar/iron oxychloride heterostructures for sulphamethoxazole pollution mitigation in water: Influential factors, environmental relevance, and mechanistic insights, Sur. Inter. 72 (2025) 107351. https://doi.org/10.1016/j.surfin.2025.107351.

[17] M.E. Malefane, P.J. Mafa, P.P. Mamba, M. Managa, T.T.I. Nkambule, A.T.

Kuvarega, Induced S-scheme CoMn-LDH/C-MgO for advanced oxidation of amoxicillin under visible light, Chem. Eng. J. 480 (2024) 148250. https://doi.org/10.1016/j.cej.2023.148250.

[18] Y. Zeng, H. Qin, F. Wu, J. Gao, W. Li, J. Li, S. Wu, P. Xu, C. Lai, Z. Wang, Oxygen doping enables tailored built-In electric fields in FeOCl/g-C_3N_4 heterojunctions for enhanced peroxymonosulphate activation, Adv. Funct. Mater. 35 (2025) 1–11. https://doi.org/10.1002/adfm.202423664.

[19] F. Wen, B. Liu, S. Liu, H. Liu, C. Li, Constructing Z-scheme hollow coral-like carbon nitride/FeOCl heterojunction coupled with 1T-MoS_2 cocatalyst for efficient photocatalytic hydrogen production, Int. J. Hydrogen Energy. 205 (2026) 153302. https://doi.org/10.1016/j.ijhydene.2025.153302.

[20] R. Fiedler, R. Herzschuh, An XPS investigation of the effects of heat treatment on the chlorine surface chemistry of some lignites, Fuel. 72 (1993) 1501–1505. https://doi.org/10.1016/0016-2361(93)90007-O.

[21] D. Mao, A. Yu, S. Ding, F. Wang, S. Yang, C. Sun, H. He, Y. Liu, K. Yu, One-pot synthesis of BiOCl half-shells using microemulsion droplets as templates with highly photocatalytic performance for the degradation of ciprofloxacin, Appl. Surf. Sci. 389 (2016) 742–750. https://doi.org/10.1016/j.apsusc.2016.07.178.

[22] M. Li, J. Liu, Y. Shi, J. Yang, H. Zhang, H. Xie, D. Xia, Built-in electric field-enhanced electron super-exchange interactions for non-radical activation in ultra-thin FeOCl/g-C_3N_4 nanosheets, J. Environ. Chem. Eng. 12 (2024) 114805. https://doi.org/10.1016/j.jece.2024.114805.

[23] H. Li, L. Li, Y. Tang, X. Zhang, S. Ji, L. Luo, F. Jiang, Photoinduced RhB-sensitized effect on a novel AgI/BiOCl/biochar photocatalyst to boost its photocatalytic performance for 17α-ethinyl estradiol degradation, Sep. Purif. Technol. 332 (2024) 125774. https://doi.org/10.1016/j.seppur.2023.125774.

[24] L. Cheng, Z. Zhu, G. Wang, S. Du, g-C_3N_4 Enhanced Fe^{3+}/Fe^{2+} cycling to activate PMS for pharmaceuticals degradation under solar irradiation, Catal. Letters 155 (2025) 1–19. https://doi.org/10.1007/s10562-025-04979-w.

[25] M.E. Malefane, J.T. Khutlane, M. Managa, C.G.C.E. van Sittert, T.T.I. Nkambule, A.T. Kuvarega, Triple S-scheme BiOBr@$LaNiO_3$/$CuBi_2O_4$/Bi_2WO_6

heterojunction with plasmonic Bi-induced stability: deviation from quadruple S-scheme and mechanistic investigation, Adv. Compos. Hybrid Mater. 7 (2024) 181. https://doi.org/10.1007/s42114-024-01014-1.

[26] R. Ma, Y. Sun, H. Zhang, J. Zhu, H. Tian, X. Guo, R. Wang, X. Cui, X. Hou, S. An, Intense interaction between biochar/g-C_3N_4 promotes the photocatalytic performance of heterojunction catalysts, RSC Adv. 14 (2024) 19707–19717. https://doi.org/10.1039/d4ra03232b.

[27] Y. Xue, M. Kamali, M.E. V. Costa, I.P. Thompson, W. Huang, B. Rossi, L. Appels, R. Dewil, Activation of peroxymonosulphate by Fe,N co-doped walnut shell biochar for the degradation of sulphamethoxazole: Performance and mechanisms, Environ. Pollut. 355 (2024) 124018. https://doi.org/10.1016/j.envpol.2024.124018.

[28] M. Li, J. Liu, Y. Shi, J. Yang, H. Zhang, H. Xie, D. Xia, Built-in electric field-enhanced electron super-exchange interactions for non-radical activation in ultra-thin FeOCl/g-C_3N_4 nanosheets, J. Environ. Chem. Eng. 12 (2024) 114805. https://doi.org/10.1016/j.jece.2024.114805.

[29] Q. Yu, M. Ding, Z. Wei, J. Zhao, H. Zhang, Ginkgo biloba-derived biochar loaded with FeOCl for photo-Fenton degradation of tetracycline, Mater. Sci. Semicond. Process. 184 (2024) 108790. https://doi.org/10.1016/j.mssp.2024.108790.

[30] J. Luo, Y. Gao, T. Song, Y. Chen, Activation of peroxymonosulphate by biochar and biochar-based materials for degrading refractory organics in water: a review, Water Sci. Technol. 83 (2021) 2327–2344. https://doi.org/10.2166/wst.2021.147.

[31] Y. Huang, Y. Chen, K. Zhu, X. Wu, R. Luque, K. Yan, Visible light-assisted peroxymonosulphate activation by high-purity FeS_2 nanoplates for dye pollutant control, Appl. Phys. 2403 (2024) 10839. https://doi.org/10.48550/arXiv.2403.10839.

[32] Z. Wang, J. Ali, A. Shahzad, Y. Chen, H. Ma, Q. Huang, L. Xie, F. Xing, Boosting PMS activation through Fe_3S_4/WO_3: The essential impact of WX and SX on catalyst activity and regeneration Fe active sites for efficient pollutant removal, Catalysts. 15 (2025) 230. https://doi.org/10.3390/catal15030230.

[33] G. Liu, Q. Wang, L. Dong, X. Zhang, M. Zhang, P. Rao, N. Gao, W. Zhang, J. Deng, New insights into dual metals boost PMS activation over iron tungstate: The role of surface hydroxyl, Sep. Purif. Technol. 352 (2025) 128147. https://doi.org/10.1016/j.seppur.2024.128147.

[34] J. Gao, J. Xue, Q. Shen, T. Liu, X. Zhang, X. Liu, H. Jia, Q. Li, Y. Wu, A promoted photocatalysis system trade-off between thermodynamic and kinetic via hierarchical distribution dual-defects for efficient H2 evolution, Chem. Eng. J. 431 (2022). https://doi.org/10.1016/j.cej.2021.133281.

[35] P. Shao, X. Yin, C. Yu, S. Han, B. Zhao, K. Li, X. Li, Z. Yang, Z. Yuan, Q. Shi, J. Ren, H. Hu, K. Cui, T. Li, J. Jiang, Enhanced activation of peroxymonosulphate via sulphate radicals and singlet oxygen by SrCoxMn1−xO_3 Perovskites for the degradation of rhodamine B, Processes. 11 (2023). https://doi.org/10.3390/pr11041279.

[36] Z. Wang, L. Liang, N. Li, S. Wu, Z. Cheng, B. Yan, G. Chen, Peroxymonosulphate activation by Bi-Fe oxide co-doped graphitic carbon nitride for degradation of sulphamethoxazole: Performance and mechanism, Appl. Sci. 14 (2024). https://doi.org/10.3390/app14083181.

[37] T.S. Ntelane, U. Feleni, N.H. Mthombeni, A.T. Kuvarega, Heterogeneous activation of persulphate using delafossite $AgFeO_2$/α-MnO_2 for efficient degradation of tartrazine under visible light, Colloids Surfaces A Physicochem. Eng. Asp. 670 (2023) 131492. https://doi.org/10.1016/j.colsurfa.2023.131492.

[38] G. Dong, B. Chen, B. Liu, Y. Cao, B. De Jourdan, S.R. Stoyanov, J. Ling, X. Ye, K. Lee, B. Zhang, Comparison of O_3, UV/O_3, and UV/O_3/PS processes for marine oily wastewater treatment: Degradation performance, toxicity evaluation, and flocs analysis, Water Res. 226 (2022) 119234. https://doi.org/10.1016/j.watres.2022.119234.

[39] J. Zhang, W. Zhao, Z. Li, G. Lu, M. Zhu, Visible-light-assisted peroxymonosulphate activation over Fe(II)/V(IV) self- doped $FeVO_4$ nanobelts with enhanced sulphamethoxazole degradation : Performance and mechanism, Chem. Eng. J. 403 (2021) 126384. https://doi.org/10.1016/j.cej.2020.126384.

[40] M. Li, D. Xia, H. Xu, Z. Guan, D. Li, Iron oxychloride composite sludge-derived

biochar for efficient activation of peroxymonosulphate to degrade organic pollutants in wastewater, J. Clean. Prod. 329 (2021) 129656. https://doi.org/10.1016/j.jclepro.2021.129656.

[41] B. Nie, H. Dong, J. Yan, S. Zhang, S. Zhong, Enhanced oxidative degradation of 2,4-dichlorophenol by iron oxychloride supported on graphitic carbon nitride via peroxymonosulphate activation: Significant role of Fe(II)/Fe(III) conversion cycle, Environ. Res. 264 (2025) 120398. https://doi.org/10.1016/j.envres.2024.120398.

[42] S. Wang, J. Wang, Radiation-induced degradation of sulphamethoxazole in the presence of various inorganic anions, Chem. Eng. J. 351 (2018) 688–696. https://doi.org/10.1016/j.cej.2018.06.137.

[43] Y. Shi, J. Li, D. Wan, J. Huang, Y. Liu, Science of the total environment peroxymonosulphate-enhanced photocatalysis by carbonyl-modified g-C_3N_4 for effective degradation of the tetracycline hydrochloride, Sci. Total Environ. 749 (2020) 142313. https://doi.org/10.1016/j.scitotenv.2020.142313.

[44] Z. Gao, X. He, W. Li, K. Xiong, Insitu carbon coated TiO_2 boosting the visible light photocatalytic hydrogen evolution, Appl. Sur. Sci.565 (2015) 150554. https://doi.org/10.1016/j.apsusc.2021.150554.

[45] H. Zhang, Z. Yan, J. Wan, Y. Wang, G. Ye, S. Huang, C. Zeng, J. Yi, Synthesis of Fe-Nx site-based iron-nitrogen co-doped biochar catalysts for efficient removal of sulphamethoxazole from water by activation of persulphate: Electron transfer mechanism of non-free radical degradation, Colloids Surfaces A Physicochem. Eng. Asp. 654 (2022) 130174. https://doi.org/10.1016/j.colsurfa.2022.130174.

[46] H. Zhang, M. Zhang, H. Zhang, T. Yu, C. Qu, Recent development of sludge biochar-based catalysts in advanced oxidation processes for removing wastewater contaminants: A review, Fuel 348 (2023) 128444. https://doi.org/10.1016/j.fuel.2023.128444.

[47] X. Chen, S. Qian, Y. Ma, J. Zhu, S. Shen, J. Tang, Y. Ding, S. Zhi, K. Zhang, L. Yang, Z. Zhang, Efficient degradation of sulphamethoxazole in various waters with peroxymonosulphate activated by magnetic-modified sludge biochar:

Surface-bound radical mechanism, Environ. Pollut. 319 (2023) 121010. https://doi.org/10.1016/j.envpol.2023.121010.

[48] W. Qin, J. Peng, J. Yang, Y. Song, J. Ma, UV absorbance and electron donating capacity as surrogate parameters to indicate the abatement of micropollutants during the oxidation of Fe(II)/PMS and Mn(II)/NTA/PMS, Environ. Res. 232 (2023). https://doi.org/10.1016/j.envres.2023.116253.

[49] T.I. Nkambule, R.W.M. Krause, J. Haarhoff, B.B. Mamba, A three step approach for removing organic matter from South African water sources and treatment plants, Phys. Chem. Earth 50–52 (2012) 132–139. https://doi.org/10.1016/j.pce.2012.08.009.

[50] X. Zhang, P. Sun, K. Wei, X. Huang, X. Zhang, Enhanced H_2O_2 activation and sulphamethoxazole degradation by Fe-impregnated biochar, Chem. Eng. J. 385 (2020) 123921. https://doi.org/10.1016/j.cej.2019.123921.

[51] N. Li, X. He, J. Ye, H. Dai, W. Peng, Z. Cheng, B. Yan, G. Chen, S. Wang, H_2O_2 activation and contaminants removal in heterogeneous Fenton-like systems, J. Hazard. Mater. 458 (2023) 131926. https://doi.org/10.1016/j.jhazmat.2023.131926.

[52] P. Compton, D. Nr, L.C. P, A. An, Promoting charge separation of biochar-based Zn-TiO_2/pBC in the presence of ZnO for efficient sulphamethoxazole photodegradation under visible light irradiation, Sci. Total Environ. 659 (2023) 529-539. https://doi.org/10.1016/j.scitotenv.2018.12.401.

[53] M. Zhang, Z. Wen, L. Zhang, Q. Wang, L. Zang, Q. Feng, Y. Gu, W. Wang, K. Ma, H. Zhang, D. Ji, J. Liu, X. Shi, F. Yu, Radical and non-radical peroxymonosulphate activation induced by a novel ferromagnetic Fe1-xS/lignin-based biochar nanocomposite: Multi-pathway synergistic effects for bisphenol A removal, Chem. Eng. J. 520 (2025) 166153. https://doi.org/10.1016/j.cej.2025.166153.

[54] G. Liang, Z. Yang, Z. Wang, X. Cai, X. Zhang, X. Xie, Relying on the non-radical pathways for selective degradation organic pollutants in Fe and Cu co-doped biochar/peroxymonosulphate system: The roles of Cu, Fe, defect sites and ketonic group, Sep. Purif. Technol. 279 (2021) 119697.

https://doi.org/10.1016/j.seppur.2021.119697.

[55] G. Liang, Z. Yang, Z. Wang, X. Cai, X. Zhang, X. Xie, Relying on the non-radical pathways for selective degradation of organic pollutants in Fe and Cu co-doped biochar / peroxymonosulphate system : The roles of Cu, Fe, defect sites and ketonic group, Sep. Purif. Technol. 279 (2021) 119697. https://doi.org/10.1016/j.seppur.2021.119697.

CHAPTER 6

CONCLUSION AND RECOMMENDATIONS

6.1 Conclusion

This study successfully demonstrated the development and application of biochar-supported iron oxychloride (BC/FeOCl) nanocomposite as a multifunctional catalyst for the degradation of sulphamethoxazole (SMX) in aqueous systems. Through a systematic investigation, the research highlighted how coupling FeOCl with biochar enhances physicochemical and catalytic properties, leading to improved pollutant degradation performance under visible light-driven and advanced oxidation conditions. In the first part of the study, the 6-BC/FeOCl composite was synthesised via an ultrasonic-assisted wet impregnation and calcination method. Comprehensive characterisation using TEM, SEM, XRD, XPS, FTIR, and BET confirmed the formation of a well-defined nanocomposite with improved surface area, charge separation, and redox characteristics. Compared with pristine FeOCl, the composite exhibited significantly enhanced photocatalytic activity, achieving up to 90.1% SMX removal under optimal conditions (10 mg L^{-1} SMX, 0.2 g L^{-1} catalyst, pH 5). This superior performance was attributed to the synergistic interface between biochar and FeOCl, which facilitated efficient electron transfer, suppressed charge carrier recombination, and provided enhanced pollutant adsorption. Reactive species analysis revealed that hydroxyl radicals (•OH) and photogenerated holes (h^+) were the dominant contributors to SMX degradation, underscoring the hybrid mechanism of oxidative and photonic processes.

Building upon the demonstrated synergistic interaction between biochar and FeOCl, particularly the enhanced charge transfer, redox activity, and pollutant adsorption observed in the photocatalytic system (**Chapter 4**), the second part of the work (**Chapter 5**) explored the catalytic performance of BC/FeOCl prepared through a wet impregnation and pyrolysis method and an ultrasonic assisted mechanical mixing towards peroxymonosulphate (PMS) activation. The WP-BC/FeOCl nanocomposite demonstrated superior degradation efficiency (94.9%) compared to its MM-BC/FeOCl counterpart (82.3%) in 120 min, primarily due to its higher Fe^{2+} content, improved morphology, and greater oxidative potential. The main reactive species were identified

as singlet oxygen ($^1O_2$), followed by sulphate and hydroxyl radicals ($SO_4^{\bullet-}$), indicating that the degradation proceeded via a nonradical–radical mixed pathway. These results emphasized the critical role of synthesis methods and catalyst composition in determining the reactivity and stability of Fe-based materials for sulphate radical advanced oxidation processes (SR-AOPs). To further evaluate and extend the applicability of the developed photocatalyst, H_2O_2 activation was investigated using the WP-BC/FeOCl/visible light system. The overall degradation efficiency reached 91.8% within 120 min, which was comparable to both photocatalysis (90.1%) and PMS activation (94.8%). However, a distinct difference was observed in the initial stages of the reaction. Within the first 20 min, H_2O_2 activation exhibited the highest SMX removal (89.0%), outperforming PMS activation (77.0%) and photocatalysis alone (51.0%). This rapid degradation performance highlights the strong synergistic interaction between H_2O_2 and FeOCl, where the biochar-supported FeOCl facilitated the decomposition of H_2O_2 through Fe^{2+}/Fe^{3+} redox cycling, resulting in the generation of abundant hydroxyl radicals and enhanced oxidative degradation of SMX. Optimal degradation occurred under slightly acidic conditions, consistent with the behaviour of Fe-based Fenton-like systems, while excessive oxidant concentrations led to the self-scavenging of reactive oxygen species. These findings confirmed that the biochar–FeOCl interface effectively promotes H_2O_2 activation by enhancing electron transport, increasing surface reactivity, and improving the accessibility of Fe active sites further validating the composite's efficiency beyond photocatalysis alone.

Overall, this study provides comprehensive insight into the design, synthesis, and mechanism of BC/FeOCl composites for the degradation of antibiotic contaminants in water. The integration of biochar was shown to play a critical role in stabilizing FeOCl, enhancing visible-light absorption, facilitating charge separation, and providing additional adsorption and redox-active sites. As a result, the 6-BC/FeOCl catalyst achieved superior catalytic performance and excellent stability, maintaining high degradation efficiency over multiple reaction cycles. These findings underscore the environmental significance and versatility of BC/FeOCl nanocomposites as robust, multifunctional catalysts for pollutant removal in water. The synergistic contributions of heterojunction formation, Fe^{2+}/Fe^{3+} cycling, and biochar support present a scalable route for advanced oxidation processes, offering a promising and sustainable strategy to mitigate pharmaceutical pollution in both natural and engineered water systems.

6.2 Recommendations

The following recommendations are proposed to guide future work on BC/FeOCl-based PMS and photocatalytic systems for SMX removal, with specific emphasis on catalyst design, long-term stability, degradation pathways, and oxidant utilisation.

- The clear dependence of PMS activation efficiency on the synthesis route highlights the need for data-driven optimisation of material composition. Future work could employ artificial intelligence and machine-learning models to correlate synthesis parameters (biochar properties, Fe speciation, calcination conditions, and interfacial chemistry) with catalytic performance, enabling predictive design of BC/FeOCl composites with optimised redox behaviour and pollutant removal efficiency.
- While this study demonstrated effective SMX degradation, real wastewater contains mixtures of pharmaceuticals and emerging contaminants. Future studies should therefore evaluate the performance of BC/FeOCl across a broad spectrum of pharmaceutical compounds with varying structures and reactivities to assess the versatility and selectivity of the material.
- The practical applicability of PMS-based systems requires understanding not only pollutant removal but also the toxicity of treated water. Future work should include ecotoxicological assessment of treated samples to determine whether degradation leads to detoxification or formation of harmful transformation products.
- In this work, reactive species responsible for degradation were identified; however, the degradation pathway and intermediate products were not investigated due to the unavailability of LC-MS instrumentation. Future studies employing LC-MS analysis are necessary to map transformation pathways and confirm complete mineralisation of SMX, particularly under PMS activation condition
- The observed decline in degradation efficiency at elevated oxidant concentrations for both PMS and H_2O_2 systems highlights the need for strategies that improve oxidant utilisation rather than increasing oxidant dosage. Future work should therefore prioritise catalyst-centred optimisation, such as enhanced light-assisted PMS activation or sequential adsorption–

oxidation approaches, to achieve efficient SMX removal under more sustainable operating conditions.

APPENDICES

A1: Mott-Schottky analysis of (a) FeOCl, (b) 6-BC/FeOCl

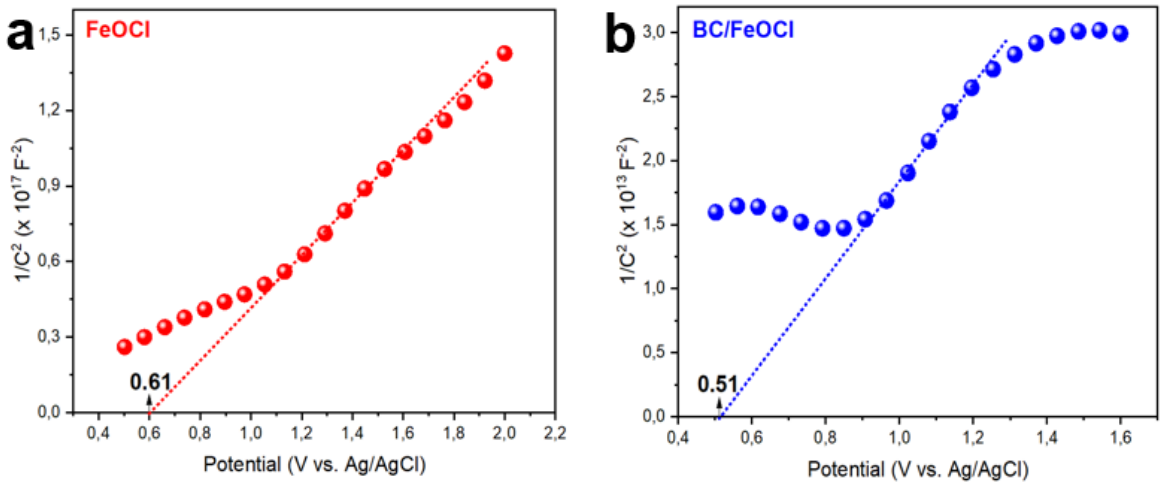

A2: Pseudo first order kinetics plots for SMX degradation (a) using different catalysts, (b) effect of SMX concentration, (c) effect of catalyst dosage, and (d) pH optimization using 6-BC/FeOCl

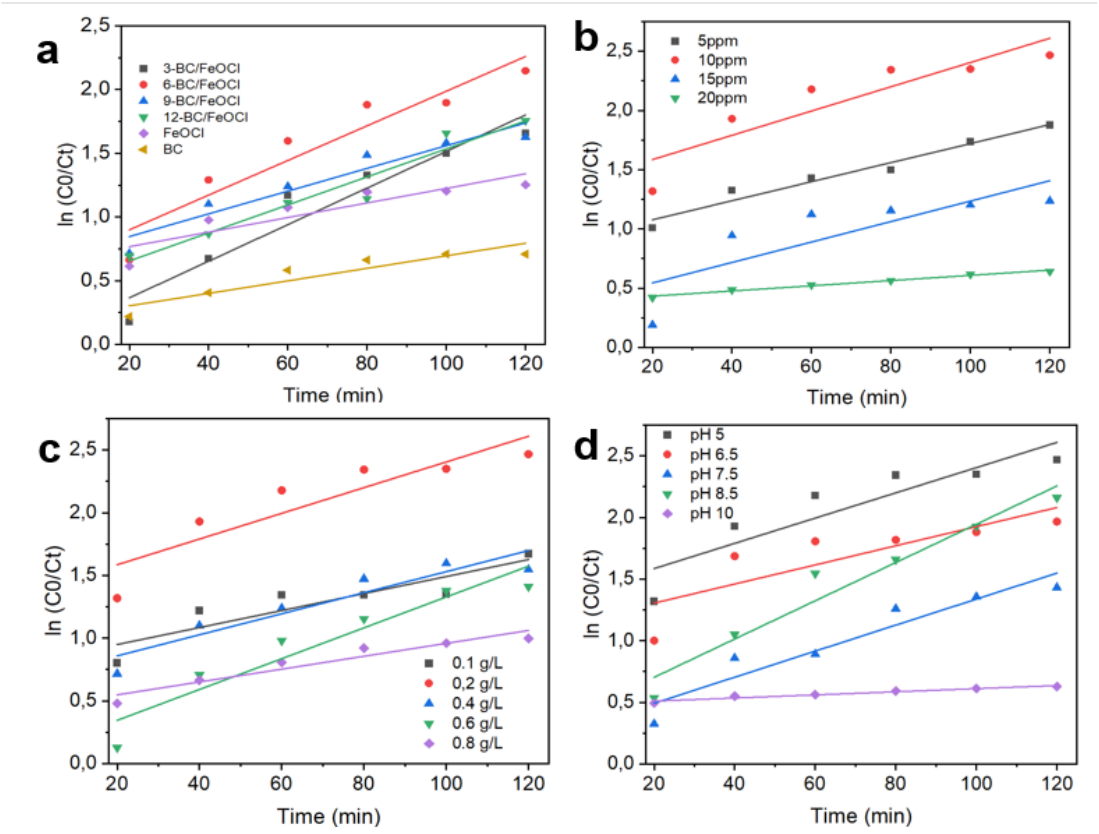

A3 (a) SEM of FeOCl and (b) TEM of FeOCl.

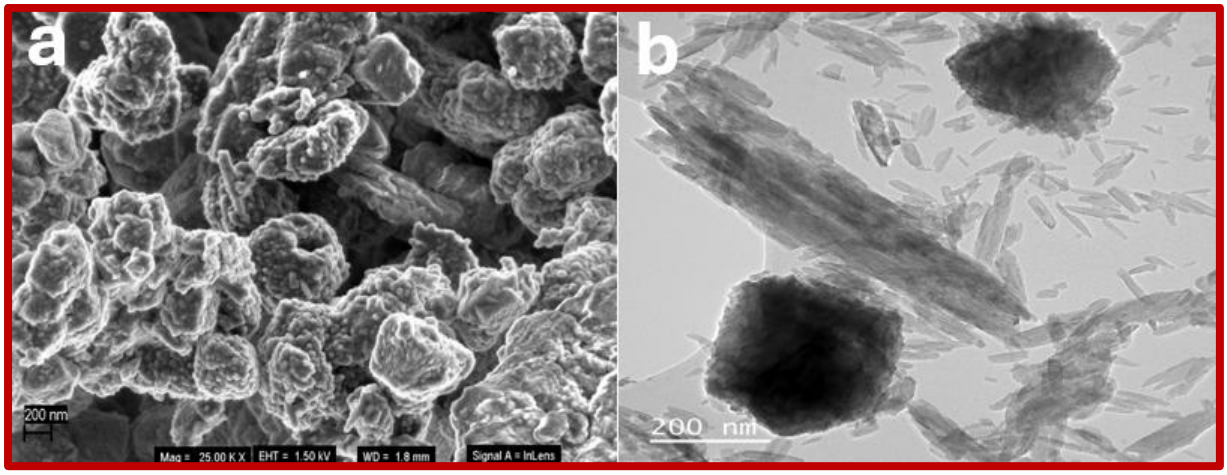

A4: XRD analysis for FeOCl

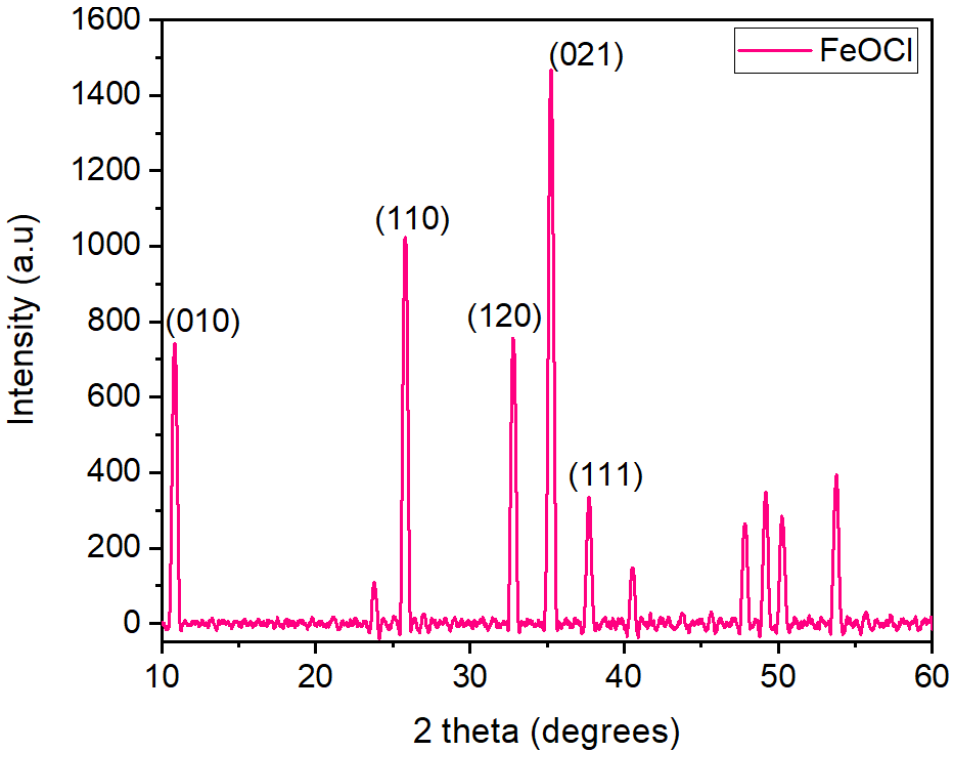

Figure: A5 Tauc plots for (a) FeOCl, (b) MM-BC/FeOCl and (c) WPBC/FeOCl

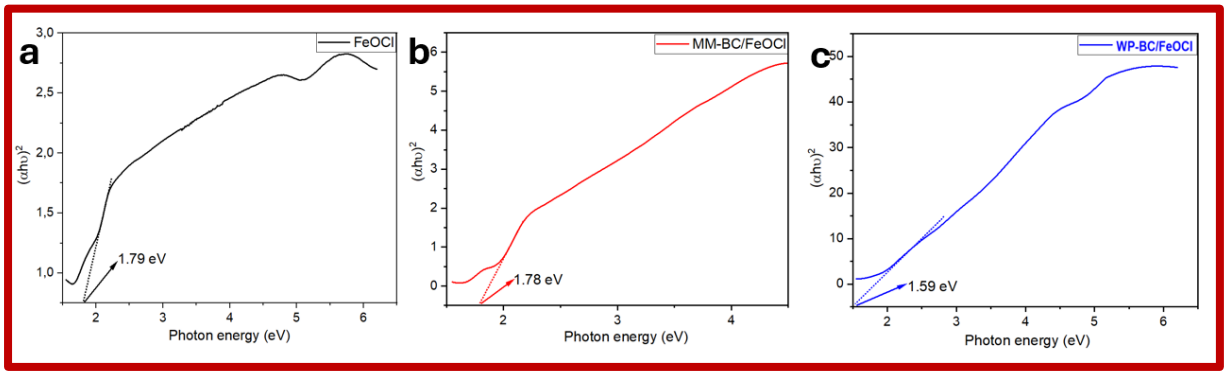

Table: A6. XPS elemental composition of WPBC/FeOCl.

Name	Peak BE	Atomic %
C 1s	285.7	40.29
O 1s	532.2	31.17
Cl 2p	199.9	17.42
Fe 2p	712.4	10.94
N 1s	401.9	0.18

Table: A7. XPS elemental composition of MM-BC/FeOCl.

Name	Peak BE	Atomic %
C 1s	285.1	52.46
O 1s	531.0	35.52
Fe 2p	711.5	9.21
Cl 2p	199.7	2.06
N 1s	400.1	0.75

A8: Pseudo first order kinetics plots for SMX degradation (a) using different catalysts, (b) effect of SMX concentration, (c) effect of PMS concentration, (d) effect of catalyst dosage and (e) pH optimization using 6WPBC/FeOCl

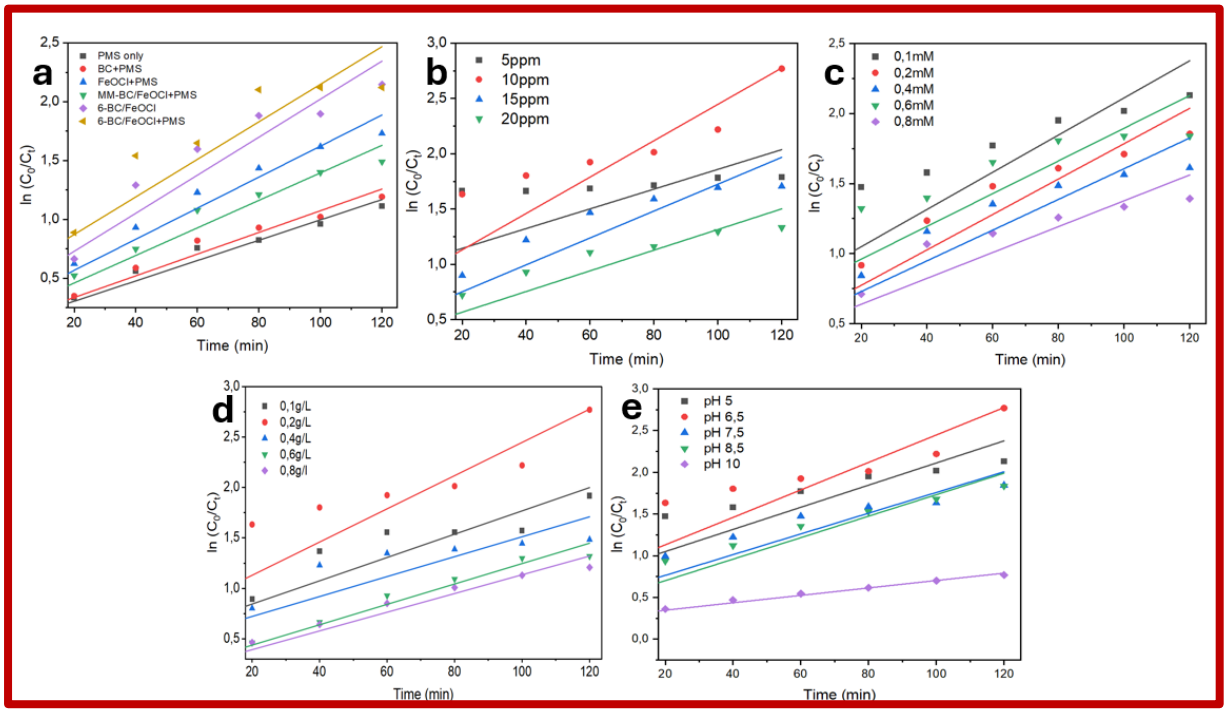

Table: A9. Different organic compounds found in water and detected in five different regions on the fluorescence excitation-emission matrix (FEEM)

Description	**Excitation max (nm)**	**Emission max (nm)**
UV humic-like, less aromatic	<260	380-460
Visible humic-like, more aromatic	320-360	420-460
Marine humic-like	290-310	370-410
Tyrosine-like substances	260	280
Protein-like Tryptophan	250-300	305-355